The People's Democratic Republic of Algeria

Ministry of Higher Education and Scientific Research

Amar Telidji University - Laghouat

Faculty of Sciences

Doctoral thesis

Specialty: Material Physics

Publicly presented on 19/10/2021
by:

SARI Ibrahim

THEME

Study of the Effect of Forced Convection by Electromagnetic Stirring on the Phase Change Process: Application on the Metallic Alloy Solidification

Thesis committee:

LEFKAIER Iben Khaldoun	**President**	Professor, Laghouat University
HACHANI Lakhdar	Supervisor	Professor, Laghouat University
ZAIDAT Kader	Co-supervisor	Ass-Prof , Grenoble inp University
BELGACEM-BOUZIDA Aissa	**Examiner**	Professor, Batna University
BOTTON Valery	**Examiner**	Professor, INSA-Lyon University
BACHIRI Mohamed	**Examiner**	Ass-Prof, Laghouat University
KHARICHA Abdellah	**Invited**	Ass-Prof, Montanuiniversitaet Leoben-Austria

Acknowledgement

No thesis manuscript would be complete without words of thanks to the people who contributed to its completion. Because one thing is certain, throughout this period of work I was not alone behind this thesis project. Many people were by my side, encouraged me and finally helped me to accomplish a difficult work.

Firstly, and mostly, I thank the almighty ALLAH for his mercy and grace, which enabled me to complete this work.

I will start by addressing my thankful gratitude to the person who actually gave me the great opportunity to write this thesis, my supervisor Prof. Lakhdar HACHANI. He always trusted me and encouraged me to continue this work. Without his persistent help, the goal of this project would not have been realized. I have known an exceptional man both on the scientific level with an extraordinary rigor and on the human level where I have known a man who makes me want to be like him. Thank you for everything Lakhdar!

My thanks and appreciations go toward Sir Kader ZAIDAT my co-supervisor for having directed my thesis in your respectful laboratory: the EPM/SIMaP of Grenoble University, and for having done everything possible to make this work successful. It is really honor to work under your supervision.

I thank respectfully Associate Prof. Abdellah KHARICHA who assisted me during my stay in Leoben (and even after) for his useful contribution and collaboration in the numerical simulation domain. It is your kind help and support that have made my study and life in Austria a wonderful time. It has been an honor to know you and to have worked with you.

I also thank Prof. Yves Fautrelle for his advice and support throughout my work and especially for his assistance in publishing my article.

My sincere gratefulness is dedicated to the thesis committee members, President LEFKAIER Iben Khaldoun, the examiners: Prof. BELGACEM-BOUZIDA Aissa, Prof.

BOTTON Valery and Associate Prof. BACHIRI Mohamed for taking time to assess this work and to attend the PhD defense.

I wish to acknowledge the support and great love of my family, my Father, Mohamed; my mother, Fatima Zahra; my brother Mahmoud and my sisters. They kept me going on and this work would not have been possible without their input.

I also thank all the staff of the LPM laboratory, the director Lefkaier Iben khaldoun and all the permanent, PhD students, and other, who allowed me to achieve my thesis work in a good conditions, and especially to A. Abdelhafidh, all my wishes of success for your PhD.

I do not forget to send my most sincere thanks to all the staff of the EPM laboratory of Grenoble University, and Christian-Doppler Laboratory for Metallurgical Applications of Magnetohydrodynamics of Leoben University, for the welcome and the honorable reception that they have reserved for me during my long stay in their honorable laboratories.

The Algerian Ministry of higher education and scientific research is highly appreciated for its financial support during my scholarship (PNE) period.

I cannot forget my family and all my friends who have always supported me during these years of study.

Thanks to all those I could have forgotten but who also brought a contribution to the achievement of this thesis.

SUMMARY

Chapter III: Enthalpy approach for modelling solidification processes

Chapter IV: A three phase columnar model for metallic alloy solidification

Figures list

Tables list

Nomenclatures

CR	Cooling rate, ($K\ s^{-1}$).
G	Thermal gradient, ($K\ m^{-1}$).
T	Temperature, (K).
T_m	Melting temperature, (K).
T_L	Liquidus temperature, (K).
T_S	Solidus temperature, (K).
ΔT	Melting temperature range, (K).
DT	Thermal gradient, (K).
uc	Initial undercooling, ($°C$)
C_l	Liquidus concentration, ($wt.\ \%$).
C_s	Solidus concentration, ($wt.\ \%$).
C_0	Initial concentration, ($wt.\ \%$).
C_l^*	Liquid concentration at the tip, ($wt.\ \%$).
C_s^*	Solid concentration at the tip, ($wt.\ \%$).
C_1	Liquid concentration at the enveloped cylinder.
$C_{0\ avr}$	Liquid average concentration.
C_l^{inter}	Inter dendritic concentration.
C_{mix}	Mixture concentration.
$C_{mix(coarsening)}$	Mixture concentration during the coarsening.
k	Partition coefficient.
m_l	Liquidus slope, ($K\ wt\%^{-1}$).
C_p	Specific heat, ($J\ kg^{-1}\ K^{-1}$).
ΔH_f	Latent heat of fusion, ($J\ Kg^{-1}$).
μ	Dynamic viscosity, ($Pa\ s$).
ρ	Density, ($kg\ m^{-3}$).
λ	Thermal conductivity, ($W\ m^{-1}\ K^{-1}$).
h	Enthalpy, ($J\ kg^{-1}$).
p	Pressure, (Pa).
L	Latent heat, ($J\ kg^{-1}$).
S	Porosity.
D	Gaussian distribution.
ρ_l	Liquid density, ($Kg\ m^{-3}$).
λ_l	Liquid thermal conductivity, ($W\ m^{-1}\ K^{-1}$).
λ_s	Solid thermal conductivity, ($W\ m^{-1}\ K^{-1}$).
β_T	Thermal expansion coefficient, (K^{-1})
β_c	Solutal Thermal expansion coefficient, (K).
D_l	Liquid diffusion coefficient, ($m^2\ s^{-1}$).
A_m	Coefficient of mushy zone.
g	Acceleration of gravity, ($m.s^{-2}$).
U	Characteristic velocity, ($m\ s^{-1}$).
U_T	Projected velocity, (m/s)

$\vec{u}$	Velocity field, ($m\ s^{-1}$).
f_l	Liquid fraction.
f_s	Solid fraction.
α_s^c	Volume fraction of solid phase.
α_d^c	Volume fraction of inter dendritic phase.
ΔG_n	The activation energy, (*Watt*).
k_b	Boltzmann constant.
t_f	Local solidification time, (s).
ΔT_T	Thermal undercooling, (K).
ΔT_c	Chemical undercooling, (K).
ΔT_r	Gibbs-Thomson undercooling, (K)
Γ	Gibbs Thomson coefficient, ($m\ K$).
K_l	The curvature of the interface, (m^{-1}).
δc	Diffusion distance. (m)
Ω	Suppersaturation.
I_v	Ivantsov function.
R_{tip}	Tip radius, (m)
V_{tip}	Tip velocity, (m s^{-1})
F	Lorentz force, (N)
$F_{flottability}$	Buoyancy force, (N)
$F_{braking}$	Darcy term.
E_a	The activation energy, ($J.mol^{-1}$).
E_1	The integral exponential function.
r_c	Cylinder radius, (m)
K	Permeability, **(m^2)**
λ_1	Primary dendrite arm spacing (PDAS), (m)
λ_2	Secondary dendrite arm spacing (SDAS), (m)
a	Characteristic length, (m).
$\vec{B}$	Magnetic induction, (T).
B_0	Amplitude of the magnetic field, (T)
$\vec{A}$	Magnetic vector potential, (T).
A_0	Amplitude of the vector potential, ($T.m$)
$\vec{J}$	Current density, ($A\ m^{-2}$).
I	Current, (A).
$\vec{E}$	Electric fields, ($V\ m^{-1}$).
σ	Electrical conductivity, ($\Omega^{-1}m^{-1}$).
μ	Magnetic permeability, ($H.m^{-1}$).
ω	Magnetic field pulsation, (Hz).
φ	Electrical potential, (V).
$\vec{F}$	Lorentz force, (F).
ρ_{elc}	Electrical resistivity, ($\mu\Omega\ cm$).
f	Frequency, (Hz).

J_{TE}	Thermoelectric current, ($A\ m^{-2}$).
F_{TE}	Laplace force of thermoelectric origin, (N).
F_0	The magnitude force
φ	Electric potential, (V)
k^*	Wave number in narrow liquid domain, (m^{-1})
Dimensionless number	
Re	Reynolds number
Rm	Magnetic Reynolds number
Gr_T	Thermal Grashof number
Pr	Prendtl number
N_m	Non-dimensional interaction parameter
R_m	Magnetic Reynolds number.
U_{Alf}	Alfvén velocity.
N	Interaction parameter.
H_a	Hartman number**.**
Pe	Peclet number.
Subscripts	
l	Liquid
s	Solid
x, y, z	Directions
exp	Experimental
num	Numerical
L, H, W	Length, height and width of the cavity, (mm)

GENERAL INTRODUCTION

The solidification process of pure metals and metal alloys is accompanied by a hydrodynamic movement in the liquid phase, associated with heat transfers that take place in the liquid and solid zones and in particular at the liquid/solid interface. The flows in the liquid phase are mainly caused by the effect of thermosolutal convection due to a heterogeneous distribution of temperature and species fields in the case of alloys. Convection can also be caused by an external force (e.g., electromagnetic stirring).

In metallic alloys, the convective movements occurring within the liquid zones during solidification play a dominant role on the growth dynamics. This influence is even more evident in metallic alloys which, in addition to thermal convection, are subject to solutal convection due to the segregation of the alloy elements. This segregation is often the source of large compositional heterogeneities within the materials obtained. These segregations are detected at the micro-scale (the micro-segregation), which is the source of all segregations, directly affect the mechanical and chemical properties of the material. The study of these phenomena is therefore importance.

The aim of this thesis is to develop reliable numerical models for the simulation of the solidification of pure materials (tin) and metal alloys (tin-lead) in a furnace similar to those used in horizontal Bridgman growth. The geometry considered is a differentially heated parallelepipedic cavity corresponding to the crucible of the 'AFRODITE' experimental setup developed in the SIMAP-EPM laboratory in Grenoble. Two 3D numerical models (two-phase models) were proposed to control the effects of natural and forced convection on the solidification process of pure tin, based on the resolution of the momentum, energy and electromagnetic equations (in the case of forced convection) with a Cerman-Kozney term to take into account the mushy zone. Another 2D model (three-phase model) based on the resolution of the momentum, energy and solute equations to simulate the solidification of metallic alloys (tin-lead) under thermosolutal convection will be performed. All the numerical results obtained will be systematically compared with the results of the AFRODITE experiment in order to validate them, and then discussed. This 2D model gave significant results to the physical reality despite the non-taking into account of the friction in the liquid bath along the side walls (no slip condition). However, the 3D model remains very expensive in terms of computation time.

This thesis carried out as part of the PNE project (*Programme National Exceptionnel*), is the result of a collaboration between three scientific research structures: the Laboratory of Physics of Materials (LPM) of Amar Telidji University of Laghouat/Algeria, the laboratory of Sciences and Engineering of Materials and Processes (SIMaP/EPM) of Grenoble/ France and Christian-Doppler Laboratory for Metallurgical Applications of Magnetohydrodynamics of Leoben University/Austria.

This thesis has four chapters:

The first chapter, is a bibliography. It summarizes the different basic notions related to the phenomenon of solidification of pure substances and metallic alloys, and establishes the basis on which the rest of the work will be based. It also provides a brief overview of the studied subject and the equation models.

The second chapter, will deal with the basic principles of magneto-hydro-energetics (MHE) and its application in the field of solidification of metallic alloys. A summary of previous work, dealing with the effect of different configurations of electromagnetic stirring on the solidification process, will be presented in this chapter.

The third chapter, deals with the solid-liquid phase change of pure substances (pure tin) under the effect of natural and forced convection. Also, part of this chapter will be devoted on the description of the experimental setup 'AFRODITE' used as a benchmark for the numerical models developed in this chapter and in the following chapter. The numerical method used is based on the enthalpic approach with a fixed mesh (Front tracking) is also detailed.

The fourth chapter, is devoted to the numerical simulation of a three-phase model based on Ivantsov dendrite growth. We are interested in the formation of the microsegregation that occurs during the solidification of binary metal alloys (tin-lead) with the development of a mushy zone through the description of the phase diagram. In order to confirm the numerical results, comparisons with experimental results will be realized (e.g., qualitative comparison with X-ray of the solidified ingot).

CHAPTER I
Fundamental notions of solidification

I.1 Introduction

This chapter is devoted to a synthesis study of the solidification concepts of pure metals and binary alloys, in particular those phenomena that occur during the phase change process especially for the thermal (latent heat of the phase change) and solute transports phenomena at the level of solid-liquid instabilities interface. As well as the presentation of the different grain structures obtained during the solidification process (growth kinetics). In specific, a description of the formation of structures (columnar or equiaxed) originating from the solidification of two essential phenomena: the germination-growth of the microstructure as well as the transition between the two forms of structures, including the CET (column-equiaxed transition). The emphasis is then on the phenomenon of segregation (the effect of the convection in the mushy zone) and the main factors that can influence it.

Generally, the main factors that control segregation are:

- The cooling rate *CR* (*K/s*).
- The thermal gradient *G* (*K/m*).
- The orientation of the grain.
- The re-melting phenomenon.
- The permeability of the solid in the mushy zone.
- The exchange of the solute.

I.2 Thermodynamic aspects through phase diagram

In this part, the notions on solidification of pure metals and metal alloys are largely inspired by classical and fundamental references in the field of solidification, such as Flemings [1], Kurz and Fisher [2] and Rappaz *et al* [3]. The main aim is to understand the basics of the solidification of pure metals and metallic alloys that will be developed in more detail in the continuation of this work.

I.2.1. Solidification diagram of pure and binary metallic alloy

The solidification, or solid-liquid phase change, is the transition from the liquid state to the solid. When a pure material is cooled, at constant pressure, the phase change occurs always at a constant temperature; this latter is the melting temperature. At this melting point, both liquid and solid phases of the material co-exist. During the solid-liquid phase change, the melting point is usually defined by melting temperature only. In the case of pure metal, primarily in a

liquid state (molten) which is then slowly cooled in a crucible until its completely cooled, this cooling curve is achieved by recording the change of the temperature at each point within the process over time.

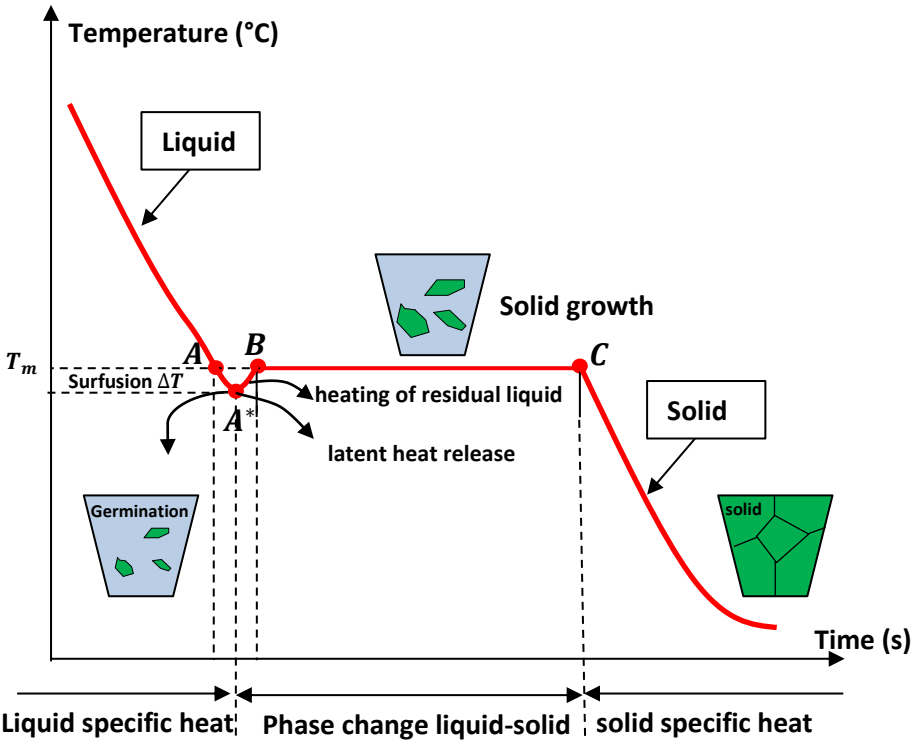

Fig. I.1. Typical changes in the temperature of a pure material during its solidification. T_m is the melting temperature.

Fig.I.1 presents the typical cooling curve of a pure metal. This curve is divided into three separate parts. Firstly (from the beginning to point A), a decrease in temperature corresponding to the cooling of the liquid metal is observed. It ends at the melting temperature T_m (at point A) when the first solid crystals are formed (first crystals appear in the liquid melt). The second phase is the isothermal stage (from B to C) in which the temperature remains constant and equal to the melting temperature, and here both solid and liquid phases of the material coexist. In the beginning, the first solid crystals are hardly formed; these crystals then grow until the liquid phase around the melting point has completely disappeared (at point C); the metal is then completely solidified (from C to the end). This isothermal plateau become larger as the cooling is slower and the mass solidified is greater. Since solidification is an exothermic phenomenon, latent heat is rejected along this plateau. The third part (beyond point C) is the temperature decrease corresponding to the cooling of the solid metal. The heat extracted during the two temperatures decrease (temperature of the liquid, then of the solid) is a sensible heat, while the heat rejected during the isothermal stage is a latent heat (latent heat release); it is the latent heat of solidification. In addition, undercooling may occur however the cooled liquid remains in the

liquid state even below the melting temperature T_m (from A to A*). Also, the first crystals that formed in "A" will re-melt (from A to A*) due to the release of the latent heat that occurs in this period, this behavior called the re-melting phenomenon. The first stable solid crystals are large enough to grow only those formed at point A*. As soon as these first stable crystals are formed, the temperature increases (heating of residual liquid) by rejection of latent heat and returns to the melting temperature T_m (from A* to B), as the solidification progresses, the solidification rate is greater than the melting rate. This is the phenomenon of recalescence and is due to the release of latent heat as the result of solidification.

The solidification of binary alloys is different from that of pure metals. In alloys, solidification will not occur at a particular temperature. It happens at a temperature range. This range depends on the alloy composition. During their solidification, metallic alloys move into the transitional phase between the liquid phase and the solid phase called the mushy zone. As we can see in the cooling curve of a binary metal alloy (see Fig.I.2), initially in a liquid state, there is a temperature called the liquidus temperature T_L above this latter the alloy is completely liquid.

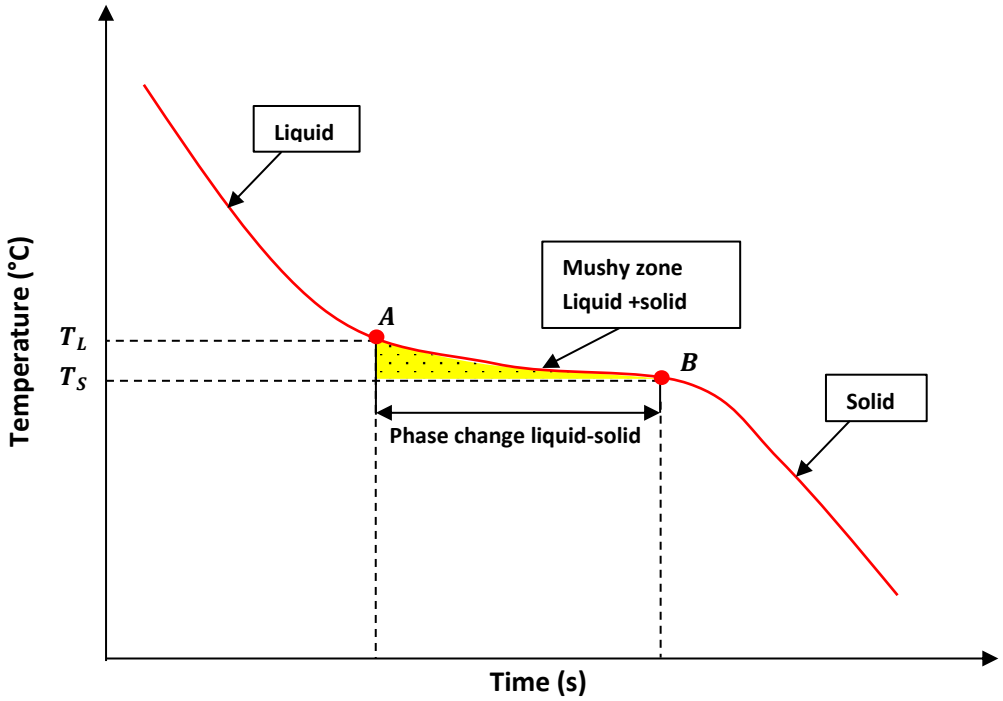

Fig. I.2. Typical evolution of the temperature of a binary alloy during its solidification. $\boldsymbol{T_L}$ and $\boldsymbol{T_S}$ are, respectively, the liquidus and solidus temperatures.

However, when the temperature is lower than the liquidus temperature, the first solid crystals are formed (in the zone presented by yellow in Fig.I.2). There is also another temperature called the solidus temperature T_S where the alloy is completely solid and a total disappearance of any liquid trace. Between these two temperatures, the alloy passes through a mushy zone, where

both solid and liquid phases are presented. The typical temperature evolution of an alloy during its solidification is represented in Fig.I.2. This representation gives one of the classical cases of the temperature evolution of an alloy during its solidification. In reality, this evolution can even present an isothermal phase change plateau similar to pure metal for certain compositions of alloys. The cooling curves for a given alloy and for different concentrations of the alloy are used to interpret the phase diagram.

I.2.2. Solidification, phase diagram and partition coefficient

During the solidification process at a local scale, in the beginning, the alloy is completely liquid characterized by its initial temperature T_0, this latter is cooled by applying a weak cooling rate *CR* (*K/s*), its solidification is not immediate. The initial temperature T_0 will decrease until it reaches certain temperature T_L, called the liquidus temperature, the mixture is completely liquid (l). Below there is another temperature T_S, lower than T_L, called the solidus temperature, the mixture is solid (s). Between these two temperatures, it passes through an intermediate zone called mushy, where the two phases coexist (liquid + solid), see Fig.I.3. The solid that formed has the concentration C_s^* which is different from that of the liquid found at the solid-liquid interface C_l^*, the upper star ()* refers to concentrations that present in the solid-liquid interface.

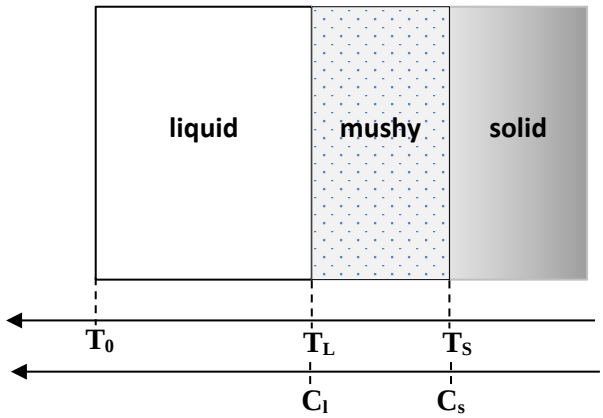

Fig. I.3. The evolution at thermodynamic equilibrium of the solidification of a binary alloy, at a various temperature between an initial temperature higher than T_L, and the final temperature, lower than T_S.

Flemings [1], Kurz and Fischer [2], and G. Lessoult [4], have defined that at the interface, the solid concentration, C_s^* is related to the liquid concentration C_l^* by the partition coefficient *k* as follow:

$$k = \frac{C_s^*}{C_l^*} \tag{I.1}$$

In the case of thermodynamics equilibrium, the liquid and solid concentrations at the level of solid-liquid interface are C_l^{eq} and C_s^{eq}, respectively. These conditions are proved if the melt is perfectly mixed during the phase change process. However, at a considered temperature, the concentration of the liquid C_l and solid C_s evolve according the value given by the phase diagram specific to the alloy via the liquidus and solidus lines respectively. Therefore, the liquid and the solid concentrations at thermodynamics equilibrium are depend only on the temperature for a binary phase diagram at constant pressure, and defined as follow:

$$C_s^{eq} = C_s(T) \tag{I.2}$$

$$C_l^{eq} = C_l(T) \tag{I.3}$$

It is convenient to define an equilibrium partition coefficient *k* in describing solidification under these conditions, where:

$$k(T) = \frac{C_s^{eq}(T)}{C_l^{eq}(T)} \tag{I.4}$$

As assumed by Flemings [1], Kurz [2], Hachani [5], Boussaa [6], M. Stefen-Kharicha [7] and Hamzaoui [8], that the partition coefficient *k* is constant to simplify the mathematics, when the liquidus and solidus concentrations are straight lines (see Fig.I.4).

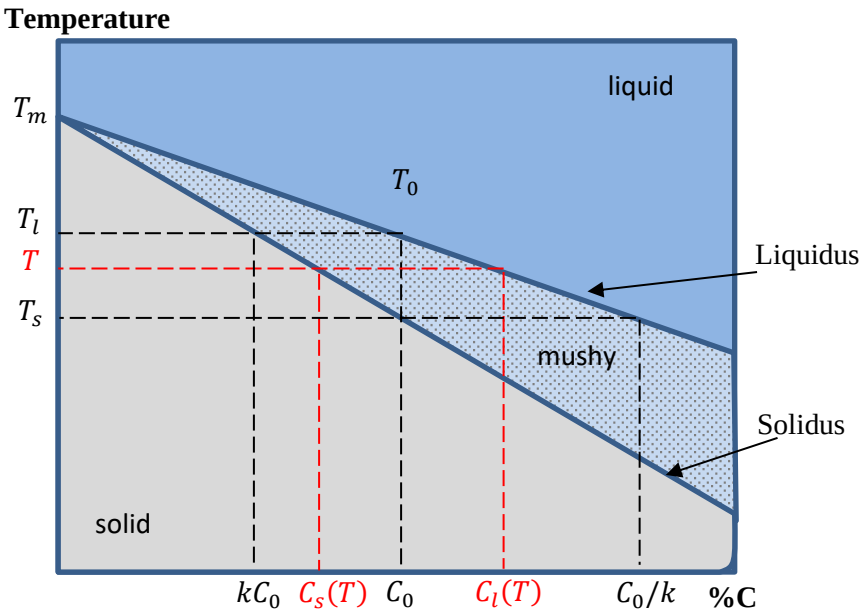

Fig. I.4. Schematic representation of a binary phase diagram with compositions of each phase ($k < 1$).

It is important to mention that the liquidus and solidus concentrations are presented as straight lines in the phase diagram is a preliminary assumption that is relatively lacking in accuracy and will be revised in chapter IV.

The phase diagrams of the alloys studied can be consulted in appendix I. This can only be achieved if the temperature, liquid and solid compositions remain uniform throughout the system during solidification process.

Similarly, the local slope m_l (*K. %$^{-1}$ wt*) of the liquidus curve is defined by the derivative of the temperature T_L as a function of the concentration C:

$$m_l = \frac{\partial T}{\partial C} \tag{I.5}$$

However, in this case the liquidus slope m_l (*K. %$^{-1}$ wt*) is negative.

We can also define the liquidus slope that presented in Eq.I.5 as follow:

$$m_l = -\frac{T_l - T_s}{C_0\left(\frac{1}{k} - 1\right)} \tag{I.6}$$

The liquidus curve is defined as a function of the melting temperature T_m; the liquidus slope m_l and the liquidus concentration C_l by the following equation:

$$T = T_m + m_l\, C_l \tag{I.7}$$

At a certain initial concentration C_0, the solidification occurs between the liquidus and solidus lines (mushy zone), i.e. cooling starts at liquidus temperature and ends at solidus temperature, from Eq.I.6 this temperature interval is defined as, [5, 7]:

$$\Delta T = T_l - T_s = m_l\, C_0 \left(1 - \frac{1}{k}\right) \tag{I.8}$$

During subsequent cooling and solidification, both liquid and solid are filled in solute; at temperature T^*, the solid of the composition C_s^* is formed in equilibrium state at the liquid-solid interface with the liquid of the composition C_l^*. Since the diffusion in the solid and liquid is complete. The whole solid has a uniform composition $C_s = C_s^*$ and it is the same for liquid where $C_l = C_l^*$. In the case of well diffusion, the initial alloy composition C_0 in the liquid and the solid can be represented as (conserving solute atoms):

$$C_0 = f_l C_l + f_s C_s = f_l C_l + (1 - f_l)\, C_s \tag{I.9}$$

where f_l and f_s are weight fractions liquid and solid, respectively. Which can be readily solved for fraction solidified at a given temperature since $f_l + f_s$ equals unity, which will be detailed in the next part.

I.2.3. Solid and liquid fraction

As mentioned in the previous part, in the beginning, the liquid phase (molten) has no solid crystals. Then at a certain temperature, we have shown that the nucleation of the solid crystals appears then they grow until the total disappearance of any liquid trace in the system. It is possible to deduce that we may express this change by the liquid and solid fractions, from Eq.I.9, as follow:

$$f_l = \frac{C_0 - C_s}{C_l - C_s} \; ; \; f_s = \frac{C_l - C_0}{C_l - C_s} \tag{I.10}$$

This known by *Lever rule* which gives at each temperature the proportion (in atoms or in mass) of the two phases at equilibrium, that is to say, as far as we are concerned, liquid and solid.

In the case of thermodynamic equilibrium. Lever rule supposed that the diffusion in both solid and the liquid should be infinitely fast (no concentration gradient in the liquid or solid). Thus, during solidification, the first crystal emerges at the temperature of the liquid, T_L, and the last drop of the liquid will solidify at the temperature of the solid, T_S.

The composition of the liquid at equilibrium is then given by Lever rule, [5]:

$$C_l = \frac{C_0}{1-(1-k)f_s} \tag{I.11}$$

The solid fraction which supposed by *Lever rule* [5] is defined as a function of temperature as follow:

$$f_s = \left(\frac{1}{1-k}\right)\left(\frac{T_L - T}{T_m - T}\right) \tag{I.12}$$

where f_s corresponds to the solid fraction. This solid fraction equal unity when the sample is completely solid and 0 when it is liquid and T_m is the melting temperature of the pure body. However, in reality, solidification is out of equilibrium phenomenon, in particular due to chemical diffusion phenomena.

Scheil and Gulliver [5] then proposed a model giving a simplified account of the release of the solute into the liquid. Indeed, the model assumes zero diffusion in the solid, but infinite

diffusion in the liquid (no concentration gradient in the liquid). In this case, the solid fraction can be written as

$$f_s = 1 - \left(\frac{T_m - T}{T_m - T_L}\right)^{\left(\frac{1}{k-1}\right)} \quad \text{(I.13)}$$

As in the case of equilibrium solidification, the first small amount of solid to form is of kC_0 composition at the liquidus temperature T_L (see Fig.I.4). In addition to those assumptions that given above (*Lever rule*), those of equilibrium solidification are simply complete diffusion in the liquid state and complete diffusion in the solid state. During solidification, the liquid becomes richer in solute and therefore the solid that forms, at later stages of solidification, has a higher solute content. However, since there is no diffusion in the solid phase due to rapid mass transport in the liquid ($C_l = C_l^*$), (*Scheil and Gulliver*, [1, 2]), the composition of the solid formed during the initial stages of cooling remains unchanged. At temperature T^*, the solid of the composition C_s^* is cooled from the liquid of the composition C_l^* and the distribution of the solute along the length of the growing crystals. Flemings [1] and Kurz [2] have developed a quantitative expression which is easily obtained by attributing the rejected solute when a small amount of solid forms with the resulting increase in the liquid solute, as follows;

$$(C_l - C_s)\, df_s = (1 - f_s)\, dC_l \quad \text{(I.14)}$$

Therefore, substituting the equilibrium partition coefficient and integrating from $C_s^* = kC_0$ at $f_s = 0$ ($C_l^* \approx C_0$) gives the composition of the solid at the liquid-solid interface C_s^* as a function of solid fraction, [1]:

$$C_s^* = KC_0(1 - f_s)^{(k-1)} \quad \text{(I.15)}$$

however, the liquid fraction is defined as:

$$C_l = C_0 f_l^{(k-1)} \quad \text{(I.16)}$$

Eqs.I.14, I.15 and I.16 are achieved in the case where there is no diffusion in solid that called *non equilibrium Lever rule*, or *Scheil and Gulliver* equation.

I.3 Liquid-Solid interface and their instabilities

During the liquid-solid phase change process of an alloy, leads to a thermodynamic change of state: from the disordered liquid state to the solid crystalline state (solidification).

This change of state requires an atomic reorganization initiated by solid germs that formed in the liquid at liquidus temperature T_l. A liquid-solid interface is then created within the metal whose morphology depends on its stability during solidification.

I.3.1. Instabilities of the interface

In the case of a binary alloy with C_0 initial composition of the concentration and a plane interface progressing with a steady state velocity v. During solidification of the alloy, the lower solubility of the solid (the partition coefficient, k, is less than unity) causes a solute release in front of the interface. This rejection is localized in a boundary layer δ_c (the diffusion length) characterized by the diffusion of the solute in the liquid D_l, and the interface advancing velocity v.

$$\delta_c = \frac{D_l}{v} \tag{I.17}$$

The resulting concentration profile is shown in Fig.I.5. A smooth exponentially decrease (see Fig.I.5) of the solute in this boundary layer with the distance x from C_0/k to C_0.

$$C(x) = \left(\frac{C_0}{k} - C_0\right) exp\left(-\frac{v}{D_l}\right) \tag{I.18}$$

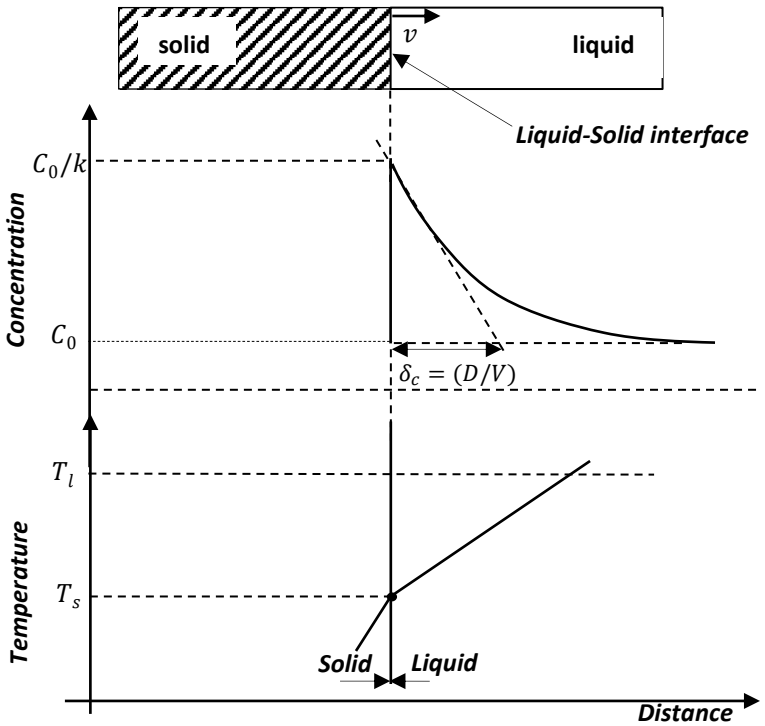

Fig. I.5. Concentration (above) and temperature profiles at the solid-liquid interface. Solute release is localized in the liquid zone in front of the interface.

The equilibrium temperature of the liquid that presented in phase diagram (see Fig.I.4) can be described as a function of the liquidus temperature T_l, liquidus slope m_l and the initial concentration C_0 with the equation:

$$T_l\big(C(x)\big) = T_l + m_l(C(x) - C_0) \tag{I.19}$$

Also, the heat flux that presents during the solidification can impose an evolution on the temperature $T(x)$, this latter can affect the interface stability (see Fig.I.6), [5, 7].

$$T(x) = T_m + m_l \frac{C_0}{K} + G.x \tag{I.20}$$

where G is the temperature gradient at the interface, defined by ($K.m^{-1}$).

$$G = \left(\frac{d}{dx}T(x)\right)_{x=0} \tag{I.21}$$

The temperature gradient G that presented in Eq.I.21 makes it possible to determine the conditions of stability and to deduce the morphologies of the resulting interface that will be detailed later.

It is necessary to mention that the stability of the solid-liquid front it depends on both T_l (C(x)) and T(x) that presented in Eqs.I.19 and I.20, respectively. Indeed, the situation remains stable, the solidification front is planar as the $T(x) > T_l(C(x))$ locally. On another hand, the situation becomes unstable (see Fig.I.6), the solidification front is destabilized as $T(x) < T_l(C(x))$ locally. This condition of instability is called constitutional undercooling, because it depends only on the solute rejection in a given temperature gradient. The word constitutional indicates that the undercooling arises from a change in composition, not temperature. The instability of the plane front (perturbation) that caused by the undercooling since any protuberance forming on the interface would be in undercooled liquid and therefore would not disappear.

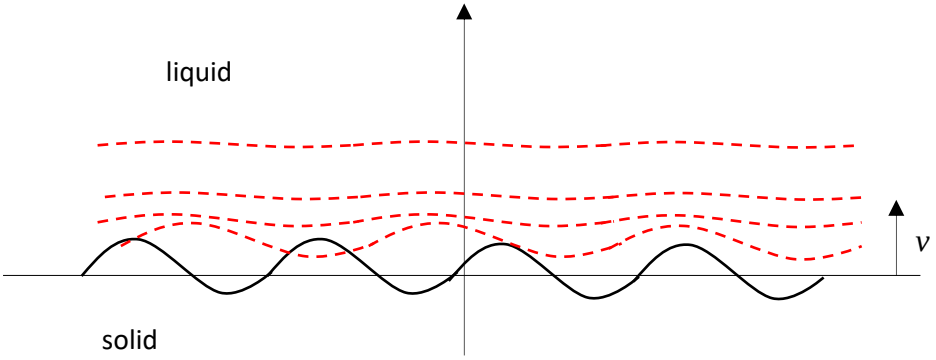

Fig. I.6. Perturbed solid-liquid interface moving at average velocity v, [9].

The instability of the interface gives an indication that initial appearance of cells or dendrites (dendrite is a descriptive word derived from the Greek, "*dendron*", which means tree) during the solidification at the microstructure scale which will be more detailed later.

I.3.2. Nucleation notion

As mentioned previously that nucleation occurs when there is perturbation of the solid-liquid interface, i.e., the perturbation of the solid-liquid interface gives an indication that the nucleation will occur. In metals, considerable deviations from the interface equilibrium should be achievable that occur when the solidification rate is sufficiently rapid, Thermodynamics cannot predict what these variants would be, but can describe the field of possible interface compositions. The nucleation (germination) is the phenomenon according to which the first germs of a solid phase or component appear; these germs constitute centers for the development of a new structure (chemical or physical). In solution, several types of nucleation and germination are possible [10]. Primary nucleation happens as germs are formed in a crystal-free medium, as opposed to secondary nucleation when new germs grow from crystals of the same phase already developed or already formed in solution.

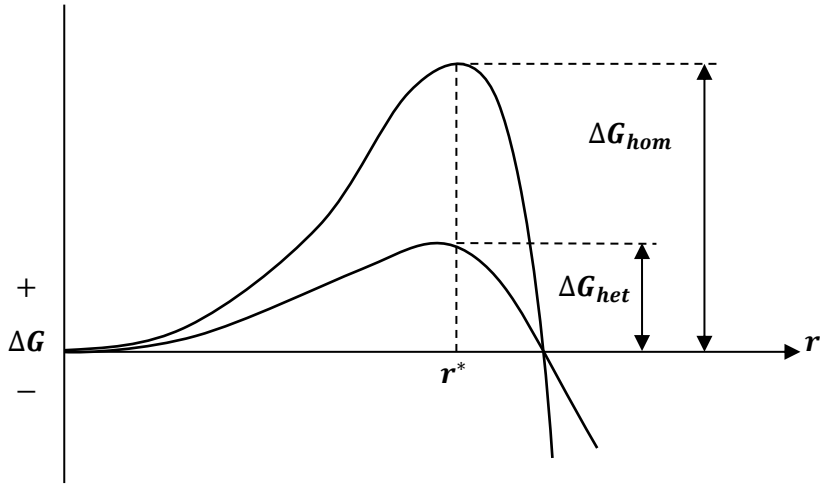

Fig. I.7. Comparison of free-energy changes associated with homogeneous and heterogeneous nucleation, [11].

The primary nucleation is classified into two forms of nucleation. Thus, as germs emerge inside the solution without any specific interaction with the walls of the crystalliser or any other solid particle, the nucleation is homogeneous. In the other side, as germs form a substrate (wall, crystal of another phase or probably of the same phase), the primary nucleation becomes heterogeneous. From a theoretical point of view, the hypothesis of a homogeneous nucleation facilitates the modeling of the phenomenon. However, the industrial context results in the

presence of many solid impurities in the medium often invisible to the eye and possibly variable from one operation to another in quantity and quality. The result is a heterogeneous primary nucleation that is very difficult to predict, control and model. The secondary nucleation is almost reserved to condensed mediums and in particular to solutions. From the extensive literature devoted to this subject, it can be retained that the sources of secondary germs are essentially found on the surface of pre-existing crystals in the system.

From a thermodynamic point of view, Askeland *et al* [12], have defined that when cooling below the solidification temperature, the metallic materials can move from the liquid state to the solid state since the energy associated with solid crystals is smaller than that of liquid metal. According to the classical nucleation theory, total free energy is defined which corresponds to the difference between the energy of the liquid and the energy of the solid and which is defined by the Eq.I.22.

$$\Delta G = \frac{4}{3}\pi r^3 \Delta G_v + 4\pi r^2 \sigma_{sl} \quad \text{(I.22)}$$

where $\frac{4}{3}\pi r^3$ is the volume of a spherical solid of radius *r*, $4\pi r^2$ is the surface zone of a spherical solid, σ_{sl} is the surface free energy of the solid-liquid interface and ΔG_v is the free energy change per unit volume, this latter is negative since the transition process is supposed to be thermodynamically feasible.

$$r^* = \frac{2\sigma_{sl} T_E}{\Delta H_f \Delta T} \quad \text{(I.23)}$$

where ΔH_f is the latent heat of fusion per unit volume, T_E is the equilibrium solidification temperature in kelvin, $\Delta T = (T_E - T_l)$ is the undercooling when the liquid temperature is T_l, and r^* is the critical radius.

On another hand, J. D. Hunt [13], J. W. Christian [14] and Thomas Campanella [15] have defined the nucleation rate during the solidification as follow:

$$I = (N_0 - N) I_0 \, exp\left(-\frac{\Delta G_n}{k_b T}\right) \quad \text{(I.24)}$$

where N_0 is the total number of germination sites per unit of volume, N is the number of activated sites, I_0 is constant, ΔG_n is the activation energy, k_b is the constant of Boltzmann and T the temperature.

I.4 Solidification structures and CET mechanism

As we have shown in the previous part, the interface between the solid and the liquid phase becomes unstable resulting in formation of small interface curvature perturbations. This latter caused by thermal or solute gradients, this triggers the growth of different interface shapes that contribute to the configuration of the solid phase, called the microstructure.

I.4.1. Morphology of the solidification front

The solid-liquid phase change process is generally realised out of equilibrium, for a given alloy solute content and temperature gradient in the liquid, it is well known that a planar solidification front is morphologically unstable after a velocity threshold. A columnar structure is then observed in the solid, which is due to the non-planar shape of the interface. This work is part of a study of the limit of morphological stability of a flat solid-liquid interface, i.e. of its first bifurcation, and on the cells or dendrites that appear for higher growth rates [16].

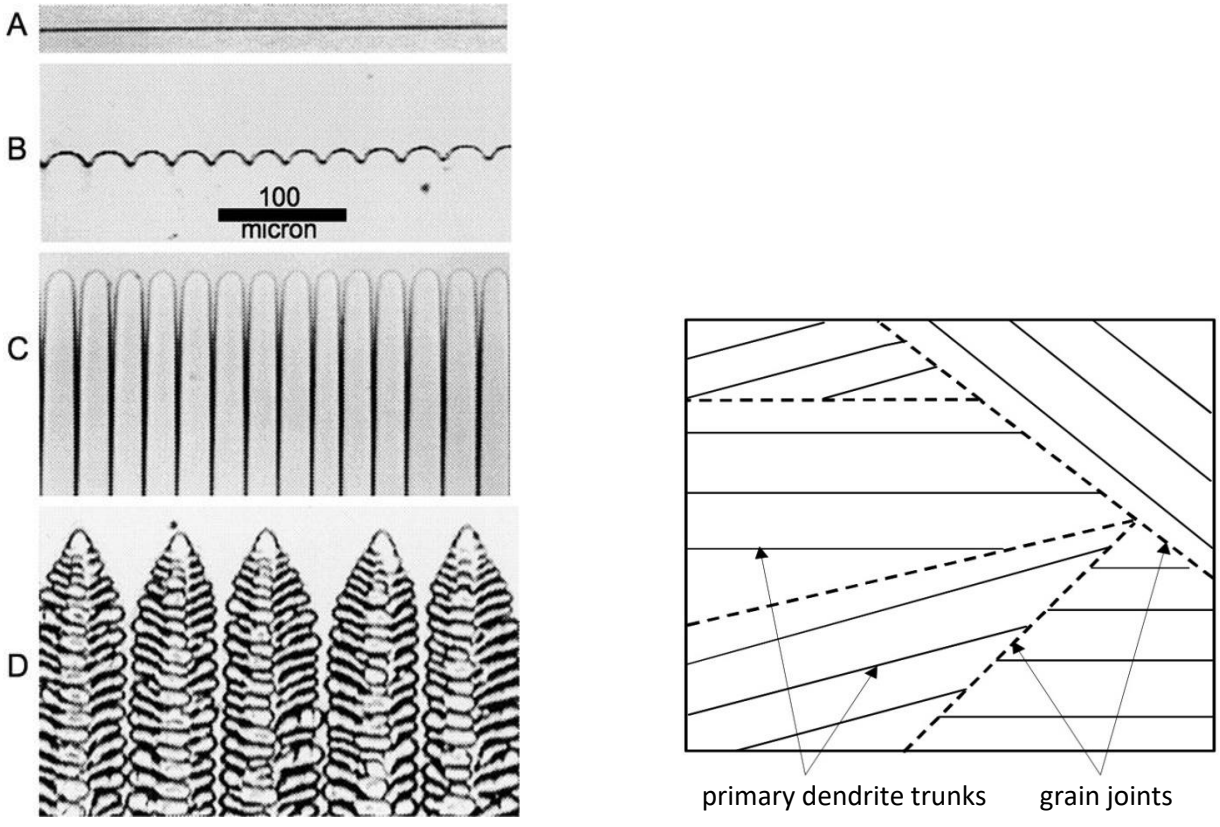

(a) (b)

Fig. I.8. (a) Schematic representation of the different interface morphologies and the resulting microstructures, Steady-state solidification fronts of the dilute SCN-CM152 alloy growing at an increase in growth rates from A to D. (A) Steady plane-front growth; (B) Periodic ripple with higher harmonic content; (C) Deep cells; (D) Aligned dendrites. [17], (b) Schematic representation of a macroscopic structure of the grain during dendritic growth, [15].

Three separate shapes of interface morphologies can be described for a single, solid phase: planar front, cells and dendrites (Fig.I.8 (a)). High-amplitude features develop on the interface by non-linear processes to form deep cells, which grow into much more complex solidification structures, called dendrites that are non-equilibrium structures that exist during the subsequent solidification process.

Fig.I.8 (a) in (left) presents a series of micrographs taken from SCN-CM152 alloy during steady directional cooling at increasing rates in a thin solidification cell. One observes the progressive creation of low-amplitude ripples, which are simply not pure sine waves, but include higher harmonics that define their form. Careful scrutiny of Fig.I.8 (a) "B" shows that perturbation of the solid-liquid interface due to the thermal and solute gradient. At higher growth rate, Fig.I.8 (a) "C" the ripples have amplified into deep finger- like cells. Fig.I.8 (a) "D", observed at the highest growth rate, shows the interface fully evolved into aligned dendrites. The Cell-to-Dendrite Transition (CDT) is of considerable interest in interpreting cast microstructures of dilute alloys, but its explanation remains not clear. Fig.I.8 (b) shows the structure and distribution of the grains define the macrostructure of the sample.

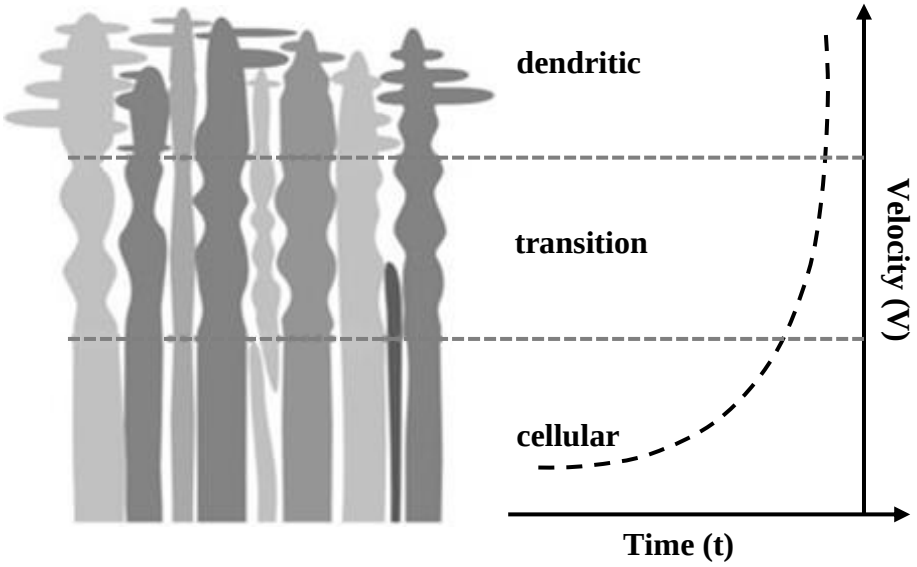

Fig. I.9. Influence of solidification velocity on microstructure formation during vertical solidification, [27].

In addition, as one of the typical problems of pattern formation, solidification microstructures are interesting for both scientific and technologic reasons [18-20]. Tough remarkable progress in the study of microstructure evolution during solidification has been made, the mechanism of sidebranching dynamics is still unsatisfactorily understood [21-23]. During directional solidification, the onset of sidebranches means the occurrence of cell-dendrite transition (CDT).

Over past few years, the identification of CDT has been widely performed experimentally [24-26], which showed that cell and dendrite coexist over a large range of control parameters. Given pulling velocity *V*, thermal gradient *G* (see Fig.I.10) and the alloy composition C_0, small primary spacing corresponds to cellular morphology in CDT region, while large primary spacing corresponds to dendrite.

Daniel M. Rosa *et al* [27], have also treated the cell-dendrite transition (CDT) of the solidification of Pb-Sb alloys. Indeed, further increase in the solidification velocity changes the interface morphology from dendritic back to cellular and finally planar (see Fig.I.9).

I.4.2. Morphology of solidified structures

During transformation from liquid to solid, the solidification behavior controls the distribution of solute, and the size and morphology of grains. The critical parameters determining the solidification microstructure are the temperature gradient *G*, solidification rate *V*, undercooling ΔT, and alloy composition C_0. Depending on these conditions, the microscopic shape of the solid–liquid interface varies from planar to cellular dendritic, to columnar dendritic, and to equiaxed dendritic (small-sized grains of different crystallographic orientations surrounded by grain joints). Pure metals have a planar solid–liquid interface and solidify as a single crystal.

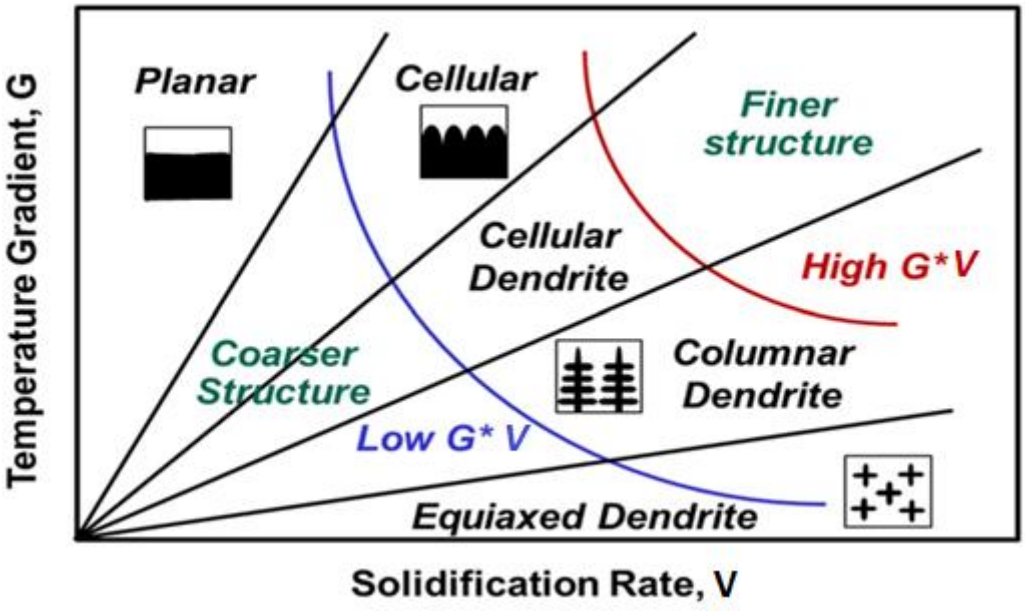

Fig. I.10. The effect of G and *V* on the solidification morphology and size, [28].

However, in alloys, the factors affecting solidification morphology are more complicated because redistribution of alloy elements leads to concentration gradients adjacent the solid–liquid interface. The size and morphology of the solidified microstructure can be revealed by

using the combined form of temperature gradient *G* and solidification growth rate *V* which is shown in Fig.I.10. [28]. The ratio of *G/V* indicates solidification morphology whereas the product of G and *V* represents the scale of the solidification microstructure.

A planar solidification growth happens when G is very high or/and *V* is extremely low value. As *V* increases, the solidification morphology can shift to cellular, columnar, and then equiaxed dendritic (see Fig.I.10). Most metal alloys are solidified in cellular or columnar dendritic mode. The cellular and columnar growth modes are produced when the growth of crystal structures occurs without formation of any secondary dendrite arms. If additional dendrite arms form, the structures are shifted to dendritic mode. Equiaxed morphology is possible only when G is very low. The equiaxed structures appear at the end of the solidification (see Fig.I.11), this is due to the fact that the thermal gradient became very low whatever the solidification rate.

If we look at the morphologies obtained after solidification, we can observe a very large variety of structures of different sizes, related to the different solid phases present as shown in Fig.I.11 (a, b):

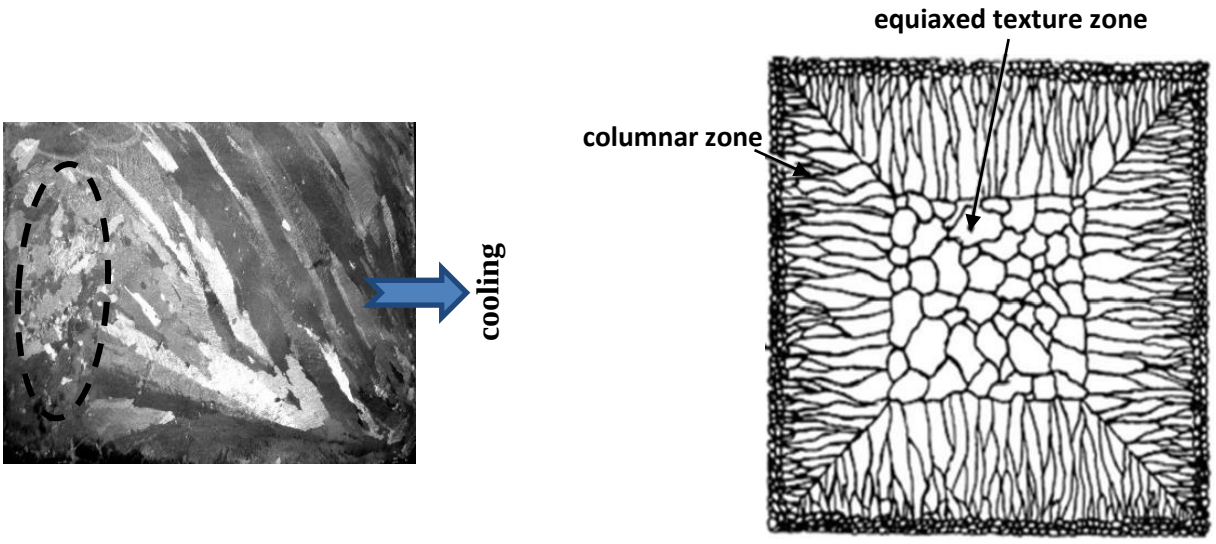

(a) (b)

Fig. I.11. (a) Typical macrostructure of a Sn-3wt.%Pb ingot (10×6×1 cm) cooled from the right side [29]. This situation, close to that of a foundry, illustrates the variety of structures obtained and the transition between columnar and equiaxed structures at the end of solidification. (b) Schematic representation of an ingot section showing the two crystallization zones: columnar zone and equiaxed textured zone, [30].

It is important to note that all these structures can coexist within the same ingot (cellular, dendrite and equiaxed). Their establishment depends on the nature of the material and the thermal history of solidification.

I.4.3. Development of dendritic microstructures

Implicit in our discussions of solid–liquid interface are the related concepts of thermodynamic equilibrium. However, transport phenomena play a role at the level of solid-liquid interface. Heat transfer due to the latent heat release during the phase change process, and mass transfer due to the distribution of the solute between solid-liquid interface. The temperature of the interface would be higher either solid or liquid, it is due to the release of the heat of fusion at the interface. These conditions can affect the growth in term of thermal field, velocity behavior and the shape of the solid germs.

I.4.3.1 Growth Kinetics

The growth kinetics of a dendrite is essentially dependent on the phenomena that occur near its tip. These can be summarized by the notion of undercooling of the tip of the dendrite, ΔT^*, which is defined for velocity not too high, as the sum of the deviations from equilibrium and the thermal point of view, ΔT_T, chemical, ΔT_c (rejection of heat and solute) and of the curvature, ΔT_r, (see Fig.I.12):

$$\Delta T^* = \Delta T_T + \Delta T_c + \Delta T_r \qquad \text{(I.25)}$$

Thermal supercooling is mainly due to the rejection of latent heat, i.e., when the thermal gradient in the liquid is negative (equiaxed solidification).

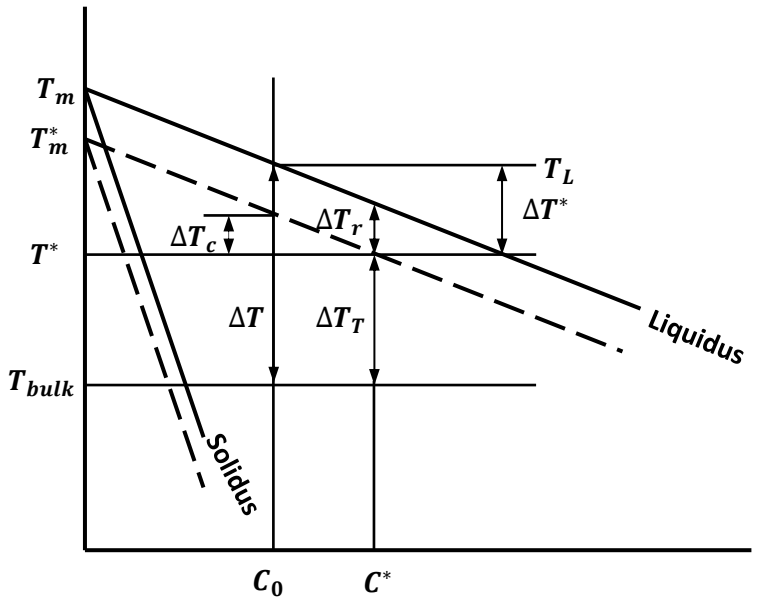

Fig. I.12. The various components of interface undercooling with respect to the bulk temperature under the condition of local interface equilibrium, [31].

Chemical undercooling corresponds to the phenomenon of constitutional undercooling, therefore to the rejection of solute in front of the interface:

$$\Delta T_c = m_l(C_0 - C_l^*) \quad \text{(I.26)}$$

where C_l^* is the concentration of the liquid at the interface solid/liquid (see Fig.I.13).

The temperature gradient of this type may be achieved by considerable undercooling. The change in the melting point from T_m to T_m^* (see Fig.I.12), due the curvature effect, often called the curvature or Gibbs Thomson undercooling:

$$\Delta T_r = \Gamma K_l \quad \text{(I.27)}$$

Γ: is Gibbs-Thomson coefficient, $\Gamma = \sigma/\Delta S_f$, where σ is the solid-liquid interfacial energy and ΔS_f is the entropy of fusion. $K_l = \frac{1}{R_{tip}}$ is the curvature of the interface of this kind of curvature.

Note that for directional solidification (G > 0), thermal undercooling, ΔT_T, can be overlooked due to the effect of chemical undercooling, ΔT_c, for most industrial metal alloys. Indeed, Eq I.25 can be rewrite as follow:

$$\Delta T^* = \Delta T_c + \Delta T_r = T_l - T^* \quad \text{(I.28)}$$

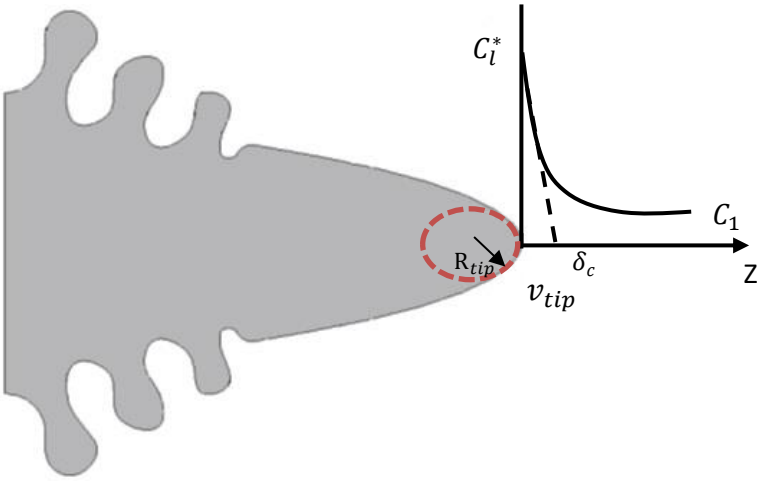

Fig. I.13. Dendrite tip having a shape of a paraboloid of evolution, [32].

T^*: corresponds to the temperature of the dendrite tip. It is then a question of determining the effect of the solute rejection at the dendrite tip and the effect of its curvature on the growth morphology. Fig.I.13 presents a schematic of the dendrite composition ahead of the dendrite along its *Z* axis, not that the composition of the tip is C_l^* and decline to some value C_1 at distance δ_c ahead of the tip, this latter is the diffusion distance of the solute:

$$\delta_c = \frac{2D_l}{v_{tip}} \quad \text{(I.29)}$$

where D_l and v_{tip} are the liquid diffusion coefficient and the velocity of the tip, respectively.

To account for the diffusion at the tip of the dendrite (case of the stationary diffusion field), we define the Peclet number "*Pe*", which is corresponds to the ratio of the characteristic dimension of the system, R_{tip} (the radius of curvature of the dendrite) and the diffusion distance of the solute δc:

$$Pe = \frac{R_{tip} v_{tip}}{2D_l} \tag{I.30}$$

Extension to the *Ivantsov* dendrite growth model is presented by Kurz [2], which is allowed for increase solute levels in the field ahead the tip dendrite.

A model for the tip dendrite is a paraboloid of revolution. *Ivantsov* [2] was the first to develop a mathematical analysis for this shape, he has found that the supersaturation is defined as follow:

$$\Omega = I_v(Pe) \quad \Omega = \frac{C_l^* - C_0}{C_l^*(1-K)} \tag{I.31}$$

Where the *Ivantsov* function (a function of Peclet) corresponding to a paraboloid of revolution is given by [2]:

$$I_v(Pe) = Pe \exp(Pe) \, . \, E_1(Pe) \tag{I.32}$$

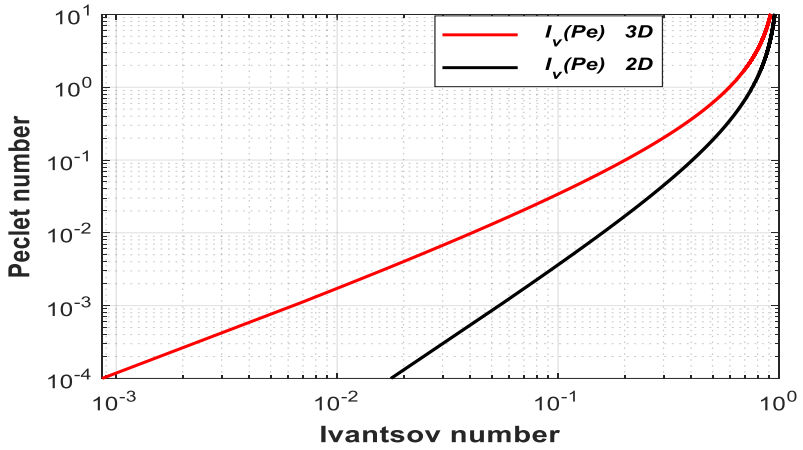

Fig. I. 14. 3D and 2D Ivantsov evolution vs Peclet number varie accordance with Eqs I.32 and I.33, respectively.

The *Ivantsov* function can do the treatment of the steady-state transport process at the solid liquid interface by diffusion.

Ω is defined as supersaturation, I_v (*Pe*) corresponds to the *Ivantsov* function and E_1 (x) is the integral exponential function.

and the *Ivantsov* function for parabolic cylinder [2] (plate) by:

$$I_v(Pe) = (\pi.\mathrm{Pe})^{1/2} \exp(Pe)\, erfc(\mathrm{Pe})^{1/2} \quad \text{(I.33)}$$

In order to determine the tip radius, R_{tip} and its velocity, v_{tip}, (see Fig.I.13), A Kharicha *et al* [33] have proved that the selection criteria for tip should also be updated; it can be achieved by again rescaling the diffusivity and the Gibbs Thomson coefficient as follow:

$$R_{tip} = \frac{\Gamma}{2\, Pe\, m_l\, \sigma\, (C_l - C_s)} \quad \text{(I.34)}$$

where σ is the stability constant. We can conclude the tip velocity from Eqs.I.30 and I.34 as, [33]:

$$v_{tip} = \frac{2\, Pe\, D_l}{R_{tip}} \quad \text{(I.35)}$$

The velocity of the solid front can predict the shape of the solid front. Whereas, solidification front presented as a planar when the velocity of the solidification front is low. Furthermore, the solidification front takes cellular to dendrite transition shape (CDT) as the velocity increase.

I.4.3.2 Primary and secondary dendrite arm spacing

As discussed previously, when a metallic alloy is solidified, the most frequent morphology of the solid formed is a dendritic microstructure [2], It is an array of primary (λ_1), secondary (λ_2), and sometimes higher-order arms that form a very complex network (Fig.I.15). The dendrite characterized also by its tip radius R_{tip} (see Fig.I.13) which varies accordance with Eq.I.34 during the solidification process.

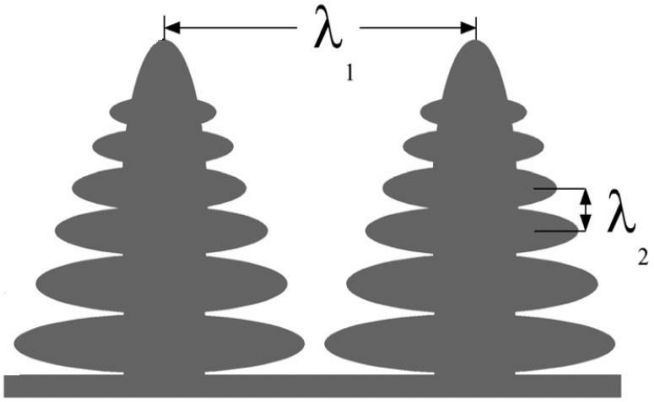

Fig. I.15. Definition of primary (λ_1) and secondary (λ_2) dendrite arm spacing, [34].

W. Kurz and D. J. Fisher [35] have mentioned that the values of the tip radius R_{tip} are much larger than the extremum values; one of the most important quantities used to describe dendritic

structures in columnar growth is the primary dendrite spacing (PDAS), λ_1. Several estimates exist for (λ_1) [36-38]. This latter generally expressed as a function of the temperature difference between liquidus and solidus ($\Delta T_0 = T_l - T_s$), the liquid diffusion coefficient D_l, the Gibbs Thomson coefficient Γ, the partition coefficient *k*, the temperature gradient *G* and the velocity growth *V*. Eq.I.36 [35] and Yousub Lee [28] in Eq.I.37 show an example of PDAS model [35]:

$$\lambda_1 = 4.3\left(\frac{\Delta T_0 D_l \Gamma}{k}\right)^{\frac{1}{4}} V^{-1/4} G^{-1/2} \qquad \text{W. Kurz and D. J. Fisher [35]} \qquad \text{(I.36)}$$

$$\lambda_1 = 2.83(L\Delta T_0 k D_l \Gamma)^{0.25} V^{-1/4} G^{-1/2} \qquad \text{Yousub Lee [28]} \qquad \text{(I.37)}$$

The values of λ_2(secondary dendrite arm spacing, SDAS) were measured, [34] by averaging of the length between the adjacent side branches on the longitudinal part of the primary dendrite as a function of the length *L* of the dendrite. λ_2 define as *L/(n-1)* where "n" is the number of side branches.

Secondary dendrite arm spacing is mainly determined by coarsening processes [39-40]. Independent of the physics of coarsening each model for secondary dendrite arm spacing, a basic power law expression is eventually expected if diffusive mass transport governs between dendrite arms of different curvature radius. These basic models contribute to power regulations of the type [41]:

$$\lambda_2 = M.t_f^b \qquad \text{(I.38)}$$

with *M* a factor containing material constants (diffusion coefficient, Gibbs-Thomson coefficient, eutectic concentration, global concentration, liquidus slope and segregation coefficient), t_f the solidification time, that is the time for which both solid and the liquid co-existed and b = ⅓ for diffusive mass transport.

I.4.4. Transition Columnar-equiaxed

The formation of dendritic structures at the solid-liquid interface is commonly the phenomenon observed in crystal growth and the solidification process.

Dendrite formation begins with the advent of instability of the solid-liquid interface [42]; these instabilities can occur in two solidification regimes, columnar and equiaxed growth. Three types of dendrites can be distinguished:

- Equiaxed dendrites of a pure metal governed by thermal diffusion.

- Columnar dendrites which exist only for alloys, governed by solute diffusion.
- Equiaxed dendrites of an alloy which are governed by thermal and solute diffusion [43].

The columnar trunk may grow according to a cellular or dendritic morphology (see Fig.I.8). Two different zones can be seen during columnar dendritic growth, the zone containing the columnar trunks and the zone containing the tips of the primary dendrites.

Equiaxed grains may nucleate and grow ahead of the columnar front, creating an unexpected columnar to equiaxed transition (CET) along a plane parallel to the cold wall (see Fig.I.18). The equiaxed structures appear at latter stage of the solidification. This type of growth had been treated by Lipton *et al* [44] and Trivedi *et al* [45]. It only occurs in an undercooled liquid, so that the crystals maintain their growth [43]. It is thus possible to have crystals growing radially within the liquid phase, which then produce axisymmetric crystals [46]. After nucleation, an equiaxed grain begins to grow in a globular (spherical) form. Following the globular-dendritic transition, the equiaxed grain is defined as the surface contour connecting the tips of the primary and secondary dendrites as shown in Fig.I.16.

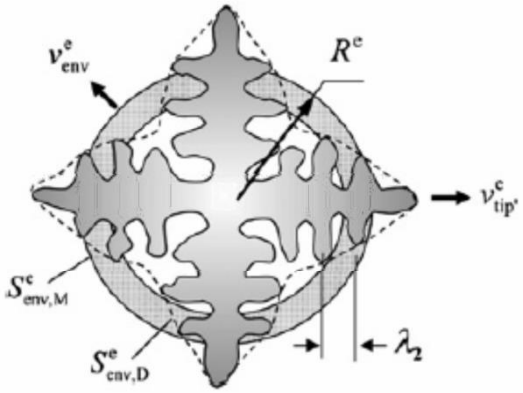

Fig. I.16. The shape of the equiaxed dendrite: the envelope of the equiaxed grain is simplified to a sphere whose volume is equivalent to that of the envelope connecting the tips of the primary and secondary dendrites, [47].

The equiaxed structures formation can have two origins:

- Fragmentation: The germs could be defined by fragments of dendrite separated from the mushy zone by local remelting and transported through convection in the undercooled liquid zone (Fig.I.17). Fragmentation is not a well-understood phenomenon, but observation on organic alloy solidification have been made by C.J. Paradies [48] and T. Sato [49], fragmentation linked to the local remelting of the finest dendrite arms at their necks. Liu [50] concluded that the fragmentation is mainly due to

the dissolution of dendrites arms due to solute difference in the mushy zone (solute variation caused by deceleration of the cooling velocity). Gu and Beckermann [51] as Hellawell [50] linked fragmentation to the solutal dissolution of dendrites arms in segregated channels (freckles). It should be noticed that Pilling's work [52] states that interdendritic liquid flow causing mechanical deformation is not responsible for dendrites fragmentation.

- Inoculation: the introduction of seed particles would constitute favorable growing sites (heterogeneous nucleation) for additional equiaxed crystals and will therefore favor CET even with a minimum undercooling. If the undercooling required for heterogeneous nucleation is lower than the maximum undercooling present in the liquid and if appropriate seed particles are present, CET will be promoted.

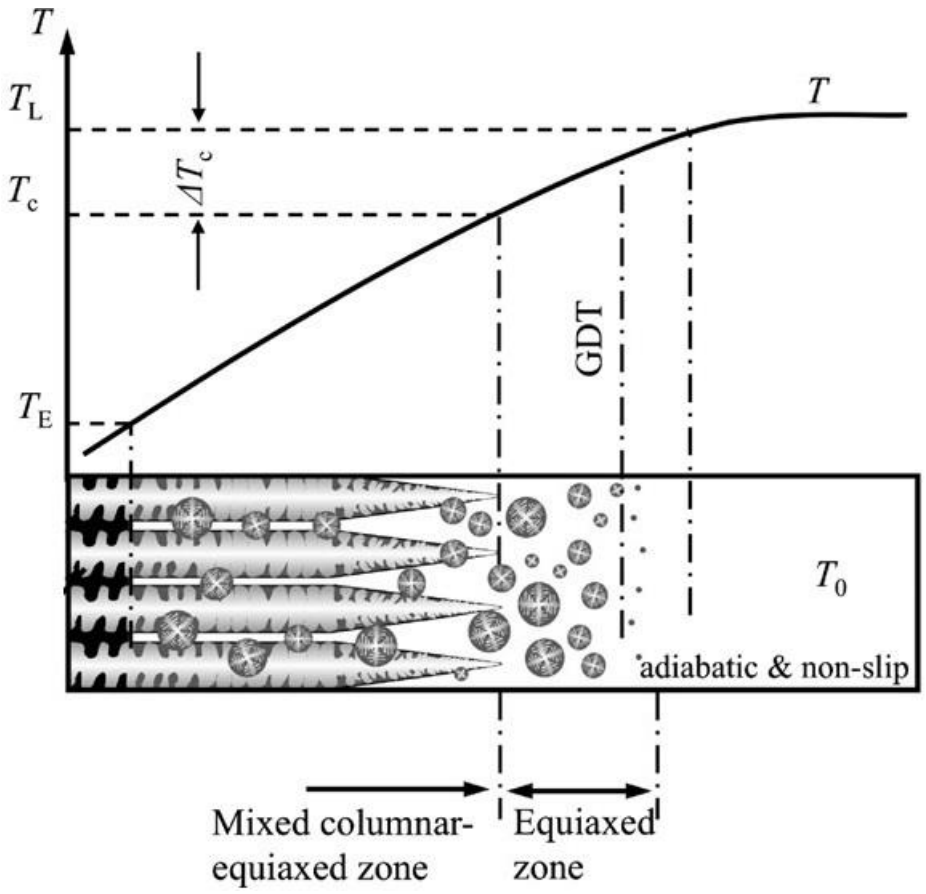

Fig. I.17. Representation of CET, T_L is the liquidus temperature, T_c is the dendrite tip temperature,T_E is the eutectic temperature and $\mathbf{\Delta T_c}$ is the undercooling at the columnar primary dendrite tip, [53].

The columnar - equiaxed transition (CET) in the grain structure of metal alloys has fascinated researchers in the field of solidification for more than 50 years. During the growth of an alloy, upstream of the interdendritic zone, the redistribution of solute in the liquid can lead to the

generation of undercooled zones. This allows the appearance of equiaxed crystals, including, the coexistence of the two regimes (columnar and equiaxed) [54], which is called columnar-equiaxed transition (see Fig.I.18). Once the germs are formed, in the undercooled zone, the equiaxed grains will develop with different volume fractions, which depend on the thermal gradient or the solidification rate. The equiaxed grains, which may appear below and above the ingot, will be incorporated into the columnar zone if their volume fraction is small, and replace the columnar zone if their volume fraction is large.

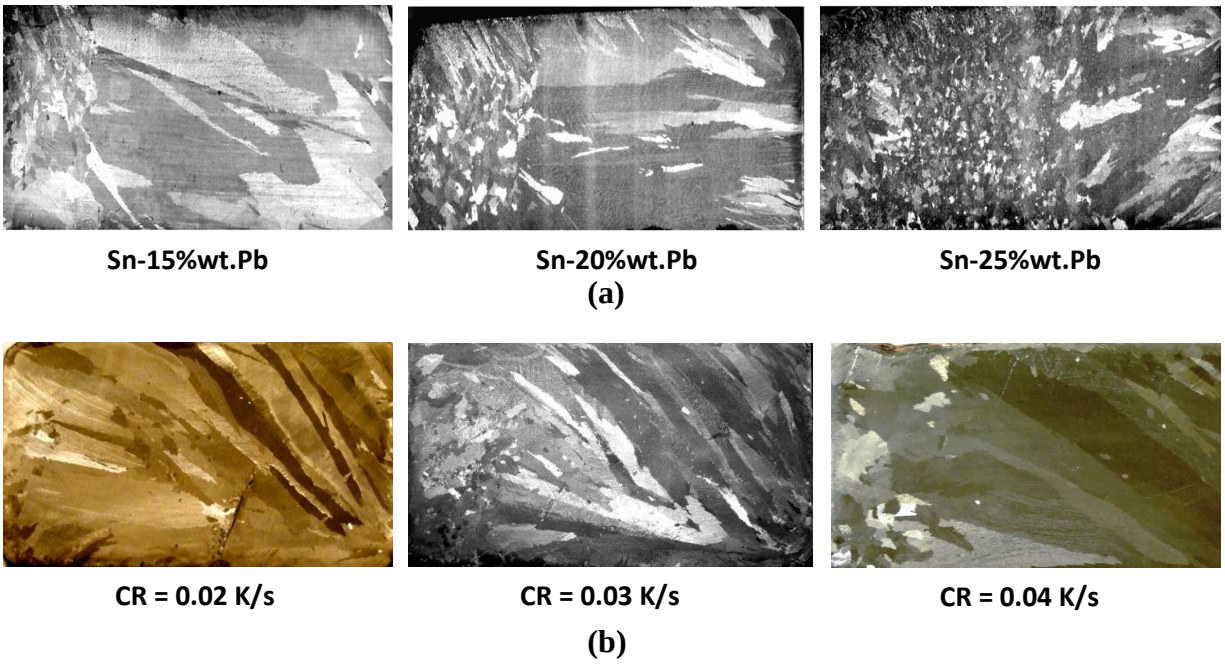

Fig. I.18. Columnar to equiaxed transition (CET), (a) for different concentration composition Sn-15%wt.Pb, Sn-20%wt.Pb and Sn-25%wt.Pb directionally solidified sample, [55]. (b) Typical macrostructure of a Sn-3wt.%Pb ingot (10×6×1 cm) cooled from the right side for different cooling rate, [29].

Generally, equiaxed growth is favored consequently the CET mechanism if the solidification rate, the concentration of the alloying element (see Fig.I.18 (a)), the cooling rate CR (see Fig I.18 (b)), as well as the number of nucleation sites are increased, and if the nucleation undercooling or the thermal gradient is decreased. However, the columnar growth occurs at low velocities and high thermal gradients. It can be shown that the macrostructures have an important effect on the composition of the alloy in anticipation of a structural transition with an increase in the solute content (see Fig.I.18 (a)). The main principle of the CET shown by these macrostructures is that the transition is not sharp, i.e., there is strong evidence that the columnar-equiaxed transition occurred in the zone rather than in the plane parallel to the cooling wall.

The understanding of different phenomena that occur during CET will help to fully understand the final microstructure obtained in castings.

I.4.4.1 CET blocking mechanism: mechanical

Fragmentation usually refers to the separation of dendrite fragments from the main crystal network and possibly lead to CET if the solid fragments may be transported to or beyond the columnar front either by liquid flow or by buoyant forces exerted on the separated solid. The CET location specifies the amount of columnar and equiaxed grains that have a strong effect on the properties of the castings. Various mechanisms have been suggested to explain CET during solidification, but it is widely agreed that this happens when equal grains block the growth of columnar grains [56, 57]. Mechanical blockage occurs when there is insufficient space between equiaxed grains for extended grain growth (columnar grains unable to grow). Hunt [13] proposed that a fraction of the equiaxed-grain volume would occur at the columnar front.

In the beginning, a columnar dendritic front progressing at a velocity *v* in a thermal gradient *G*, with the growing dendrite causing an undercooled zone ahead of the columnar front, two cases can be distinguished:

1) Columnar growth when the undercooling is lower than the nucleation.

2) Equiaxed crystals will grow ahead of the columnar front (see Fig.I.17) when the undercooling is higher than the nucleation undercooling.

Hunt [13] has developed the Column-to-Equiaxed Transition (CET) Theory. During columnar growth, aligned dendrites grow in the opposite direction of heat flow, from the casting wall to the center of the casting. When the required chemical and thermal conditions are established, the equiaxed crystals grow in the melt ahead of the dendrite tips, which prevents the growth of the dendrite. This will happen when a critical fraction of the equiaxed grains is achieved, the temperature gradient G (°C/mm) at the dendrite tip will be less than, [58]:

$$G < 0.617 N^{1/3} [1 - (\Delta T_N / \Delta T_c)^3] \Delta T_c \quad \text{(I.39)}$$

Otherwise, the grains will be columnar, where *N* is the heterogeneous nuclei density (mm^{-3}), ΔT_N is the supercooling necessary for nucleation and ΔT_c is the constitutional undercooling on the tip of the dendrite, this latter is defined by Eq I.40 and I.41:

$$\Delta T_c = (vC_0/A)^{1/2} \quad \text{(I.40)}$$

$$A = D_l/[8m_l(k-1)\Gamma] \quad \text{(I.41)}$$

Where v is the dendrite tip velocity, D_l is the diffusion coefficient of solute element, m_l is the liquidus slope, k is the partitioning coefficient, and Γ is the Gibbs-Thomson parameter.

It is generally accepted that for technical purity alloys $\Delta T_N/\Delta T_c < 1$ and after arrangement of Eqs. (I.39 – I.41) The Hunt criteria for CET will be as follows:

$$G/v^{0.5} < 0.617N^{1/3}(C_0/A) \quad \text{(I.42)}$$

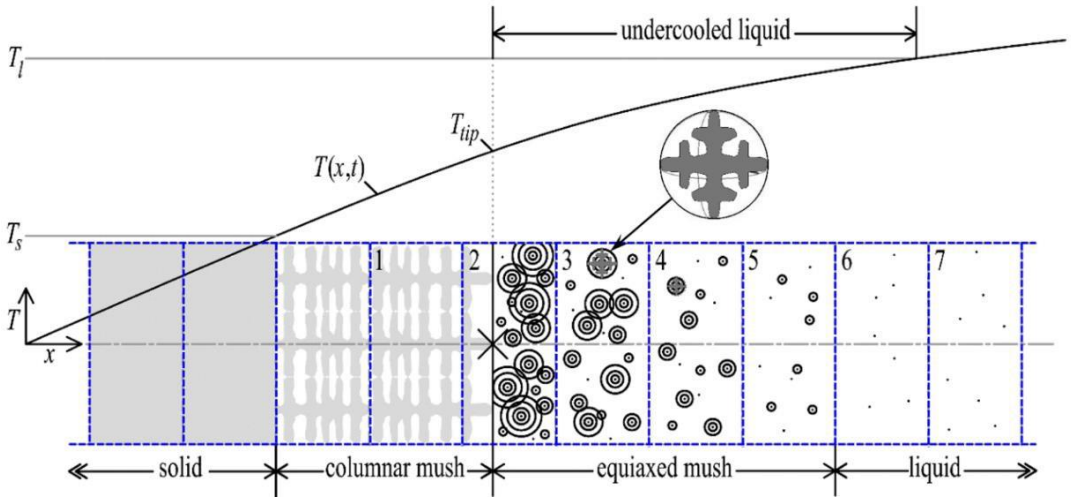

Fig. I.19. Representation of columnar to equiaxed transition and the mechanical blocking, [59].

The Hunt criterion was developed for solidification case in assumption that a critical fraction of equiaxed grains will stops the growth of columnar grains. Regardless of the blocking mechanism (see Fig.I.19), experiments and theoretical models have shown that CET is significantly influenced by the number density of equiaxed grains and the undercooling nucleation. In the Hunt [13] model for unidirectional steady-state solidification, a decrease in undercooling nucleation or an increase in the number of equiaxed grains promotes the mechanical blocking (see Fig.I.19) of columnar grains and, subsequently, the occurrence of CET.

I.4.4.2 CET blocking mechanism: solute

The CET occurs when the progress of the columnar front is blocked due to the equiaxed grains that nucleate ahead of the solidification front (columnar front). This mechanism occurs when the solute rejected by the equiaxed grains (solutal blocking) growing ahead of the front decreased the undercooling available for dendritic growth. Also, when the extradendritic liquid

concentration, C_l, increases at the front as a result of the solute transported from the grain envelopes solutal blocking of the columnar front occurs, removing the undercooling necessary for columnar growth (see Fig.I.20). The CET occurs earlier for solutal blocking because C_l increases before the solid volume fraction ε_g as a result of the intense solute rejection from the envelopes into the extradendritic liquid.

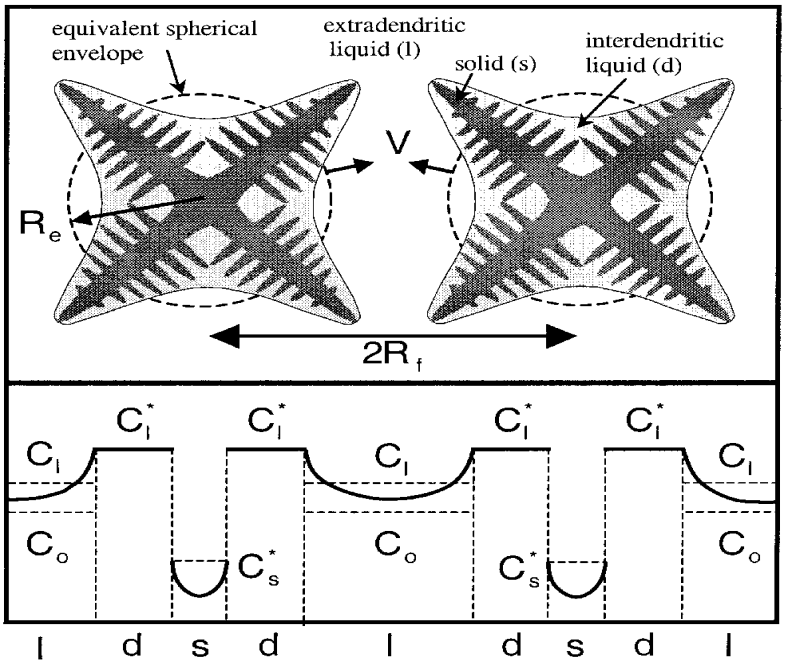

Fig. I.20. System consisting of the two equiaxed grains envelopes and the local solute concentration profiles of the average composition C_o and the uniform temperature T, [60].

In an order to separate the different length scales present in dendritic solidification, Wang and Beckermann [61] classified three phases within the representative elementary volume (REV): solid (s), interdendritic liquid (d) and extradendritic liquid (l), the distance between two grains is $2R_f$, where R_f represents the final grain radius. Volume fractions of the three processes are indicated by ε_s, ε_d and ε_l respectively, i.e. $(\varepsilon_s + \varepsilon_d + \varepsilon_l = 1)$. As seen in Fig.I.20. Interdendritic and extradendritic liquids are isolated by a hypothetical dendrite or grain envelope that is a smooth surface that extends across the tips of the dendrite. The area of the envelope per unit volume in the REV is indicated by (S_e). The volume of the grain envelope fraction is defined as $(\varepsilon_g = \varepsilon_s + \varepsilon_d = 1 - \varepsilon_l)$. It is this grain fraction on which the traditional mechanical blocking criteria for CET is focused (i.e. CET happens as $\varepsilon_g = 0.49$ in the Hunt [13] criterion).

The CET model suggested by Martorano *et al* [60], which uses the solutal-blocking mechanism of the columnar front, has been introduced. In contrary to the Hunt and stochastic models, the transfer of solute between the grain envelopes and the extradendritic liquid was taken into

consideration using the differential equations suggested by Wang and Beckermann [61]. The following equations were eventually adopted for the measurement of the solid fraction (ε_s) and the solute concentration of the extradendritic liquid, C_l, [60]:

$$(1-k)C_l^* \frac{\partial \varepsilon_s}{\partial t} = \varepsilon_d \frac{\partial C_l^*}{\partial t} + S_e \frac{D_l}{\delta_e}(C_l^* - C_l) \quad \text{(I.43)}$$

$$\frac{\partial(\varepsilon_l C_l)}{\partial t} = C_l^* \frac{\partial \varepsilon_l}{\partial t} + S_e \frac{D_l}{\delta_e}(C_l^* - C_l) \quad \text{(I.44)}$$

where δ_e is the effective diffusion length in the liquid adjacent to the grain envelopes.
The term $(C_l^* - C_l)$ that presented in Eqs.I.43 and I.44 identifies the diffusion of solute that results from growing dendrites/grains toward the extradendritic liquid undercooled. In the absence of extradendritic liquid ($\varepsilon_l = 0$), the term disappears and the Eq.I.44 reduces the *Scheil and Gulliver* equation to the differential form. The last equations are coupled to the liquid line of the binary equilibrium phase diagram as:

$$C_l^* = \frac{(T-T_m)}{m_l} \quad \text{(I.45)}$$

In addition, Eq.I.43 can be fixed for the solid fraction, ε_s and Eq.I.44 represents the average concentration of solute in the extradendritic liquid, C_l. The following equation is used to measure the proportion of the volume of the grain (or extradendritic liquid):

$$\frac{\partial \varepsilon_g}{\partial t} = -\frac{\partial \varepsilon_l}{\partial t} = S_e v_{tip} \quad \text{(I.46)}$$

where v_{tip} is velocity of the dendrite tip. This velocity is obtained from the growth model suggested earlier by Lipton *et al* [43].

$$v_{tip} = \frac{4\sigma D_l m_l (k-1) C_l^*}{\Gamma} \left(I_v^{-1}(\Omega)\right)^2 \quad \text{(I.47)}$$

where σ is the stability constant, I_v^{-1} is the inverse of the *Ivantsov* function, this latter can be approximated as follow, [60]:

$$I_v^{-1}(\Omega) = 0.4567 \left(\frac{\Omega}{1-\Omega}\right)^{1.195} \quad \text{(I.48)}$$

where Ω is the undercooling, is defined as:

$$\Omega = \frac{C_l^* - C_l}{C_l^*(1-k)} \quad \text{(I.49)}$$

In Eq.I.49 it should be noted that the undercooling is specified in relation to the average concentration of solute in the extradendritic liquid undercooled, C_l. Hunt [13] Gäumann *et al* [62] and Kurz *et al* [63] instead used the initial alloy composition, C_0, to determine undercooling for dendrite formation. Wang and Beckermann [61] adopted C_l for equiaxed growth, but C_0 for columnar growth. C_l may be also used for both equiaxed and columnar growth.

In addition, Banaszek *et al* [64] and Mc Fadden and Browne [65] demonstrated a third type of blocking, denoted as thermal blocking. Banaszek *et al* [64] used the model suggested by Browne and Hunt [66] to simulate the solidification of the Al-2 pct Cu alloy and demonstrated that the columnar-front velocity started to decrease and gradually stopped due to the thermal interactions with equiaxed grains growing ahead of the front.

Finally, it is very important to note that the classical CET models do not take into account natural or forced convection, which nevertheless has a major influence (movement of fragments, particles and equiax grains, modification of solute distribution...) nor effects due to gravity (sedimentation of particles and equiax grains...).

I.5 Segregation: main factors and consequences

During the solidification of the alloys, as presented in the previous part, both columnar and equiaxed zones have developed. However, the growth of these structures also interacts with the compositional fields of the alloy elements. Indeed, the solid usually has a lower composition compared to the liquid from which it crystallizes. As solidification progresses and dendrites grow, an imbalance in composition will develop between the solidified metal and the remaining molten metal, this imbalance in composition will eventually result in the segregation of the element. At the microscopic level, the chemical composition varies with each grain, as a result to out of equilibrium of the composition between the first solidified zone and the last one, the difference of the chemical composition within the single grains of the casting occurs, the microsegregation is described the related inhomogeneity of the solute elements as it occurs on the scale of growing crystals. Also, at the macroscopic scale, the chemical composition changes in the whole casting. Since the casting zone that cooled first (near the mold walls) are richer in one component than in the other. The remaining molten metal has been reduced by the time cooling occurs at the mold center, which produces a distinct composition of a different cross-section of the casting, called ingot segregation. These macroscopic inhomogeneities of solute

elements are referred to as macrosegregation, [67]. The distinction between microsegregation and macrosegregation is that heat treatment can not eliminate macrosegregation since diffusion in solids is slow even at elevated temperatures, and large diffusion distances can result in impracticably long homogenization holding times. Finally, at the scale of the process, the displacement of equiaxed grains and the permeability of structures affect liquid movement and composition profiles. These in turn modify the growth of the dendrite tips. Beckermann [68] considers that numerous final characteristics of the fields of segregation cannot be predicted without taking into consideration the microstructure. Thus, the progress to be made in modeling the evolution of the composition field cannot be done without the knowledge, in parallel, of the solidification structure. In return, the study of granular structures requires knowing the evolution of the composition fields in the ingot, at both grain and processing scales. These propositions were confirmed by the experimental studies of Lesoult *et al* [69]. Beckermann [68] gives a general review of the causes of macrosegregation and the models developed to model it.

When casting metal ingots, macrosegregation of the added alloying elements is usually observed at the scale of the cast product [1, 68]. Thus, the lower part of the ingot, shown in Fig.I.21, exhibits a composition profile below the nominal composition (negative segregation). This is due to the sedimentation of equiaxed crystals which are relatively poor of solute. After nucleation and sedimentation, they accumulated at the bottom of the ingot in the form of a conical grain stack. Conversely, the upper part of the ingot has an alloying element composition higher than the nominal composition (positive segregation). This part of the ingot solidifies last and accumulates by solutal convection, the solute rejected in the liquid. In fact, the enrichment in alloying elements tends to decrease the density of the liquid in the case of steels where the iron is alloyed with the lighter carbon. The convective currents that then appear move the solute upwards.

Finally, meso-segregation profiles known as ‘A’ or ‘V’ forms due to their shapes are also noticeable (Fig.I.21 b). The first profiles are in the form of ascending segregated lines directed toward the center of the ingot. These freckles are due to the solute enrichment of the liquid coming from the mushy zone, which may contribute to the partial remelting of the solid.

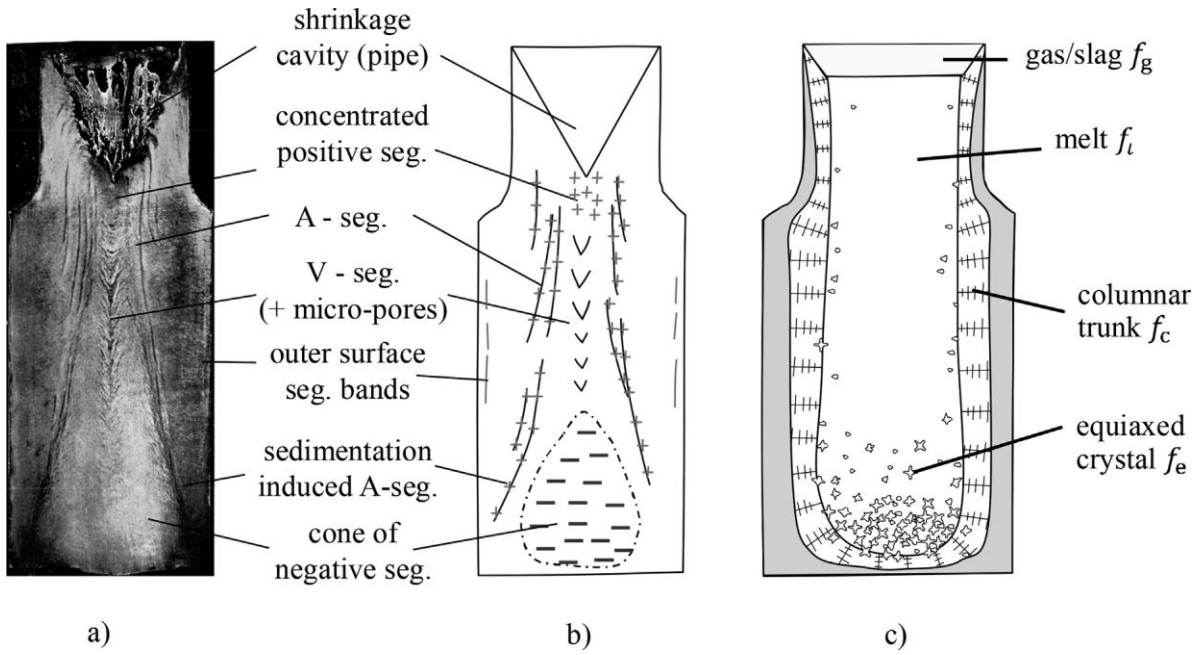

Fig. I.21. Typical macrosegregation pattern as observed in steel ingots. a) Sulfur prints of a 10.5-ton steel ingot with nominal composition of 0.30wt% C; b) schematic description of the different types of macrosegregation; c) schematic of the solidification process and involved phases (melt, columnar, equiaxed, covering slag), [70].

I.5.1. The segregation channels

Wang and Beckermann [71] have studied the solidification of NH_4Cl-H_2O alloys, they show the progressive development of these solute-rich bands along the path followed by the liquid leaving the pasty zone. Freckles formed in nickel-based superalloys are shown in Fig.I.22 (a), [68]. These photographs show the presence of equiaxed grains that accompany this type of mesosegregation. The V-shaped segregated channels (see Fig.I.22 (a)), visible in the center of the ingot, are explained by the movement of the last equiaxed grains present at the end of solidification and the displacement of the liquid at these instants.

These segregations, such as microsegregation, are in order of interdendritic space scale, indicating hundreds of micrometers. As diffusion is accelerated, these concentration differences can be eliminated by heat treatment. Nevertheless, at the ingot scale, the composition can be quite different in certain alloys, which is known as macrosegregation. Macro-segregation can be predicted using the *Scheil and Gulliver* law. In the case of a partition coefficient lower than 1, the solute rejected during solidification caused macrosegregation. Macrosegregation can take various forms [4], segregated channels (also known as freckles or chimneys) with compositional variation in strip-like shape, hot tears (crackings) (Fig.I.22 (b)). The incidence of these defects is closely related to the effect of the convection on the mushy zone.

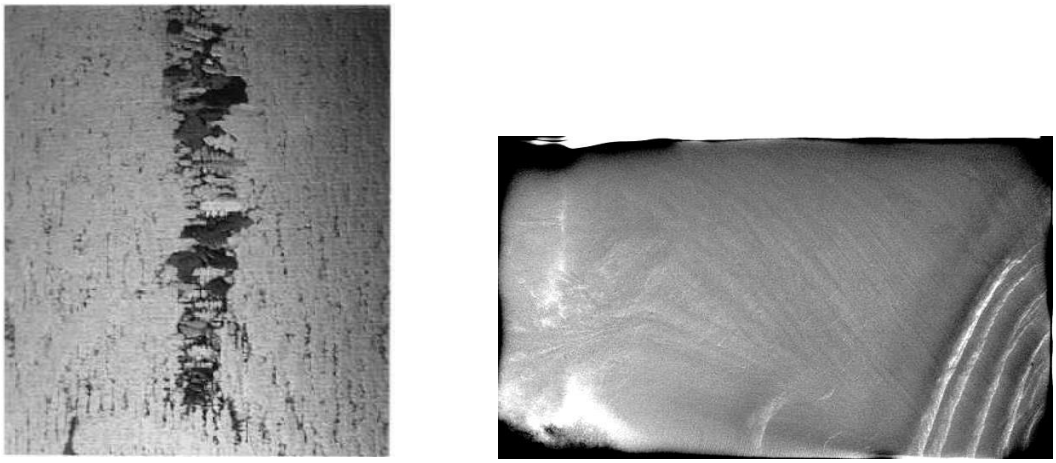

(a) (b)

Fig. I.22. (a) Zoom of single Freckles in a nickel-based superalloy. The Freckles has a diameter of about 2 mm. (b) X-ray photography showing freckles in a Sn-3wt.% Pb ingot (10*6*1 cm), [5].

I.5.2. Microsegregation interdendritic

The easiest expression of the evolution of the solid fraction as a function of the composition of the alloy elements remains the law of levers. In a binary system, the composition is considered to diffuse perfectly in the phases present. The composition profiles are presented in the phase diagram in Appendix I and the solid fraction formed is then given by Eq.I.10. Subsequently, *Scheil and Gulliver* [72, 73] developed a microsegregation model in which the solute diffusion hypothesis in the solid phase is neglected. The reason for this non-diffusion is easy to justify by referring to the characteristic diffusion times $\frac{\lambda_2^2}{D_c^s}$, i.e., at the scale of the secondary interendritic spacing, (λ_2), and D_c^s is the chemical diffusion coefficient in the solid phase. The *Scheil and Gulliver* relation comes from the conservation equation in an alloy element at the scale of a closed elementary volume:

$$C_s^* \delta f_s + \delta(C_l f_l) = 0 \tag{I.50}$$

where C_s^* presents the solid concentration at the solid/liquid interface, C_l is the composition of the liquid phase, assumed to be uniform and in thermodynamic equilibrium with the solid phase at the solid/liquid interface, with $C_s^* = kC_l^* = kC_l$, from Eq.I.1, Also, by using the equation $f_s + f_l = 1$, we then obtain an expression of the liquid fraction as a function of the composition, valid until the eutectic composition is reached C_E:

$$f_l = \left(\frac{C_l}{C_0}\right)^{\frac{-1}{1-k}} \tag{I.51}$$

Finally, it is also possible to consider a partial diffusion of the solute in the solid phase. Brody and Flemings [29] and Clyne and Kurz [74] propose to consider that the diffusion occurs over a characteristic thickness in the solid; the resulting law of solidification is then written:

$$uf_s = 1 - \left(\frac{C_l}{C_0}\right)^{\frac{-u}{1-k}} \tag{I.52}$$

where $u = (1 - 2\alpha' k)$ and:

$$\alpha' = \alpha\left[1 - exp\left(-\frac{1}{\alpha}\right)\right] - \frac{1}{2}exp\left(-\frac{1}{2\alpha}\right) \tag{I.53.a}$$

$$\alpha = \frac{D_c^s\, t_f}{\delta^2} \tag{I.53.b}$$

and t_f is the local solidification time, In terms of temperature, it is the necessary time that elapses between the moment when the point in question changes from the liquidus temperature T_L to the end of solidification temperature T_S.

I.5.3. Macrosegregation induced by liquid flow

On a macroscopic scale, segregation appears in the ingots. This may be due to solutal diffusion phenomena taking place at the scale of the process and to the displacement of equiaxed grains, causing in particular the sedimentation cone. However, the main origin of macrosegregation lies in the movement of the liquid allowing the transport of the alloy elements throughout the ingot.

There are many reasons for this movement:

- Shrinkage phenomenon: With the exception of some bodies with specific physical properties (diamond, water, semiconductors...), the liquid/solid transformation is always accompanied by an increase in density. Indeed, the ordered structure of the solid phase material increases its compactness compared to its state in the liquid phase. As a consequence, a sudden decrease in mass volume is observed at the solidification interface, of the order of a few percent in the case of metallic alloys. The main consequence of this decrease, called 'shrinkage', is an inflow of liquid towards the front that seeks to fill the areas that left vacant by the solidified liquid. This type of convection is responsible for the inverse segregation observed at the beginning of solidification on metal ingots. Flemings [1] consider a small volume element (Fig.I.23) through which the liquid traverses at a relative velocity compared to the solid $v^{s/l}$.

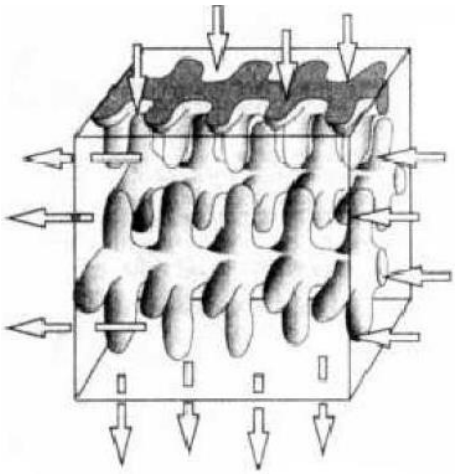

Fig. I.23. Diagram of the dendritic network traversed by the liquid, [5].

According to the hypothesis of zero solutal diffusion in the solid phase, the authors arrive at an expression that relates macrosegregation to the intensity of liquid movement:

$$\frac{df_l}{dC_l} = \frac{(1-\beta)}{(1-k)}\left(1 + \frac{v^{s/l}}{CR}\right)\frac{f_l}{C_l} \tag{I.54}$$

where *CR* is the cooling rate, β is the solidification shrinkage, expressed as the ration between the density difference (solid and liquid) and the solid density:

$$\beta = \frac{\rho_s - \rho_l}{\rho_s} \tag{I.55}$$

Ch. Beckermann [75], has defined a flow factor ξ as follows:

$$\xi = (1-\beta)\left(1 - \frac{u_n}{v_T}\right) \tag{I.56}$$

u_n is the flow velocity of the liquid in the direction normal to the isotherms, v_T is the advance velocity of the isotherms.

In the presence of solidification shrinkage (β positive) and zero liquid velocity, the relation (I.54) also shows that there is positive segregation. The inverse segregation observed at the beginning of solidification (Fig.I.22 (a)) corresponds to this type of phenomenon. Finally, if the velocity has a direction opposite to the temperature gradient ∇T, the term $v^{s/l}.\nabla T$ would be negative. If this latter is sufficiently important, the derivative of the solid fraction compared to the concentration of the liquid phase is positive. A remelting phenomenon then occurs, leading to an enrichment of the liquid in the alloy element. This phenomenon explains the formation of the segregated channels described above.

- Natural convection: The density of the liquid changes with temperature or composition. Thus, during cooling, the liquid contracts. An enrichment in solute also makes it possible to increase or decrease the density of the liquid. These variations in density are characterized by the thermal expansion coefficients β_T and solutal β_C defined by the equations:

$$\beta_T = -\frac{1}{\rho_l}\frac{\partial \rho_l}{\partial T} \quad \text{(I.57)}$$

$$\beta_C = -\frac{1}{\rho_l}\frac{\partial \rho_l}{\partial C_l} \quad \text{(I.58)}$$

Density gradients create convective movements as a result of the differences in buoyancy that they induce.

- Forced convection: it is possible to apply external volume forces to the liquid during solidification, e.g., by applying a magnetic field. The forces created allow the liquid to be stirred and homogenized.

Another source of movement is the fall of the equiaxed grains which causes the liquid to rise to their periphery. This grain sedimentation movement and the associated composition maps are studied by Wang and Beckermann in the case of the solidification of two alloys Al-4%wt Cu [71] and NH_4Cl-70%wt H_2O [76]. For this, they propose to model the evolution of the solid and liquid phases in an Eulerian approach, developed by considering the solid and liquid interendritic and extradendritic domains [77].

I.5.4. Influence factors

As detailed in the last section. On a macroscopic scale, during solidification the chemical species released are transported by convection movements in the liquid phase. These convection movements are caused by density gradients, themselves generated by temperature and solute concentration gradients. It is this thermosolutal convection that gives birth to macrosegregations (heterogeneities of concentration at the scale of the part or the solidified ingot), which will affect various properties (mechanical, chemical...). Segregation is often the cause of certain defects such as hot cracking, micro-shrinkage. In some cases, it also leads to an increase in the solidification interval by the presence of pockets still liquid below the solidus temperature, which can lead to ruptures in these zones at the end of solidification. The flow of the liquid through the mushy zone, where there is the development of the solid assumed as a fixed and rigid network, is considered as the main cause of the phenomenon of

macrosegregation. There are two obvious possibilities for not having the phenomenon of segregation on a macroscopic scale ($\xi = 1$):

1- Either no shrinkage of the solid phase ($\beta = 0$) and no flow in the normal direction to the isotherms ($u_n = 0$);

2- Or no flow of liquid other than that necessary to support the shrinkage of the solid phase during solidification in a given dimension.

On another side, a simplified formulation consists in considering this liquid + solid system as a closed system, partitioned by dendrite branches. This interdendritic liquid is at the origin of the so-called dendritic segregation (micro-segregation). The magnitude and the direction of the flow in the mushy zone depend on several factors: The permeability of the mushy zone is the most critical parameter which can restrict the flow within the mush [78]. Generally, permeability decreases with an increase in the solid fraction, which reduces the permeability of small interdendritic areas. The permeability of the solid in the mushy zone, how much liquid can penetrate inside, this factor can influence the appearance of those freckles. In addition, it is very important to mention that there are other main factors as the exchange of the solute between the concentration interdendrite (inside the envelope) and the extradendritic liquid concentration. A remelting phenomenon may occur when the liquid flows in the direction of temperature increase to the zone of a low solid fraction, with a velocity higher than the velocity of the isotherms. This means that the flow factor is negative $\xi < 0$. In view of Flemings equation (Eq I.54), which results in a decrease in solid fraction and temperature. This means that the remelting will be created and the segregated channels will be established in the mushy zone. Once the solidification has been completed in this zone, a positive micro-segregation can be seen within these channels. Thus, the initial composition of the concentration, the cooling rate and the thermal gradient are also main factors that can affect appearance of the freckles.

Furthermore, the interdendritic liquid is also originally due to the random direction of the dendrite and the coalescence of the side branches of the dendrite as known by the coarsening phenomena which will be detailed in chapter IV.

I.6 Partial conclusion

Based on the concepts presented, it can be deduced that growth morphologies are strongly dependent on solidification conditions, in particular the solidification rate and the thermal gradient; two main variables having the most important influence on the shape that metals and alloys take during their growth. In particular, it is the temperature gradient/solidification rate ratio, which is a major factor in determining changes in growth morphology: from the plane front for high values, to the equiaxed dendritic form for low values, to the columnar cellular and dendritic structures.

References chapter I

[1] M. C. Flemings, *Solidification Processing*. New York: McGraw-Hill College, 1974.

[2] W. Kurz et D. J. Fisher, *Fundamentals of Solidification*, 4th edition. Uetikon-Zuerich, Switzerland ; Enfield, N.H: CRC Press, 1998.

[3] M. Rappaz, M. Bellet, et M. Deville, *Modélisation numérique en science et génie des matériaux*. Presses polytechniques et universitaires romandes, 1998.

[4] G. Lesoult, « Solidification - Cristallisation et microstructures », *Tech. L'ingénieur*, 1986.

[5] L. Hachani, « Etude de l'influence de la convection naturelle et forcée sur le processus de la solidification : cas d'un alliage métallique binaire. », These de doctorat, Grenoble, 2013.

[6] R. Boussaa, « Étude de l'influence de la convection naturelle lors de la solidification de métaux purs et d'alliages métalliques binaires : expériences et simulations », These de doctorat, Lyon 1, 2014.

[7] M. Stefan-Kharicha, « Observation of Flow Phenomena during Dendritic Solidification », PhD thesis, University of Leoben, 2018.

[8] I. Hamzaoui, « Effet de la convection naturelle et forcée lors des transitions de phases : Application à la croissance cristalline », These de doctorat, Lyon, 2019.

[9] P. Pichon, « Solidification kinetics versus wetting kinetics relevant to Ribbon Growth on Substrate (RGS) casting of Silicon », PhD, Physics and Astronomy, the Ruhr University Bochum, 2015.

[10] L. Lafferrere, « Nucléation et transitions de phases en chimie pharmaceutique », These de doctorat, Aix-Marseille 3, 2002.

[11] J. Tchuindjang, M. Sinnaeve, et J. Lecomte-Beckers, *Effects of High Solidification Rates on Segregations and Solid Phase Transformations in High Speed Steels*. 2017.

[12] D. R. Askeland, P. P. Fulay, et W. J. Wright, *The Science and Engineering of Materials*. Cengage Learning, 2010.

[13] J. D. Hunt, « Steady state columnar and equiaxed growth of dendrites and eutectic », *Mater. Sci. Eng.*, vol. 65, n° 1, p. 75-83, juill. 1984.

[14] J. W. Christian, *The theory of transformations in metals and alloys - Part I - Equilibrium and General Kinetic Theory*, 2e éd. 1975.

[15] T. Campanella, « Etude de l'effet du brassage électromagnétique sur les microstructures d'alliages cuivreux », Thesis. Federal Institute of Technology Lausanne, EPFL, 2003.

[16] H. Jamgotchian, B. Billia, et L. Capella, « Morphology of the solidification front during undirectional growth of Pb-TI alloys », *J. Cryst. Growth*, vol. 64, n° 2, p. 338-344, nov. 1983.

[17] M. E. Glicksman, *Principles of Solidification: An Introduction to Modern Casting and Crystal Growth Concepts*. New York: Springer-Verlag, 2011.

[18] J. S. Langer, « Instabilities and pattern formation in crystal growth », *Rev. Mod. Phys.*, vol. 52, n° 1, p. 1-28, janv. 1980.

[19] M. C. Cross et P. C. Hohenberg, « Pattern formation outside of equilibrium », *Rev. Mod. Phys.*, vol. 65, n° 3, p. 851-1112, juill. 1993.

[20] W. J. Boettinger, S. Coriell, A. Greer, A. Karma, W. Kurz, M. Rappaz, and R. Trivedi, « Solidification microstructures: recent developments, future directions », *Acta Mater.*, vol. 48, n° 1, p. 43-70, janv. 2000.

[21] A. Karma et W. J. Rappel, « Phase-field model of dendritic sidebranching with thermal noise », *Phys. Rev. E Stat. Phys. Plasmas Fluids Relat. Interdiscip. Top.*, vol. 60, n° 4 Pt A, p. 3614-3625, oct. 1999.

[22] M. E. Glicksman, J. S. Lowengrub, S. Li, et X. Li, « A deterministic mechanism for dendritic solidification kinetics », *JOM*, vol. 59, n° 8, p. 27-34, août 2007.

[23] W. Zhijun, J. Wang, et G. Yang, « Phase-field investigation of effects of surface-tension anisotropy on deterministic sidebranching in solutal dendritic growth », *Phys. Rev. E Stat. Nonlin. Soft Matter Phys.*, vol. 78, p. 042601, nov. 2008.

[24] M. Georgelin et A. Pocheau, « Onset of sidebranching in directional solidification », *Phys. Rev. E*, vol. 57, n° 3, p. 3189-3203, mars 1998.

[25] R. Trivedi, Y. Shen, et S. Liu, « Cellular-to-dendritic transition during the directional solidification of binary alloys », *Metall. Mater. Trans. A*, vol. 34, n° 2, p. 395-401, févr. 2003.

[26] J. Teng, S. Liu, et R. Trivedi, « Onset of sidewise instability and cell–dendrite transition in directional solidification », *Acta Mater.*, vol. 57, n° 12, p. 3497-3508, juill. 2009.

[27] D. M. Rosa, J. E. Spinelli, I. L. Ferreira, et A. Garcia, « Cellular/Dendritic Transition and Microstructure Evolution during Transient Directional Solidification of Pb-Sb Alloys », *Metall. Mater. Trans. A*, vol. 39, n° 9, p. 2161-2174, sept. 2008.

[28] Y. Lee, M. Nordin, S. S. Babu, et D. F. Farson, « Effect of Fluid Convection on Dendrite Arm Spacing in Laser Deposition », *Metall. Mater. Trans. B*, vol. 45, n° 4, p. 1520-1529, août 2014.

[29] L. Hachani B. Saadi, X. D. Wang, Ab. Nouri, K. Zaidat, A. Belgacem-Bouzida, L. Ayouni-Derouiche, G. Raimondi, Y. Fautrelle., « Experimental analysis of the solidification of Sn–3 wt.%Pb alloy under natural convection », *Int. J. Heat Mass Transf.*, vol. 55, n° 7, p. 1986-1996, mars 2012.

[30] S. Suwas et R. K. Ray, « Texture Evolution During Solidification and Solid-State Transformation », in *Crystallographic Texture of Materials*, S. Suwas et R. K. Ray, Éd. London: Springer, 2014, p. 73-93.

[31] D. Stefanescu, « Equilibrium and non-equilibrium during solidification », in *Science and Engineering of Casting Solidification*, Second Edition, Springer., 2009, p. 5-24.

[32] S. Mcfadden et D. Browne, « A Generalized Version of an Ivantsov-based Dendrite Growth Model Incorporating a Facility for Solute Measurement Ahead of the Tip », *Comput. Mater. Sci.*, vol. 55, avr. 2012.

[33] A. Kharicha, M. Stefan-Kharicha, A. Ludwig, et M. Wu, « A scale adaptive dendritic envelope model of solidification at mesoscopic scales », *IOP Conf. Ser. Mater. Sci. Eng.*, vol. 84, juin 2015.

[34] S. Steinbach et L. Ratke, « Effects of controlled convections on dendritic microstructure and segregation during microgravity solidification », *ESA-SP 647*, vol. 647, p. 373-378, juin 2007.

[35] W. Kurz et D. J. Fisher, « Dendrite growth at the limit of stability: tip radius and spacing », *Acta Metall.*, vol. 29, n° 1, p. 11-20, janv. 1981.

[36] G. F. Bolling et W. A. Tiller, « Growth from the Melt. III. Dendritic Growth », *J. Appl. Phys.*, vol. 32, n° 12, p. 2587-2605, déc. 1961.

[37] R. Trivedi et G. M. Pound, « Growth Kinetics of Plate-Like Precipitates », *J. Appl. Phys.*, vol. 40, n° 11, p. 4293-4300, oct. 1969.

[38] C. Atkinson, « Diffusion-Controlled Growth of an Array of Plates », *J. Appl. Phys.*, vol. 42, n° 5, p. 1994-1997, avr. 1971.

[39] J. D. Hunt et S. Z. Lu, « Numerical modeling of cellular/dendritic array growth: spacing and structure predictions », *Metall. Mater. Trans. A*, vol. 27, n° 3, p. 611-623, mars 1996.

[40] J. D. Hunt, « Pattern formation in solidification », *Sci. Technol. Adv. Mater.*, vol. 2, n° 1, p. 147-155, mars 2001.

[41] D. H. Kirkwood, « A simple model for dendrite arm coarsening during solidification », *Mater. Sci. Eng.*, vol. 73, p. L1-L4, août 1985.

[42] P. Zhao, M. Vénere, J. C. Heinrich, et D. R. Poirier, « Modeling dendritic growth of a binary alloy », *J. Comput. Phys.*, vol. 188, n° 2, p. 434-461, juill. 2003.

[43] J. Lipton, M. E. Glicksman, et W. Kurz, « Dendritic growth into undercooled alloy metals », *Mater. Sci. Eng.*, vol. 65, n° 1, p. 57-63, juill. 1984.

[44] J. Lipton, W. Kurz, et R. Trivedi, « Rapid dendrite growth in undercooled alloys », *Acta Metall.*, vol. 35, n° 4, p. 957-964, avr. 1987.

[45] R. Trivedi, J. Lipton, et W. Kurz, « Effect of growth rate dependent partition coefficient on the dendritic growth in undercooled melts », *Acta Metall.*, vol. 35, n° 4, p. 965-970, avr. 1987.

[46] V. Pines, A. Chait, M. Zlatkowski, et Christoph Beckermann, « Equiaxed dendritic solidification in supercooled melts », *J. Cryst. Growth*, vol. 197, n° 1, p. 355-363, févr. 1999.

[47] M. Wu et A. Ludwig, « Modeling equiaxed solidification with melt convection and grain sedimentation-I: Model description », *Acta Mater.*, vol. 57, n° 19, p. 5621-5631, nov. 2009.

[48] C. J. Paradies, R. N. Smith, et M. E. Glicksman, « The influence of convection during solidification on fragmentation of the mushy zone of a model alloy », *Metall. Mater. Trans. A*, vol. 28, n° 3, p. 875-883, mars 1997.

[49] T. Sato, W. Kurz, et K. Ikawa, « Experiments on Dendrite Branch Detachment in the Succinonitrile-Camphor Alloy », *Trans. Jpn. Inst. Met.*, vol. 28, n° 12, p. 1012-1021, 1987.

[50] S. Liu, S.-Z. Lu, et A. Hellawell, « Dendritic array growth in the systems NH4Cl–H2O and [CH2 CN]2–H2O: the detachment of dendrite side arms induced by deceleration », *J. Cryst. Growth*, vol. 234, n° 4, p. 740-750, févr. 2002.

[51] J. P. Gu et C. Beckermann, « Simulation of convection and macrosegregation in a large steel ingot », *Metall. Mater. Trans. A*, vol. 30, n° 5, p. 1357-1366, mai 1999.

[52] J. P. Gu, C. Beckermann, et A. F. Giamei, « Motion and remelting of dendrite fragments during directional solidification of a nickel-base superalloy », *Metall. Mater. Trans. A*, vol. 28, n° 7, p. 1533-1542, juill. 1997.

[53] M. Wu, A. Ludwig, et A. Fjeld, « Modelling mixed columnar-equiaxed solidification with melt convection and grain sedimentation – Part II: Illustrative modelling results and parameter studies », *Comput. Mater. Sci.*, vol. 50, n° 1, p. 43-58, nov. 2010.

[54] M. A. Martorano et V. B. Biscuola, « Predicting the columnar-to-equiaxed transition for a distribution of nucleation undercoolings », *Acta Mater.*, vol. 57, n° 2, p. 607-615, janv. 2009.

[55] J. N. Silva, D. J. Moutinho, A. L. Moreira, I. L. Ferreira, et O. L. Rocha, « The columnar to equiaxed transition during the horizontal directional solidification of Sn–Pb alloys », *J. Alloys Compd.*, vol. 478, n° 1, p. 358-366, juin 2009.

[56] J. Hutt et D. Stjohn, « The origins of the equiaxed zone—Review of theoretical and experimental work », *Int. J. Cast Met. Res.*, vol. 11, n° 1, p. 13-22, juill. 1998.

[57] H. Nguyen-Thi G. Reinhart, N. Mangelinck-NoeL, H. Jung, B. Billia, T. Schenk, J. Gastaldi, J. Hartwig, and J. Baruchel., « In-Situ and Real-Time Investigation of Columnar-to-Equiaxed Transition in Metallic Alloy », *Metall. Mater. Trans. A*, vol. 38, n° 7, p. 1458-1464, juill. 2007.

[58] S. Lekakh, R. O'Malley, M. Emmendorfer, et B. Hrebec, « Control of Columnar to Equiaxed Transition in Solidification Macrostructure of Austenitic Stainless Steel Castings », *ISIJ Int.*, vol. 57, p. 824-832, mai 2017.

[59] G. Zimmermann, L. Sturz, H. Nguyen-Thi, N. Mangelinck-Noel, Y.Z. Li, C.-A. Gandin, R. Fleurisson, G. Guillemot, S. Mcfadden, R.P. Mooney, P. Voorhees, A. Roosz, A. Ronafoldi, C. Beckermann, A. Karma, C.-H. Chen, N. Warnken, A. Saad, G.-U. Grun, M. Grohn, I. Poitrault, T. Pehl, I. Nagy, D. Todt, O. Minster, and W. Sillekens., « Columnar and Equiaxed Solidification of Al-7 wt.% Si Alloys in Reduced Gravity in the Framework of the CETSOL Project », *JOM*, vol. 69, n° 8, p. 1269-1279, août 2017.

[60] M. A. Martorano, C. Beckermann, et C.-A. Gandin, « A solutal interaction mechanism for the columnar-to-equiaxed transition in alloy solidification », *Metall. Mater. Trans. A*, vol. 34, nº 8, p. 1657-1674, août 2003.

[61] C. Y. Wang et C. Beckermann, « Prediction of Columnar to Equiaxed Transition during Diffusion-Controlled Dendritic Alloy Solidification », *Metall. Mater. Trans. A*, vol. 25, nº 5, p. 1081-1093, mai 1994.

[62] M. Gäumann, C. Bezençon, P. Canalis, et W. Kurz, « Single-crystal laser deposition of superalloys: processing–microstructure maps », *Acta Mater.*, vol. 49, nº 6, p. 1051-1062, avr. 2001.

[63] W. Kurz, C. Bezençon, et M. Gäumann, « Columnar to equiaxed transition in solidification processing », *Sci. Technol. Adv. Mater.*, vol. 2, nº 1, p. 185-191, janv. 2001.

[64] J. Banaszek, S. McFadden, D. J. Browne, L. Sturz, et G. Zimmermann, « Natural Convection and Columnar-to-Equiaxed Transition Prediction in a Front-Tracking Model of Alloy Solidification », *Metall. Mater. Trans. A*, vol. 38, nº 7, p. 1476-1484, juill. 2007.

[65] S. Mc Fadden et D. J. Browne, « Meso-scale simulation of grain nucleation, growth and interaction in castings », *Scr. Mater.*, vol. 55, nº 10, p. 847-850, nov. 2006.

[66] D. J. Browne et J. D. Hunt, « A Fixed Grid Front-Tracking Model of the Growth of a Columnar Front and an Equiaxed Grain During Solidification of an Alloy », *Numer. Heat Transf. Part B Fundam.*, vol. 45, nº 5, p. 395-419, mai 2004.

[67] A. Ludwig, M. Wu, et A. Kharicha, « On Macrosegregation », *Metall. Mater. Trans. A*, vol. 46, nº 11, p. 4854-4867, nov. 2015.

[68] C. Beckermann, « Modeling of macrosegregation: Past, present and future », *Proc. Merton C Flemings Symp. Solidif. Mater. Process.*, janv. 2000.

[69] M. M'Hamdi, H. Combeau, et G. Lesoult, « Modelling of heat transfer coupled with columnar dendritic growth in continuous casting of steel », *Int. J. Numer. Methods Heat Fluid Flow*, vol. 9, nº 3, p. 296-317, janv. 1999.

[70] M. Wu, A. Ludwig, et A. Kharicha, « Simulation of As-Cast Steel Ingots », *Steel Res. Int.*, vol. 89, nº 1, p. 1700037, 2018.

[71] C. Y. Wang et C. Beckermann, « Equiaxed dendritic solidification with convection: Part II. Numerical simulations for an Al-4 Wt pct Cu alloy », *Metall. Mater. Trans. A*, vol. 27, nº 9, p. 2765-2783, sept. 1996.

[72] G.H. Gulliver, « The quantitative effect of rapid cooling upon the constitution of binary alloys », *J Inst Met.*, vol. 9, p. 120-157, 1913.

[73] E. Scheil, « Bemerkungen zur schichtkristallbildung », *Z. Für Met.*, vol. 34, 1942.

[74] T. W. Clyne et W. Kurz, « Solute redistribution during solidification with rapid solid state diffusion », *Metall. Trans. A*, vol. 12, nº 6, p. 965-971, juin 1981.

[75] C. Beckermann, *Macrosegregation*, vol. 15. ASM Handbook, 2008.

[76] C. Beckermann et C. Y. Wang, « Equiaxed dendritic solidification with convection: Part III. Comparisons with NH4Cl-H2O experiments », *Metall. Mater. Trans. A*, vol. 27, n° 9, p. 2784-2795, sept. 1996.

[77] C. Y. Wang et C. Beckermann, « A unified solute diffusion model for columnar and equiaxed dendritic alloy solidification », *Mater. Sci. Eng. A*, vol. 171, n° 1, p. 199-211, nov. 1993.

[78] D. R. Poirier, « Permeability for flow of interdendritic liquid in columnar-dendritic alloys », *Metall. Trans. B*, vol. 18, n° 1, p. 245-255, mars 1987.

CHAPTER II

Electromagnetic stirring applied to solidification processes

II.1. Introduction

This chapter is devoted to study those phenomena that related to the magneto hydrodynamics. Indeed, this field basically deals the interaction between magnetic fields and moving conducting fluids. However, the purpose of the application of the magnetic field is mainly to eliminate those problems of segregation that appear at the end of solidification. This phenomenon was described in several studies as R. Berton [1], R. Moreau [2, 3] and P. A. Davidson [4]. However, only its application to the solidification of metal alloys will be discussed in this chapter. Also, this part retraces the basic principles used in magneto-hydro-energetics (MHE) and some works concerning the study of convection movements induced by magnetic fields in metallurgy and their influence on solidification. In addition, a review of previous work, dealing with the effect of different electromagnetic stirring configurations on the solidification process, will also be presented in this chapter. Emphasis will of course be placed on the effect of forced convection induced by electromagnetic stirring on the final structure.

II.2. Electromagnetism and convection: general concepts

Since Magneto-Hydro-Energetics (MHE) is a large field enough to constitute a science in itself, general application of this field to the solidification will be discussed in this chapter, without claiming to study this phenomenon with precision.

Magnetohydrodynamics (MHD) covers the study of the physical phenomena present in an electrically conductive fluid where the velocity field u and the magnetic induction B are coupled. To understand the fundamental mechanisms of this coupling, it is interesting to distinguish two essential effects that are present simultaneously:

- Any movement in an electrically conductive fluid causes the appearance of an electromotive force, and produces electric currents of density J which induce their own magnetic field, (i.e., the penetration of the magnetic field inside the conductive charge creates induced current).

- In this same fluid subjected to the action of a magnetic field, forces of Laplace $\vec{J} \times \vec{B}$ develop (body force). They act on each unit of volume of the material. These forces also called Lorentz forces which are created thanks to the coupling between the magnetic field $\vec{B}$ and the induced current.

The purpose of introducing this force (Lorentz force) in the solidification process is to homogenize the temperature as well as the concentration of the alloy in the liquid phase; in this

case the solidification process occurs under the effect of forced convection generated by Electro Magnetic Stirring (EMS) that will be the main part in this chapter. The system of governing equations of MHD therefore consists of Maxwell's equations for the electromagnetic part and Navier-Stokes equations for the hydrodynamic part. The basic equations of MHD are defined in this section as follow:

II.2.1. Electromagnetism

Electromagnetic phenomena influence the flow of a fluid via Lorentz forces that will be define later. They express the interaction of magnetic induction and electric currents either applied or induced. The Maxwell equations and generalized Ohm's law are the main fundamental equations governing the electrical behaviour of a conductive charge subjected to a magnetic field. For example, within the MHD approximation context, Maxwell's equations can be found in R. Berton [1] and R. Moreau [2] can be written in the approximation of electromagnetism as follows:

- The first equation expresses the conservation of the magnetic induction flux $\vec{B}$:

$$div\ \vec{B} = 0 \qquad \text{(II.1)}$$

- The Ampere equation where the displacement current is neglected in front of the conduction current:

$$rot\ \vec{B} = \mu\ \vec{J} \qquad \text{(II.2)}$$

where μ and $\vec{J}$ represent the magnetic permeability (in void $\mu = 4\pi\ 10^{-7}\ H\ m^{-1}$) and the electric current density, respectively.

- Faraday law which relates the temporal variations of the magnetic induction field to the spatial variations of the electric field:

$$rot\ \vec{E} = -\frac{\partial \vec{B}}{\partial t} \qquad \text{(II.3)}$$

where $\vec{E}$ represents the electric fields.

Generalized Ohm's law governs the density of electric current in a moving environment subjected to an electromagnetic field. It is defined by:

$$\vec{J} = \sigma\left(\vec{E} + \vec{u} \wedge \vec{B}\right) \quad \text{(II.4)}$$

with σ and $\vec{u}$ represent the electrical conductivity of the assumed isotropic fluid, and the velocity field of the fluid, respectively.

According to Maxwell's equations and generalized Ohm's law, it seems that the magnetic field $\vec{B}$ is a fundamental electromagnetic property; the other properties such as $\vec{E}$ and $\vec{J}$ are simply deduced from it.

It is therefore possible to express with a single equation called the "induction equation", the evolution of the magnetic field as a function of the electric field and the current density.

- **Term $\vec{u} \wedge \vec{B}$**

The flow of a conductive fluid acts on the magnetic problem through the velocity field $\vec{u}$. These interaction results in the term $\vec{u} \wedge \vec{B}$ in the generalized Ohm's law. The distribution of the magnetic induction $\vec{B}$ is then controlled by diffusion and convection mechanisms due to the velocity field $\vec{u}$. The study of these phenomena is based on the equation of induction and this term presents the MHD part in Ohm law.

II.2.2. The induction equation, [5]

The induction equation (Eq. II.5), one of the MHD equations, is a partial differential equation that relates the magnetic field and velocity of an electrically conductive fluid. It can be derived from Maxwell's equations and Ohm's law (rotation of the generalized Ohm's law); i.e., substituting in this law Eq. II.3 and Eq. II.4.

$$\frac{\partial \vec{B}}{\partial t} = rot\left(\vec{u} \wedge \vec{B}\right) + \frac{1}{\mu\sigma}\nabla^2\vec{B} \quad \text{(II.5)}$$

Following this equation, the temporal evolution of the field $\vec{B}$ can be separated into two phenomena:

- a phenomenon of convection governed by the first term:

$$rot\left(\vec{u} \wedge \vec{B}\right)$$

- and a diffusion phenomenon governed by the second term:

$$\frac{1}{\mu\sigma}\nabla^2\vec{B}$$

II.2.3. Dimensionless characteristic numbers of the MHD

The dimensionless numbers characterizing the nature of the preponderant phenomena are introduced. They make it possible to specify the degree of MHD coupling.

II.2.3.1. Magnetic Reynolds number R_m

This number delivers an estimation of the relative effects of magnetic field advection compared to magnetic diffusion, i.e., the magnetic field tends to relax to a purely diffusive state:

$$R_m = \sigma \mu U a \tag{II.6}$$

where U and a denote respectively a characteristic velocity and a characteristic length of the studied physical system. At the laboratory scale and with classical liquid metals, the magnetic Reynolds number is always low in front of the unit ($R_m << 1$). Thus, any convection effect of the magnetic field can be neglected. The induction equation is reduced to a classical diffusion equation. In contrast, for $R_m \gg 1$, the distribution of B is essentially controlled by convection phenomena. This regime is convective.

II.2.3.2. Alfvén Velocity UAlf

The Alfvén velocity U_{Alf}, allows expressing the magnetic induction as a quantity which has the dimension of velocity. It is given by the following relation:

$$U_{Alf} = \frac{B_0}{\sqrt{\mu \rho}} \tag{II.7}$$

where B_0 and ρ represent a characteristic value of the magnetic field and the density of the electrically conductive charge, respectively.

II.2.3.3. Interaction parameter N

To characterize the importance of the electromagnetic forces, especially to quantify the surface oscillations in relation to the inertial forces of the fluid, an interaction parameter N is defined by the following relation:

$$N = \frac{\sigma B_0^2}{\rho \omega} \tag{II.8}$$

Where ω represents the magnetic field pulsation, this parameter presents the ration of Lorentz force to inertia.

II.2.3.4. Hartman number Ha

The Hartmann number (Ha) is the ratio of electromagnetic force to the viscous force; it is frequently encountered in fluid flows through magnetic fields, it is defined by:

$$H_a = Ba\sqrt{\frac{\sigma}{\mu}} \tag{II.9}$$

where l and μ are the characteristic length and the dynamic viscosity, respectively.

II.2.4. Lorentz force

In the case of an alternating electromagnetic field applied to an electrically conductive fluid, (for example metal alloys), induced electric currents $\vec{J}$ develop in this fluid, which according to the generalized Ohm's law are written according to R. Moreau [2]:

$$\vec{J} = \sigma\left(\frac{\partial \vec{A}}{\partial t} + \nabla\varphi\right) \tag{II.10}$$

where $\vec{A} = A(\cos\omega t + \emptyset)$ represents the magnetic vector potential with $\emptyset$ phase, φ is the electrical potential and ω is the pulsation of the magnetic field.

The mechanism of electromagnetic stirring (EMS) is based on the creation of a Laplace force (Lorentz force) in the conductive materials, causing the appearance of forced convection in the liquid and mushy zone. Indeed, if we consider a metallic sample surrounded by an induction coil, the circulation of an electric current $\vec{J}$ in the induction spire creates a magnetic field B (see Fig. II.1) that penetrates the sample and generates an induced current (eddy current), $\vec{J}_{ind}$, whose direction is opposite to $\vec{J}$. The interaction between the induced current and the magnetic field B, which is the sum of the fields induced by $\vec{J}$ and $\vec{J}_{ind}$, creates the Lorentz force [6]:

$$\vec{F} = \vec{J}_{ind} \wedge \vec{B} = -\sigma\left(\frac{\partial \vec{A}}{\partial t} \wedge \left(\nabla \wedge \vec{A}\right) + \nabla\varphi \wedge \left(\nabla \wedge \vec{A}\right)\right) \tag{II.11}$$

This body force produces a stirring within the fluid. The physical characteristics of the stirring are strongly influenced by the frequency and intensity of the magnetic field used. Furthermore, the application of this force on the solidification of pure metal (pure tin) will be presented and discussed in Chapter III.

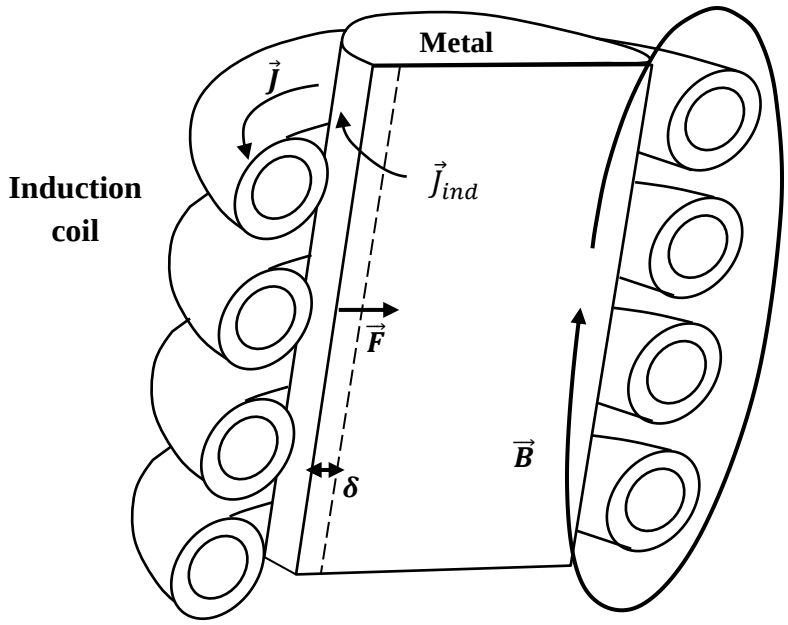

Fig. II.1. Représentation d'une coupe longitudinale d'un système de chauffage par induction illustrant le principe du brassage électromagnétique, [7].

In the particular case of alternative current systems, the induced current and the magnetic field are present only in a portion of the metal domain, the electromagnetic skin, of thickness, [6]:

$$\xi = 50\sqrt{\rho_{elc}/f} \tag{II.12}$$

where ρ_{elc} denotes the electrical resistivity of the material in [$\mu\Omega\ cm$] and *f* the frequency of the current in [*Hz*]. The motion of the liquid is then created by the inhomogeneity of the Lorentz force along the sample. This force varies depending on the setup that creates it (rotating field, pulsed field, traveling field...).

II.3. Electromagnetic stirring and its effect on the solidification process

II.3.1. Permanent magnetic field

Let us first consider the case of the action of a permanent magnetic field on a conducting liquid. This permanent magnetic field can be created either by a coil fed by a direct current or by a magnet. It can be used to brake, or even eliminate the natural convection that occurs during the solidification of alloys.

Laskar *et al* [8] have shown the existence of a thermoelectric current $\vec{J}_{TE}$ inside the mushy zone which associated with the permanent magnetic field $\vec{B}$, produces a Laplace force of

thermoelectric origin (simultaneous appearance of an electric current and a heat flow in the presence of a temperature gradient and an electric potential gradient):

$$\vec{F}_{TE} = \vec{J}_{TE} \times \vec{B} \qquad \text{(II.13)}$$

This force generates a movement inside the mushy zone, which remains relatively localized.

Application to directed solidification

The work of Lehmann *et al* [9] shows that the application of a uniform magnetic field prevents segregation in two Cu-Ag and Al-Cu alloys by counterbalancing the natural convection inside the mushy zone. Another example of effect on macrosegregation is studied by Tewari *et al* [10] in the case of the Pb-Sn 18%pds alloy, for which the formation of "*freckles*" can be suppressed by limiting the natural convection.

These studies show the importance of the direction of the field compared to the growth direction for the braking effect to be effective. Moreover, this technique is dependent on the thermoelectric capacity of the material. Let us remind that $\vec{J}_{TE}$ depends on the difference of the thermoelectric capacity of the alloy compounds and that the studies cited above were made with alloys having a rather large difference of thermoelectric capacity.

II.3.2. Rotating magnetic field, RMF

Stirring by Rotating Magnetic Field (RMF) is the most widely used technique in metallurgy. This technique is based on the principle of an asynchronous motor. The motor is powered by a polyphase alternating current. The case of a three-phase motor is the most common, as all three phases of the network are generally used, with a motor operating frequency of 50 Hz. Each phase is shifted by $2\pi/3$ in space and time.

Application to directed solidification

The application of a RMF in the liquid imposes a toroidal rotation movement. In addition, the RMF has also an effect on the solidification process, more particularly on the final microstructure. M. Xiaohua *et al* [11] have studied the effect of rotating magnetic field on the solidification microstructures of Pb-Sn alloys and they have found that that RMF can totally eliminate the gravity induced macrosegregation, refining microstructures, resulting in dendrite fragmentation and increasing solute diffusion velocity.

M. Svéda *et al* [12] have studied the effect of RMF on solidification of Sn-Cd alloys and they have shown that the melt flow has a significant effect on the solidified structure. Indeed, during the solidification of Sn-1.6wt%Cd alloy with applying RMF, two forms of flow appear in the melt. However, the melt flows in two directions: along the sample axis (primary flow) and parallel to it (secondary flow) (see Fig. II.2). Moreover, the solidification front is in form of cells (Sn-based primary solid solution) in α phase (light region in the Fig. II.2) started to solidify from the melt (L) while the liquidus concentration is C_0 = 1.6-wt%. The darker region that located in between the cells directly from the melt with significant supercooling (T_β^s temperature) in β phase (CdSn4 based secondary solid solution) compound solidified (see Fig. II.2). At T_β^f the solidification of β phase will be completed.

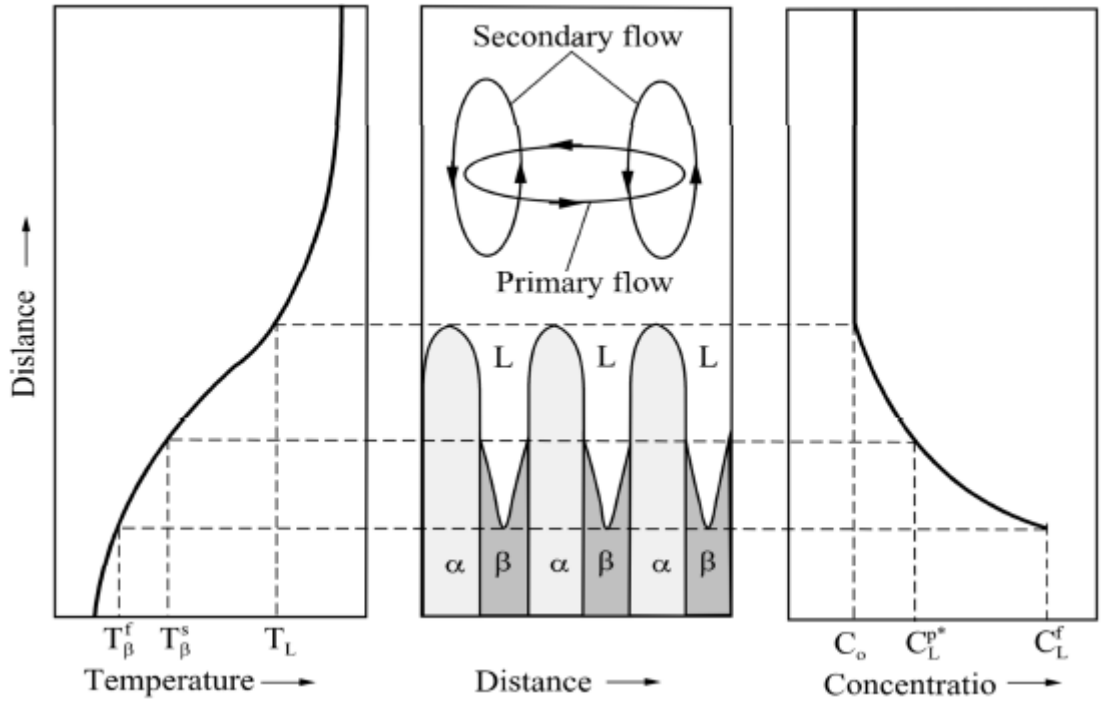

Fig. II.2. Temperature distribution, microstructure, concentration distribution in the melt during solidification, [12].

A columnar (cellular) microstructure is formed when a Sn-1.6wt% Cd alloy is solidified at a velocity of 0.02 mm/s in a temperature gradient of 6 K/mm. As the melt is stirred with RMF at 3 mT magnetic induction, the columnar structure is maintained, while an equiaxial microstructure is solidified at 10 mT or higher values,

II.3.3. Traveling magnetic field, TMF

In this case, the inductor is traversed by three-phase current, creating a moving magnetic field, [7]:

$$B(r,t) = B_0(r)\cos\left(\omega t + \varphi(r)\right) \quad \text{(II.14)}$$

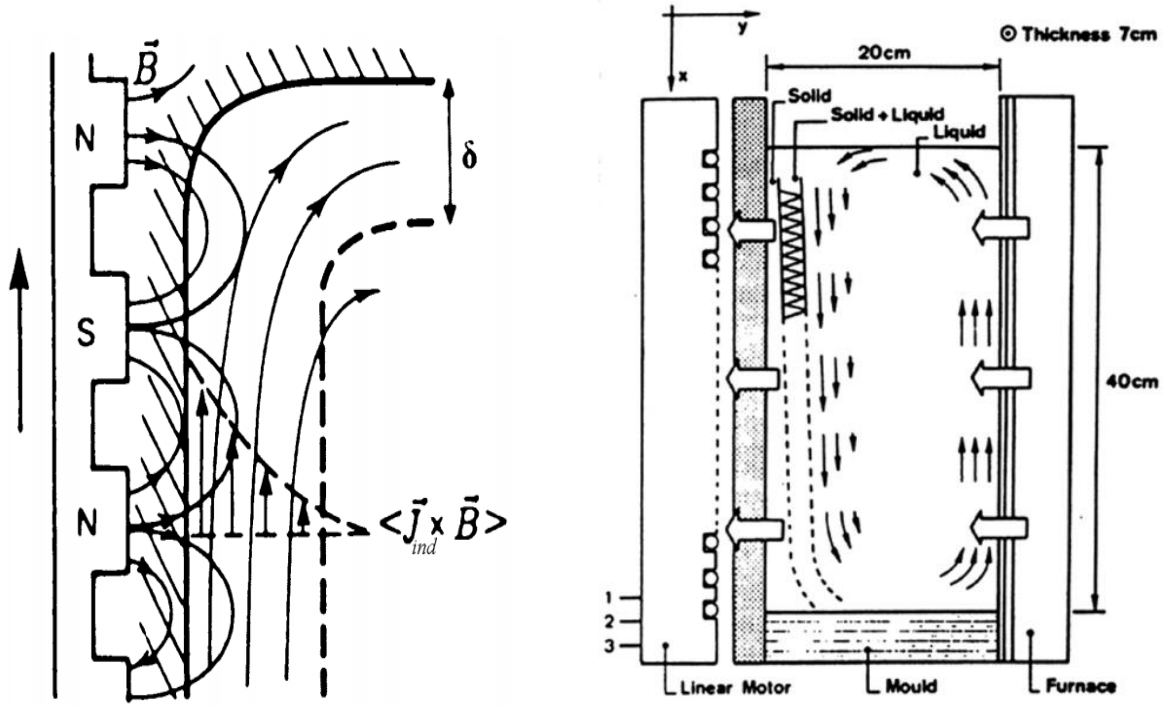

(a) **(b)**

Fig. II.3. (a) Orientation and variation of the Lorentz force in the case of a TMF. (b) EMS applied to the casting of an aluminum alloy by travelling field, [7].

Due to the configuration of the induction coils (Fig. II.3 (a)), the direction of the Lorentz force applied to a component is parallel to the wall. The convection movements thus created follow the direction of movement of the inductors along the walls (see Fig. II.3 (b)). This technique is mainly used during the solidification of steel [13].

Application to directed solidification

Several numerical models developed in the literature [14-16] coupling the hydrodynamic equations to those of directed solidification. Most of them are macroscopic models only interested in the effect of convection in the liquid bath as well as in the shape of the macro-front represented by the liquidus temperature.

Mazuruk [17] and Yesilyurt *et al* [18] show that they are able to counterbalance gravity-driven flows by applying a travelling magnetic field in the case of planar-front solidification (semiconductor).

Medina *et al* [14] showed the existence of a recirculation zone in the mushy zone induced by the flows in the liquid bath. An improvement was made by Quillet [19] who completed this

model in order to study the effects of a travelling magnetic field on the macro-segregations. They have shown that the position of the freckles induced by the deformation of the mushy zone by forced convection could be controlled in the case of a Pb-Sn alloy.

The predictions of his model are in qualitative agreement with experimental studies [19]. Dagner *et al* [15] have also developed a code based on the model of Heinrich and Poirier model. They study the effect of a travelling magnetic field on macrosegregation. In their comparative study between the solidification of an Al-Si alloy under a travelling field and then under a rotating field, they obtain a better control of the position of the radial macrosegregation, a peripheral eutectic border or a segregated channel in the center.

All these models need to be confronted with experiments. Except Mazuruk [17] who performed plane-front experiments using semiconductors.

The application of TMF has also an effect on the solidification of pure metals as will be discussed in the next chapter (chapter III) in the solidification of pure tin. Indeed, the TMF has shown its effect on dynamic, thermal fields and the morphology of the solidification front.

II.3.4. Pulsed magnetic field, PMF

The inductor is traversed by a single-phase current, creating a fixed alternating magnetic field, [7]:

$$B(r,t) = B_0(r)\cos(\omega t + \varphi) \qquad \text{(II.15)}$$

This type of field is also called a "pulsating field". In the case of stirring near the top of a cast ingot (continuous or not), this force applies mainly in the corners of the liquid pocket (see Fig. II.4), creating also an acceleration of the liquid in this region. In the case of electromagnetic stirring in the volume of the ingot (absence of free surface, which corresponds to the situation encountered in the continuous casting of copper alloys into wires), the divergence of the Lorentz force is reinforced by the use of a single spire which creates a field whose field lines are toroidal (Fig. II.4). The induced force tends to create two convection vortices, in opposite directions, as long as the region in question is still liquid. Note the importance of the positioning of the induction spire in relation to the liquidus of the alloy. This latter being influenced by the heating, inevitably associated with the induction.

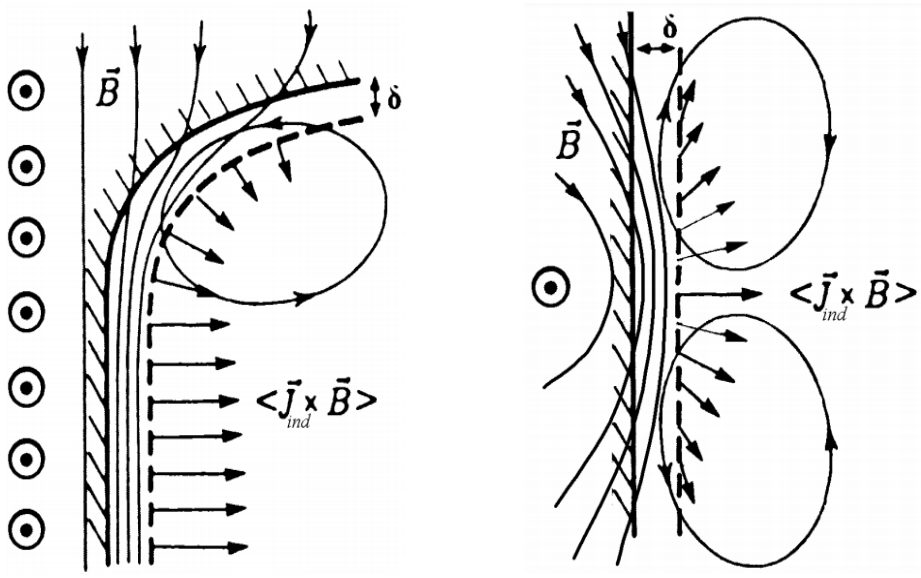

(a) **(b)**

Fig. II.4. Orientation and variation of the Lorentz force in the case of a pulsating field near a free liquid surface (a) and in volume (b), [7].

Application to directed solidification

The effect of a pulse magnetic field on the structure was studied experimentally by L. Xi-Liang *et al* [20]. Indeed, the results showed that as the pulse voltage increased, the solidification structure changed from coarse columnar crystal to fine globular crystal. C.Y. Ban *et al* [21] have studied the solidification of 2124 Al-alloy under the effect of pulsed magnetic field (PMF). However, they found that a remarkable change occurs in the solidification structures. Moreover, a change from thick continuous eutectic network to thin discontinuous one at grain boundaries in the eutectic phase. Furthermore, the application of PMF results also a homogenization of the distribution of solute elements and the segregation of Mg decreased.

II.3.5. RMF-TMF coupling

Among the recent works dealing with the application of the alternating current magnetic field having a significant effect on the solidification of metallic alloys, we should mention the work of D. Räbiger *et al* [22]. In this study, they use a coupling technique between a rotating magnetic field and a travelling magnetic field (RMF-TMF). This work examines the impact of different alternating current magnetic fields on the directional solidification of the Sn-15wt%Pb alloy. A variety of electromagnetic stirring was achieved by combinations between RMF and TMF (Fig. II.5). The results show that the stirring by a TMF is more efficient, but shows a strong tendency

to form large segregation zones. The interference of RMF can decrease the segregation phenomena, but cannot avoid it completely.

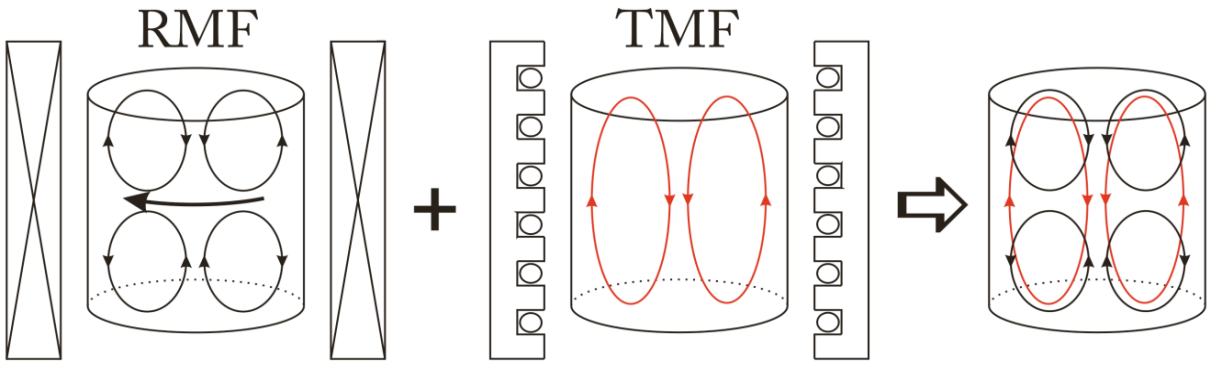

Fig. II.5. Illustrative diagram showing flow configurations from different types of magnetic fields, [22].

Basically, in this work the experimental results demonstrate the effectiveness of using a coupling between a rotating magnetic field RMF in the form of successive impulses and a travelling magnetic field TMF directed upwards on the modification of the structure, in particular the TEC, the refinement of the grain structure and the prevention of segregation in the form of Freckles (see Fig. II.6). However, the problem of controlling the dynamics of the liquid bath during solidification seems to be very complex and requires further study.

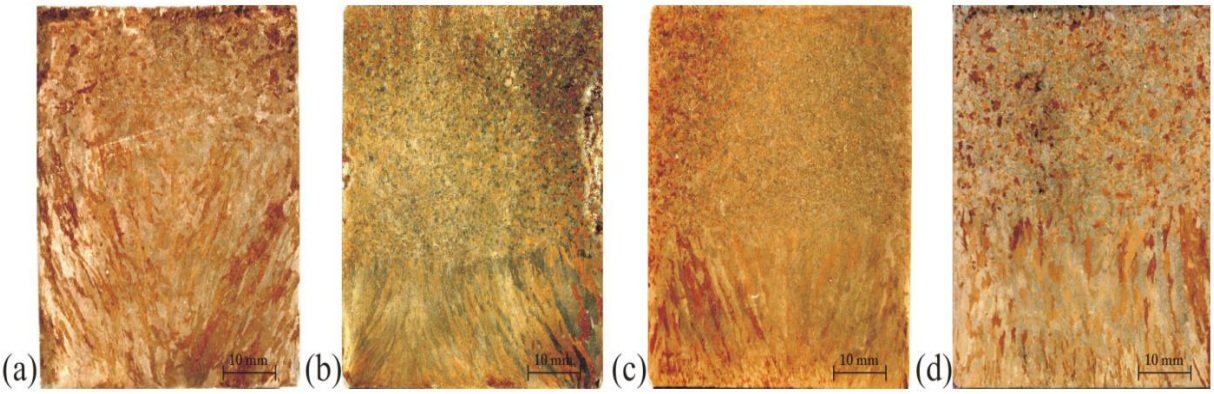

Fig. II.6. Macrostructures of longitudinal sections of solidified samples under the influence of different magnetic field configurations: (a) continuous RMF at 3.5 mT (b) TMF upward at 48.5 mT, (c) RMF at 3.5 mT and TMF downward at 34 mT, (d) RMF at 3.5 mT and TMF upward at 34 mT, [22].

II.4. Refining of the casting structure

The effects of electromagnetic stirring on the solidification of steels, and more particularly in continuous casting, have been widely studied [13]. However, the EMS technique in the case of steel is very different from that of aluminum or copper. In the case of aluminum solidification,

Vivés developed an electromagnetic stirring system during continuous casting, the CREM (Casting, Refining, ElectroMagnetic) process [23, 24]. The stirring is created by a pulsating field. The main results of this experimental study of the process are: the higher induction power, the finer the equiaxed particles (see Fig. II.7). Therefore, the EMS process has been adapted to obtain fine equiaxed grains.

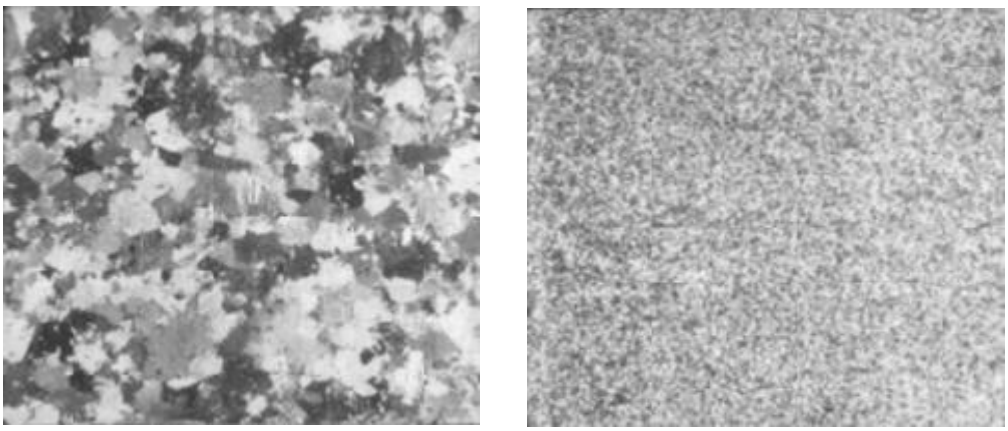

Fig. II.7. Macrostructure of 1050 aluminum alloy (cross section of 70 mm wide bar) solidified by classical continuous casting (left) and with EMS (right), [7].

The solidification of pure copper have also studied by L. Xi-Liang *et al* [20] under the effect of pulse magnetic field. The results show that as the voltage increase, the final solidification structures change gradually from coarse columnar crystal to fine globular crystal as illustrated in Fig II.8. Where, the solidification structure without pulse magnetic field (0 V) is presented in (a), and in Figs. II.8 (b)-(e) the solidification structures under various voltages of PMF are also presented.

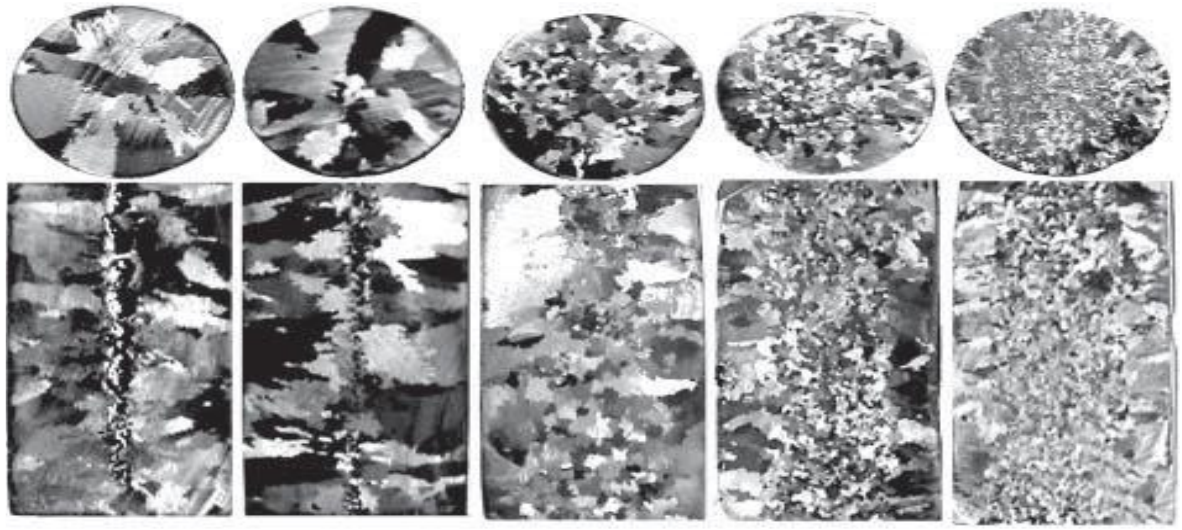

(a) 0 V (b) 1000 V (c) 2000 V (d) 3000 V (e) 4800 V

Fig. II.8. Effect of pulse magnetic field on solidification structure of pure copper, [20].

X. Ma *et al* [25] have studied the super alloy IN718 microstructure solidification under the effect of PMF, the effects of exciting frequency and exciting voltage. The results showed that the grains are refined as the exciting voltage or/ frequency increases. In addition, When the PMF frequency is 0 Hz, coarse equiaxed grains are formed, indicating that PMF is not applied in solidification. The equiaxed grains are refined when the PMF frequency is 2.5 Hz. The 5-Hz PMF has the best effect on grain refinement.

II.4.1. Grain refinement process by fragmentation of dendrite arms

In the absence of inoculant particles in the liquid, the formation of equiaxed grains is generally attributed to two types of phenomena: the conditions of germination in homogeneous or heterogeneous reaction from impurities especially at the walls (temperature gradient at the interface, cooling rate, concentration of alloying elements) or by fragmentation of the dendrite arms. The latter explains why it is possible to obtain an equiaxed growth in a case where all models predict a columnar growth. A very complex phenomenon, it has been little discussed in the literature. Only a few authors have described the fragmentation mechanisms of dendrites during solidification.

In a general way, five fundamental steps of equiaxed grains formation by fragmentation of the dendrites arms (see Fig. II.9), [7]:

II.4.1.1. Fragmentation of dendrite arms by local remelting

Fragmentation is not a well-known phenomenon, only a few deductions from observations on the solidification of organic alloys have been made C. J. Paradies [26] and T. Stato [27]. They attribute this fragmentation to the consequence of a local remelting of the finest sections (neck effect, Fig. II.10) of the dendrite arms. For his part, Liu [28] has concluded that the fragmentation is mainly generated by the dissolution of the dendrite arms, itself induced by the deceleration of the cooling rate (see Fig. II.11). Indeed, he reduced the phenomenon of thermal remelting of the arms, assuming that it is possible but that it has not been observed in their case. He prefers to talk about the dissolution caused by a solutal variation in the mushy zone. In accordance with this concept, fragmentation has also been studied in the formation of "Freckles" during solidification. Gu and Beckermann [29] as well as Hellawell [30], attribute the formation of fragments to the solutal dissolution of dendrites, in this particular case of creation of segregated channels. It should be noted that Pilling [31], concerning the effect of the liquid movement on the dendritic network, definitively concluded that the mechanical

deformations induced by convection of inter dendritic liquid could not be the cause of the dendrite arms (side branches) detachment.

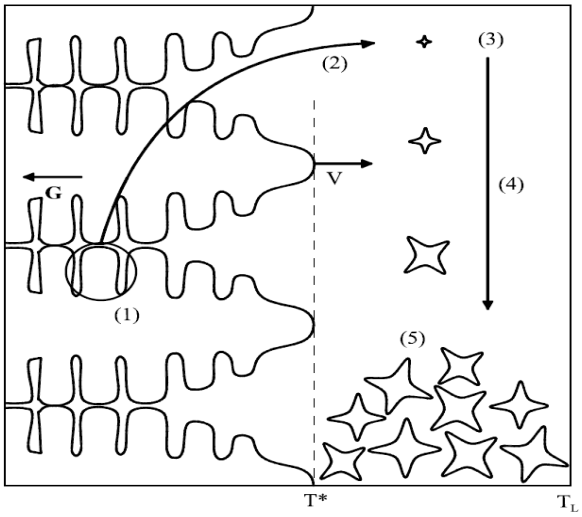

Fig. II.9. Steps of the creation of equiaxed grains by fragmentation of dendrite arms: (1) local remelting of dendrite arms, (2) fragments transport, (3) fragments survival, (4) growth and sedimentation and (5) formation of the equiaxed structure, [7].

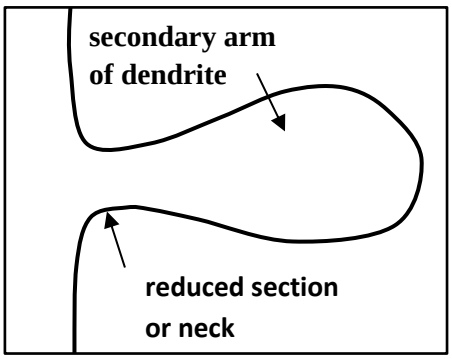

Fig. II.10. Illustration of a secondary arm of a dendrite. The remelting phenomenon is localized on the finest part of this secondary arm called "neck", [5].

II.4.1.2. Transport of the fragments from mushy to liquid zone

The transport of fragments from the mushy zone to the liquid ahead of the columnar growth front is a phenomenon that requires either a settling effect or natural or forced convection in the region concerned. This step has hardly been studied. Hellawell [32] assumes that interdendritic convection is responsible for the transport of fragments from the mushy zone to the liquid. In the case of electromagnetic stirring, the convection in the interdendritic regions is induced by the convection of the liquid, produced in volume. In the case of the formation of "Freckels", the transport of the fragments located at the bottom of the channel is ensured by thermo-solutal convection, this transport was modelled by J. P. Gu [29].

II.4.1.3. Fragments survival

The fragments are transported to hotter regions, so their survival will depend on the path they take in the hot liquid (either away or ahead the solidification front), the time they take to melt completely and the extent of the undercooling zone ahead of the interface. Only Q. Han [33] has estimated fragment remelting rates in a simple case of spherical particles in a liquid, thus without convection. J. P. Gu [29] has taken into account the influence of the fragment path to study its survival in a numerical model, but only in the case of solutal remelting and natural convection.

II.4.1.4. Growth and sedimentation

In the case of the survival of a dendritic fragment, its growth can take place. By trapping (the solidification front can trap a fragment while advancing) or by sedimentation, the equiaxed structure takes place. The sedimentation towards the liquid can cause a total or partial remelting of the grains.

II.4.1.5. Equiaxed structure formation

The formation of equiaxed grains in front of the solidification front blocks the growth of columnar dendrites. The structure then becomes equiaxed. As one of the few authors to study this phenomenon when it is related to fragmentation, Jang [34] estimated sedimentation rates in the case of an organic alloy, using a Stokes-type flow, as well as an analytical criterion of growth blocking of a columnar solidification front. However, for simplification reasons, we consider that as long as the fragments have survived, the final structure will be equiaxed.

(a) t = 4 min, 4.2% detachment **(b) t = 16 min, 67.4% detachment**

Fig. II.11. Observation of the dendrite arms fragmentation, for the organic alloy SCN-5.6%H2O, during the deceleration of the advanced rate of the growth front. Over time, the proportion of fragments thus increases. (a) Shows dendrite arms still attached to the primary trunk. (b) The local remelting of these arms has created numerous fragments (the black circle locates an example of remelted fragments), [7].

II.4.2. Influence Factors

The conditions of fragmentation remain rather unclear. However, all studies related to the fragmentation of dendrite arms agree that there are preponderant parameters:

II.4.2.1. The convection velocity

The intensity of the convection (thus the power of the electromagnetic induction) decreases the temperature and chemical gradients near the interface. It seems reasonable to think that this decrease in gradients is responsible for the remelting of the dendrite arms. Under these conditions, the more convection is vigorous the more effective refining will be, J. J. Moore [13], Ch. Vivès [24] and W. D. Griffiths [35].

II.4.2.2. The flow mode

The presence of turbulent or laminar convection seems to influence the refining. Kishida [36] has shown, by temperature measurements during turbulent convection that the temperature instabilities induced by this mode of convection can promote a remelting of the dendrite arms, by destabilization of the solidification front.

II.4.2.3. The concentration of the alloy element

An increase in the initial concentration of the alloy element increases the extent of the undercooling zone ahead of the solidification front. This phenomenon therefore increases the probability of fragment survival but also decreases the radius of the dendrites (thus the neck of each dendrite secondary arm), facilitating the remelting of the secondary arms, T. Sato [27].

II.4.2.4. The deceleration of the cooling rate

The deceleration of the growth rate induces a punctual increase of the temperature and concentration in inter dendritic zone. This phenomenon induces the thermal and solutal remelting of the dendrite arms.

II.5. Partial conclusion

This chapter presented the basic concepts of Magneto-Hydro-Energetics (MHE). The different dimensionless numbers useful for the description and analysis of the cases treated in this work have been explained. Only the energetic aspect of these equations in the form of an electromagnetic stirring energy has been addressed, in order to adapt it to the applications of the solidification of metallic alloys. A study on the different configurations used for electromagnetic stirring and their influence on the solidification structures has been performed. Several EMS techniques have shown their effectiveness to: reduce or even eliminate defects related to segregation, especially at the micro scale in side, and in other side, improving the final structure and even the physical properties of the materials, in particular the RMF-TMF (rotating magnetic field-travelling magnetic field) coupling technique on the refinement of the structure. In addition, the application of EMS has shown its significant ability to "*break up*" the structure (form the equiaxed grain) consequently promoting the columnar-equiaxed transition (CET) mechanism.

References of chapter II

[1] Roland Berton, *Magnétohydrodynamique*, Masson. 1991.

[2] R. Moreau, « The fundamentals of MHD related to crystal growth », *Prog. Cryst. Growth Charact. Mater.*, vol. 38, nº 1, p. 161-194, janv. 1999.

[3] R. J. Moreau, *Magnetohydrodynamics*. Springer Netherlands, 1990.

[4] P. A. Davidson, « Magnetohydrodynamics in Materials Processing », *Annu. Rev. Fluid Mech.*, vol. 31, nº 1, p. 273-300, 1999.

[5] L. Hachani, « Etude de l'influence de la convection naturelle et forcée sur le processus de la solidification : cas d'un alliage métallique binaire. », PhD thesis, Cotutelle Université de Grenoble ; 352 Université Hadj Lakhdar de Batna, 2013.

[6] K. Zaïdat, « Influence d'un champ magnétique glissant sur la solidification dirigée des alliages métalliques binaires », These de doctorat, Grenoble INPG, 2005.

[7] Thomas CAMPANELLA, « Etude de l'effet du brassage électromagnétique sur les microstructures d'alliages cuivreux », Lausanne, EPFL, 2003.

[8] O. Laskar, « Phénomènes thermoélectriques et magnétohydrodynamiques en solidification des alliages métalliques », These de doctorat, Grenoble INPG, 1994.

[9] P. Lehmann, R. Moreau, D. Camel, et R. Bolcato, « Modification of interdendritic convection in directional solidification by a uniform magnetic field », *Acta Mater.*, vol. 46, nº 11, p. 4067-4079, juill. 1998.

[10] S. N. Tewari, R. Shah, et H. Song, « Effect of magnetic field on the microstructure and macrosegregation in directionally solidified Pb-Sn alloys », *Metall. Mater. Trans. A*, vol. 25, nº 7, p. 1535-1544, juill. 1994.

[11] X. Meng, C. Chen, Z. Hong, et J. Wang, « Effect of rotating magnetic field on the solidification microstructures of Pb-Sn alloys », *Sci. China Ser. E*, vol. 49, nº 3, p. 274-282, juin 2006.

[12] M. Svéda, A. Sycheva, J. Kovács, A. Rónaföldi, et A. Roósz, « The Effect of Rotating Magnetic Field on the Solidified Structure of Sn-Cd Peritectic Alloys », *Mater. Sci. Forum*, vol. 790-791, p. 414-419, mai 2014.

[13] J. J. Moore et L. J. Heaslip, *Continuous Casting: The application of electromagnetic stirring (EMS) in the continuous casting of steel*. Iron & Steel Society of AIME, 1983.

[14] M. Medina, Y. Du Terrail, F. Durand, et Y. Fautrelle, « Channel segregation during solidification and the effects of an alternating traveling magnetic field », *Metall. Mater. Trans. B*, vol. 35, nº 4, p. 743-754, août 2004.

[15] J. Dagner, M. Hainke, J. Friedrich, G. Mueller, « Effects of time-dependent magnetic fields on directional solidification of AlSi7 alloys », *4th Int Conf Electromagn. Process. Mater. EPM*, oct. 2003.

[16] A. Ciobanas, Y. Fautrelle, F. Baltaretu, A. M. Bianchi, et A. Noeppel, « Ensemble Averaged Two-phase Eulerian Model for Columnar/Equiaxed Solidification of a Binary Alloy. Simulation of the Columnar-to-Equiaxed Transition », Proc. of the SG04 conference, Miskolc, Hongrie, 2004.

[17] K. Mazuruk, « Control of melt convection using traveling magnetic fields », *Adv. Space Res.*, vol. 29, n° 4, p. 541-548, janv. 2002.

[18] S. Yesilyurt, S. Motakef, R. Grugel, et K. Mazuruk, « The effect of the traveling magnetic field (TMF) on the buoyancy-induced convection in the vertical Bridgman growth of semiconductors », *J. Cryst. Growth*, vol. 263, n° 1, p. 80-89, mars 2004.

[19] G. Quillet, « Influence de la convection, naturelle ou forcée, sur l'apparition des mésoségrégations lors de la solidification des alliages métalliques », These de doctorat, Grenoble INPG, 2003.

[20] L. Xi-liang, G. Yong-yong, L. Ren-xing, C. Wen-jie, et Z. Qi-jie, « Effect of pulse magnetic field on solidification structure and properties of pure copper », *China Foundry*, p. 4, 2007.

[21] C. Y. Ban, J. Cui, Q. Ba, G. M. Lu, et B. J. Zhang, « Influence of pulsed magnetic field on microstructures and macro-segregation in 2124 Al-alloy », *Acta Metall. Sin. Engl. Lett.*, vol. 15, p. 380-384, août 2002.

[22] D. Räbiger, M. Leonhardt, S. Eckert, et G. Gerbeth, « Flow control during solidification of SnPb-alloys using time-modulated AC magnetic fields », *IOP Conf. Ser. Mater. Sci. Eng.*, vol. 27, n° 1, p. 012053, janv. 2012.

[23] C. Vives, « Electromagnetic refining of aluminum alloys by the CREM process: Part I. Working principle and metallurgical results », *Metall. Trans. B*, vol. 20, n° 5, p. 623-629, oct. 1989.

[24] C. Vives, « Electromagnetic refining of aluminum alloys by the CREM process: Part II. Specific practical problems and their solutions », *Metall. Trans. B*, vol. 20, n° 5, p. 631-643, oct. 1989.

[25] X. Ma, Y. Li, et Y. Yang, « Grain refinement effect of pulsed magnetic field on solidified microstructure of superalloy IN718 », *J. Mater. Res.*, vol. 24, n° 10, p. 3174-3181, oct. 2009.

[26] C. J. Paradies, R. N. Smith, et M. E. Glicksman, « The influence of convection during solidification on fragmentation of the mushy zone of a model alloy », *Metall. Mater. Trans. A*, vol. 28, n° 3, p. 875-883, mars 1997.

[27] T. Sato, W. Kurz, et K. Ikawa, « Experiments on Dendrite Branch Detachment in the Succinonitrile-Camphor Alloy », *Trans. Jpn. Inst. Met.*, vol. 28, n° 12, p. 1012-1021, 1987.

[28] S. Liu, S.-Z. Lu, et A. Hellawell, « Dendritic array growth in the systems NH4Cl–H2O and [CH2 CN]2–H2O: the detachment of dendrite side arms induced by deceleration », *J. Cryst. Growth*, vol. 234, n° 4, p. 740-750, févr. 2002.

[29] J. P. Gu, C. Beckermann, et A. F. Giamei, « Motion and remelting of dendrite fragments during directional solidification of a nickel-base superalloy », *Metall. Mater. Trans. A*, vol. 28, n° 7, p. 1533-1542, juill. 1997.

[30] A. Hellawell, J. R. Sarazin, et R. S. Steube, « Channel convection in partly solidified systems », *Philos. Trans. R. Soc. Lond. Ser. Phys. Eng. Sci.*, vol. 345, n° 1677, p. 507-544, déc. 1993.

[31] J. Pilling et A. Hellawell, « Mechanical deformation of dendrites by fluid flow », *Metall. Mater. Trans. A*, vol. 27, n° 1, p. 229-232, janv. 1996.

[32] A. Hellawell, S. Liu, et S. Z. Lu, « Dendrite fragmentation and the effects of fluid flow in castings », *JOM*, vol. 49, n° 3, p. 18-20, mars 1997.

[33] Q. Han et A. Hellawell, « Primary particle melting rates and equiaxed grain nucleation », *Metall. Mater. Trans. B*, vol. 28, n° 1, p. 169-173, févr. 1997.

[34] J. Jang et A. Hellawell, « Use of NH4Cl-H2O Analogue Castings to Model Aspects of Continuous Casting. Part 2; Columnar-Equiaxed Grain Transition and Crystal Sedimentation Rates », *undefined*, 1991.

[35] W. D. Griffiths et D. G. McCartney, « The effect of electromagnetic stirring during solidification on the structure of Al-Si alloys », *Mater. Sci. Eng. A*, vol. 216, n° 1, p. 47-60, oct. 1996.

[36] Y. Kishida, K. Takeda, I. Miyoshino, et E. Takeuchi, « Anisotropic Effect of Magnetohydrodynamics on Metal Solidification », *ISIJ Int.*, vol. 30, n° 1, p. 34-40, 1990.

CHAPTER III
Enthalpy approach for modelling solidification processes

This chapter was inspired directly from my paper [1], published in "International Journal of Thermal Sciences" (IJTS), which is based on the description of enthalpy approach that applied on the solidification of pure tin under the effect of both natural and forced convection.

III.1. Introduction

In the modern-day world, numerical modeling has proven to be an indispensable tool aiding industry fields, research, and academics. Numerical modeling has now become an essential part of various process optimizations including processes involving solidification. From the way in which the solid-liquid interface is followed, how the existing phases are described and the nature of the mesh used. Two main families of approaches are distinguished: the first is the "single-domain approach" or "the mono-domain approach", and the second is the" multi-domain approach":

- **Single domain approach:** In these methods, also called enthalpy methods, the two phases coexist within the same single computational domain (i.e., the presence of liquid and solid phases). The fractions volumes of each phase are introduced in order to distinguish them from each other. The transition from one phase to the other is no longer isothermal but occurs over a range of temperature variation. This temperature range, which is only physically justifiable for the alloys solidification case, is a mathematical artifact to enable a smooth and continuous transition between the two states and thus facilitate numerical resolution. The solid-liquid interface separating the two phases is not explicitly described but diffuses over this interval of coexistence of the two phases also called "mushy zone". These methods allow the resolution of a single and complete system of partial differential equations over the entire domain studied. The equations system can be obtained with two different approaches, a single-phase approach (one-fluid model) or a multi-phase approach (two-fluid model).

In the multi-phase approach, a distinction is made between the two phases, which describes two different materials that coexist in a single computational domain. Each of these phases is modeled by its own system of equations (energy conservation, Navier- Stokes ...). In the mono-phase approach, the system of equations is defined, on the whole domain, for a single equivalent phase containing, in proportion of the fraction volume, the solid and liquid phases. These two phases therefore share the same velocity fields, pressure and temperature. These models are also widely used for the study of the solidification of alloys and are well detailed by Bennon *et al* [2] and Beckermann *et al* [3-5].

The different ways of taking into account the latent heat release of phase change as well as the forcing of the velocities to be zero in the solid will be detailed later in this chapter.

- **Multi-domain approach:** as indicated by their name, with these methods, each of the phases of the material is associated with its own computational domain. They are generally based on the complete formulation of Stefan. The displacements of the solid-liquid front cause deformation in both domains considered. Multi-domain methods are generally classified into two categories, variable mesh methods and Eulerian methods. In variable mesh methods, also known as dynamic or adaptive mesh methods, the mesh is continuously deformed in order to keep the solid-liquid interface defined on a line or a surface of the same mesh. The purpose is also to have and keep a finer mesh near the front. This is usually done in two different ways. In the first, the initial mesh is adapted (refined) at each iteration, either by adding or removing nodes. The number of nodes in the mesh changes at each iteration. This is called "h-method" in the literature [6, 7]. In the second approach, the mesh is moved with a certain velocity to follow the interface, but the number of nodes remains unchanged during the simulation. This velocity at which the interface is moved can be the same as the velocity of the fluid (Lagrangian method), or chosen arbitrarily (ALE method for Arbitrary-Lagrangian-Eulerian method). In the literature, these methods are called "r-method" [8, 9].

In Eulerian methods, the interface is either followed or reconstructed, with keeping a fixed mesh. "Front tracking" methods allow the explicit following of the solid-liquid interface. This clear interface separates the two phases into two distinct domains and serves as a boundary condition. These displacements are obtained from the energy balance. The reconstruction, or the implicit tracking of the interface is also possible, we then talk about methods of "front capturing". The interface is no longer clear, but is considered to be diffuse and its macroscopic description may include microscopic phenomena. The implicit tracking of the interface is achieved through a new equation that can be based on physical considerations or just on a numerical function playing the role of a marker. In phase-field methods, a rapid variation but continuous of properties is assumed across the interface. The interface is then determined through a phase field variable [10, 11]. In the volume of fluid (VOF) [12, 13] and Level-Set [14] methods, numerical functions (distance function or color function) that vary between 0 and 1 or between -1 and 1 are used to reconstruct the interface which is described as a level or an iso-value of these functions.

It is necessary to mention that there are other numerical approaches dealing with solidification. They differ from the previous mentioned approaches because they derive or are based on radically different approaches, as Lattice Boltzmann Method and the meshless method are the most interesting:

- **Lattice Boltzmann Method (LBM):** In the LBM method, instead of Navier-Stokes equations, Boltzmann's discrete equation is solved to simulate fluid behavior on a mesoscopic scale. This simulation is performed using a collision-propagation scheme of a set of quasi-particles called population. By the alternation of this collision and propagation process and the use of statistical averaging methods, it is possible to reproduce the macroscopic behavior of the fluid [15]. Jiaung *et al* [16] have shown the possibility of using the LBM method to study thermal conduction problems with phase change by incorporating an enthalpy formulation in the Lattice Boltzmann scheme. For phase change convection-diffusion problems, where the resolution is done for velocity and temperature fields, either double population LBM methods are used [17, 18], or the LBM method is coupled with one of the single or multi-domain approaches that previously presented [19-21].
- **Meshless Method:** or called “Mesh-free Method”, this method does not require a mesh with interconnected nodes, but rather is based on a set of nodes, arbitrarily distributed and without any topological relation between them, representing the domain of the problem studied and its limits. Different interpolation methods are used to construct the approximation of unknown functions (variable fields) on these nodes. These unknown functions are replaced by their approximation with an error residual from the system of solved equations and its boundary conditions. Finally, the problem is solved by minimizing the integral (strong form) or the step integral (weak form) of this residue, but weighted over the whole domain and its boundaries [22]. The classification of these meshless methods based on the way that the approximation of the unknown function (variable field) is constructed, as given by Liu [23]. This method has been used for the study of solid-liquid phase change [24], the tracking of thermal stress during the simulation of a solidification process in continuous casting [22] and for the study of the macro-segregation of binary alloys [25].

The LBM method and the meshless method are known to have a great potential for parallelization, which is a significant advantage in resolution, but they require more programming efforts and a thorough mastery of numerical methods.

This chapter based on using the single domain approach (Enthalpy approach) to simulate the phase change of pure tin (solidification of pure tin (Sn)) within the 'AFRODITE' set-up that will be described later. This approach is one of the most popular fixed-domain methods. Several works [26-31] have used this approach and it has shown its ability to predict the solidification process and consequently its effectiveness to validate the models with the experimental results. The major advantage of this approach is that there is no need to explicit treatment of the moving boundary.

III.2. Single domain approach (Enthalpy formulation)

Enthalpy approaches and similar techniques take into account the latent heat release have been effectively applied over recent years to the case of thermal phase-change problems, distinguished by the existence of moving solid/liquid interface due to the cooling of the system under investigation. Voller and Prakash [28], Bennon and Incropera [2, 32] and Brent *et al*. [33] developed these techniques, which have been vastly improved over years with different structures and conditions as Beckermann *et al* [34].

With regards to this context, it is important to note how the approaches used to date by many researchers seem to fall basically into two categories: "adaptive methods" as Rao and Shyy [35], and "fixed-grid techniques" (related by a certain theoretical kinship to volume of fluid (VOF) and level-set methods). In the first method, numerical solutions are acquired by means of a numerically generated orthogonal curvilinear coordinate system, which is automatically adjusted to suit the front of the solidification (boundary where the phase change takes place) at any instant. In contrast, the so-called enthalpy formulation, which requires a fixed-grid solution to be identified, eliminates the need to explicitly satisfy conditions at the solidification front and is thus able to use standard solution methods for fluid flow and energy equations directly, without resorting to mathematical manipulations and transformations. Therefore, enthalpy methods are part of a single-domain method where the same and unique system of equations is solved everywhere in the computational domain of solid and liquid phases defined by a single fluid.

III.2.1. Fixed grid technique

These methods have been usually used by the researchers, because these techniques do not make explicit reference to the position of the moving boundary. In these methods, the problem is reformulated to allow the solution of the governing equations in a fixed space grid, and treat

the solid and liquid regions as one continuous region. Indeed, the fixed-grid techniques have used in numerous works [27, 36] due to the simplicity of the phase change problem and proved its numerical accuracy compared to the experimental results.

The advantages of these methods are:

- The governing equation is similar to the single-phase equation.
- There is no condition to be satisfied at the solid/liquid interface as it automatically obeys the interface condition.
- The enthalpy formulation (fixed-grid method) takes into account the mushy zone between the two phases.
- Ease of implementation of the phase change within an existing conduction program.
- The unnecessity of tracking the interface in each time step.
- Re-meshing is not required.
- Capability of tackling mushy phase change problems or complicated shaped, multi-dimensional problems.

In this approach, the heat flow equation is estimated by the finite-difference replacements used to determine the temperature and time values for the interface zone [37]. The most popular technique for demonstrating the fixed grid method, based on earlier research, is the enthalpy method [38]. Due to a wide variety of uses, the use of enthalpy approach can be divided into two subsections: pure conduction with a problem of phase transition, and convection based problems [28].

III.3. Model description

In order to simulate the experiment ‘AFRODITE’ setup that will described later, we have proposed the enthalpy approach to solve the problem of the phase change process (solidification of pure tin). This approach has been used in two numerical simulation models of the solidification of pure tin in the current chapter; these models are implemented in COMSOL Multiphysics software. Indeed, the first model noted ‘Case I’ deals with the solidification of pure tin under the effect of natural convection, was simulated without any external forces but rather by variations in the density of the fluid produced by a horizontal temperature gradient, called also thermal convection. In this case (Case I), 'Laminar Flow' and 'Heat Transfer in Fluid' modules have used for hydrodynamic and thermal resolution (natural convection case). In other side, the second model noted ‘Case II’ is the case of forced convection, characterized by the

application of a driving electromagnetic force (Lorentz force) induced by an external Traveling Magnetic Field (TMF). However, in this model the same previously mentioned modules ('Laminar Flow' and 'Heat Transfer in Fluid') have kept with additional of 'magnetic field' modules to simulate the case of forced convection, grouping the energy, Navier-Stokes, conservation equations and also the electromagnetic forces (in Case II) formulated for mixing and valid everywhere in the studied domain.

In order to take into consideration the process of phase change (solidification/melting), two major ingredients are essential. Firstly, the rejection or absorption of the latent heat of fusion, denoted H_f, must be taken into account in the energy conservation equation. Where, H_f is the energy (in the form of heat) rejected (or absorbed) by a substance when there is undergoing from liquid to solid state (or vice versa) in constant pressure and temperature called the melting temperature as described in the first chapter. Secondly, the velocities within the solid phase must be forced to zero. Indeed, different methods and formulations existing: the method "*switch-off"*, the variable viscosity method, Darcy method and Carman-Kozeny equation.

III.3.1. Energy equation

Solidification of pure metals is an isothermal form of phase change when latent fusion heat is released at melting temperature (for example T_m = 505 K of pure tin). Thermal convection forces are produced in the liquid region during the solidification of pure metals by the difference in density due to temperature gradients contained in the liquid. The existence of both solid and liquid phases during the solidification of the metals makes it relatively difficult to apply the governing equations in their classical form, as the solid phase supposes a non-flow region and a pure heat transfer conduction mode, while the liquid phase considers a region where the classical form of the momentum equation is valid to the fluid flow. In the liquid zone, the heat transfer is often controlled by convection. Numerical investigations have been performed to date to investigate the flow patterns attributed to thermal convection during the solidification of pure metals. In previous numerical simulations [39-41], a separate series of governing equations was used in the solid and liquid regions to analyse solidification process. This method of modelling requires a moving interface that is controlled by using the energy balance at the interface to keep track of the quantity of energy released at solid-liquid interface.

In order to solve the fluid flow and heat transfer equations during the solidification of pure Sn, with using a single domain approach which is the main advantage of the porosity formulation that introduced in COMSOL software, this latter suggests the implementation of a mushy zone

that will be described in the next part. However, it requires an additional user treatment by specifying a series of complimentary algebraic equations for material properties. Latent heat during the undergoing liquid to solid phase change is integrated into the energy equation using the following concept of enthalpy for each phase:

$$h = CpT + \Delta H \tag{III.1}$$

where $\Delta H = f_l(T).L$, L is the latent heat, C_P the specific heat coefficient and $f_l(T)$ is the liquid fraction defined by Eq. III.2 and shown in Fig. III.1 (a):

$$f_l(T)\begin{cases} 1 \; for \; T > T_m + {}^{\Delta T}/_{2} \\ \frac{T-(T_m-{}^{\Delta T}/_{2})}{\Delta T} \quad for \;\; T_m + {}^{\Delta T}/_{2} \geq T \geq T_m - {}^{\Delta T}/_{2} \\ 0 \; for \; T < T_m - {}^{\Delta T}/_{2} \end{cases} \tag{III.2}$$

In the present chapter, as mentioned that the governing equations are expressed by using the fixed-grid continuum formulation with the single-domain approach. The specific heat is written as a function of the latent heat L (Eq. III.3) that shown in Fig. III.1 (c), and the Gaussian distribution function $D(T)$ in (Eq. III.4) as follow:

$$Cp(T) = Cp_s + f_l(T).(Cp_l - Cp_s) + D(T).L \tag{III.3}$$

with:

$$D(T) = \frac{e^{-\left(\frac{T-T_m}{\Delta T/4}\right)^2}}{\sqrt{\pi}\Delta T/4} \qquad \text{(see Fig. III.1 (b))} \tag{III.4}$$

The mechanism of phase change is modelled by using a temperature-based formulation enthalpy approach [28, 42, 43]. In a fluid undergoing a liquid to solid phase transformation (i.e. solidification), the classical energy equation may be written as follow, [44]:

$$\frac{\partial \rho h}{\partial t} + \nabla(\rho u h) = \nabla(\lambda \nabla T) \tag{III.5}$$

By using Eq. III.1 and $\Delta H = f_l(T).L$, the energy equation will be defined as follow:

$$\frac{\partial(\rho C p T)}{\partial t} + \frac{\partial(\rho f_l L)}{\partial t} = -\nabla(\rho u h) + \nabla(\lambda \nabla T) \tag{III.6}$$

where ρ is the density, λ is the thermal conductivity and u is the flow velocity, and the unsteady latent heat L content term on the left side of Eq. III.6 is equal to zero for $T < T_m - \Delta T/2$ and $T >$

$T_m + \Delta T/2$ (It affects the energy equation only within the temperature range specified by the user ΔT).

Also, the first term that presented in the Eq. III.5 in the left-hand side presents the enthalpy, and the term in the right-hand side is the conduction heat transfer. Enthalpy is a function of temperature and is usually known to be a step function for isothermal phase change problems, and it define in both solid and liquid as follow, [45]:

$$h = \begin{cases} C_{p\,s}\,T, & T \leq T_m \\ C_{p\,l}\,T + H_f, & T > T_m \end{cases} \text{ for isothermal phase change} \qquad \text{(III.7)}$$

III.3.1.1. Control of temperature transition range ΔT

The enthalpy-porosity formulation introduced in COMSOL software proposes the implementation of a mushy zone in order to circumvent the divergence problems where both liquid and solid phases coexist, for which the thermophysical properties of both phases are distributed over a user-defined temperature range ΔT (in our analysis $\Delta T = 1.2\ K$) for the solidification of pure tin. It is well known that the phase change transformation occurs in a very narrow zone, although the model uses a transition half-width, ΔT. Furthermore, in the case of the solidification of metallic alloys the temperature range ΔT is larger. It is necessary to mention that there is a relation between ΔT (as used in our case: $\Delta T = 1.2\ K$ for pure tin) and the mesh resolution. Indeed, if we want to reduce ΔT we should refine the mesh resolution. However, the simulation will be quite costly in terms of computational time, more particularly for a 3D geometry. Therefore, the selection of the temperature transition range ΔT must be accurate in terms of computational time. We may have convergence problems caused by the sharp gradients of the adjusted heat capacity if ΔT is small (e.g., ≈ 0.1 K). In addition, these problems may also occur if the mesh resolution at the interface does not cover the required range. As we reduce ΔT, we will have more accuracy, and in parallel, the computational time will be costly and it needs more efforts (in the case of forced convection, it takes about 55 days).

III.3.2. Momentum equation

In the single-domain approach, the phase change problem is dealt within the same single domain where both solid and liquid phases are assimilated to a single fluid. However, during phase change process, more particularly during the transition from liquid to solid at the interface, the velocities become zero as the liquid solidify (solid region). The hydrodynamics modelling must necessarily include a treatment of the solid part. The phase considered thus describes both solid and liquid states of the material. The EDP system consists of the mass

conservation equation (Eq. III.13) and the momentum conservation equations (Eq. III.8). For an incompressible Newtonian fluid, the incompressible momentum equation assumes constant density yielding:

$$\rho\frac{\partial u}{\partial t}+\rho(u.\nabla)u=\nabla(\mu(T).\nabla u)-\nabla p-S(T).u+F \qquad \text{(III.8)}$$

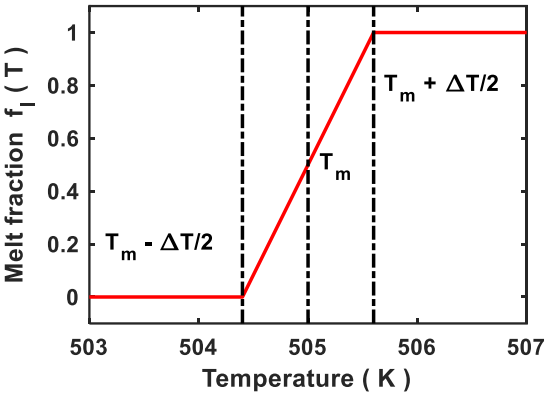

(a) Melt fraction function $f_l(T)$, implemented as a piecewise function

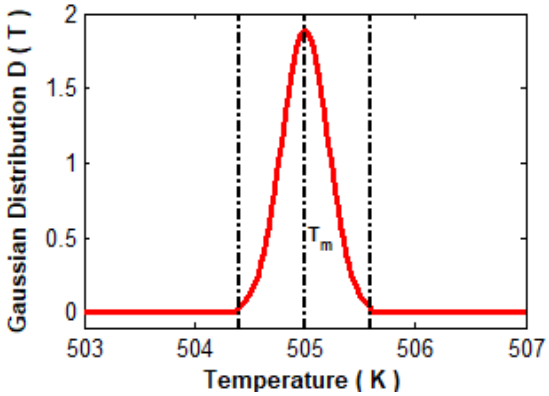

(b) Gaussian distribution function $D(T)$, for $\Delta T = 1.2$ K.

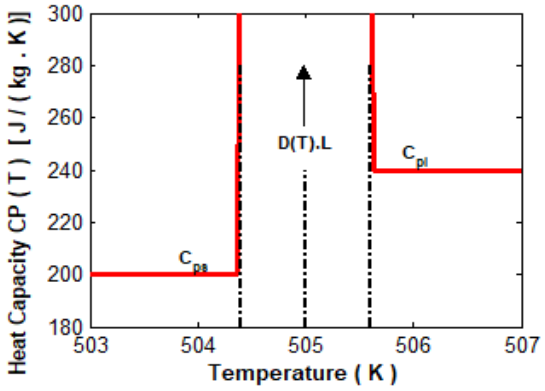

(c) Heat capacity function Cp(T), rising to a the maximum value of D(T).L = 120000 J.kg^{-1}.K^{-1}.

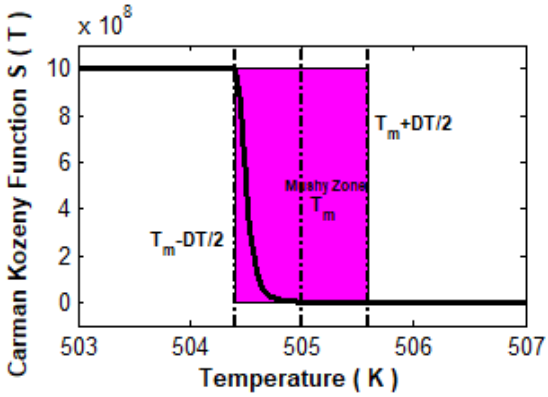

(d) Carman-Kozeny function to model sink-term and viscosity of the solid fraction.

Fig. III.1. Temperature-dependent modelling functions implemented in the numerical model for pure tin.

For accounting the last term on right-hand side (Eq. III.8) which presents the body force *'F'* comprising two types of forces: Buoyancy force which is implemented by using Boussinesq approximation [46] and Lorentz force that only introduced in 'Case II' caused by the application of an electromagnetic force (see Eq. III.9) which will be detailed later.

$$F=\underbrace{\rho g\beta\left(T-T_{ref}\right)}_{Buoyancy\ force}+\underbrace{(J\times B)}_{Lorentz\ force} \qquad \text{(III.9)}$$

where β is thermal expansion coefficient, T_{ref} is the reference temperature (Melting temperature for pure metals).

The source term (*S(T).u*) that presented in the momentum equation (Eq. III.8) is defined for handling sharp jump in velocity across solid-liquid interface. This latter is described in a way as the Carman-Kozeny equation, as follow, [46, 47]:

$$S(T).u = A_m \frac{(1-f_l(T))^2}{f_l(T)^3+\epsilon} u \quad \text{(III.10)}$$

where A_m is the mushy zone constant, this latter is a constant controlling the mushy region morphology, and ϵ is a small positive computational constant defined in order to avoid division by zero. In our model, the mushy zone constant is taken $A_m = 10^6$ kg.m^{-3}.s^{-1} and $\epsilon = 10^{-3}$ (Samara *et al.*, [48]; Kheirabadi and Groulx, [49]).

Furthermore, in Eq. III.10 and as defined in the momentum equation, *S(T)* is a sink-term. In order to ensure immobility in the solid zone, we have supposed a solution of zero velocity ($u = 0$). Fig III.1 (d) shows the evolution of the Carman-Kozeny function which varies in accordance with Eq. III.10, as it can be seen clearly that the liquid zone ($T > T_m$) is not concerned in this function. However, the *S(T)* function affects the region lower than the melting temperature ($T < T_m$) which contains the solid fraction and the solid dominated part of the mushy zone ($T_m - \Delta T/2 < T < T_m$). The simulating term *S(T)* overpowers any other term in the momentum equation in the solid region. In other side, it is suggested that the viscosity [49] that defined in the COMSOL Multiphysics™ also be modified in order to ensure convergence in the model as follows:

$$\mu(T) = \mu_l\big(1 + S(T)\big) \quad \text{(III.11)}$$

with the empirical viscosity-temperature relation (E. V. Rozhitsina *et al.*, [50]), for pure tin;

$$\mu(T) = 31 \times 10^{-5}\left(\frac{6.171\times10^3}{RT}\right) \quad \text{(III.12)}$$

where *T* is the temperature in [K], μ_l is the dynamic viscosity in [Pa.s].

Hence, the dissipation term that presented in the momentum equation overrides the other terms within the solid regime. This approach ensures that the flow is produced only in the liquid fraction within the computational domain, considering the resolution of the momentum equation for both solid and liquid fractions.

The conservation equation of pure metal (e.g., pure tin) is defined as follow:

$$\nabla(\rho u) = 0 \qquad \text{(III.13)}$$

In fact, the major issue is how the mushy zone constant (A_{mush}) affects the anticipated solidification performance and how to evaluate A_{mush} exist for even more study. A_{mush} is the flow resistance parameter of the enthalpy porosity model that presented in the momentum equation. This later is ranging between 10^3 to 10^9 kg.m^{-3} s^{-1}. The main role that A_{mush} plays in the forecasting of the solidification performances is still poorly recorded to date. In order to get a good agreement with the experiment results of pure tin solidification in term of the solidification front morphology, it has been found that the choice of A_{mush} values has a significant effect on phase change process in global way. Furthermore, there is a direct relation between A_{mush} and ΔT, of which these two parameters one is depends on the other within the computational domain. We have tried several tests to get precious and significant physical results that can be validate with the experimental results from side, and from other side to avoid the slow solidifying rates. In this study for a temperature transition range ΔT equal to 1.2 K, is A_{mush} = 10^6 kg.m^{-3}.s^{-1}.

III.3.3. Numerical solver

Three-dimensional numerical simulations are implemented with a grid consisting of 240040 domain elements, 21168 boundary elements, and 524 edge elements. The results presented in this chapter, are obtained with J = 8 A and magnetic vector potential $A_0 = 2\ 10^{-4}$ T.m. The Delaunay tetrahedralization generator is used for meshing domain. A free backward differentiation formula (*free BDF*) was used in the time step technique in the implicit time-dependent solver. A segregated solver is used, where the *Newton* method is still implemented at every time step, but for the various variables independently and with Newton corrections and minimal *Jacobian update* are got by an iterative solver (*GMRES*) for pressure and velocity and by a direct solver (*PARDISO*) for the temperature. In the case of solidification simulation, the *implicit time-dependent BDF* solver (free backward differentiation formula) was used in our numerical model in order to avoid the well-known prospective strong nonlinearity that may occurs as a result of the physical domain properties being a function of the solution or the feedback of solved equations. This solver computing the solution of a likely nonlinear equation framework at each time-step via a series of iterative techniques based on *Newton's* method. The predefined algorithms in the *free-BDF* solver increment the resolution column called *NLFAIL* in the case of those iterative techniques failed at any time-step. The previous mentioned techniques that are based on *Newton* method to solve nonlinear system of equations evaluate

both a function and its derivative at each time step. The COMSOL software will attempt to reduce *Jacobian* reassessment by default, because this derivative or is also recognized as the *Jacobian* is relatively costly in terms of computing. Also, another technique is that it can minimize the necessary time-step size and attempt to compute the solution in case of the nonlinear solver found a difficulty in converging. Another column (called *TFAIL*) is incremented when the time-step is decreased. This is an appropriate method if the solution fields change quickly in time, as in the case of problems of phase change. In addition, various mesh refinements have been used to test the convergence of the model implemented and the minimal refinement has been used to ensure the mesh independence of the solution.

III.4. Experimental solidification benchmark (AFRODITE)

The experimental part presented in this thesis is fundamentally inspired by the Hebditch and Hunt experimental work [51], which have focused on the observation of segregation during the formation of various alloy ingots (Sn-5wt%Zn, Sn-5wt%Pb and Pb-48wt%Sn) in a crucible of 100 mm in length, 60 mm in height and 10 or 30 mm in width and cooled only from one wall by circulating water or air. Significant macrosegregation has been observed by simulating horizontal solidification (perpendicular to gravity) of pure tin with considerable density differences during solidification. The experiment has been developed as quasi-2D and has been used as a basis in several numerical studies, including benchmark problems [52, 53] and analyses of the effects of modelling microsegregation [54].

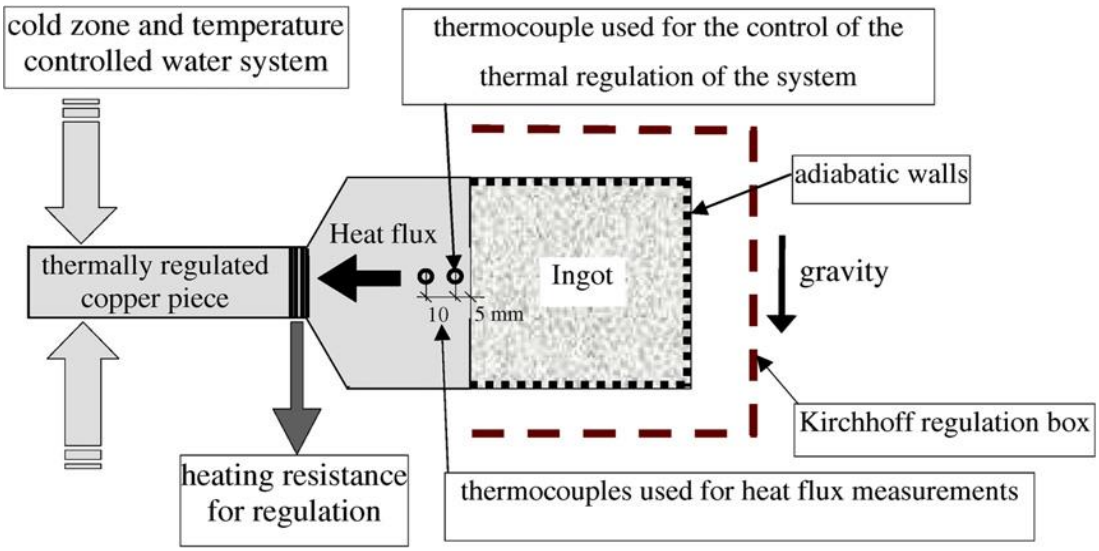

Fig. III.2. Illustrative scheme of the experimental installation ("AFRODITE I"), [55].

The first version of the experiment named "AFRODITE I" (see Fig. III.2) was performed by Quillet *et al* [55]. The samples were solidified in a 50×60×10 mm^3 crucible, all of whose walls were adiabatic, except the right vertical one by which the cooling was applied.

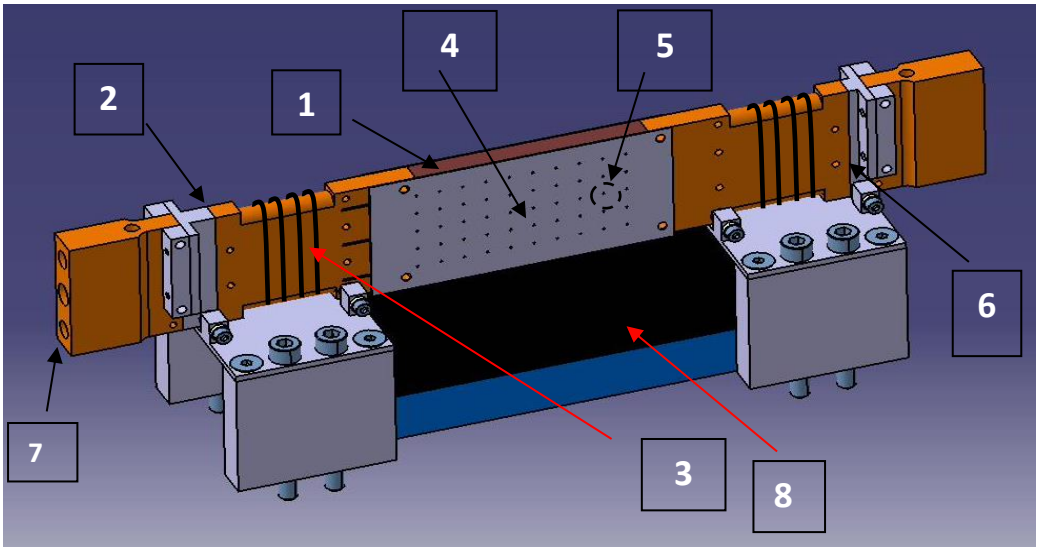

Fig. III.3. Schematic of the experiment set-up ("AFRODITE II"): 1. Pure tin sample, 2. Left heat exchanger, 3. Resistance, 4. The stainless-steel crucible, 5. Thermocouples positions matrix, 6. Right heat exchanger, 7. Water cooling system, 8. Linear motor, [56].

The experimental setup ("AFRODITE I") was modified by Wang [57], to lead in a second version called "AFRODITE II" as illustrated in Fig. III.3. These modifications can be summarized as follows:

- The size of the solidified samples was changed from (50×60×10 mm^3) to (100×60×10 mm^3).
- The addition of a second heat exchanger located on the opposite side of the initial heat exchanger. These two exchangers give the possibility to impose a horizontal thermal gradient between the vertical walls of the exchangers in contact with the sample, thereby allowing the application of different thermal heating and cooling configurations.
- Intensification of the temperature measurement points (80 type K thermocouples) in order to have more precision in the thermal maps.
- Addition of an electromagnetic stirrer of the traveling magnetic field type to stir the liquid charge in order to homogenize the concentration of solute element (in the alloys case) and to improve the thermal exchanges.
- Modifications on the thermal insulation system, in particular on the Kirchhoff box, in order to reduce the thermal losses by radiation (losses < 0.18 Watt).
- Modifications on the installation enclosure to be able to work under a primary vacuum (between 10^{-2} and 10^{-3} mbar) in order to reduce convection losses.

The "AFRODITE II" device is well described and documented by Wang *et al* [57] and has served as a validation reference for several numerical simulations works [58].

A third version of the device, named “AFRODITE III”, has been proposed by Hachani *et al* [59]. In this later, the total number of thermocouples was increased to 86 (see Fig. III.4), including only 18 at the heat exchangers for a better estimate of the temperature. The heat fluxes extracted from their exchange walls are remarkably better controlled. This latest version of the experiment will be referred in the rest of this work by "AFRODITE".

Indeed, Hachani *et al*. [60] have studied experimental solidification work on binary tin alloy and demonstrate that, though regular patterns in the solidified ingot mesostructure are predicted, considerable statistical differences are also to be predicted in their position. This is a powerful new argument that supports the use of statistical methods to develop models. Based on benchmark ‘AFRODITE’ setup, we have studied the horizontal directional solidification. The solidified samples are 10 cm long, 6 cm high and only 1 cm thick, which is the topic of this study that was suggested by Fautrelle and co-workers as a 'quasi-2D' experiment [26, 27, 57, 61, 62]. The need to develop adequate functional boundary conditions for the problem of heat transfer [31] is a very difficult subject in comparing computational models with this type of experimental analysis. Boussaa *et al* [26, 27], validated a model based on a two-phase volume-average approach with using Sn-3wt%Pb alloy experimental results. They found that the 2D approximation method exaggerates the velocity field by a factor of 1.5, which means there is a lack of accuracy between simulation and experimental results. They also observed that in the 3D models, the damping effect of the lateral walls taken into account, it gives very consistent with the experimental measurement results, as it could predict the main behaviour of meso/macrosegregation in the solidified ingot. Botton *et al* [63] have proposed that it is a close approximation to assume the temperature field to be 2D because the cavity is confined, the liquid metals are significant thermal conductors (relatively low Prandtl number) and the heat flux is in the longitudinal horizontal direction. Conversely, due to the velocity variations in the transverse direction that caused by the no-slip condition on the lateral sides, the velocity field should not be considered to be similar to 2D. In order to take the three-dimensionality of the velocity field into consideration, an alternative to fully 3D simulations can be obtained by integrating the motion equations in the transverse direction, assuming the specified forms for velocity, temperature and electromagnetic stirring. Note that one of the major keys in the simulation of the solidification problems is an accurate presentation of the thermal field. We suggest that the very first mandatory step towards the implementation of an effective binary

alloy solidification model is to validate its possibility to: (1) recreate the thermal field in natural convection configurations; (2) Expect the morphology and location of the solid-liquid interface in the case of pure metal solidification. The latent heat release at the advancing solid/liquid interface, whose location is generally an undefined function of time and space and can be calculated as part of the solution, is the complexity presented by phase-change problems. The apparent heat capacity method [64] (AHCM), which has some special computational attributes, is one of the techniques that are applied to process latent heat release for the solidification problems. The application of a magnetic field in the solidification process influences the microstructure in the case of forced convection and improves the characteristics of the mechanical alloy [65-69]. The effect of EMS on the pure Sn and Sn-Pb alloy microstructure was analysed by Ch. Vivès [70] and CHEN Zhao [71]. Again, a purpose is to check in particular the effect of both natural and forced convection via the thermally controlled solidification of the pure metal in the bath (caused by an induction magnetic field).

III.4.1. Description of experimental set-up 'AFRODITE'

In order to validate the numerical simulation results, we need an experimental data to verify the accurate of our simulations. The benchmark experiment developed in the SIMAP/EPM laboratory is a reference tool for this validation with well-controlled initial and thermal boundary conditions. Hachani *et al* [58, 59, 61] have suggested a three dimensional solidification experiment; the purpose was to provide useful quantitative data to validate the numerical models. The experiment was conducted with pure tin. The simulation chosen solidification configuration corresponds to domain with adiabatic walls, with the exception of the two vertical walls that allow solidification of the sample. However, in the experiment we have used two heat exchangers in both right and left sides that allow independent sample control, horizontal temperature gradient and cooling rate. The temperature difference *DT* between the two lateral sides, i.e., left and right exchangers, is 40 K in this current experimental analysis with applying the same cooling rate (CR = -0.03 K/s) in both right and left walls such that they are cooled simultaneously. This benchmark experiment deals those problems that related to the solidification, where the gradient of cooling temperature is perpendicular to gravity (the direction of the advanced solidification front is horizontally). In the case of alloys, such a setup guarantees natural convection and hence macro-segregation. The selection of a cooling rate of -0.03 $K.s^{-1}$ is mainly related to the appearance of the macrosegregation and segregated channels at a compatible cooling rate in a solidified ingot, frequently 2-5 $K.min^{-1}$.

In order to provide adequate time to get well establishment in thermal convection in the case of pure materials, and also for strictly control of the experimental conditions, especially the heat losses, this slow cooling rate was kept.

Fifty thermocouples on the lateral walls (front view) were welded to record the instantaneous temperature distribution. The temporal profile of the temperature field is measured and analyzed. This allows us to analyze the variation that induced by natural convection, therefore its effect on the initial macrostructure solidification conditions. The design of the benchmark experiment is shown in Fig. III.4 and Fig. III.5 and helps to interpret the results given below. The temperature measurements chosen are taken on a fifty-point grid numbered from 1 to 50 (see Fig. III.4). Each exchanger is equipped with 9 thermocouples and a feedback control is implemented to govern cooling conditions. Other sides of the cavity may be considered as adiabatic due to special precautions taken to reduce convective and radiative heat exchange with the environment [60]. Two classes of both exchangers thermocouples measure the heat flux: FL1 to FL9 and FR1 to FR9 (see Fig. III.4).

The experimental setup formed of five major parts: the pure tin sample, the welded thermocouple stainless steel crucible and the temperature measurement system, the two heat exchangers, the linear motor used to create the traveling magnetic field, the Kirchhoff box and the vacuum chamber.

III.4.2. Measurement procedure

A rectangular cavity of 100 mm in length, 60 mm in height and 10 mm in width encloses the pure tin pre-sample. During the whole process, all walls except for two narrow vertical ones are held in relatively insulating condition by means of a Kirchhoff box and the vacuum chamber. Two controllable heat exchangers solidify the molten metal. Each exchanger's location is shown in Fig. III.4. For both exchange faces and removed flux, strict temperature control is required. This is possible by the high thermal conductivity of copper ($\lambda_{cu} = 380\ W.m^{-1}K^{-1}$) used to make the two exchangers. The choice of copper is on purpose because it causes chemical restrictions (copper-tin interaction), it is important thermally. A thin layer of chromium on each exchanger's contact face with the liquid metal guarantees the chemical neutrality. FL3 and FR3 thermocouples for both left and right exchangers (nearest to the mid-height sample-exchanger interface) allow control of the placed temperatures on the exchanger walls, by means of instructions transmitted to the two thermocouples by an automatic PID (proportional-

integral-derivative) controller, that controls the electrical power output of the heating element of each exchanger.

The temperature field is measured every second by an array of 50 type K thermocouples on the wider surfaces of the stainless-steel crucible, track the advance of solidification. For all the thermal considerations that previously mentioned, the thermocouples have a diameter of 1.5 mm. The fixation of the thermocouples on two side walls of the crucible is the result of a compromise between mechanical resistance, heat loss and, if necessary, easy reproducibility of the welded operation. Laser spot welding is used on all thermocouples. The welding of all thermocouples is properly reinforced to reach ideal consistency of measurement. In order to prevent any influence on the dynamic configuration, in particular the friction with the melt, it is necessary to remember that all the thermocouples are flush with the load-bearing internal faces of the crucible.

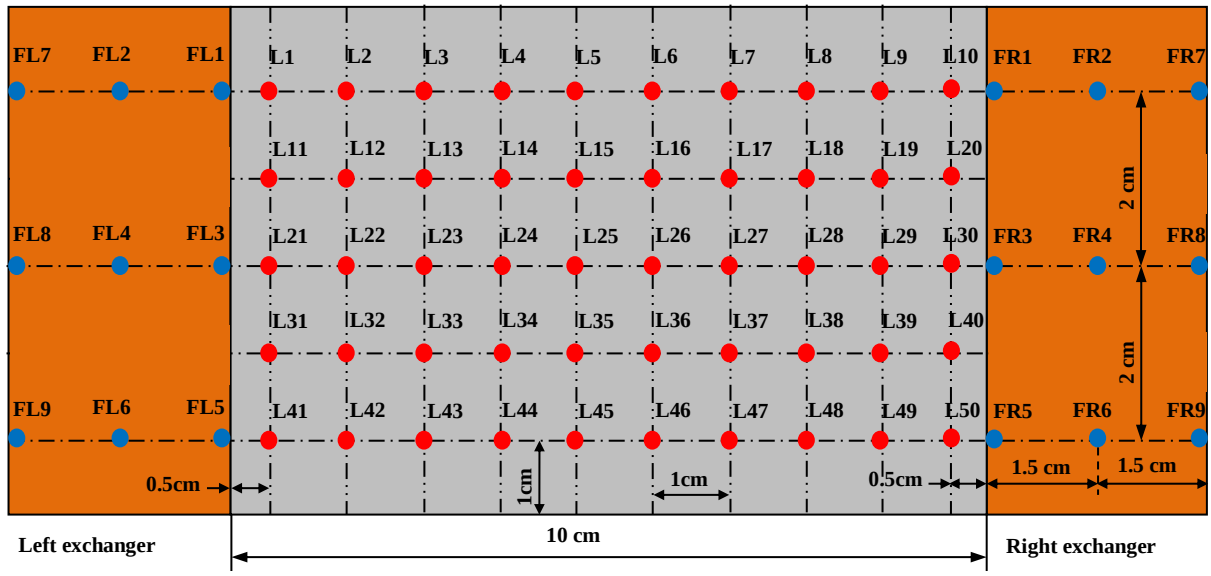

Fig. III.4. Diagram illustrating the distribution of all the thermocouples (L1 to L50) welded on one of the larger faces of the crucible, and thermocouples (FL1 to FL9) of the left exchanger and (FR1 to FR9) of the right exchanger.

The entire experiment involves five steps illustrated in Fig. III.5: melting, first temperature stabilization to achieve a uniform temperature field, creation of the temperature difference *DT* between the heat exchangers, second temperature field stabilization, sample cooling (solidification). In the melting stage, the solute in the case of alloys was homogenized by the application of electromagnetic stirring, applying the concept of a linear motor producing an electromagnetic field. In order to control the initial conditions, this step is very important.

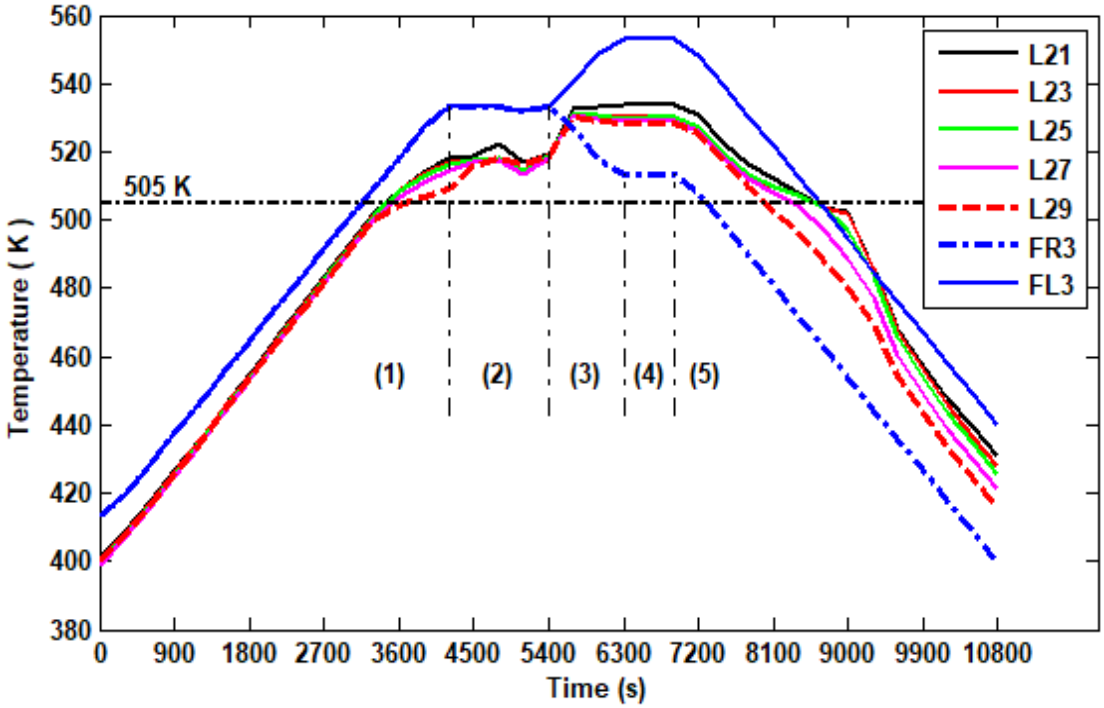

Fig. III.5. Time profile of the measured temperature during the solidification of a tin ingot without electromagnetic stirring. The process for all solidification experiments performed consists of five stages: (1) melting, (2) temperature stabilization and electromagnetic stirring to acquire a homogenous temperature field, (3) application of the average thermal gradient, (4) second temperature field stabilization stage and (5) solidification. Applied temperature difference *DT* = 40 K, cooling rate CR = - 0.03 K/s. FR3, FL3, and L21, L23, L25, L27 and L29 respectively correspond to thermocouples located on the side of the heat exchangers and along the horizontal centreline (mid-height as shown in Fig. III.4). The discontinuous black line at 505 K represents the melting temperature.

Numerous solidification studies were performed experimentally on pure tin and metallic alloys. Pure tin was selected in this chapter in order to check the adopted numerical approach. In the present case, the experimental conditions are: *DT* = 40 K, cooling rate CR = -0.03 K/s.

As mentioned previously, the experimental process consists of five main steps presented in Fig. III.5 as follow:

1) Melting stage:

The initial state corresponds to the solid ingot at 25 °C. A first temperature ramp is applied on the exchange surfaces between the ingot and the two exchangers, at a heating rate of about 0.052 K/s. This first ramp is followed by a plateau at a fixed temperature of 140 °C for 15 min, and then a second ramp with a different melting rate according to the case treated. Note that for most of the experiments performed this melting ramp is equal to the cooling rate (CR= -0.03 K/s).

2) First stabilization stage:

During this step, an electromagnetic stirring is applied using a linear motor placed at a distance of 5 mm under the crucible and used to generate a traveling magnetic field. The stirring has a double effect, firstly to have a stationary thermal state (thermal stabilization of the ingot) and secondly to homogenize the solute element concentration in the case of alloys.

3) Application of temperature difference *DT*:

The average experimental temperature difference (*DT*), is applied between the two heat exchange surfaces, using the PID system that controls the set-points imposed on the two pilot thermocouples, FL3 and FR3. For example, for a temperature difference of 40K, a temperature increases from 260°C to 280°C is imposed on the FL3 thermocouple (left hot side) and a decrease from 260°C to 240°C on the FR3 thermocouple (right cold side). It is very important to mention that this latter step is the stage that distinguishes between natural and forced solidification, because in the case of solidification under the effect of natural convection, the electromagnetic stirring stops at the beginning of this stage, whereas in the case of solidification under the effect of forced convection the stirring is maintained until the end of the experimental process.

4) Second stabilization stage:

After applying the experimental temperature difference (*DT*), between the two heat exchangers, a second stabilization step is imposed. During this step, both temperatures of the thermocouples FL3 and FR3 are kept constant (FL3 = 280 °C and FR3 = 240 °C) for a period of 45 min, in order to allow the convection to be well established. The deformation of the isothermal lines gives indications on the flow pattern generated by natural convection.

5) Solidification:

The last stage is the cooling or solidification process. The same cooling rate is imposed on both exchangers through the temperature control of the two thermocouples FL3 and FR3, in order to have solidification under a constant temperature difference. Note that in all the solidification experiments carried out, the heat extraction is done from the right side. However, during solidification under a very slow cooling rate (e.g., CR= -0.03 K/s), the heat exchange through the right exchanger is not enough to extract the quantity of heat released by the liquid and the latent heat released by the solid layers formed, in this case the regulation system involves the

second exchanger on the left side and the extraction is done from both sides while keeping a constant temperature difference.

III.4.3. Thermal boundary conditions

As a first step to set the initial boundary conditions, it is important to extrapolate the temperatures at the interfaces between the ingot and the two exchangers in order to determine the effective temperature difference currently applied to the ingot. The exact thermal boundary conditions for the numerical simulation reflect these temperatures. The analysis is mainly based on the notion of heat flux conservation exchanged on both sides (details of this approach are given in Appendix II.1). What is suggested in [62] is accompanied by:

$$\varphi_L = \lambda_{tin} \frac{(T_{left\ interface} - T_{21})}{e} \quad \text{(III.14)}$$

$$\varphi_R = \lambda_{tin} \frac{(T_{30} - T_{right\ interface})}{e} \quad \text{(III.15)}$$

Where λ_{tin} is the thermal conductivity of the ingot, e = 5 mm is the distance between the vertical exchange interfaces and the nearest thermocouples (L_{21} and L_{30} for the left and right side respectively). The analysis indicates that there are changes between the temperatures calculated by the FL3 and FR3 thermocouples (slightly in contact with the sample) and the extrapolated temperatures ($T_{Interface\_Left}$, $T_{Interface\_Right}$) of up to about 7 K for the right side and about 13 K for the left side. This can be justified by the presence of a considerable thermal resistance between the exchangers and the sample on both sides (see Fig. III.6). The origin of this latter is due to:

1) A thin layer of boron nitride is deposited on both contact surfaces between the copper and the sample in order to avoid a chemical reaction between the sample and the two heat exchangers. This creates a thermal resistance due to the low thermal conductivity of the boron nitride layer.
2) During the solidification stage of the tin-lead alloy [37], a shrinkage phenomenon was observed due to the effect of wettability of the walls by melt, on motion of liquid and on distribution of liquid fraction. The vacuum created will be filled by an air pocket, resulting in additional thermal resistance.

As demonstrated in earlier studies [26, 27], a contact resistance may exist between the two exchangers (FL3 and FR3) and the sample (see Fig. III.6 (b)). This means that the current temperature difference across the bulk of the sample may be smaller than that imposed on heat

exchangers which changes with liquid solid phase transition. In addition, during the experiment, a deviation may occur of the cooling rate that applied on both sides, from the configured rate if there is intense solidification accompanied by considerable heat release or if there is a lack of water cooling. In order to consider these aspects, the temperature at the inner face of the lateral sample walls is corrected by means of temperature records acquired by the thermocouples welded on the heat exchangers and on the front of the cavity close to the lateral faces.

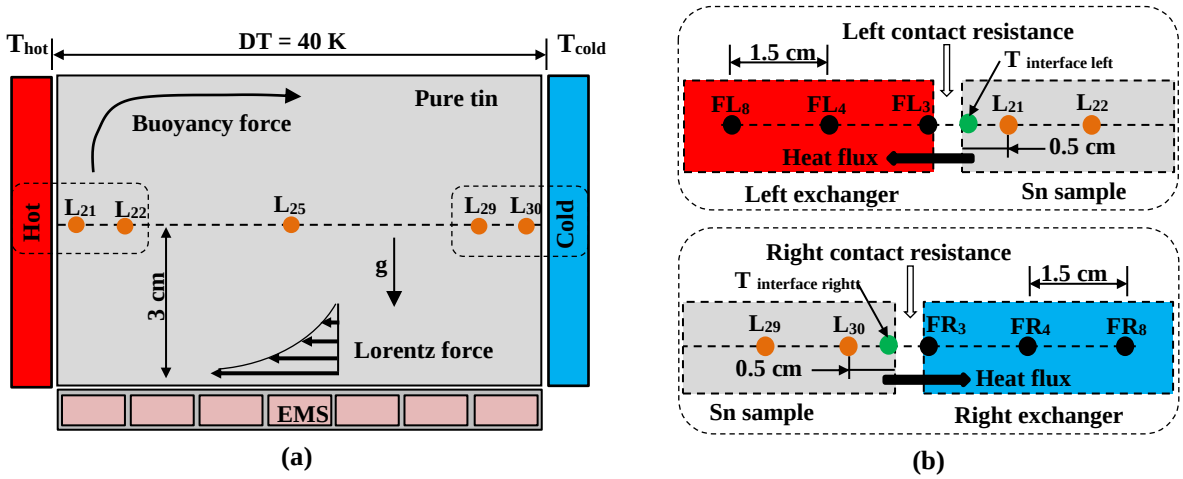

Fig. III.6. (a) Diagram of the experimental set-up (AFRODITE) showing the position of some thermocouples: L21 (x = 0.5 cm), L22 (x = 1.5 cm, L25 (x = 4.5 cm), L29 (x = 8.5 cm) and L30 (x = 9.5 cm) all at the same height z = 3 cm and (b) contact resistance between the two heat exchangers (left and right) and the solidifying volume.

An extrapolation analysis of the temperature at the exchange interface for the solidification of pure tin with an average experimental temperature difference of 40 K and a cooling rate of 0.03 K/s without any stirring as can be seen in Fig. III.7. This temperature extrapolations is based mainly on the quantification of the resistance in order to determine the effective temperature differential applied to the ingot walls and to calculate the thermal boundary conditions in the computational modelling. The curves of both extrapolated temperatures illustrate that the effective temperature differential is about 20 K. An extrapolation approach (finite elements) is suggested to measure the heat fluxes exchanged. The demonstration of this method is explained in Appendix II.1, including equations (II.1.7) and (II.1.8) calculating heat flows exchanged on both left and right sides.

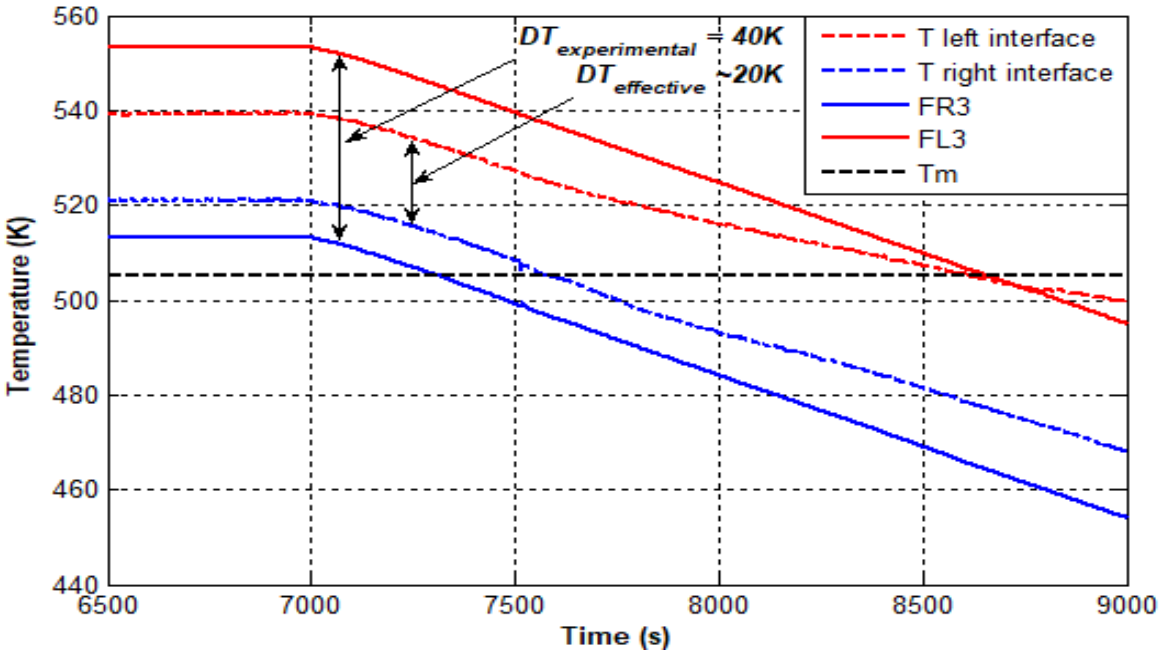

Fig. III.7. The experimental time profile of the extrapolated temperatures during the solidification of pure tin. Effective temperature difference DT ≈ 20 K, cooling rate CR = 0.03 K/s. The time profiles of the right (FR3) and left (FL3) exchangers (see Fig. III.4) are also shown. The black discontinuous line represents the melting temperature.

III.4.4. Heat losses analysis

In order to control the heat losses, we have measured the time evolution of the heat fluxes by the18 thermocouples placed in the heat exchangers as illustrated in Fig. III.8. The conservation of heat fluxes is not completely achieved. However, the relative difference between the left and right heat fluxes is not greater than roughly 12%. Notice that the precision of heat flux measurements is constrained by the small temperature differences calculated in copper heat exchangers. Regardless these issues, the decay of the temperature difference nearer to the end of the solidification in the upper-left corner of the sample is checked by the weak heat flux value offered by the thermocouples located at the top-left of the heat exchanger (i.e., FL1-FL2). This implies that the heat flux extracted from the wall of the sample is far from uniform.

The most prevalent mode of heat transfer between the crucible and its surrounding is radiation from the second stage of the experimental profile (first thermal stabilization, see Fig. III.5). A temperature-controlled Kirchhoff box surrounding the sample was used to recompense these radiation losses and thereby achieve adiabatic boundary conditions on the lateral walls. It comprises a temperature-organized system containing of a cooling part and an electrical thermal resistance part. The estimation of radiative heat losses through the crucible walls by Stefan Boltzmann law gives an order of less than 1.8 W. In addition, heat exchange by convection and conduction is negligible as the sample is placed in the vacuum chamber.

Furthermore, the top surface of the sample was covered with an isolate material sealed in aluminium foil to minimize the radiant heat transfer.

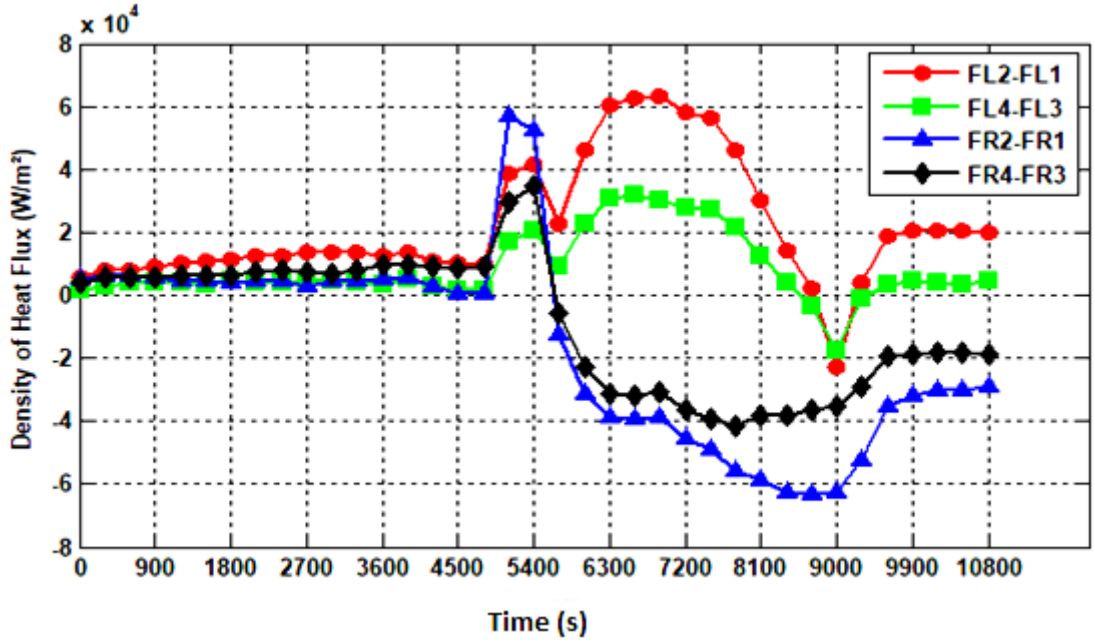

Fig. III.8. Time profile of the heat flux density $(-\lambda \nabla T)$ obtained from the temperature differences recorded in the two heat exchangers (the thermal conductivity of the copper is 380 $W.m^{-1}.K^{-1}$). The solidification parameters are DT = 40 K, CR = - 0.03 $K.s^{-1}$. FL1, FL2, FL3 and FL4 are the thermocouples placed at the left exchanger, and FR1, FR2, FR3 and FR4 are the thermocouples placed at the right exchanger, as shown in Fig. III.4.

Particular attention is paid to numerous connections of all thermocouples flushed with the inner lateral faces of the stainless-steel crucible in order to avoid parasitic currents. Actually, additional electrical current (called Seebeck current) may be produced by any established parasitic thermal gradient on the connections, which distorts the results relatively. To avoid this, all connections are included in the temperature control box. The relative precision of temperature measurements is about ±0.1 K. Even so, the offset value may even be present in the measurement of temperature. We corrected this offset by a calibration obtained from pure tin solidification/melting experiments. It can be linked with the measured melting temperatures as the precise melting temperature of this metal is known. The remaining doubt concerning the absolute value of the temperature is in the order of 1 K. All measurements are recorded in ASCII files on a computer.

III.5. Electromagnetism

Following what we have explained in the previous chapter (Chapter II) concerned the application of the electromagnetic force, it is necessary to mention that only its application to

the solidification of pure metals (pure tin) will be discussed in this chapter. However, there are several works concerning the study of forced convection movements induced by magnetic fields in metallurgy and their influence on solidification, [1, 57, 58, 69, 72]. Emphasis will obviously be focused on the effect of forced convection generated by a Traveling Magnetic Field (TMF) on the solidification of pure tin (Sn) in term of thermal field, velocity field and the morphology of the solidification front. Indeed, the configurations according to the direction of the stirring force (Lorentz force) applied with respect to the direction of the natural convection circulation loop that will also be discussed in this chapter. Special interest will be given to the possibility of using stirring with a TMF (see Fig. III.10) as a technical solution to control the temperature homogenization in the liquid bath. A linear motor placed 5 mm under the bottom face of the stainless-steel crucible was used to generate this TMF. Numerically, in this chapter we can classify two simulation models (two cases as mentioned previously) that treat pure tin phase change process, as follow:

- **Case I:** The solidification of pure tin under natural convection without any stirring applied, a clockwise eddy flow created caused by the temperature difference between the right and the left walls of the cavity (see Fig. III.11).
- **Case II:** The conditions that were introduced in the first case are kept the same. Whereas, an electromagnetic force applied in the same direction as natural convection. Therefore, a clockwise eddy flow generated by this external force (EMS), (see Fig. III.9-a). This case characterized by the application of this EM Stirring during the whole process, i.e., from the beginning of stage 4 until the end of stage 5 (see Fig. III.5), with 50 Hz of a working frequency.

III.5.1. Lorentz force

The fundamental governing equations in magnetohydrodynamics are known by the famous Maxwell equations and the generalized Ohm's law (see chapter II). Indeed, the resulting Lorentz force produces a stirring within the fluid. The physical characteristics of the stirring are strongly influenced by the frequency and intensity of the magnetic field used.

For a confined configuration similar to that of our case, Wang *et al* [73] have analysed the electromagnetic force expressions (Fx, Fy and Fz) as are presented in Appendix I.3.

In the melt, the active averaged electromagnetic force can be defined by its two components as follow, [58, 73]:

$$\begin{cases} \langle F_x \rangle = \frac{\sigma\omega k^*}{2} A_0^2 \, exp(-2k^* z) \\ \langle F_z \rangle = \frac{A_0^2}{2}\left[\sigma\omega\beta^* - \left(\frac{\pi}{2e}\right)\frac{k^*}{\mu}\right] exp(-2k^* z) \end{cases} \quad \text{(III.16)}$$

with $k^{*2} = k^2 + \left(\frac{\pi}{2e}\right)^2$ and $\beta^* = -\frac{\mu\sigma\omega}{2k^*}$.

where σ, ω, k^*, A_0 and e are the electrical conductivity, basic angle frequency, wave number in narrow liquid domain, amplitude of the vector potential and the *half-width* of liquid domain in *y-direction*, respectively. In this study, the upper index ( )* refers to quantities that take into account the narrowness of the fluid domain.

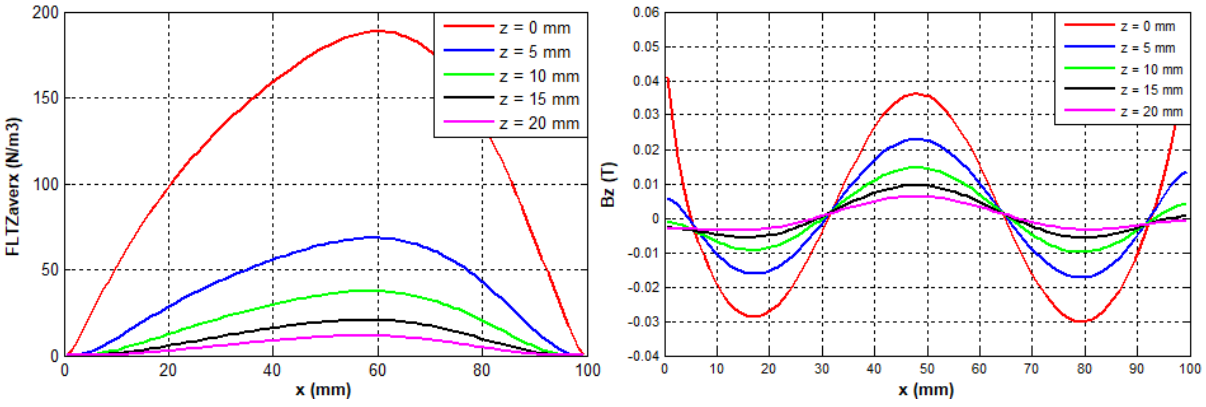

(a) (b)

Fig. III.9. Variation of (a) Lorentz force averaged in time in the driving direction (x) and (b) vertical magnetic flux density (B_z) for several vertical levels (z) taken at mid-thickness of the cavity (y = 5 mm). f = 50 Hz, J = 8 A and $A_0 = 2\ 10^{-4}$ T.m.

In order to estimate the effect that caused by the application of magnetic field, several tests have been treated to examine the influence of the electromagnetic force (i.e., the maximum distance affected by the applied magnetic field). Fig III.9 gives the profile of the Lorentz force contribution in the horizontal direction (x) and the vertical component of the magnetic field (B_z), calculated at mid-thickness of the cavity ($y = 5\ mm$) for various vertical levels ($z = 0$, *5, 10, 15* and *20 mm*). Fig III.9 also shows that the corresponding effective skin depth of the magnetic field is approximately $\delta \approx 5$ mm and the corresponding magnetic field amplitude is around *45 mT* for an applied current $I = 8\ A$ and frequency $f = 50\ Hz$.

III.5.2. Traveling magnetic field (TMF)

A numerical simulation of a traveling magnetic field using COMSOL software was carried out under identical geometry and conditions of AFRODITE configuration set-up.

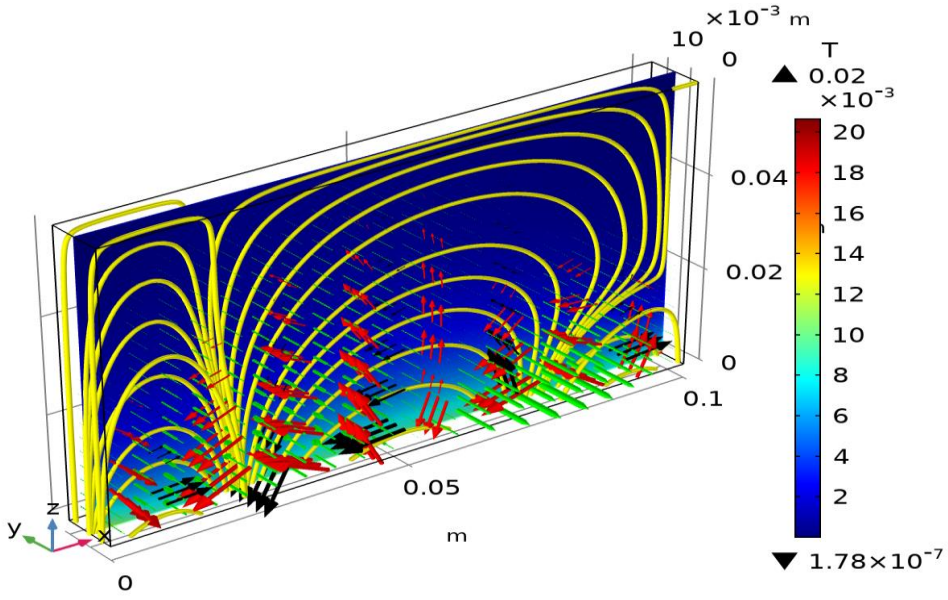

Fig. III.10. 3D numerical simulation at one time of the spatial evolution of traveling magnetic field for the conditions: (f = 50 Hz and J_0 = 5500 A/m^2), the red, black and green arrows present the Lorentz force, magnetic field and induced current respectively. Also, the magnetic flux density presented by the yellow streamlines.

Fig. III.10 gives a 3D graphical representation at one time of the electric current lines as well as the spatial distribution of the magnetic field in the cavity for a frequency of (f = *50Hz*) and a current density of (J_0 = *5500 A/m*^{2}).

III.6. Geometrical and thermal configuration

The geometrical configuration for this analysis is shown in Fig. III.11. it is a differentially heated parallelepipedic cavity. The dimensions are chosen in order to correspond to the crucible of the benchmark experiment proposed by Fautrelle and co-workers [56, 60]. This cavity is confined in the transverse z direction. Its aspect ratios are: $A_w = W/H = 1/6$ and $A_l = H/L = 6/10$, where L is the length in the x direction (L = 10 cm), H is the height in the y direction (H = 6 cm) and W is the width in the z direction (W = 1 cm). The top, bottom and side walls are adiabatic, while the two end walls at x = 0 cm and x = 10 cm are at constant temperatures T_h and T_c, respectively. Some simplifying hypotheses are applied in our model:

- Newtonian incompressible fluid in the Boussinesq approximation for the liquid phase.
- All physical properties are expressed as a temperature function in both liquid and solid metal.
- The solid phase is supposed to be non-deforming and free of internal stress.

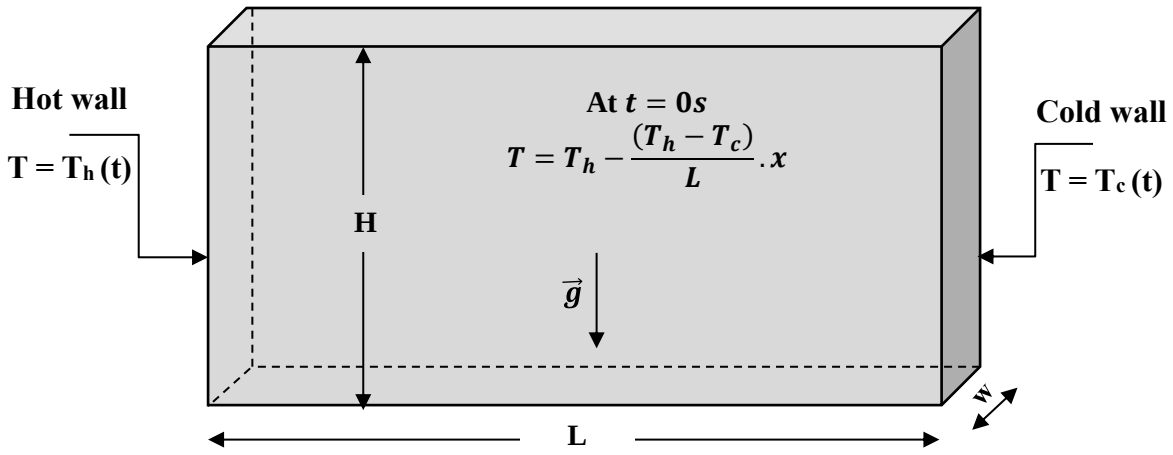

Fig III.11. Diagram of simulated domain and the boundary conditions.

III.7. Results and discussions

We report in this section the results obtained with different models for both cases as mentioned previously of solid-liquid phase change considered. The reliability of the different 3D models with respect to the experimental results is examined. We have devoted this results part, to the stage dealing with the solidification process of a pure tin only. This process is carried out by cooling liquid tin, initially at a temperature above the melting temperature, until it has completely solidified. The results of our numerical simulations of this process are directly compared with the experimental results obtained with the reference experimental set-up 'AFRODITE', [56, 58, 60, 61]. These experimental results are also reported in this part. As detailed previously, in numerical simulations, the initial step refers to the uniform distribution inside the cavity of the temperature gradient corresponding to the temperatures 541.29 K and 521.24 K imposed on left and right lateral sides. This corresponds to about 16900 s of the physical time in the solidification experiment as shown previously in Fig. III.7. in this multidisciplinary process, several physical phenomena are strongly coupled. The fluid flow configuration governed by buoyancy and electromagnetic forces can significantly affected the distributions of temperature and consequently the transformation of phase. In addition, solidification is followed by the release of heat that can influence the temperature field too. During the experiment, the evolution of the temperature distribution was measured at every second, which may act as the key guide for validation between numerical and experimentally recorded results. Consequently, the results will estimate with showing the effect of EM Stirring in term of dynamic field during the fourth stage of the experimental setup (second stabilisation stage) before solidification, and therefore the temperature evolution during solidification

process (stage 05). The examination will more detailed of the phase change system with evolution of multiphase flow and phase fraction.

III.7.1. Effect of electromagnetic stirring on dynamic configuration

At first, the equations of the treated problem can be present in 2D in the plane (x, z) if we assume that the quantities are constant according to y axis (thickness). The results that present as maps in all next sections are presented in middle plane vertical view that located at mid-thickness in the transverse direction *(y =5 mm)* over the small width *W*. Fig. III.12 (a) and (b) show the velocity magnitude for both natural and forced convection models, respectively. The velocity fields are presented by the black arrows and the black isotherm lines present the temperature field. The main aim of this comparison between these two models which are presented the cases of natural and forced convection, i.e., with and without stirring, is to examine how extent the effect of the electromagnetic stirring on the velocity field.

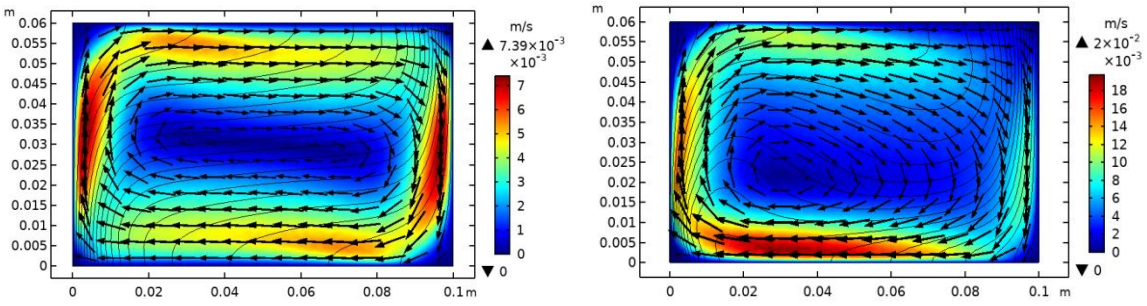

(a) ***(b)***

Fig. III.12. Velocity fields (coloured magnitude levels and arrows) and temperature field (isotherms) obtained without solidification and with different convection: (a) 3D model for natural convection (view in the vertical middle plane), (b) 3D model for forced convection (electromagnetic stirring in the same direction as natural convection).

For both cases considered, the contrast between the results (case (a) and (b) is very marked. However, the case that characterized by the application of EMS (case (b)) gives a highly convective flow with velocity intensities much higher than the other case (about 10-fold). This contrast is originally caused by EMS that creates an intense movement in the pool liquid. These liquid motions which give large recirculation zones are in form of vortex that located in different zone depends on the configuration under consideration. Indeed, in the natural case (case (a) the mentioned vortex is located in the centre of the cavity because the maximum velocity is in the lateral sides of the cavity. Whereas, the EMS that applied in the bottom surface characterized by its maximum value at the level of magnetic skin (see Fig. III.12 (b)) which is the responsible of the recirculation zones location. In this case, the vortex is located in the middle-left part of the sample near the hot wall.

These differences in velocity fields between the models also lead to differences in temperature fields. Indeed, in case (b) the isotherms are highly deformed compared to case (a), especially in regions where the velocity is maximum (at the level of magnetic skin). As well known the lateral walls clearly affect the structure of the resulting flow. The adhesion of the liquid to these walls induces dissipative effects that modify both velocity and temperature field. These dissipative effects are well taken into account in the 3D model.

$$Gr_T = \frac{g\beta_T \Delta T\left(\frac{H^4}{L}\right)}{\nu^2} \quad \text{(III.17)}$$

$$N_m = \frac{F_0}{g\rho\beta_{T\Delta T}} \quad \text{(III.18)}$$

$$F_0 = C\,\frac{\sigma\omega k^* B_0^2}{2} \quad \text{(III.19)}$$

$$Re = \frac{u(u=1)\left(\frac{H^2}{L}\right)}{\nu} = 1440 \quad \text{(III.20)}$$

It is necessary to introduce some adequate dimensionless numbers that have a direct relation to treated process, namely the thermal Grashof number given by Eq. III.17 and based on the vertical aspect ratio, (H/L), which is set at (3/5) in the present study (characteristic length), with ν is the kinematic viscosity (ν = 2.54 10^{-7} m².s^{-1}). In second stabilization stage (stage 04), Gr_T (8.67×10^6) considered as the most important parameter for defining natural convection. Moreover, by using a dimensionless interaction parameter N_m defined as the ratio of Lorentz forces to buoyancy (Eq. III.18), where F_0 expressed by (Eq. III.19) is the electromagnetic force derived from (Eq. III.16). Where C ≈ 0.05 is a coefficient that takes into account the finite size of the inductor [74]. Indeed, for B_0 = 45 mT (or J = 8 A), the value of N_m is 4, this means that the electromagnetic forces are stronger than buoyancy and consequently it will be the dominant force in the system. Eventually, in the second stabilization stage (stage 04), the Reynolds number corresponds to the average velocity (u_{aver} = *0.01* m/s) is defined in Eq. III.20. The value of Reynolds number (Re = 1440) indicates that for the analyzed dynamic configuration, the overall flow pattern is likely to be laminar.

III.7.2. Comparison of projected velocity between experiment and numerical simulation

In this part, a particular approach in experimental analysis called the projected velocity was compared to the velocity field that obtained in the simulations of pure thermal convection, i.e., during stage 4 of the experimental profile. In order to obtain some key information about the dynamic configuration during the solidification process, including the velocity field magnitude

in the liquid region, experimental data through the temperature field was analysed. The approach is mainly based of measuring the projected velocity magnitude U_T on the temperature gradient vector that corresponding to the internal thermocouple location at each node. As long as the Peclet number is high, the approach is valid, indicating that convection is significant. Further information concerning this method is given by Hachani *et al* [62].

The concept of the approach [59] is mainly based on integrating the heat equation in the liquid zone over the sample thickness, as follows:

$$\int_0^e \frac{\partial T}{\partial t} dz + \int_0^e \vec{U} . \vec{\nabla} T \, dz = \alpha \int_0^e \nabla^2 T \, dz \qquad \text{(III.21)}$$

where e, $\vec{U}$ and α and are the thickness of the sample, the instantaneous velocity field and the liquid thermal diffusivity, respectively. If we claim that in the transverse direction, the temperature field is uniform which is confirmed experimentally, then the integral of Eq. III.21 will be simplified to:

$$\frac{\partial T}{\partial t} + \vec{u} . \vec{\nabla} T = \alpha \nabla^2 T \quad \text{with } \vec{u} = \frac{1}{e} \int_0^e \vec{U} \, dz \qquad \text{(III.22)}$$

The estimated algebraic velocity U_T is defined as follows:

$$U_T = \vec{u} . \vec{\nabla} T / \left| \vec{\nabla} T \right| \qquad \text{(III.23)}$$

The vector $\vec{u}$ is the average value of the instantaneous velocity across the thickness of the sample, where $\left| \vec{\nabla} T \right|$ is the norm of the temperature gradient.

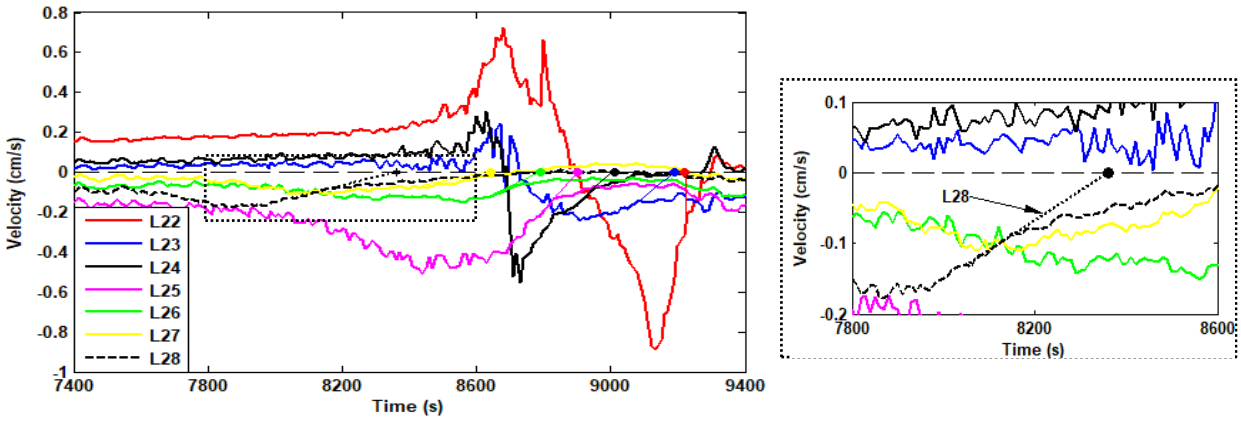

(a) **(b)**

Fig. III.13. (a) Time profile of the modulus of the projected velocity U for different internal nodes (L22, L23, L24, L25, L26, L27, and L28) located at mid-height of the ingot. Fig. III.13 also shows the extrapolation to zero used to estimate the time when the solidification front passes through the position of the nodes. Pure Sn, *DT* = 40 K, CR = 0.03 K/s. (b) zoomed-in view of projected velocity at the node corresponding to thermocouple L28.

The value of U_T is obtained by discretizing the heat equation in the liquid state (without taking into account the release of latent heat) and with introducing the measured temperature data. A centred finite differences method is used for spatial discretization and a second order (*Leap-frog*) scheme for temporal discretization. Details of this method containing the computational mesh and the discretization of the equations are given in the Appendix (III.2).

Fig. III.13 illustrates the time profile of the projected velocity on the thermal gradient vector at nodes L22- L28 (see Fig. III.4) located in the ingot at mid-height, where it is claimed that the scalar products of the velocity vector $\vec{u}$ and the temperature gradient $\vec{\nabla}T$ are not too small.

The results are presented in Fig. III.13 for the case of the solidification of pure tin, under the experimental conditions: DT = 40 K and CR = -0.03 K/s. It is not easy to determine the precision of the method. Analysis of the projected velocity profiles (Fig. III.13) shows that the velocity estimate becomes less than 7 mm/s of amplitude. It should be noted that the current estimate is probably lower than the maximum convective velocity (discussed in the previous section). First of all, the different steps of the solidification process are shown, i.e., the global stabilization of the velocity during the natural convection regime before cooling. On the other hand, the velocity decreases as the solidification front reaches the node (see Fig. III.13 (b)). Indeed, if we take for example node 25 in Fig. III.13 (a), we can see that during the solidification process, the norm of the projected velocity increases and then decreases significantly close to zero. It has been demonstrated by numerical calculations that convection is a little particular to low Prandtl number and it consists of a recirculation jet (well established vortex). Such a scheme is qualitatively in agreement with the observations shown in the Fig. III.13 (a), we observe changes of signs in the behaviour of the projected velocities of L22, L23 and L24 (red, blue and black lines, respectively) towards the end of solidification, this behaviour is not easy to interpret. Indeed, the experimental data are only the projections of the velocity field on the local temperature gradient, i.e., an image of the velocity. Thus, temperature and changes in the heat flow configuration could be responsible for this behaviour. When the node coincides with the solidification front, the use of this approach is no longer accurate because the latent release of heat has not been taken into account.

3D numerical simulation results (black dashed line) were compared with the experimental data (blue continuous line) of the projected velocity U_T for L22 and L23 nodes and are presented in Fig. III.14. The presented results were analysed during the pure convection period (second stabilization stage of the experimental profile) and without any stirring for a period of 160 s.

The time evolution of the projected velocity is in a good agreement between the simulation and the experimental measurement. Moreover, the maximum convective velocity amplitude at node L22 is higher than at node L23, this behaviour is originally based on the location of the thermocouples, where the velocity is almost perpendicular and the velocity at the sides (L22 is near to the left side) is higher than in the centre (L23 is near to the centre).

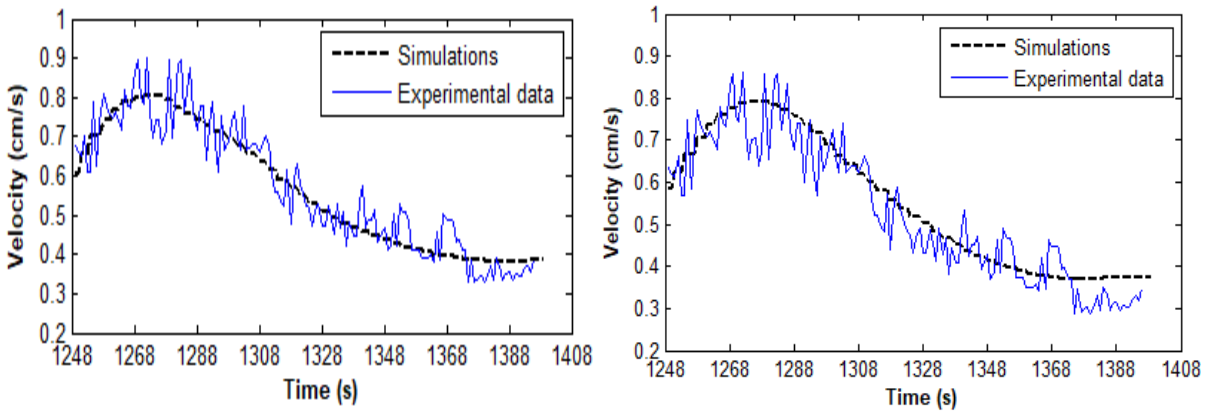

(a) (b)

Fig. III.14. The time profile of the projected velocity on thermal gradient between the 3D model (black discontinuous line) and the experiment (blue continuous line) for nodes L22 (a) and L23 (b).

III.7.3. Temperature evolution: experiment/numerical simulations

The temperature contours and thermal gradients corresponding to three selected instants (7609, 7897, and 8735 s) during the cooling stage (stage 5 in the experimental profile) are presented in Fig. III.15. The corresponding numerical values of the instantaneous temperature field are given in the Table II.1 in Appendix II.2. A comparison study was carried out between the experimental results (Exp) and both of pure thermal convection (case I) and forced convection with EM stirring (case II), see Fig III.15. The temperature field was measured at the same locations as the thermocouples in the vertical middle plane. The results show a clear representation of the temperature field which is presented as 2D corresponding to the main circulation plane.

It is necessary to mention that the experimental results are presented within the zone covered by the array of 50 thermocouples shown in the central column in Fig. III.15. This zone is marked by a white dashed rectangle on both cases of numerical simulation results, i.e., natural convection (left column, Case I) and forced convection (right column, Case II).

The first snapshots (Fig III.15 (a) at t = 7609 s) are taken at the first instant of the cooling stage (solidification) where the behaviour of natural convection during the solidification process is

presented. At this time, the sample is totally liquid (no solid growth yet). The deformations of the isotherms give a clear indications of the flow configuration generated by natural convection (Case I and Exp) despite the weak Prandtl number ($Pr \approx 0.015$). The flow configuration consists of a clockwise flow loop caused by the large temperature difference existing at the beginning of the process with a maximum velocity of 0.739 cm/s. On another hand, the isotherms are more deformed in the case of forced convection (Case II) due to the application of the EM stirring which creates a significant movement in the liquid bath with a maximum velocity of 2 cm/s.

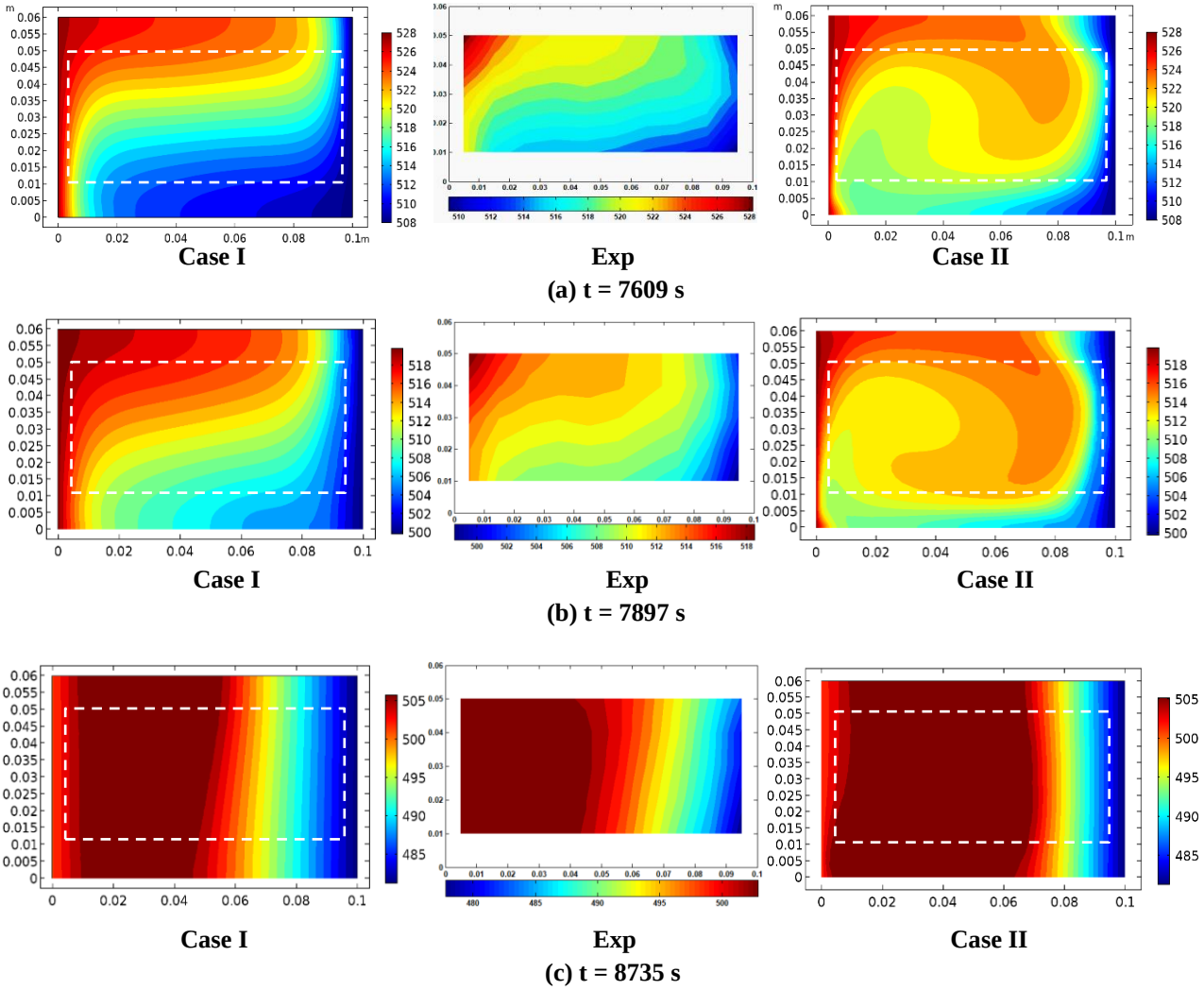

Fig. III.15. Temperature maps at selected instants during the solidification of a pure tin: (a) t = 7609 s, (b) t = 7897 s and (c) t = 8735 s. Case I, Exp and Case II correspond to the numerical calculations for the case of natural convection (on the left), the experimental data (in the center), and the numerical calculations for the case of forced convection (on the right), respectively. The white dashed rectangle on the numerical snapshots represents the part of the domain in which thermocouples are present. Conversely, the white stripe all around the color map in the experimental snapshots corresponds to the part of the domain in which no thermocouple is present. The temperature color bar scales are in Kelvins.

In Fig. III.15 (b) at t = 7897 s, the snapshots are taken at the appearance of the solidification front at the cold side (right endwall of the sample). At this instant, the sample is still mainly liquid. It can also be noted that the flow is still strong enough to deform the isotherms. It is observed that natural convection plays a very important role in the solidification process of tin material. From this preliminary analysis, it is concluded that the solid-liquid interface is significantly affected by the influence of buoyancy-driven convection. The numerical model (Case I) of pure tin phase change is validated and is in good agreement against experimental result (Exp). In comparison, in the case of forced convection (Case II), a remarkable great velocities generated by Lorentz force are created, that lead to the significant deformation of the isotherms compared to Case I.

Finally, the last chosen instant (t = 8735 s), shows that the contours become wavy and the isotherms are almost vertical indicating the dominance of conduction mode of heat transfer (in the right side of the sample). A progression of the solidification front from right to left side was observed. A second solidification front was appeared in the left side, indicating that the temperature imposed in this wall is now below the melting temperature of pure tin (505 K). The appearance of this latter reveals the existence of a still active convection counter-clockwise circulation loop (existing of two circulation loops have an opposite direction) completely on the left corresponding to the last liquid of the sample. Both solidification fronts will progress in opposite direction (the second solidification front will progress from left to right side), reducing the liquid zone consequently the reduction of the thermal gradient, in this case the liquid located between these two fronts become hotter than both sides. This mechanism will keep on this way until the meeting of these two fronts at 8770 s (Fig. III.15 (c)), then at later time, a total disappearance of the liquid zone to give a global solid zone at 8990 s. Globally, numerical simulations show a good consistency with the thermal field measured at all stages during this solidification experiment.

Fig. III.16 shows the temporal evolution of the temperatures measured experimentally presented by the dashed lines with different thermocouples (L21, L22, L26, L27, L28, L29 and L29) and the temperatures calculated with the 3D model at the positions corresponding to them presented by the continue lines during the solidification process (without any stirring). The melting temperature T_m is also presented. Similar to previous studies described by Hamzaoui *et al* [75], this study contain three main parts: Firstly, this part is totally liquid characterized by a slow decrease in the temperature of the selected thermocouples, the period of this stage varies from thermocouple to other (it depends on the thermocouple position). For example, L30 and

L29 (yellow and green lines) take about 200 s and 400 s, respectively. Secondly, as explained in Chapter I, in this isothermal part, the temperature of the thermocouples will stabilize at a single temperature called the melting temperature (T_m = 505 K of pure tin), this stabilisation corresponds to the well-known '*phase change plateau*' for pure metals, which characterizes by the existence of both solid and liquid with a release of latent heat. Finally, after the liquid/solid transformation that occurs in the previous part, the temperature of the thermocouples then will keep on to decrease which indicates the appearance of the solid crystals, this part characterizes by a global solid zone ($T < T_m$).

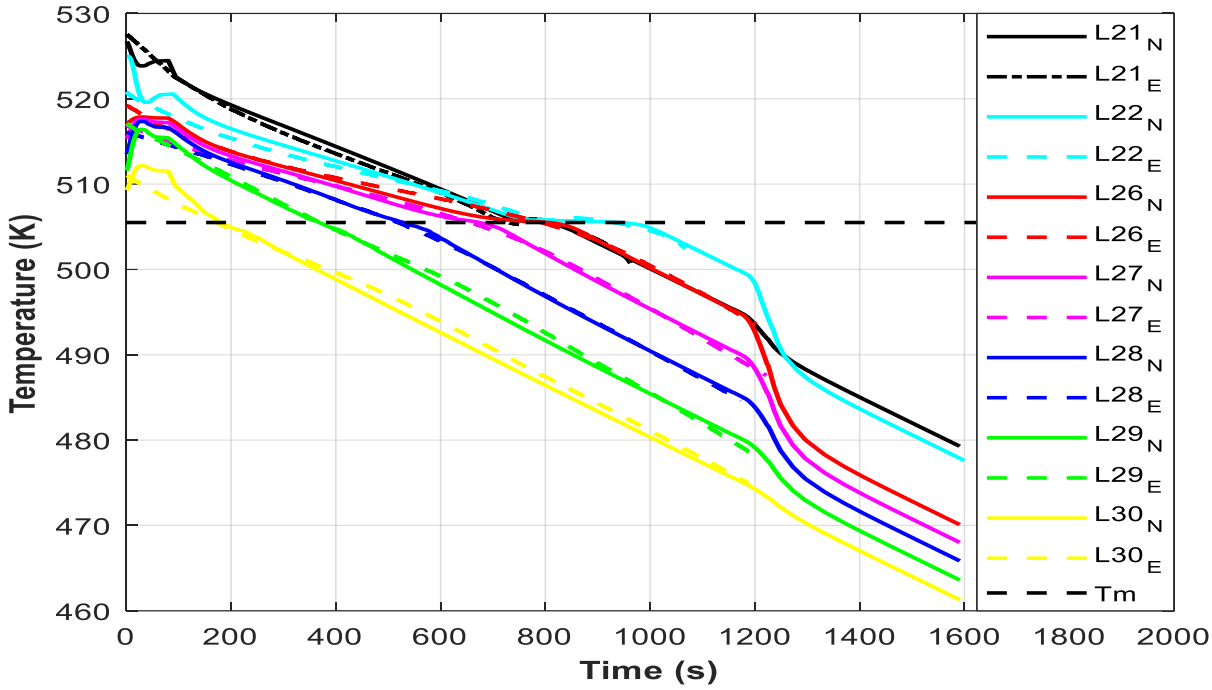

Fig. III.16. Numerical (subscript N) and experimental (subscript E) time profiles of the temperature at some thermocouple positions (see Fig. III.4) during the solidification process (without any stirring). The melting temperature T_m is represented by the dotted line.

At the same time as the solidification front reaches the thermocouple position, this means that the temperature of this latter had reached a level below the melting temperature (see Fig. III.16). For example, the temperature of thermocouple L_{30} (yellow line) is the first one that leaves the phase change plateau, because it is the nearest thermocouple to the cold wall compared to the selected thermocouples. As discussed previously, the solidification front will progress from right to left, i.e., the solidification front will reach L29 resulting the decrease of its temperature bellow T_m (see the green line in Fig. III.16), and so on. In addition, when the temperature of L21 (thermocouple near the hot wall) deceases below T_m that gives an indication of the appearance of a second front in the left side (hot side). Furthermore, a special observation in Fig. III.16 is that the thermocouples L_{26} and L_{21} (the red and the black lines, respectively) leave

the phase-change plateau of pure tin (T_m = 505 K) at the same time. That gives us an indication that when the first solidification front reaches L26 (at t = 8735 s), the left solidification front will appear. Globally, the time profile of the solidification process of pure tin (without stirring) that illustrated in Fig. III.16, showing a good agreement between the numerical and experimental results (case I and Exp).

III.7.4. Deviation between temperature fields

In order validate our 3D model; we need also to measure the temperature deviation between numerical simulation and experimental data during the solidification process under the effect of natural convection (without stirring). These measurements are recorded by the thermocouples (described previously, see Fig III.4) that placed in middle line of the sample (L21, L22, ... L30). The following relations are defined in the vertical middle plane to estimate the difference between the experimental and the numerical solutions:

$$\Delta \max_i \left| Temp\_exp_i - Temp\_num_i \right|_{max} \quad \text{(III.24)}$$

where *Temp_exp* and *Temp_num* are the experimental and the numerical temperatures in the case of pure convection.

We can also define the relative deviation $\Delta_{num/exp}$ between the numerical prediction and the experimental measurements by using the temperatures at the 50 thermocouple positions:

$$\Delta \frac{1}{50} \sum_{i=1}^{50} \left| \frac{Temp\_exp_i - Temp\_num_i}{\Delta T} \right|_{num/exp} \quad \text{(III.25)}$$

Three different selected times (t = 7609 s, t = 7897 s and t = 8735 s) present the spatial evolution and normalized deviation of the temperature field during the solidification process without any external force (natural convection only) are presented in Fig. III.17 (a) and (b), respectively. By using the selected thermocouples, the temperature profiles of numerical simulation (black line) and experimental data (blue line) can estimate the maximum relative deviation using Eq.III.24 and Eq.III.25. An estimation of the normalized deviation of the temperature field in the middle plane at different times for the given Grashof, Gr = 8.67×10^6 and Prandtl, Pr = 0.0015.

Typical maps of the deviation obtained for the same given Grashof and Prandtl numbers are presented in Fig. III.17 (b). It is clear that the zone with high deviation corresponds to the zones where the flow is separated from the wall and recirculated in the centre. This reveals that the

efficiency of this model type is related to its ability to predict heat losses and heat transfer convection at the corners of the cavity.

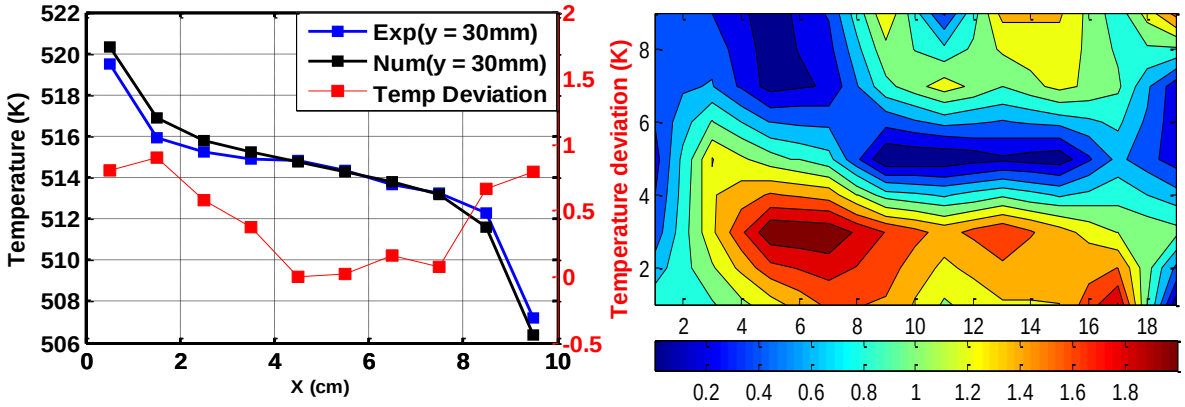

(a) *t = 7609 s* *(b)*

$\Delta_{num/exp} = 4.82\%$, $\Delta_{max} = 2.16$

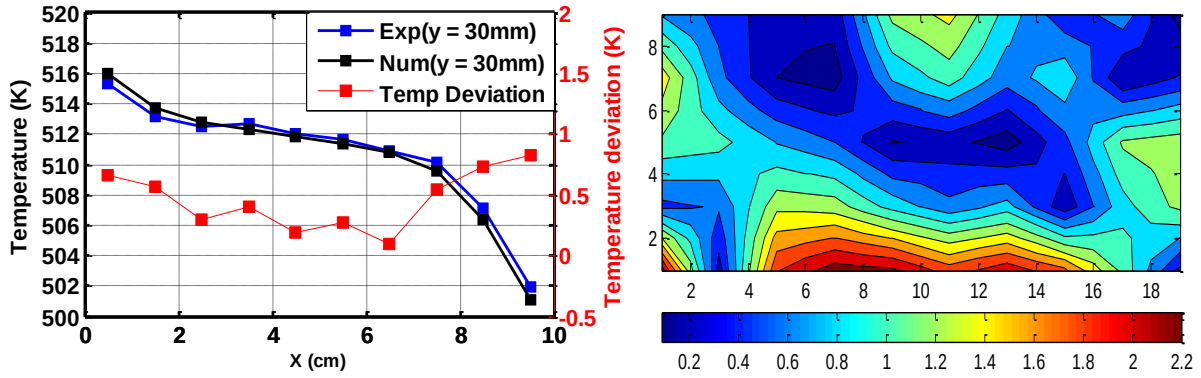

(a) *t = 7897 s* *(b)*

$\Delta_{num/exp} = 4.59\%$, $\Delta_{max} = 2.31$

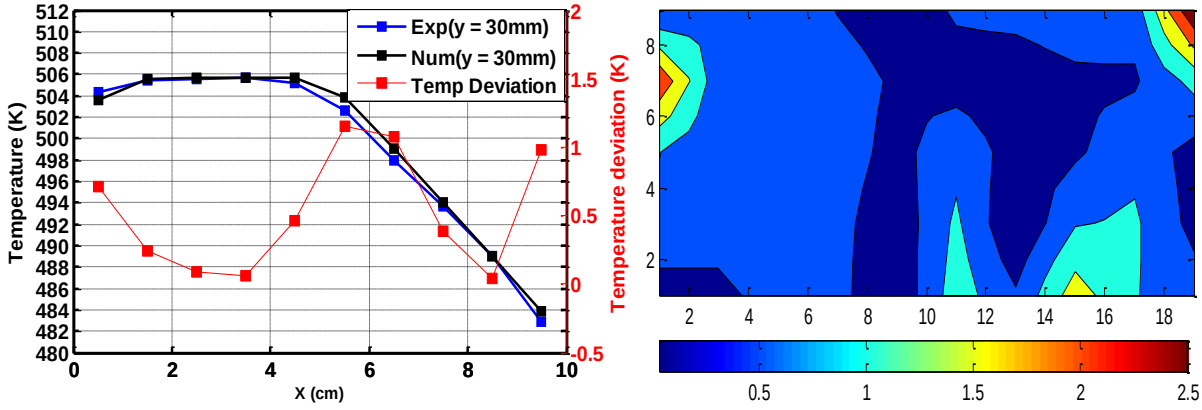

(a) *t = 8735 s* *(b)*

$\Delta_{num/exp} = 3.66\%$, $\Delta_{max} = 2.99$

Fig. III.17. (a) Numerical (black) and experimental (blue) spatial evolution of the temperature field along the line defined by thermocouples L21, L22, ... L30. (b) Corresponding deviation maps.

The maximum deviations Δ_{max} are 2.16, 2.31, 2.99 and the relative deviations are 4.82%, 4.59%, 3.66% at t = 7609 s, t = 7897 s and t = 8735 s, respectively. The comparison between the numerical and experimental results on the longitudinal temperature profile along x_1 at mid-height is illustrated in Fig. III.17 (a) and (b). It is clear that there is a good agreement between 3D numerical profile and the experimental measurement, where the maximum deviation with values below 1.25%. The deviation principally increases at the left and right corners of the sample (thermocouples L21, L22 and L29, L30), these increases are mainly due to the shrinkage that occurs in both sides.

III.7.5. Comparison of the solidification front evolution between experiment and numerical simulations

A comparison studies have devoted in this part for the solidification of pure tin between the numerical simulation results (case I and case II) and the experimental results (Exp) obtained with the AFRODITE set-up under the same initial boundary conditions as have taken in the previous parts. This comparison is mainly performed to examine the effect of both natural and forced convection on the morphology of the solidification front during the phase change process (stage 5).

To illustrate this, four representative time evolution (t= 7840 s, t = 8450 s, t = 8510 s and t = 8680 s) of the solidification front are shown in Fig. III.18. The liquid fraction varies in accordance with Eq. III.2, where the liquid fraction f_l equals unity refers to the liquid zones (red zones). In contrast, the solid zones correspond to f_l equals zero (blue zones in Fig. III.18). this latter corresponds to the total disappearance of any liquid trace in the system.

The first snapshot was taken at t = 7840 s, where the sample is mainly liquid. One can easy notice that the solidification front appears on the right side of the sample, because the temperature imposed in this wall (cold wall) is the first one to decrease below T_m. A particular observation was shown in the case of pure natural convection (case I and Exp in Fig. III.18 (a)), the first solid crystals grow from the right bottom corner of the cavity, due the effect of hydrdunamic motions of natural convection. In another side, a concave solidification front was observed (see case II in Fig. III.18 (a)) caused by the effect of forced convection generated by EM stirring.

Progression of the first solidification front from right to left side was observed in the three cases (case I, Exp and case II) at t = 8450 s then t = 8510 s with maintaining a quite similar morphology of the solidification front in all cases as the previous instant.

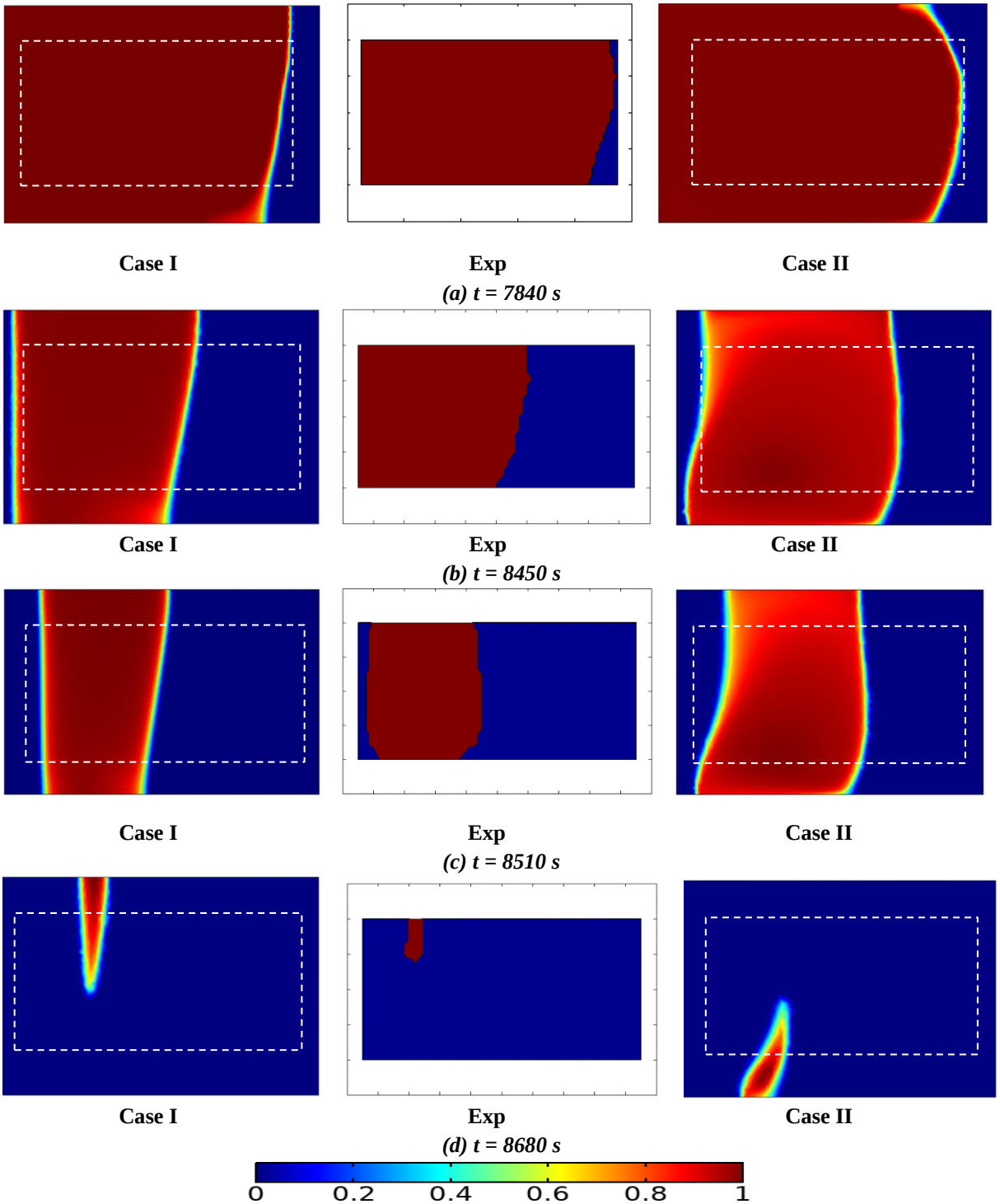

Fig. III.18. Solid-liquid front positions at different times during the solidification process. Simulation results for natural convection (case I), experimental results for pure convection (Exp) and simulation results for forced convection (case II) are shown in the left, middle and the right columns, respectively. The color bar gives the liquid fraction.

A remelting phenomenon was observed when the the solidification front regressed towards the cold wall at about t = 8450 s, due to the latent heat release as discussed previously. Then, the solidification resumes its progress as the latent heat is extracted. The application of EM stirring creates an intense movements in the liquid bath that caused a delay in the progress of the solidification front compared to case I. Moreover, a second solidification front was observed in each case at t = 8510 s (see Fig. III.18 (c)) in the left side (hot region), indicating that the temperature imposed in this wall is now below T_m. At that time, the liquid is located between the right and the left solidification front and representes the hottest region. In other side, observation in the progress of the experimental solidification fronts shows that there are fluctuations at the solid liquid interface. This can be explained by the fact that the experimental boundary conditions are not ideal as those of numerical simulations.

Finally, at t = 8680 s, both fronts then progress, reducing the liquid region and consequently the thermal gradient. One can easily notice that the location of the last liquid zone differs from case to another. Indeed, in both pure natural convection (case I and Exp in Fig. III.18 (d)) the last liquid zone is located in the upper-middle portion of the sample. In contrast, the last liquid zone is located in the left bottom-middle portion of the sample in the case of forced convection (case II in Fig. III.18 (d)), this behaviour is originally due to the higher velocity generated by the electromagnetic force which creates a great movement in the bottom of the sample and consequently prevents the growth of the solid crystals.

Generally, in the case of natural convection (without any stirring), a good agreement between numerical simulation and the experimental results (case I and Exp) was observed during the solidification process in terms of the morphology of the solidification front. Also, the application of the EM stirring shows its effectiveness in the shape of the solidification front.

III.8. Partial conclusion

A 3D solidification model, implemented in COMSOL software, was used to simulate the solidification of the pure material (tin) in a horizontal differentially heated rectangular cavity. The configuration is related to the AFRODITE solidification benchmark experimental setup. The experimental results are also available as temperature data recorded during the solidification phase, allowing comparison between numerical and experimental results. The solidification model has been derived on the basis of an enthalpy formulation based on fixed-grid techniques. It has been found that the enthalpy-porosity method converges quickly and can produce accurate results for the position and morphology of the melt front at different times. Also, good agreements are obtained with the measured thermal and velocity fields during the solidification process. The model used has also shown its effectiveness in predicting the process of tin solidification under forced convection generated by electromagnetic stirring in terms of velocity field, temperature field and morphology of the solidification front.

References chapter III

[1] I. Sari, L. Hachani, A. Kharicha, Y. Fautrelle, B. Pichat, and K. Zaidat, '3D numerical simulation and experimental investigation of pure tin solidification under natural and forced convection', *Int. J. Therm. Sci.*, p. 19, 2021.

[2] W. D. Bennon and F. P. Incropera, 'A continuum model for momentum, heat and species transport in binary solid-liquid phase change systems—I. Model formulation', *Int. J. Heat Mass Transf.*, vol. 30, no. 10, pp. 2161–2170, Oct. 1987.

[3] C. Y. Wang and C. Beckermann, 'A multiphase solute diffusion model for dendritic alloy solidification', *Metall. Mater. Trans. A*, vol. 24, no. 12, pp. 2787–2802, Dec. 1993.

[4] J. Ni and C. Beckermann, 'A volume-averaged two-phase model for transport phenomena during solidification', *Metall. Trans. B*, vol. 22, no. 3, p. 349, Jun. 1991.

[5] C. Y. Wang and C. Beckermann, 'Equiaxed dendritic solidification with convection: Part I. Multiscale/multiphase modeling', *Metall. Mater. Trans. A*, vol. 27, no. 9, pp. 2754–2764, Sep. 1996.

[6] N. Provatas, N. Goldenfeld, and J. Dantzig, 'Efficient Computation of Dendritic Microstructures Using Adaptive Mesh Refinement', *Phys. Rev. Lett.*, vol. 80, no. 15, pp. 3308–3311, Apr. 1998.

[7] M. Ainsworth and J. T. Oden, 'A posteriori error estimation in finite element analysis', *Comput. Methods Appl. Mech. Eng.*, vol. 142, no. 1, pp. 1–88, Mar. 1997.

[8] J. A. Mackenzie and M. L. Robertson, 'A Moving Mesh Method for the Solution of the One-Dimensional Phase-Field Equations', *J. Comput. Phys.*, vol. 181, no. 2, pp. 526–544, Sep. 2002.

[9] F. Duarte, R. Gormaz, and S. Natesan, 'Arbitrary Lagrangian–Eulerian method for Navier–Stokes equations with moving boundaries', *Comput. Methods Appl. Mech. Eng.*, vol. 193, no. 45, pp. 4819–4836, Nov. 2004.

[10] W. J. Boettinger, J. A. Warren, C. Beckermann, and A. Karma, 'Phase-Field Simulation of Solidification', *Annu. Rev. Mater. Res.*, vol. 32, no. 1, pp. 163–194, Aug. 2002.

[11] A. Karma and W.-J. Rappel, 'Phase-field method for computationally efficient modeling of solidification with arbitrary interface kinetics', *Phys. Rev. E*, vol. 53, no. 4, pp. R3017–R3020, Apr. 1996.

[12] C. W. Hirt and B. D. Nichols, 'Volume of fluid (VOF) method for the dynamics of free boundaries', *J. Comput. Phys.*, vol. 39, no. 1, pp. 201–225, Jan. 1981.

[13] M. Reitzle, C. Kieffer-Roth, H. Garcke, and B. Weigand, 'A volume-of-fluid method for three-dimensional hexagonal solidification processes', *J. Comput. Phys.*, vol. 339, pp. 356–369, Jun. 2017.

[14] S. Osher and R. P. Fedkiw, 'Level Set Methods: An Overview and Some Recent Results', *J. Comput. Phys.*, vol. 169, no. 2, pp. 463–502, May 2001.

[15] U. Frisch, D. d'Humieres, B. Hasslacher, P. Lallemand, Y. Pomeau, and J. P. Rivet, 'Lattice gas hydrodynamics in two and three dimensions', Los Alamos National Lab. (LANL), Los Alamos, NM (United States); Observatoire de Nice, 06 (France); Ecole Normale Superieure, 75 - Paris (France), LA-UR-87-2524; CONF-8610281-2, Jan. 1986.

[16] C.-P. K. Wen-Shu Jiaung Jeng-Rong Ho, 'Lattice Boltzmann Method for the Heat Conduction Problem with Phase Change', *Numer. Heat Transf. Part B Fundam.*, vol. 39, no. 2, pp. 167–187, Feb. 2001.

[17] G. de Fabritiis, A. Mancini, D. Mansutti, and S. Succi, 'Mesoscopic Models of Liquid/Solid Phase Transitions', *Int. J. Mod. Phys. C*, vol. 09, no. 08, pp. 1405–1415, Dec. 1998.

[18] E. A. Semma, M. El Ganaoui, and R. Bennacer, 'Lattice Boltzmann method for melting/solidification problems', *Comptes Rendus Mécanique*, vol. 335, no. 5, pp. 295–303, May 2007.

[19] D. Chatterjee and S. Chakraborty, 'An enthalpy-based lattice Boltzmann model for diffusion dominated solid–liquid phase transformation', *Phys. Lett. A*, vol. 341, no. 1, pp. 320–330, Jun. 2005.

[20] J. Miranda Fuentes, K. Johannes, F. Kuznik, M. Cosnier, and J. Virgone, 'Melting with convection and radiation in a participating phase change material', *Appl. Energy*, vol. 109, pp. 454–461, Sep. 2013.

[21] J. Miranda Fuentes, F. Kuznik, K. Johannes, and J. Virgone, 'Development and validation of a new LBM-MRT hybrid model with enthalpy formulation for melting with natural convection', *Phys. Lett. A*, vol. 378, no. 4, pp. 374–381, Jan. 2014.

[22] L. Zhang, H.-F. Shen, Y. Rong, and T.-Y. Huang, 'Numerical simulation on solidification and thermal stress of continuous casting billet in mold based on meshless methods', *Mater. Sci. Eng. A*, vol. 466, no. 1, pp. 71–78, Sep. 2007.

[23] Liu GR ,. Author and Karamanlidis D. ,. Reviewer, 'Mesh Free Methods: Moving Beyond the Finite Element Method', *Appl. Mech. Rev.*, vol. 56, no. 2, pp. B17–B18, Mar. 2003.

[24] H. Thakur, K. M. Singh, and P. K. Sahoo, 'Phase Change Problems Using the MLPG Method', *Numer. Heat Transf. Part Appl.*, vol. 59, no. 6, pp. 438–458, Mar. 2011.

[25] G. Kosec and B. Šarler, 'Simulation of macrosegregation with mesosegregates in binary metallic casts by a meshless method', *Eng. Anal. Bound. Elem.*, vol. 45, pp. 36–44, Aug. 2014.

[26] R. Boussaa, O. Budenkova, L. Hachani, X-D. Wang, B. Saadi, K. Zaidat, H. Ben Hadid, Y. Fautrelle., '2D and 3D Numerical Modeling of Solidification Benchmark of Sn-3Pb (%wt.) Alloy under Natural Convection', in *CFD Modeling and Simulation in Materials Processing*, Inc., 2012, pp. 163–170.

[27] R. Boussaa, L. Hachani, O. Budenkova, V. Botton d, D. Henry, K. Zaidat, H. Ben Hadid, Y. Fautrelle., 'Macrosegregations in Sn-3 wt%Pb alloy solidification: Experimental and 3D

numerical simulation investigations', *Int. J. Heat Mass Transf.*, vol. 100, pp. 680–690, Sep. 2016.

[28] V. R. Voller and C. Prakash, 'A fixed grid numerical modelling methodology for convection-diffusion mushy region phase-change problems', Vol 30, Issue 8, August 1987, Pages 1709-1719.

[29] V. R. Voller, M. Cross, and N. C. Markatos, 'An enthalpy method for convection/diffusion phase change', *Int. J. Numer. Methods Eng.*, vol. 24, no. 1, pp. 271–284, Jan. 1987.

[30] V. R. Voller, N. C. Markatos, and M. Cross, 'Solidification in Convection-Diffusion', in *Numerical Simulation of Fluid Flow and Heat/Mass Transfer Processes*, vol. 18, N. C. Springer Berlin Heidelberg, 1986, pp. 425-432.

[31] A. König-Haagen, E. Franquet, E. Pernot, and D. Brüggemann, 'A comprehensive benchmark of fixed-grid methods for the modeling of melting', *Int. J. Therm. Sci.*, vol. 118, pp. 69–103, Aug. 2017.

[32] W. D. Bennon and F. P. Incropera, 'A continuum model for momentum, heat and species transport in binary solid-liquid phase change systems—II. Application to solidification in a rectangular cavity', *Int. J. Heat Mass Transf.*, vol. 30, no. 10, pp. 2171-2187, Oct. 1987.

[33] A. D. Brent, V. R. Voller, and K. J. Reid, 'Enthalpy-Porosity Technique For Modeling Convection-Diffusion Phase Change: Application To The Melting Of A Pure Metal', *Numer. Heat Transf.*, vol. 13, no. 3, pp. 297–318, Apr. 1988.

[34] C. Beckermann, H.-J. Diepers, I. Steinbach, A. Karma, and X. Tong, 'Modeling Melt Convection in Phase-Field Simulations of Solidification', *J. Comput. Phys.*, vol. 154, no. 2, pp. 468-496, Sep. 1999.

[35] M. M. Rao and W. Shyy, 'Moving Boundary Computation Of The Float-Zone Process', Vol40, Issue7, 1997.

[36] A. König-Haagen, E. Franquet, E. Pernot, and D. Brüggemann, 'A comprehensive benchmark of fixed-grid methods for the modeling of melting', *Int. J. Therm. Sci.*, vol. 118, pp. 69–103, Aug. 2017.

[37] H. Hu and S. A. Argyropoulos, 'Mathematical modelling of solidification and melting: a review', *Model. Simul. Mater. Sci. Eng.*, vol. 4, no. 4, pp. 371-396, Jul. 1996.

[38] M. Lacroix and V. R. Voller, 'Finite Difference Solutions Of Solidification Phase Change Problems: Transformed Versus Fixed Grids', *Numer. Heat Transf. Part B Fundam.*, vol. 17, no. 1, pp. 25–41, Jan. 1990.

[39] C.-J. Ho and R. Viskanta, 'Heat Transfer During Melting From an Isothermal Vertical Wall', *J. Heat Transf.*, vol. 106, no. 1, pp. 12–19, Feb. 1984.

[40] R. Viskanta, 'Heat Transfer During Melting and Solidification of Metals', *J. Heat Transf.*, vol. 110, no. 4b, pp. 1205-1219, Nov. 1988.

[41] Wolff F, Viskanta R, 'Solidification of a pure metal at a vertical wall in the presence of liquid superheat', *Int. J. Heat Mass Transf.*, vol. 31(8), pp. 1735-1744, 1988.

[42] Y. Cao and A. Faghri, 'A Numerical Analysis of Phase-Change Problems Including Natural Convection', *J. Heat Transf.*, vol. 112, no. 3, pp. 812–816, Aug. 1990.

[43] Y. Cao, A. Faghri, and Won Soon Chang, 'A numerical analysis of Stefan problems for generalized multi-dimensional phase-change structures using the enthalpy transforming model', *Int. J. Heat Mass Transf.*, vol. 32, no. 7, pp. 1289-1298, Jul. 1989.

[44] A. Rakotondrandisa, G. Sadaka, and I. Danaila, 'A finite-element toolbox for the simulation of solid–liquid phase-change systems with natural convection', *Comput. Phys. Commun.*, vol. 253, p. 107188, Aug. 2020.

[45] J. Noye and Workshop on Numerical Modelling of Marine Systems, Eds., *Numerical modelling: applications to marine systems*. Amsterdam: North Holland, 1987.

[46] A. Singh, A. Kumar, and A. Kumar, 'Numerical Modelling of Pure Metal Solidification using OpenFOAM', 2019.

[47] B. Yang, F. Bai, Y. Wang, and Z. Wang, 'How mushy zone evolves and affects the thermal behaviours in latent heat storage and recovery: A numerical study', *Int. J. Energy Res.*, vol. 44, no. 6, pp. 4279–4297, May 2020.

[48] F. Samara, D. Groulx, and P. H. Biwole., 'Natural convection driven melting of phase change material comparison of two methods', presented at the In Excerpt from the Proceedings of the COMSOL Conference, 2012.

[49] R. E. Murray and D. Groulx, 'Modeling Convection during Melting of a Phase Change Material', *Proc. COMSOL Conf.*, p. 8, 2011.

[50] E. V. Rozhitsina, S. Gruner, I. Kaban, W. Hoyer, V. E. Sidorov, and P. S. Popel', 'Dynamic viscosities of pure tin and Sn-Ag, Sn-Cu, and Sn-Ag-Cu eutectic melts', *Russ. Metall. Met.*, vol. 2011, no. 2, pp. 118–121, Feb. 2011.

[51] D. J. Hebditch and J. D. Hunt, 'Observations of ingot macrosegregation on model systems', *Metall. Trans.*, vol. 5, no. 7, pp. 1557-1564, Jul. 1974.

[52] M. Bellet, H. Combeau, Y. Fautrelle, D. Gobin, M. Rady, E. Arquis, O. Budenkova, B. Dussoubs, Y. Duterrail, A. Kumar, C.A. Gandin, B. Goyeau, S. Mosbah, M. Zaloznik., 'Call for contributions to a numerical benchmark problem for 2D columnar solidification of binary alloys', *Int. J. Therm. Sci.*, vol. 48, no. 11, pp. 2013-2016, Nov. 2009.

[53] N. Ahmad, H. Combeau, J.-L. Desbiolles, T. Jalanti, G. Lesoult, J. Rappaz, M. Rappaz, and C. Stomp., 'Numerical simulation of macrosegregation: a comparison between finite volume method and finite element method predictions and a confrontation with experiments', *Metall. Mater. Trans. A*, vol. 29, no. 2, pp. 617–630, Feb. 1998.

[54] M. C. Schneider, 'A numerical study of the combined effects of microsegregation, mushy zone permeability and flow, caused by volume contraction and thermosolutal convection, on macrosegregation and eutectic formation in binary alloy solidification', *Int. J. Heat Mass Transf.*, no. 38(18): p. 3455-3473., p. 19, 1995.

[55] G. Quillet, A. Ciobanas, P. Lehmann, and Y. Fautrelle, 'A benchmark solidification experiment on an Sn–10%wtBi alloy', *Int. J. Heat Mass Transf.*, vol. 50, no. 3, pp. 654-666, Feb. 2007.

[56] L. Hachani, K. Zaidat, and Y. Fautrelle, 'Experimental study of the solidification of Sn–10wt.%Pb alloy under different forced convection in benchmark experiment', *Int. J. Heat Mass Transf.*, vol. 85, pp. 438–454, Jun. 2015.

[57] X. D. Wang, P. Petitpas, C. Garnier, J.-P. Paulin, and Y. Fautrelle, 'A quasi two-dimensional benchmark experiment for the solidification of a tin–lead binary alloy', *Comptes Rendus Mécanique*, vol. 335, no. 5-6, pp. 336-341, May 2007.

[58] K. Omdal Tveito, M. M'Hamdi, H. Combeau, M. Založnik, K. Zaidat, X. Wang, B. Saadi, Y. Fautrelle., 'Numerical analysis of the influence of melting and application of electromagnetic stirring prior to solidification on macrosegregation formation during casting of a binary alloy', *TMS Annu. Meet.*, pp. 253-260, Jan. 2012.

[59] L. HACHANI, 'Etude de l'influence de la convection naturelle et forcée sur le processus de la solidification: cas d'un alliage métallique binaire', Phd Materials, mechanics, civil engineering, electrochemistry, Amar Telidji, cotutelle between Grenoble and Laghouat University, 2013.

[60] L. Hachani, K. Zaidat, and Y. Fautrelle, 'Multiscale statistical analysis of the tin-lead alloy solidification process', *Int. J. Therm. Sci.*, vol. 110, pp. 186-205, Dec. 2016.

[61] X. Wang and Y. Fautrelle, 'An investigation of the influence of natural convection on tin solidification using a quasi two-dimensional experimental benchmark', *Int. J. Heat Mass Transf.*, p. 10, 2009.

[62] L. Hachani B. Saadi, X. D. Wang, Ab. Nouri, K. Zaidat, A. Belgacem-Bouzida, L. Ayouni-Derouiche, G. Raimondi, Y. Fautrelle., « Experimental analysis of the solidification of Sn–3 wt.%Pb alloy under natural convection », Int. J. Heat Mass Transf., vol. 55, no 7, p. 1986-1996, mars 2012.

[63] V. Botton, R. Boussaa, R. Debacque, L. Hachani, K. Zaidat, H. Ben Hadid, Y. Fautrelle, D. Henry., 'A 2D½ model for low Prandtl number convection in an enclosure', *Int. J. Therm. Sci.*, vol. 71, pp. 53–60, Sep. 2013, doi: 10.1016/j.ijthermalsci.2013.04.017.

[64] C. Bonacina, G. Comini, A. Fasano, and M. Primicerio, 'Numerical solution of phase-change problems', *Int. J. Heat Mass Transf.*, vol. 16, no. 10, pp. 1825–1832, Oct. 1973.

[65] T. Campanella, C. Charbon, and M. Rappaz, 'Grain refinement induced by electromagnetic stirring: A dendrite fragmentation criterion', *Metall. Mater. Trans. A*, vol. 35, no. 10, pp. 3201–3210, Oct. 2004.

[66] Z. Yang, P.K. Seo, C.G. Kang, 'Grain Size Control of Semisolid A356 Alloy Manufactured by Electromagnetic Stirring', *J Mater Sci Technol*, vol. 21 (2) 2005, pp. 219-225, 2005.

[67] X. Li, Y. Fautrelle, and Z. Ren, 'Influence of thermoelectric effects on the solid–liquid interface shape and cellular morphology in the mushy zone during the directional

solidification of Al–Cu alloys under a magnetic field', *Acta Mater.*, vol. 55, no. 11, pp. 3803-3813, Jun. 2007.

[68] X. Meng, C. Chen, Z. Hong, and J. Wang, 'Effect of rotating magnetic field on the solidification microstructures of Pb-Sn alloys', *Sci. China Ser. E*, vol. 49, no. 3, pp. 274-282, Jun. 2006.

[69] K. Zaïdat, N. Mangelinck-Noël, and R. Moreau, 'Control of melt convection by a travelling magnetic field during the directional solidification of Al–Ni alloys', *Comptes Rendus Mécanique*, vol. 335, no. 5-6, pp. 330-335, May 2007.

[70] Ch. Vivès, 'Solidification of tin in tile presence of electric and magnetic fields', *J. CrystalNGorrtohw-Hth*, vol. 76, pp. 170-184, 1986.

[71] Z. Chen, C. Chen, X. Wen, J. Zhu, and W. Gao, 'Effect of frequency and intensity of rotating magnetic field on the microstructures of Pb-Sn alloys', *Sci. Bull.*, vol. 53, no. 17, pp. 2575-2581, Sep. 2008.

[72] D. Samanta and N. Zabaras, 'Control of macrosegregation during the solidification of alloys using magnetic fields', *Int. J. Heat Mass Transf.*, vol. 49, no. 25–26, pp. 4850-4866, Dec. 2006.

[73] X. Wang, R. Moreau, J. Etay, and Y. Fautrelle, 'A Periodically Reversed Flow Driven by a Modulated Traveling Magnetic Field: Part II. Theoretical Model', *Metall. Mater. Trans. B*, vol. 40, no. 1, pp. 104–113, Feb. 2009.

[74] R. Moreau, 'The fundamentals of MHD related to crystal growth', *Prog. Cryst. Growth Charact. Mater.*, vol. 38, no. 1–4, pp. 161–194, Jan. 1999.

[75] I. Hamzaoui, S. Millet, V. Bottonb, A. Benzaoui, D. Henry, L. Hachani, R. Boussaa, K. Zaidat, Y. Fautrelle., 'A 2D1/2 model for natural convection and solidification in a narrow enclosure', *Int. J. Therm. Sci.*, vol. 140, pp. 167–183, Jun. 2019.

CHAPTER IV

A three-phase columnar model for metallic alloy solidification

IV.1. Introduction

This chapter deals with the segregation appearing during the solidification of binary alloys. Such a type of study, as shown in Chapter I in the state of the art, requires multi-physical studies taking into account strongly coupled phenomena. The numerical models suitable for such a study must include all types of transfer and take into account all related phenomena. A complete micro-segregation model is presented and used to simulate the phase change of a tin-lead alloy (Sn-Pb) within the 'AFRODITE' set-up. The current study simulated this benchmark using a columnar solidification model, as developed previously by the authors [1]. In the experiments of Hachani *et al* [2], both solidification experiments under natural convection (gravity only) and under forced convection (with electromagnetic stirring) were performed. In the current chapter, only the experiment under natural convection case was numerically investigated. Previously, for these benchmark experiments, simulation analysis using several numerical methods was identified [3-6]. The multiphase volume or ensemble averaging technique was proposed based on *Ivantsov* dendrite growth model. The model was implemented within the framework of the CFD software, ANSYS Fluent, Version 14.5; the alloy was Sn-10wt%Pb alloy under natural convection to model the dendritic solidification of columnar structure [6-10]. The idea of a grain envelope was introduced by the extra- and interdendritic melts, whose concentrations are significantly different, and it can be considered as different phases or phase regions. To treat the columnar solidification with dendritic morphology, three phases region are necessarily considered [8, 9]. Finally, numerical results are compared with experimental results, discussions and suggestions for improvement are proposed.

IV.2. Model description

IV.2.1. Phase definition

We propose a 2D microsegregation model able to treat the mass exchanges during the multiple phase transformations occurring during solidification. The growth of each solid is accompanied by the development of its associated zone (or envelope). Indeed, the columnar trunk can grow in a dendritic morphology. Two different zones can be seen during columnar dendritic growth, the zone containing the columnar trunks and the zone containing the tips of the primary dendrites. To simplify the problem, the dendrite trunk is drawn in a fictitious grain envelope (Fig IV.1). Near the primary dendrite tip, the envelope surrounds the primary and secondary dendrite tips, while in a far area from the primary dendrite tip, the envelope surrounds the

secondary dendrite tips. The longitudinal cross-section of the envelope near the tip of the primary dendrite is similar to a paraboloid [8].

In equiaxed or columnar solidification, Wang and Beckermann [10, 11] proposed a general multiphase method to deal with dendritic structure. A grain envelope (dashed line) is identified to separate the extra melt from the inter dendritic melt (see Fig IV.1), similar to the Rappaz and Thevoz model [12, 13]. Since the morphologies of columnar dendrite trunks vary. Indeed, (1) extra melt, (2) inter dendritic melt in the columnar trunk and (3) solid dendrites in the columnar trunk are the three phase regions as shown in Fig IV.1. The 3-phase model comprises two hydrodynamic phases: liquid melt and columnar crystals. They are quantified by their respective volume fractions f_l and f_s, and characterized by different solute concentrations. Also, the volume fraction of each phase region inside the grain envelope is denoted as $(\alpha_d^c,\ \alpha_s^c)$, with $\alpha_d^c + \alpha_s^c = 1$.

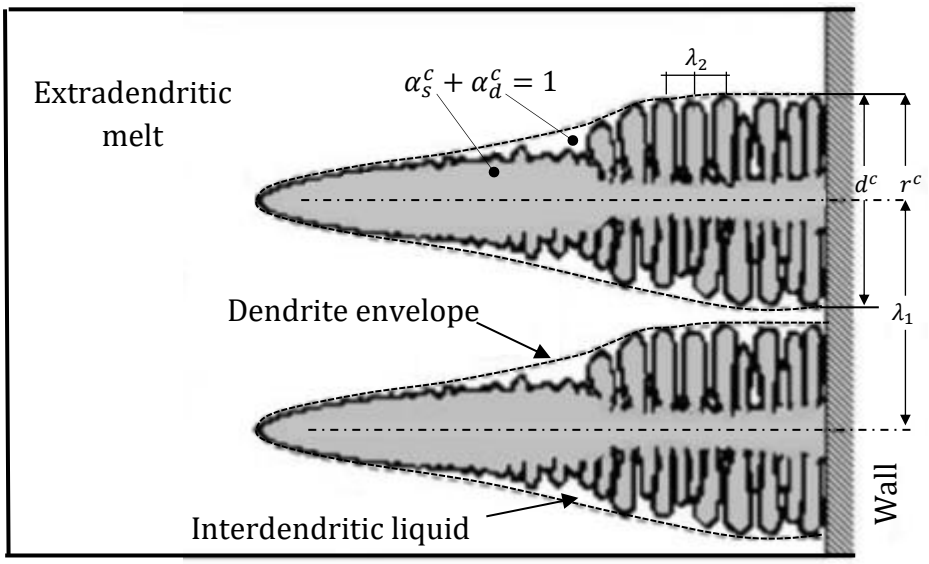

Fig. IV.1. Schematic illustration of the columnar phase showing the dendrite envelope, the volume equivalent for c- phase, and the inter- and extra-dendritic melt, [14].

The simulation of the solidification process that presented in the present chapter requires the resolution of a system including both conservation equations of the quantities needed and taking into account the segregation phenomena induced by the phase change and predicted by the phase diagram. The microscopic model considered here is based on the technique of volume averaging detailed in [15]. This 2D model assumes a columnar dendritic growth. The appearance and growth of equiaxed grains are not considered here, although these growth structures can appear experimentally in solidified ingots. This system includes conservation

equations including the modeling of physical phenomena occurring during solidification, these equations are discussed below.

IV.2.2. Conservation of mass, momentum and energy equations

This part presents the hydrodynamic aspect occurring during solidification. It includes the consideration of the buoyancy forces terms. Indeed, the liquid part is subjected to the thermo-solutal convection induced by the variations of the density of the liquid phase. These density variations can be caused by thermal dilatation of the liquid as a function of its temperature or by changes in its alloying element composition. Since lead has a greater density than tin, variations in lead concentration within the liquid phase cause variations in density. This hydrodynamic modeling also includes a braking term in the solid phase which has assumed zero velocities. This braking term also exists in the mushy zone assumed to be an isotropic porous medium.

Table IV. 1. Model

Mass and momentum

$$\nabla.\vec{u} = 0 \quad \text{(IV.1)}$$

$$\rho_0 \frac{\partial \vec{u}}{\partial t} + \frac{\rho_0}{f_l}(\vec{u}.\nabla)\vec{u} = \nabla(\mu.\nabla\vec{u}) - f_l\vec{\nabla}p + f_l.\vec{F} \quad \text{(IV.2)}$$

Volume forces

$$\vec{F} = \vec{F}_{flottability} + \vec{F}_{braking} \quad \text{(IV.3)}$$

$$\vec{F}_{flottability} = \vec{g}\tilde{\rho} = \vec{g}\rho_0\left(1 - \beta_T(T - T_0) - \beta_c(C_l - C_0)\right) \quad \text{(IV.4)}$$

$$\vec{F}_{braking} = \frac{\mu_l}{K}\vec{u} \quad \text{(IV.5)}$$

Permeability

$$K = \frac{\lambda_2^2}{180}\frac{f_l^3}{(1-f_l)^2} \quad \text{(IV.6)}$$

Heat

$$\rho_0 c_p\left(\frac{\partial T}{\partial t} + \vec{u}\nabla T\right) = \nabla(\lambda\nabla T) + \rho_0\Delta H_f\frac{\partial f_s}{\partial t} \quad \text{(IV.7)}$$

The conservation of mass equation (Eq. IV.1) and the conservation of momentum equation expressed in Eq. IV.2 for the alloy, [3, 16], where the density ρ_0 is considered constant everywhere except in the term *F* which is the sum of the volume forces and is given in Eq. IV.3. Also, $F_{flottability}$ is the buoyancy force term taking into account the density variations, it is

expressed by using the Boussinesq approximation as define in Eq. IV.4, where β_T and β_c are the thermal and solute expansion coefficients. $F_{braking}$ is the Darcy term expressed in Eq. IV.5 used to assimilate the mushy zone to a porous medium where the liquid phase moves in the spaces between the solid dendrites and *K* is the permeability of the porous medium. This Darcy term is for the case of solidification with a mushy zone, it has physical considerations. The expression of *K* (Eq. IV.6) takes into account the secondary inter-dendritic spacing λ_2 and is given by the Carman-Kozeny relation, [17].

The modelling of convective-diffusive heat transfers occurring within the domain, as well as the latent heat release during phase change is done by the energy conservation equation (Eq. IV.7). In this model, an enthalpy approach is used. This one allows the resolution of a single equation describing the variation of the temperature variable *T* on the whole domain including the two liquid and solid phases.

IV.3. Kinetics of crystal growth

As mentioned in Chapter I, the growth kinetics of a dendrite is strongly dependent on the phenomena that occur near its tip. Indeed, transport phenomena play a role at the solid/liquid interface, heat transfer due to the rejection of the latent heat during the phase change. Also, mass transfer due to the distribution of the solute between liquid and solid phases. Fig IV.2 shows a schematic of the dendrite composition ahead of the tip dendrite along its z axis. Note that the composition at the tip is C_l^* and decline to some value C_1 at distance δc (is the diffusion distance of the solute) ahead of the tip. The change in the melting point due to the curvature effect ΔT_c often called curvature or Gibbs-Thomson undercooling. The resolution of these phenomena is based on *Ivantsov* function which can treat those phenomena that occur ahead this paraboloid shape.

IV.3.1. Ivantsov solution

In order to treat those phenomena that occur at the tip dendrite that has a paraboloid of evolution shape (see Fig IV.2), extension to the *Ivantsov* dendrite growth model was proposed and presented by Kurz [18], which is allowed for increase solute levels in the field ahead the tip dendrite. This choice (*Ivantsov* solution) is based firstly on the shape of the solid liquid interface (paraboloid of evolution shape) and he was the first to develop a mathematical analysis for this

shape, the supersaturation (Ω) and the *Ivantsov* function ($I_v(Pe)$) are defined in Eqs. IV.8 and IV.9, respectively:

$$\Omega = I_v(Pe) \quad \Omega = \frac{C_l^* - C_0}{C_l^*(1-K)} \tag{IV.8}$$

$$I_v(Pe) = Pe \exp(Pe) \, . \, E_1(Pe) \tag{IV.9}$$

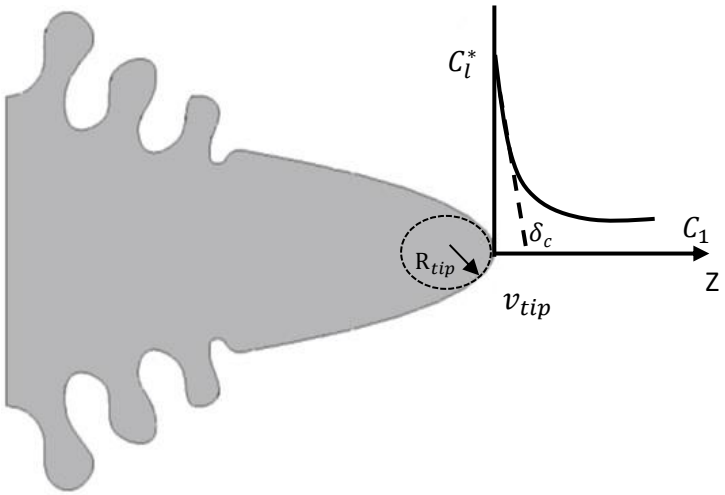

Fig. IV.2. Dendrite tip having a shape of a paraboloid of evolution, [19]

An approximation was supposed by Kurz [18] in order to calculate Peclet number by inversing *Ivantsov* solution (Eq. I.9) is defined as follow:

$$Pe_1 = -\frac{\Omega}{\ln(\Omega)} \tag{IV.10}$$

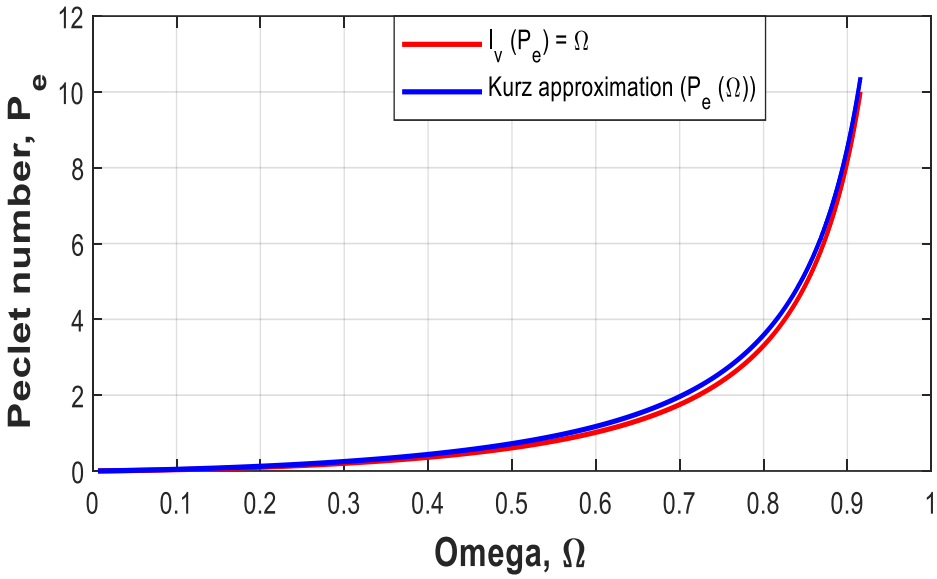

Fig. IV.3. Peclet vs the supersaturation (Ω) corresponding to the *Ivantsov* function (red line) and Kurz approximation (blue line).

Fig IV.3 illustrates the variation of Peclet number as a function of the supersaturation that given by both *Ivantsov* function and Kurz approximation which vary in accordance with Eq. IV.9 and Eq. IV.8, respectively. One can easily notice that for each value of Ω (supersaturation) has two different values of Peclet number, one from *Ivantsov* function and the other one from Kurz approximation.

In order to check the accuracy of Kurz approximation, we need to know how much the error is long, to achieve that we have defined the following equation (Eq.IV.11) that can calculate the ratio of the two Peclet which have obtained from Eqs. IV.9 and IV.10:

$$Error = \frac{\mathrm{Pe}}{\mathrm{Pe}_1} \tag{IV.11}$$

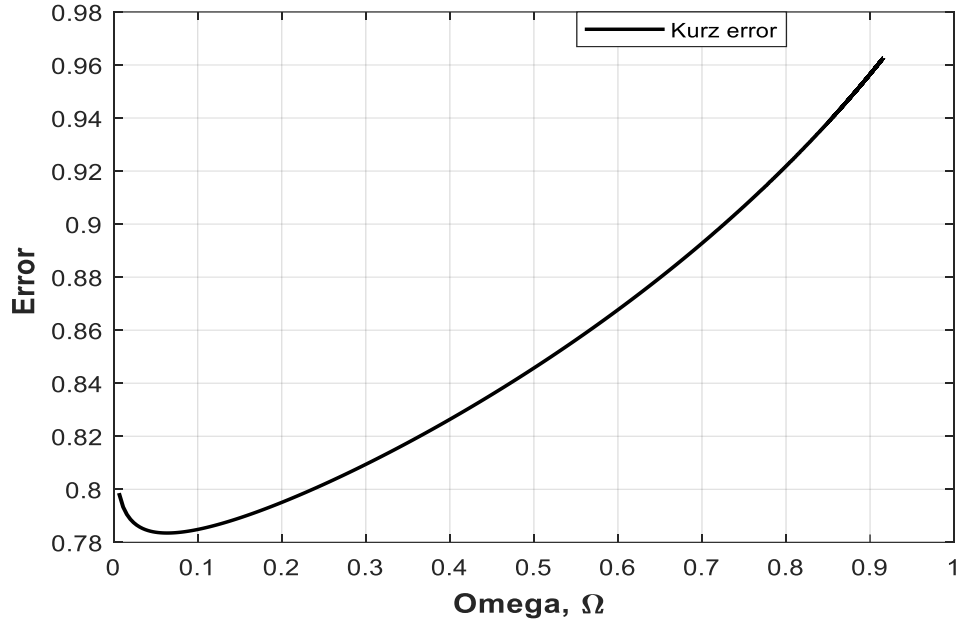

Fig. IV.4. Supersaturation vs the error equation for various (Ω).

Fig IV.4 shows the variation of supersaturation (Ω) that calculated by *Ivantsov* function vs the error equation (Eq. IV.11) The error is big at the beginning (~0.8) for small supersaturation values and then it decreases as the supersaturation increases. Thereby, the Kurz approximation lacks of accuracy for small omega value.

In order to get more accuracy approximation, we have proposed other solution (to minimize this error) as follow:

$$\mathrm{I_V}^{-1}(\Omega) = -\frac{\Omega}{\mathrm{Ln}(\Omega)}\,\mathrm{F}(\Omega) \tag{IV.12}$$

where $\mathrm{I_V}^{-1}(\Omega)$ is the inverse *Ivantsov* solution (new proposed approximation) and $\mathrm{F}(\Omega)$ is a fitting approximation function to the error equation as presented in Fig IV.5.

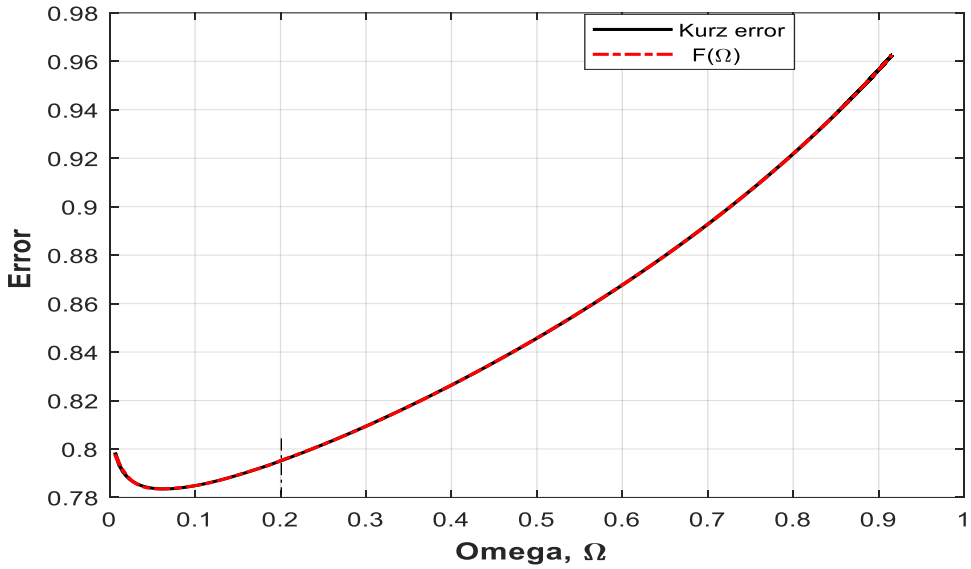

Fig. IV.5. Error equation (black line) and the fitting function (**F**(Ω)) (dashed red line) for various Ω.

We can see in Fig IV.5. that the function F(Ω) which varies in accordance with Eq. IV.13 and Eq. IV.14 gives a good fitting with the error equation. Indeed, due to the complex curve of the error equation, we have separated the function F(Ω) into two parts (as separated by black dashed line in Fig IV.5): the first one is for $\Omega < 0.2$ presented in Eq. IV.13 and the second one for $\Omega > 0.2$ defined in Eq. IV.14.

$$F(\Omega) = p_1\,\Omega^6 + p_2\,\Omega^5 + p_3\,\Omega^4 + p_4\Omega^3 + p_5\,\Omega^2 + p_6\,\Omega + p_7 \quad \text{(IV.13)}$$

$$F(\Omega) = q_1\,\Omega^4 + q_2\,\Omega^3 + q_3\,\Omega^2 + q_4\,\Omega + q_5 \quad \text{(IV.14)}$$

where p_1-p_7 and q_1-q_5 are constants presented in Table IV.2.

Table IV. 2. The corresponding constants of the fitting function **F**(Ω).

F(Ω) (Eq.IV.13)						
p_1	p_2	p_3	p_4	p_5	p_6	p_7
11460	-8248.5	2375.8	-351.2	28.753	-1.2251	0.80449

F(Ω) (Eq.IV.14)				
q_1	q_2	q_3	q_4	q_5
0.19968	-0.34927	0.34839	0.020202	0.77974

Fig IV.6 illustrates the Kurz approximation which varies in accordance with Eq. IV.10 presented by blue line and our new approximation that varies in accordance with Eq. IV.12 presented by black dashed line are compared to the original *Ivantsov* solution that presented by

red line. One can easily notice that our new approximation is in good agreement with *Ivantsov* profile (The red and the black dashed lines are congruent). However, Kurz approximation is valuable only for small value of the supersaturation.

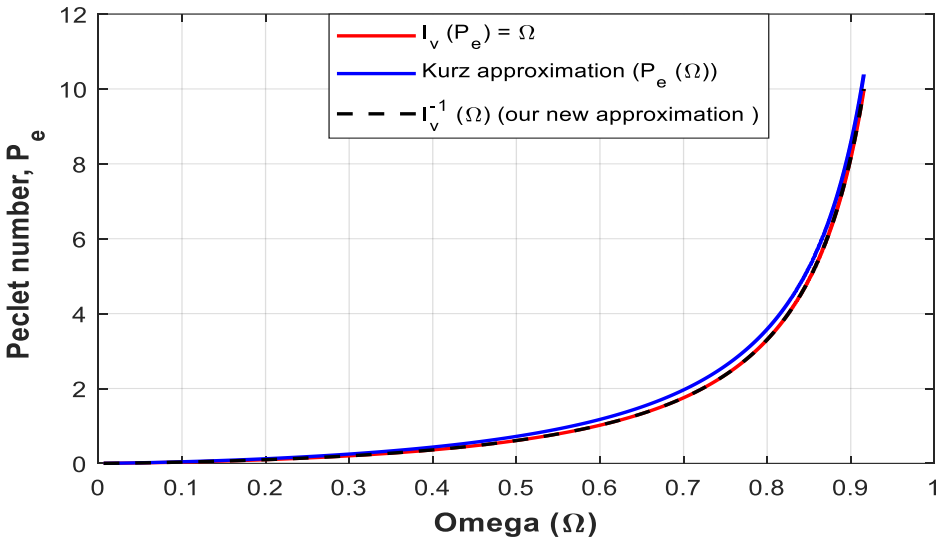

Fig. IV.6. The supersaturation Ω vs Peclet number given by: *Ivantsov* function (Eq. IV.9) presented by red, Kurz approximation (Eq. IV.10) presented by blue and our new approximation presented by black dashed line.

It is necessary to mention that the previous new approximation gives more accuracy compared to Kurz approximation. Therefore, the next section will be based on this approximation in order to calculate the Peclet number for a given supersaturation Ω.

IV.3.2. Microscopic dendritic growth

IV.3.2.1. Solid fraction and liquid concentration

In order to calculate the solid fraction of Sn-Pb alloy during the solidification process through the phase diagram that presented in Appendix IV.1, we assumed a volume contained of only liquid concentration C_0 (without any solid, $f_s = 0$) as presented in Fig IV.7 (a) taken as an initial condition. Then, the solidification starts consequently the liquid phase decrease simultaneously (see Fig IV.7 (b)), in this case we can estimate the solid fraction from $f_s = 0$ when the system is totally liquid (see Fig IV.7 (a)) until the disappearance of any liquid trace in the system $f_s = 1$. *Scheil and Gulliver* proposed a model giving a simplified account of the solute release into the liquid. Indeed, they have assumed zero diffusion in the solid, but infinite diffusion in the liquid (no concentration gradient in the liquid). In this case, the solid fraction can be written as:

$$f_S = \frac{df_S}{1-f_S} \qquad \text{(IV.15)}$$

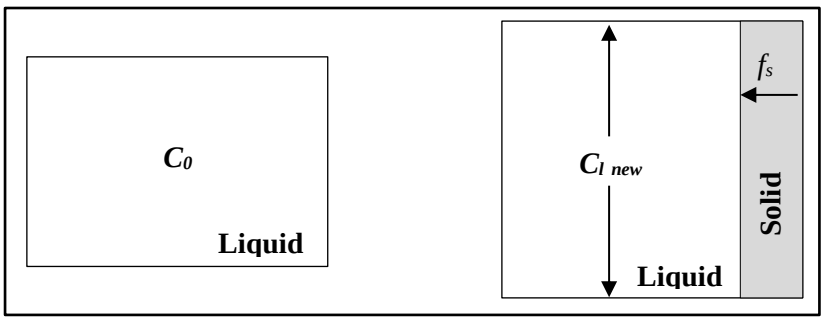

Fig. IV.7. Solidification of enclose volume, (a) initial state contains only liquid with liquid concentration C_0, (b) both liquid and solid exist in the system.

As the solidification progress, the solid regions become larger gradually. In contrast, the liquid concentration increases during this process. In order to estimate this liquid concentration evolution (namely $C_L\ new$) we expressed the following equation:

$$dC_l\ new = f_s\ (C_l\ new - C_s) \quad \text{(IV.16)}$$

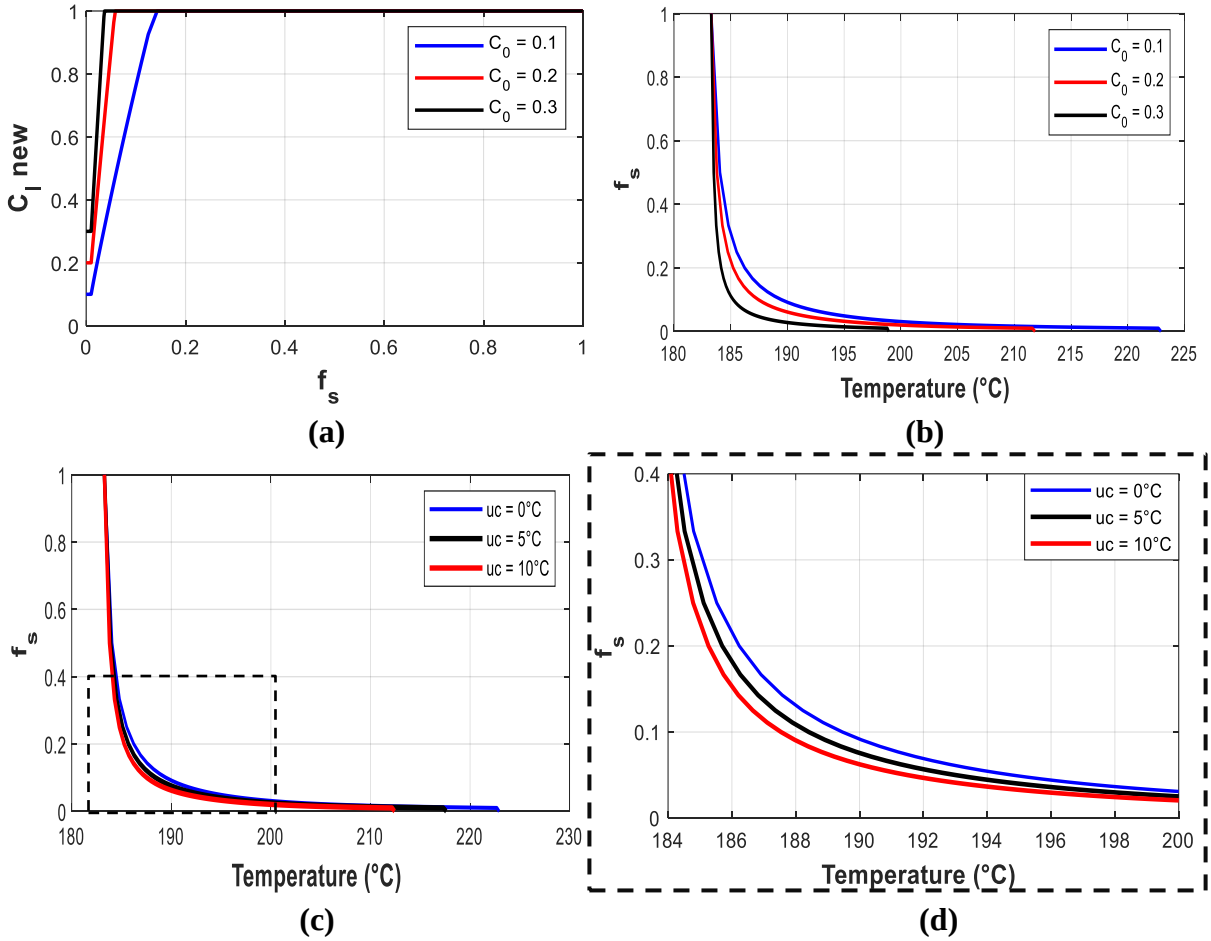

Fig. IV.8. (a) The variation of solid fraction (f_s) vs new liquid concentration ($C_l\,new$) for various initial concentrations C_0. (b) The evolution of f_s vs temperature for different initial concentration, (c) f_s vs temperature with different initial undercooling (uc) with C_0 = 0.1 and (d) zoomed-in view of the fraction with different tip undercooling as presented by dashed rectangle in (c).

Let us apply that to our studied alloy (Sn-Pb), where C_s is the solid concentration of Sn-Pb alloy taken from the phase diagram (see Appendix IV.1) for different initial Pb concentration C_0 = 0.1, C_0 = 0.2 and C_0 = 0.3 as presented in Fig IV.8 (a and b) and also for different initial undercooling *uc* = 0°C, *uc* = 5°C and *uc* = 10°C with C_0 = 0.1 as illustrated in Fig IV.8 (c).

Fig IV.8 shows the evolution of solid fraction versus: (a) liquid concentration (C_l *new*) for three different initial Pb concentrations 'C_0' (C_0 = 0.1, 0.2 and 0.3 presented by blue, red and black, respectively), (b) temperature with various C_0 and (c) temperature with different initial undercooling (*uc*). Indeed, the solid fraction and the new liquid concentration vary in accordance with Eq. IV.15 and IV.16, respectively. In addition, the liquidus temperatures of C_0 = 0.1, 0.2 and 0.3 are 222.9168 °C, 211.8185 °C and 198.9208 °C, respectively. The new liquidus concentration starts by taking the value of the initial concentration C_0 then it will increase toward infinity reducing the liquid region (see Fig IV.8. (a)) and it equals unity for weak f_s.

One can easily notice that in both Fig IV.8 (b) and (c), the smooth curve of the solid fraction shows that there is a slow increase of f_s in the mushy zone (slow advanced solidification), then a sudden fast increase of this latter to reach unity (f_s = 1) at the level of solidus temperature T_S = 183°C). This behavior is interesting to explain that this rapid solidification at the end of solidification (closed the solidus temperature) favors the appearance of the equiaxed structure. Whereas, the liquidus temperatures are 222.9168°C, 217.6066°C and 212.4247°C correspond to the cases: without undercooling (*uc* = 0°C), with 5°C and 10°C undercooling, respectively.

Also, in Fig IV.8 (b) there is a fast solidification of the Sn-30wt%Pb alloy (the black profile) in a small temperature range about $\Delta T = 15.92$°C (mushy zone). Whereas, the blue profile (C_0 = 0.1) reaches f_s =1 for larger temperature range (about $\Delta T = 39.91$°C) compared to C_0 = 0.2 and C_0 = 0.3, where the temperature range of Sn-20wt%Pb alloy is about $\Delta T = 28.81$°C.

IV.3.2.2. Predicting of dendrite tip velocity and radius from supersaturation

As discussed previously, the solidification front is in dendrite morphology at the liquid/solid interface. The diffusion in the liquid in front of each dendrite tip leads to the fact that solidification starts slightly below the liquidus temperature. With the primary stalk advancing during the dendritic growth first solidification begins. In order to explain the method as clearly as possible, a very simple technique is used. The purpose of this latter is to predict the evolution of radius and the velocity of the dendrite tip during the solidification process.

The proposed solution for the solute-diffusion limited growth of a dendrite tip is that suggested by Kurz [18] based on *Ivantsov* solution as described previously. Indeed, A. Kharicha *et al* [20] have analyzed and measured the evolution of the tip radius (the radius of curvature of the dendrite, R_{tip}) during the solidification with accounting the diffusion at the tip of the dendrite.

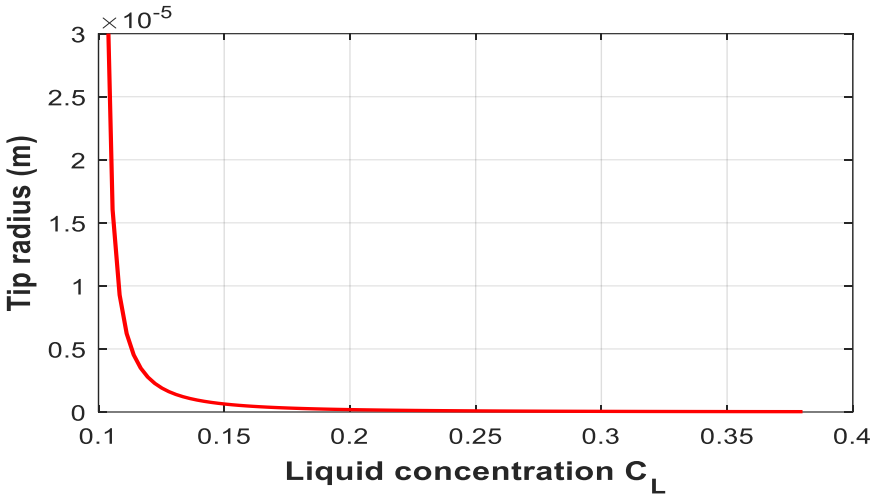

Fig. IV.9. The evolution of the tip dendrite radius during the solidification of Sn-10wt%Pb alloy vs liquidus concentration.

The same analyses were used in this study, for a given: supersaturation Ω calculated by Eq. IV.8 and its corresponding Peclet number obtained by using our new proposed approximation Eq. IV.12, it is possible to calculate the tip radius (Eq. IV.17) and consequently its velocity (v_{tip}) as define in Eq. IV.18.

$$R_{tip} = \frac{\Gamma}{2\,Pe\,m_l\,\sigma\,(C_l - C_s)} \qquad \text{(IV.17)}$$

$$v_{tip} = \frac{2\,Pe\,D_l}{R_{tip}} \qquad \text{(IV.18)}$$

where the parameters: $k = C_s^*/C_l^*$ is the partition coefficient, Γ: is Gibbs-Thomson coefficient, m_l is the liquidus slope, σ is the stability constant $(1/4\pi^2)$, $Pe = R_{tip}\,v_{tip}/2D_l$ is the Peclet number and D_l is the liquid diffusion are described in Chapter I.

Fig IV.9 presents the evolution of the tip dendrite radius (R_{tip}) as a function of liquidus concentration which varies in accordance with Eq. IV.17. Obviously, a smooth decrease of the tip radius during the solidification process. Indeed, at the beginning, we have taken a small initial undercooling corresponds to 222,8°C of liquidus temperature (uc = 0.1°C), at this temperature the tip radius characterized by its maximum value ($R_{tip} = 29{,}8\ \mu m$). Then, a fast decrease of the tip radius about 98,75% in a temperature range of $\Delta T = 7.8$°C (i.e. $R_{tip} =$

0.37 μm at T = 215°C). At the final stage of the solidification (at the eutectic level, $C_L = 0.38$), the tip radius become smaller ($R_{tip} = 0.0281\ \mu m$).

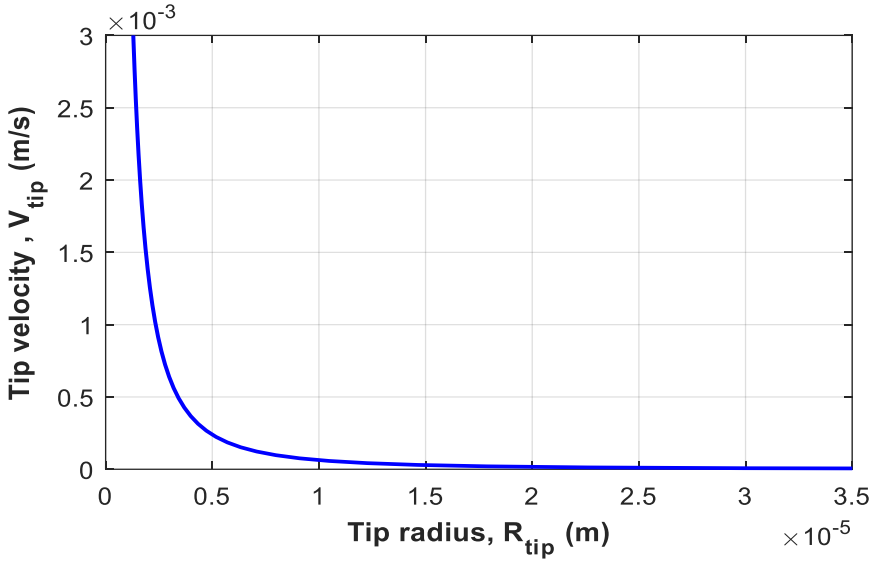

Fig. IV.10. The dendrite tip velocity ($\boldsymbol{V_{tip}}$) versus dendrite tip radius ($\boldsymbol{R_{tip}}$) during solidification with initial concentration C_0 = 0.1.

Following the previous part that shown the possibility to predict the evolution of the tip radius; it is interesting to estimate the velocity of the tip dendrite which varies in accordance with Eq. IV.18. Indeed, there is a direct relation between the velocity and the radius of the tip. As shown in Fig IV.10, V_{tip} began to increase as R_{tip} decreases. However, at the beginning, the R_{tip} starts with its maximum value ($R_{tip} = 35\mu m$) with a minimum velocity ($V_{tip} = 5.71\ \mu m/s$). Then, the R_{tip} is smaller corresponding the higher V_{tip} as can be seen in Fig IV.10.

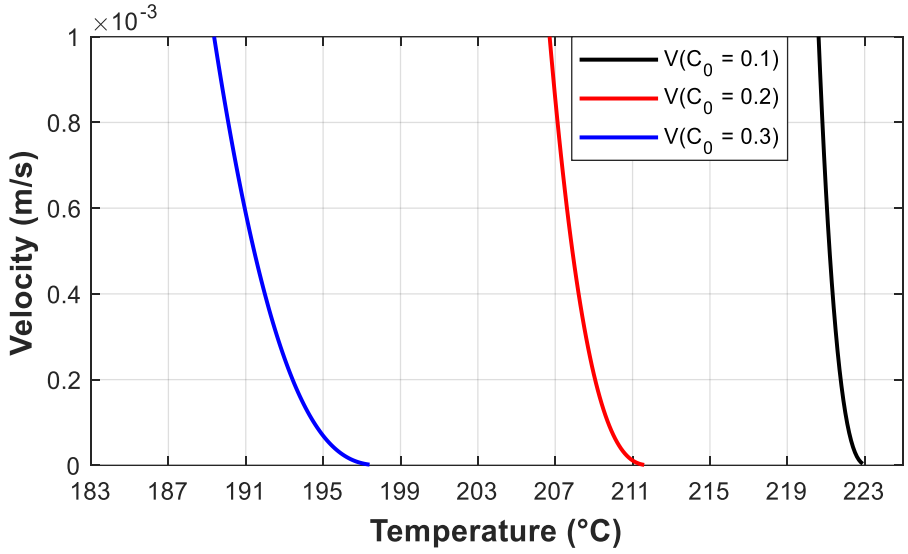

Fig. IV.11. The evolution of velocity tip dendrite vs temperature during solidification with different initial concentration C_0 = 0.1, 0.2 and 0.3 presented by black, red and blue respectively.

In the same way, consider Sn-Pb alloy with three different initial concentrations are C_0 = 0.1, 0.2 and 0.3 presented in Fig IV.11 by black, red and blue, respectively. The liquidus temperature for C_0 = 0.1, 0.2 and 0.3 are 222.9168 °C, 211.8185 °C and 198.9208 °C respectively. One can easily notice that in the three alloys, their tip velocities reach 1 mm/s for different undercooling, however, for C_0 = 0.1 (the black line), its undercooling is about $uc = 2.4°C$ to reach 1 mm/s. Then, as the initial concentration increases toward the eutectic concentration, the undercooling increases as shown in Fig IV.11, where $uc = 4.8°C$ and $uc = 8°C$ correspond to C_0 = 0.2 C_0 = 0.3. That gives us an indication that the initial concentration and the initial undercooling of the alloy are parameters which can predict the radius, the velocity and consequently the cooling rate.

IV.3.2.3. Growth of secondary arm

The specific area of the solid/liquid interface is an important integral measure for the morphological evolution during the solidification. M. Wu et al [21] and M. Založnik [22], have simplified the side branches to a cylinder (see Fig IV.12 and 13) and they have started with cylinders which are small in radius then they will grow with time in accordance with Eq. IV.28.

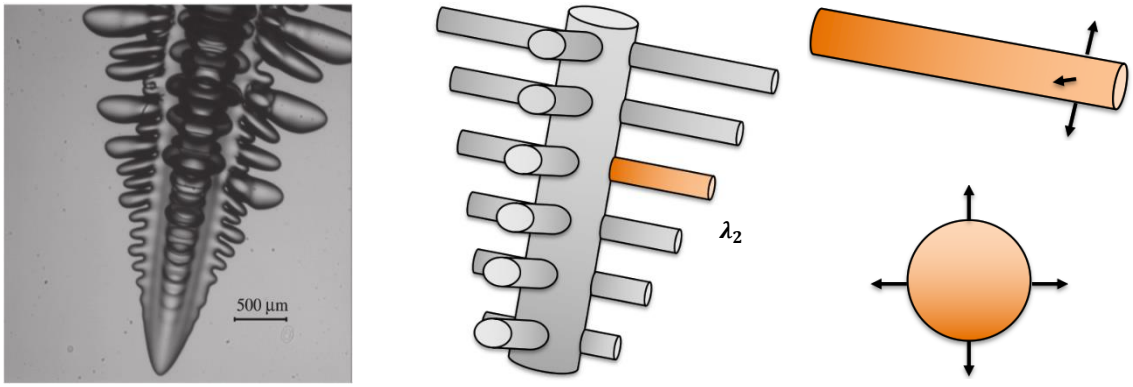

Fig. IV. 12. Schematic representation of the dendrite sidebranches which are simplified as cylinders, [22].

We consider the growth of the side branches (see Fig IV.13 (a)) as a cylinder growth as it is presented in Fig IV.13 (b) and in Fig IV.12. However, a long circular cylinder in which the diffusion is everywhere radial. The growth of the cylindrical arm is schematically shown in Fig IV.13 (b) where the growing arm is assumed to be confined in a cylindrical volume enveloped with a final radius R_f.

Fig IV.13 presents the growth of a secondary arm which characterized by its initial radius $r_c = R_{tip}$, the concentration at the solid/liquid interface of the arm noted by 'C_l^*' and expressed by

$C_l^* = C_l - \frac{\Gamma}{r}$, '$C_{0\,avr}$' is the liquid average concentration which varies in accordance with Eq. IV.27, the concentration at the cylindrical enveloped volume (at R_f) noted by 'C_1', 'v_r' is the growth rate of the arm and 'δc' is the diffusion distance it can be written as: $\delta c = {D_l}/{V}$.

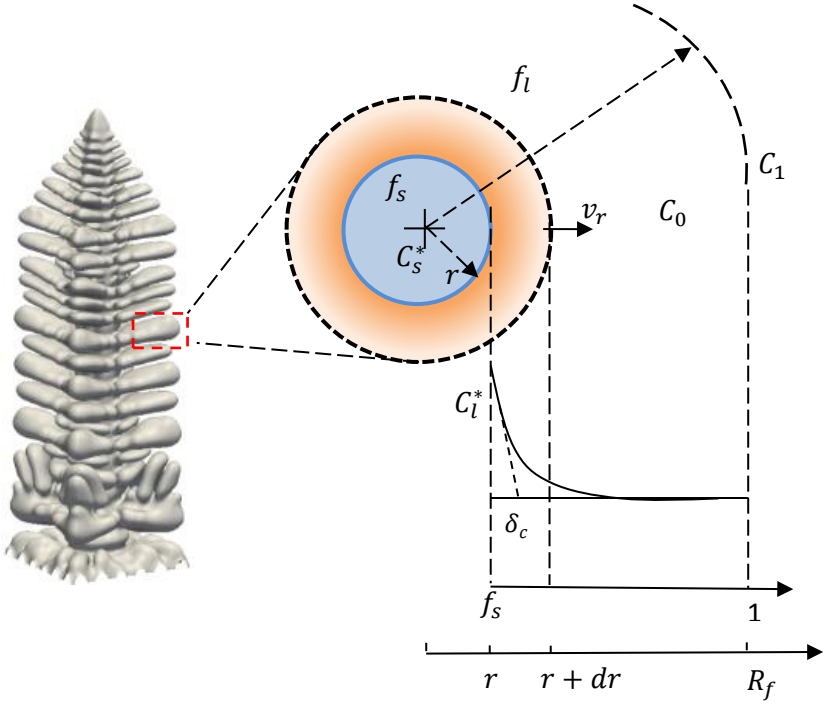

(a) **(b)**

Fig. IV.13. Growth of a cylindrical arm in a cylindrical enveloped volume with a radius R_f, [21].

The cylindrical coordinate of the diffusion equation has presented also by Kurz [18] as follow:

$$\frac{\partial C}{\partial t} = D\left(\frac{\partial^2 C}{\partial r^2} + \frac{1}{r}\frac{\partial C}{\partial r}\right) \qquad \text{(IV.19)}$$

where the concentration '*C*' is then a function of radius and time only.

We have assumed the unsteady state condition, the concentration field remains the same and the time derivative is canceled ($\frac{\partial C}{\partial t} = 0$). This is normally acceptable because once the tip has grown, the solidification after that is much slower than *Ivantsov* solution for the dendrite tip. J. Crank [23] has presented the solution of this equation which takes the form:

$$C = A\,ln(r) + \mathrm{B} \qquad \text{(IV.20)}$$

where A and B are constants to be determined from the boundary conditions:

$$\begin{cases} C = C_1 \; at \; r = R_f \\ C = C_l \; at \; r = r_c \end{cases}$$

Eq. IV.20 gives an infinite concentration at $r = \infty$. So, the boundary condition must be limited at some maximum arm (enveloped volume) noted R_f, this latter is constant and it is defined as a function of the liquid diffusion (D_l) and the initial velocity tip ($v_{tip(0)}$ at t = 0 s) as expressed in the following equation:

$$R_f = 2\frac{D_l}{v_{tip(0)}} \tag{IV.21}$$

After using the boundary conditions, the solution becomes:

$$C(r) = \frac{C_1\, ln\left(\frac{r}{r_c}\right) + C_l^*\, ln\left(\frac{R_f}{r}\right)}{ln\left(\frac{R_f}{r_c}\right)} \tag{IV.22}$$

The general form of the previous equation (Eq. IV.22) gives the possibility to estimate the concentration during the growth. Indeed, it is necessary to calculate also the average concentration 'C_{0avr}' (the liquid average concentration) as a function of 'C_1' (the concentration at 'R_f').

Mathematically, to get an average from a complex curve we have to apply the integral of the previous equation (Eq. IV.22) as follow:

$$C_{o\ avr} = \frac{1}{\pi\left(R_f^2 - r_c^2\right)} \int_{r_c}^{R_f} C(r).\, 2\pi r dr \tag{IV.23}$$

By substitution (Eq. IV.22) in (Eq. IV.23), we obtain:

$$C_{o\ avr} = \frac{1}{\left(R_f^2 - r_c^2\right) ln\left(\frac{R_f}{r_c}\right)} \begin{bmatrix} C_1 \left(R_f^2\, ln\left(R_f\right) - r_c^2\, ln(r_c) - \left(\frac{1}{2} + ln(r_c)\right)\left(R_f^2 - r_c^2\right)\right) + \\ C_l^* \left(\left(\frac{1}{2} + ln\left(R_f\right)\right)\left(R_f^2 - r_c^2\right) - R_f^2\, ln\left(R_f\right) + r_c^2 ln(r_c)\right) \end{bmatrix} \tag{IV.24}$$

As a solid/liquid interface advances with growth rate 'v_{tip}', the liquid concentration 'C_l^*', and the solid concentration 'C_s^*', the quantity of the solute rejected per unity time will be $V(c_l^* - c_s^*)$, this must be balanced by the creation of a concentration gradient in the liquid, thus [21],

$$v_{tip}(c_l^* - c_s^*) = \frac{D_l}{r_c\, ln\left(\frac{R_f}{r_c}\right)}(c^* - c_1) \tag{IV.25}$$

where $v_{tip} = \frac{dr_c}{dt}$ and $c^* = c_l^* - \frac{\Gamma}{m_l r_c}$

Knowing that the conservation of the solute at equilibrium and at the solid-liquid interface is expressed in Eq. IV.27, we can summarize the main equations that can predict the growth of

the arm (side branches) by: Eq. IV.26-28 that give the evolution of: the concentration 'C_1' at 'R_f' (obtained from Eq. IV.24), the liquid average concentration (C_{0avr}) and the arm radius 'r_c', respectively.

$$C_1 = \frac{\left(R_f^2 - r_c^2\right)\ln\left(\frac{R_f}{r_c}\right)C_{o\ avr} - C_l^*\left(\left(\frac{1}{2} + \ln(R_f)\right)\left(R_f^2 - r_c^2\right) - R_f^2\ln(R_f) + r_c^2\ln(r_c)\right)}{\left(R_f^2\ln(R_f) - r_c^2\ln(r_c) - \left(\frac{1}{2} + \ln(r_c)\right)\left(R_f^2 - r_c^2\right)\right)} \quad \text{(IV.26)}$$

$$\frac{\partial(f_l\, C_{0\ avr})}{\partial t} = -\frac{\partial(f_s)}{\partial t}(C_S^* - C_l^*) \quad \text{(IV.27)}$$

$$\frac{dr_c^2}{dt} = 2\frac{D_l}{ln\left(\frac{R_f}{r_c}\right)}\frac{c_l^* - c_1 - \frac{\Gamma}{m_l r_c}}{c_l^* - c_s^*} \quad \text{(IV.28)}$$

Also, the solid fraction 'f_s' of the arm growth is the ratio between the growing arm over the total envelope volume (its radius R_f), defined by:

$$f_s = \frac{V_r}{V} = \left(\frac{\pi r_c^2 L}{\pi R_f^2 L}\right) = \frac{r_c^2}{R_f^2}, \text{ with } f_l = 1 - f_s \quad \text{(IV.29)}$$

In these iterative equations system, we have taken the following initial condition:

$$\begin{cases} C_{o\ avr} = C_o\ of\ the\ alloy \\ r_c = R_{tip} \end{cases}$$

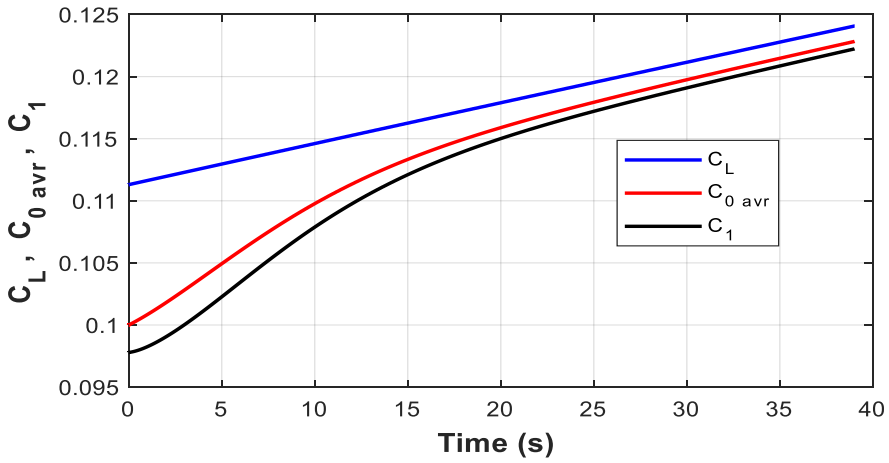

Fig. IV.14. The time evolution of liquidus concentration C_L, the liquid average concentration C_{0avr} and the liquid concentration C_1 are presented by blue, red and black respectively, under the conditions: CR = 0.03 K/s and 1°C of undercooling.

We have applied the previous system equations to Sn-10wt%Pb alloy to estimate the evolution of the concentrations (C_L, $C_{0\,avr}$ and C_1) and the arm radius as shown in Fig IV.14 and Fig IV.15, with applying a weak cooling rate (CR = 0.03 K/s) and 1°C of initial undercooling which corresponds to 220.54°C of liquidus temperature. However, Fig IV.14 shows the time evolution

of the liquid concentration: C_1 at R_f (the black line) and the average concentration C_{0avr} (the red line) which vary in accordance with Eq. IV 26-27, respectively. Also, the liquidus concentration C_L (obtained from phase diagram of Sn-Pb) presented by blue line. We can notice that at t = 0 s, $C_L \approx 11{,}2$ wt% that corresponds to 220.54°C of liquidus temperature (the blue line), then it increases during the growth of the arm (solidification). Also, C_L is the greatest concentration compared to C_1 and $C_{0\,avr}$, because it is the nearest concentration to the diffusion zone (at the liquid/solid interface). On another hand, C_1 is the lower concentration because it is the farthest concentration from where the diffusion occurs, and C_{0avr} takes the value of the initial concentration of the alloy (in this case C_0 = 10%) at t = 0s, and it should be the average concentration during the growing of the arm (between C_L and C_1).

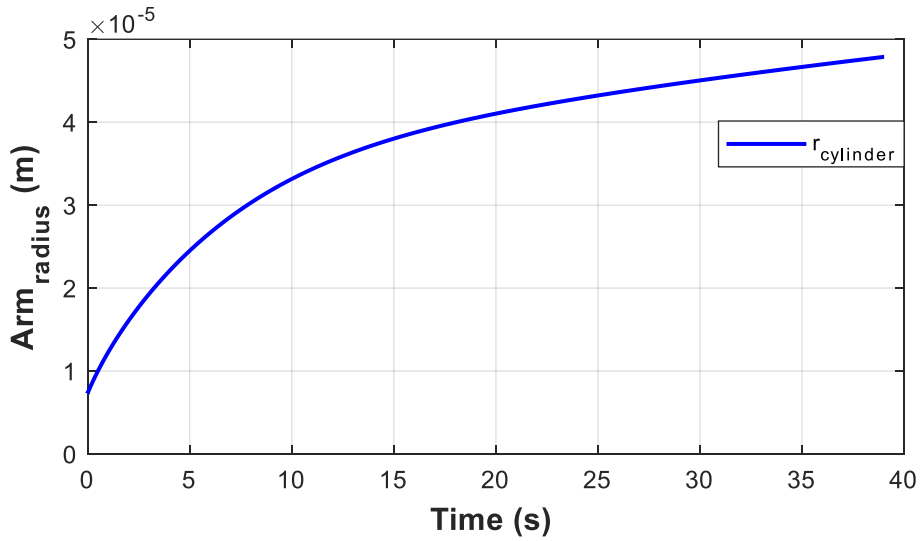

Fig. IV.15. The time evolution of the arm radius growth under the conditions: CR = -0.03 K/s and 1°C of undercooling.

Fig IV.15 illustrates the time evolution of the arm radius which varies in accordance with Eq. IV. 28 during the solidification process (arm growth) with CR = 0.03 K/s and 1°C of undercooling. At t = 0 s, as mentioned previously, the initial arm radius (initial condition) takes the value of the initial tip radius ($r_c = R_{tip} = 7.33\ \mu m$) corresponding of 0.0493 of Peclet number and 13.43 $\mu m/s$ of tip velocity. This radius then growth quickly at the first instants ($\Delta r_c = 25.86\ \mu m$ at the first 10 s) where there is a big nucleation. Then, a slow growth of the arm radius until it settles down at a value near the final radius (in this analysis $R_f = 148\ \mu m$) as presented in Fig IV.13 (b).

IV.4. Test of some experiences

In this part we will test some different experiments that have analyzed earlier which are related to the solidification process. The purpose was to examine our equations system and to check its ability to predict the process then to compare them with the real experimental results and eventually apply it to our studied alloy (Sn-10wt%Pb alloy).

IV.4.1. The directional solidification of Pb-Sn alloys, [24]

Directional solidification experiments have been analyzed by E. Çadirli *et al* [24] on different Pb-Sn alloys as a function of growth rate *V*, temperature gradient *DT* and cooling rate *CR*. The purpose was to evaluate the Primary Dendrite Arm Spacing (PDAS) λ_1, and the Secondary Dendrite Arm Spacing (SDAS) λ_2. Indeed, in our analyses we will only be interested in evaluating the (SDAS). In order to achieve that, we have created a Matlab code to reevaluate the obtained results. The technique was mainly to evaluate the corresponding initial supersaturation (Ω) which gives the same experimental and numerical velocities with fixed temperature gradient. The liquidus slope (m_l) is defined in Eq. IV.30, where the liquidus and solidus concentrations (C_L and C_S) of Pb-Sn phase diagram are presented in Appendix IV.2.

$$m_l(T) = \frac{1}{4p_1 T^3+3p_2 T^2+2p_3 T+p_4} \qquad \text{(IV.30)}$$

where p_{1-5} and q_{1-5} are constants presented in Table IV.2 in Appendix IV.2.

The cooling rate that used in these experiments was calculated as a function of the thermal gradient DT (measured in [°C/m]) multiply by the tip velocity v_{tip}, as expressed in Eq. IV.31 and the final radius R_f is expressed as a function of Peclet number, constant number (A) and tip radius (R_{tip}) as defined in Eq. IV.32.

$$CR = DT\, v \qquad [°C/s] \qquad \text{(IV.31)}$$

$$R_f = A\frac{1}{2P_e}R_{tip} \qquad \text{(IV.32)}$$

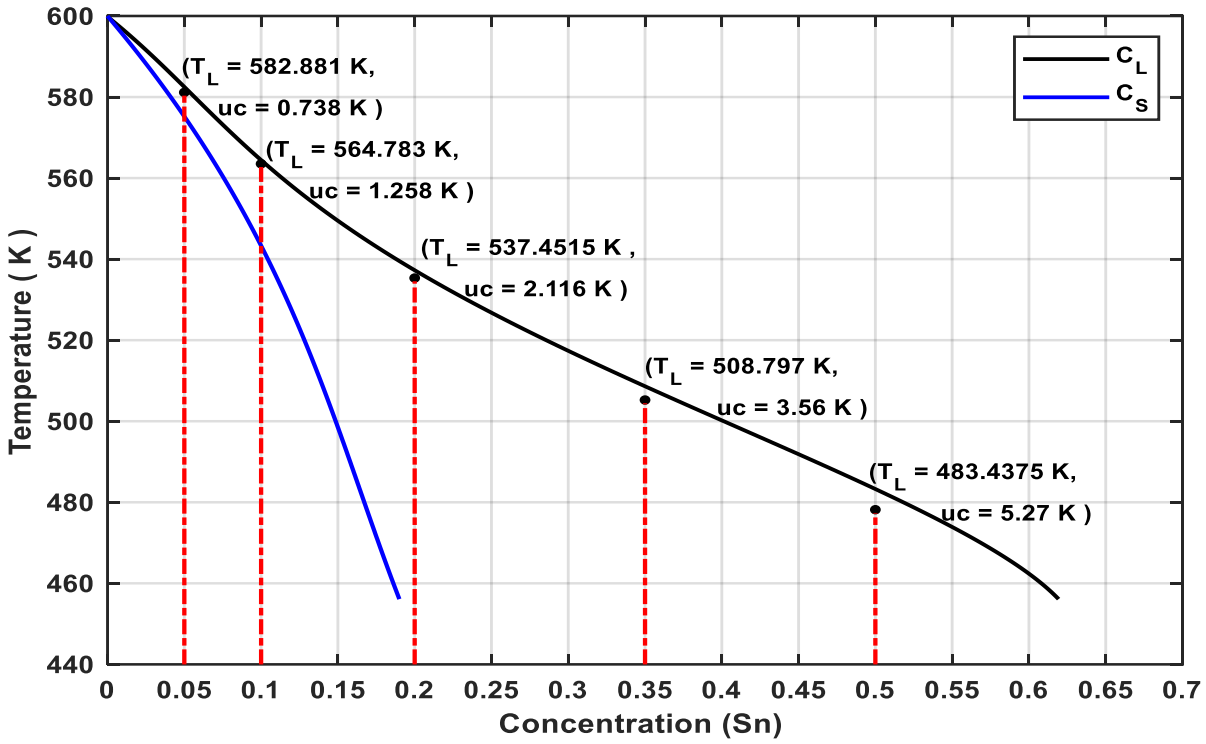

Fig. IV.16. Phase diagram of Pb-Sn (right part), liquidus and solidus concentration are presented by black and blue. Also, the blackheads correspond to initial cylinder at t = 0s (undercooling) as shown in Table IV.3.

Fig IV.16 presents the liquidus and the solidus concentrations (black and blue lines) of Pb-Sn phase diagram (right part). Also, the corresponding liquidus temperature (T_L) and the initial undercooling (*uc*) of each studied alloy (Pb-5wt%Sn, Pb-10wt%Sn, Pb-20wt%Sn, Pb-35wt%Sn and Pb-50wt%Sn) are presented by the blackheads. One can easily notice that as we increase the initial concentration of the alloy, the initial undercooling increase gradually where: *uc* = 0.738 K, *uc* = 1.258 K, *uc* = 2.116 K, *uc* = 3.56 K and *uc* = 5.27 K correspond to Pb-5wt%Sn, Pb-10wt%Sn, Pb-20wt%Sn, Pb-35wt%Sn and Pb-50wt%Sn, respectively. Moreover, usually the increase of the supersaturation tip omega (initial undercooling) leads also to a significant increase of the cooling rate (see Table. IV.3). this means that there is more chance to have more equiaxed structures in case of higher initial concentration (for example Pb-50wt%Sn, i.e., if we increase the initial concentration, we will get more equiaxed structures). In the fact, this behavior due to the far growth of the tip from the real liquidus line (equilibrium concentration).

Table IV.3. Comparison between experimental and numerical parameters of the Pb-Sn alloy.

	Experimental				**Numerical calculation (iterative calculation)**						
C_0	**Velocity (m/s) $\times 10^{-6}$**	**CR (°C/s)**	**λ_2 (m) $\times 10^{-6}$**	**Under Cooling (°C)**	**Velocity (m/s) $\times 10^{-6}$**	**A**	**Final Radius (m) $\times 10^{-6}$**	**Ω**	**Pe**	**R_{tip} (m) $\times 10^{-6}$**	**D (m^2/s) $\times 10^{-9}$**
5%	18.58	0.016	25.4-63.7	0.738	18.64	1	39.38	0.1507	0.0797	10.57	1.237
10%	16.36	0.0237	20.2-53.7	1.258	16.36	1	39.24	0.1158	0.0537	6.98	1.063
20%	15.29	0.0254	26.8-58.9	2.116	15.30	1	37.48	0.0964	0.0412	4.48	0.831
35%	18.45	0.031	13.8-29.9	3.56	18.45	1	18.49	0.0932	0.0393	2.65	0.622
50%	17.11	0.037	14.7-30.3	5.27	17.11	2	19.44	0.0825	0.0331	1.81	0.469

In Table IV.3, the numerical and the experimental measurement are in good agreement. Indeed, in our Matlab code we have fixed the thermal gradient *DT*, and then by increasing in the undercooling (*uc* (i) = *uc* (i-1) +0.001, with *uc* (0) = 0) and calculate its corresponding tip

velocity, this latter was compared each time with the experimental one and it should be almost the same (i.e., $V_{exp} - V_{num} < 10^{-9}$). Once we achieve this condition, we will take its corresponding parameters as presented in Table IV.3, and then the cooling rate can be calculated by Eq. IV.31. Also, the corrective factor "*A*" that presented in Eq. IV.32 gives the diffusion length, and it can also control the final radius R_f that should be in the range of the secondary dendrite arm spacing λ_2 as achieved in Table IV.3. However, the corrective factor "*A*" was only changed in Pb-50wt%Sn alloy.

Secondary dendrite arm spacing λ_2 changed inversely proportional to temperature gradient and cooling rate, the value of λ_2 changed for each solidification parameters (*DT, V*, *CR*), the thermal gradient *DT* and the cooling rate *CR* of both Pb-05wt%Sn and Pb-10wt%Sn are in the range 8.57–48.56°C/cm, 14.49–55.55°C/cm and 0.016–0.090°C/s, 0.027–0.090°C/s respectively, and their corresponding (SDAS) are in the range 25.4–63.7μm and 20.2–53.7 μm, respectively. On the other hand, the velocity of Pb-05wt%Sn and Pb-35wt%Sn are almost the same but they give different (SDAS). In addition, all the calculated R_f are in the range of the measured λ_2.

IV.4.2. Coarsening phenomena of Al-06wt%Cu alloy, [25]

As discussed previously, as the primary stalk advances while the dendritic formation, new secondary arms arise away from the primary tip, this latter go through a complicated ripening mechanism in which the secondary arms compete with their neighbors (other side branches), this mechanism called the coarsening phenomenon. In this talk, the term '*coarsening'* refers to the growth of solid regions of low curvature in a liquid-solid mixture at the expense of regions of higher curvature. Coarsening manifests itself in solidification of metal alloys as:

1) Growth of larger dendrite arms with simultaneous dissolution of smaller arms (ripening).
2) Filling the spaces in between dendrite arms (coalescence).
3) Dendrites Breakup (dendrite multiplication).

Neumann *et al* [25], have used a 3D phase field simulations of columnar dendritic alloy solidification model to analyze current growth and coarsening during directional solidification of Al-06wt%Cu alloy where the model configuration is similar to a Bridgman experiment. Indeed, they mentioned that there is an evolution of the dendrite geometry during the simulation, as shown in Fig IV.17. However, they presented four different snapshots of the computed dendrite at different times, the first stage characterized by a rapid increase of the interface area (see Fig IV.17 (a) and (b)), coarsening and coalescence of side branches (SDAS)

can be observed (see Fig IV.17 (c)) and at high solid fraction, liquid channels are formed inside the solid structure (see Fig IV.17 (c) and (d)).

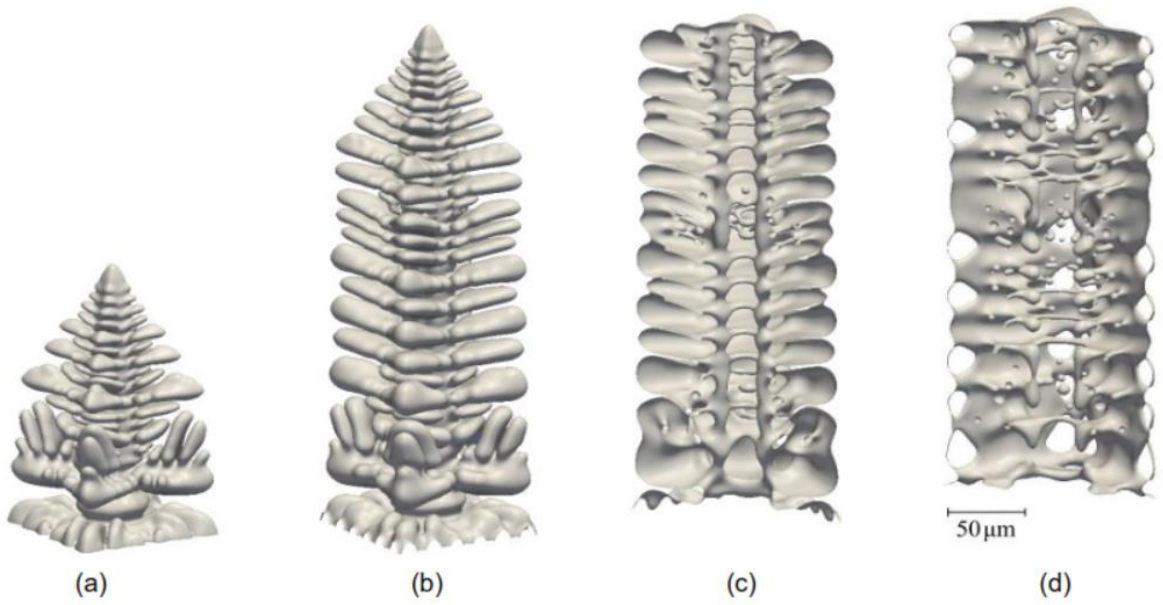

Fig. IV.17. Evolution of the dendrite geometry for the base case simulation: full view of the growing dendrite at 0.5 s (a) and 1 s (b); cutaway view of half of the dendrite at 2.5 s (c) and 7 s (d), [25].

As a result, their model shows how the specific interface area kinetics changes with cooling rate. Also, the examination of the numerical and the experimental data reveals that the coarsening exponent decreases with increasing cooling rate. On the other hand, Merton C. Flemings [26] has analyzed how coarsening of the side branches dendritic during the solidification and to some extent coalescence (see Fig IV.18 (b) and (c), begin just back from the tip. Indeed, the increasing of the solid fraction as solidification proceeds and the dissolution of smaller arms are the main factor to the growth of the dendrite arms.

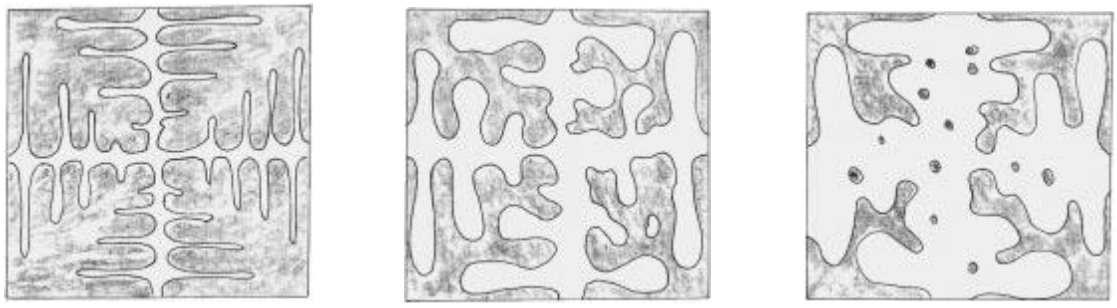

Fig. IV.18. a) Coarsening in dendritic solidification, b) structure early in solidification and c) structures later in solidification showing ripening and coalescence, [26].

Furthermore, as the spaces between dendrite arms fill in at higher solid fractions, coalescence becomes the dominant coarsening mechanism (i.e., the particle radii change with time and the

number of particles decreases). On the other hand, Merton C. Flemings [26] assumed that the 'nucleant multiplication' can increase the number of nucleating particles and decreased by coalescence.

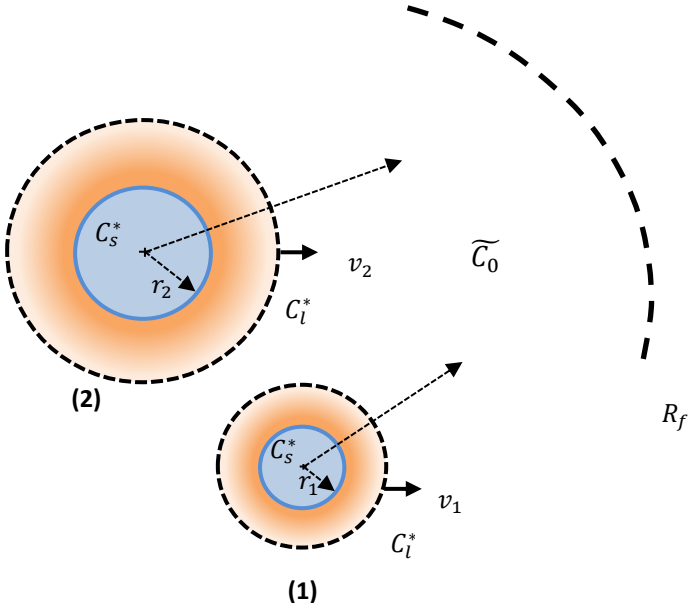

Fig. IV.19. Coarsening of arms growth during the solidification of Al-06wt%Cu alloy.

In order to reevaluate these experiments numerically, we have proposed a Matlab code to simulate this phenomenon. Indeed, we have presented the side braches as cylinders to simplify the model as shown in Fig IV.19 where the growing arms are assumed to be confined in a cylindrical volume enveloped with a final radius R_f. In fact, there are a huge number of side branches with different initial radii but in our analyses we only present two arms (two side branches, see Fig IV.19), as a general case to clarify the technique used. Moreover, it is necessary to mention that both arms have the same initial conditions because they start to solidify at the same temperature (at t = 0 s) and the only difference is in their initial radius, while the lower indexes $(\,)_1$ and $(\,)_2$ refer to the small and big arms, respectively. The equations defining the solution are presented in Table IV.4.

In this study, we evaluate the growth of the cylinder by the time evolution of its radius 'r', where $\frac{\partial r_1}{\partial t} = v_1$ and $\frac{\partial r_2}{\partial t} = v_2$ (Eq. IV.33 and (IV.34)), are the growth velocities of the arms 1 and 2, respectively. The liquid volume (V_{liq}) is the enveloped cylinder volume minus the solid volume of the arms as expressed in Eq. IV.36. Also, the liquid average concentration ($\widetilde{C_0}$) is defined in Eq. IV.35. The term $c^*_{s\,melt/soli}$ that presented on right hand side in Eq. IV.35 is the solid concentration, this latter depends on the velocity and it varies as:

- Positive velocity case: $c^*_{s\,melt/soli} = c^*_s(\text{phase diagram})$ in this case we have solidification (growth arm).
- Negative velocity case: $c^*_{s\,melt/soli} = \widetilde{C_s}$ (see Eq. IV.37 and Eq. IV.38) in this case we have melting.

where $V_1 = \pi r_1^2$ and $V_2 = \pi r_2^2$ are the solid volume of arms 1 and 2. Also, $S_1 = 2\pi r_1$and $S_2 = 2\pi r_2$ are the surfaces of the cylinder 1 and 2, respectively. Whereas, $V_{total} = \pi R_f^2$ is the total volume of the enveloped cylinder. The liquidus, solidus concentrations and the physical properties of Al-06wt%Cu alloy are presented in Appendix IV.3.

Table IV.4. Coarsening equations system.

$$\frac{\partial r_1}{\partial t} = \frac{D_l}{r_1}\,\frac{c_l^* - \widetilde{C_0} - \frac{\Gamma}{m_l r_1}}{c_l^* - c_s^*} \tag{IV.33}$$

$$\frac{\partial r_2}{\partial t} = \frac{D_l}{r_2}\,\frac{c_l^* - \widetilde{C_0} - \frac{\Gamma}{m_l r_2}}{c_l^* - c_s^*} \tag{IV.34}$$

$$\frac{\partial (V_{liq}\,\widetilde{C_0})}{\partial t} = -2\pi r_1 . v_1\left(c^*_{s\,melt/soli}\right) - 2\pi r_2 . v_2\left(c^*_{s\,melt/soli}\right) \tag{IV.35}$$

$$V_{liq} = \pi\left({R_f}^2 - {r_1}^2 - {r_2}^2\right) \tag{IV.36}$$

$$\frac{\partial (V_1\,\widetilde{C_{s_1}})}{\partial t} = v_1\left(c^*_{s\,melt/soli}\right) S_1 \tag{IV.37}$$

$$\frac{\partial (V_2\,\widetilde{C_{s_2}})}{\partial t} = v_2\left(c^*_{s\,melt/soli}\right) S_2 \tag{IV.38}$$

$$C_{mix(coarsening)} = \frac{V_1\,\widetilde{C_{s_1}} + V_2\,\widetilde{C_{s_2}} + V_{liq}\widetilde{C_0}}{V_{total}} \tag{IV.39}$$

An iterative calculation system was used in this part in order to study the coarsening phenomenon of Al-06wt%Cu alloy, 25]. However, the results of the arm growth and the evolution of the concentrations are presented in Fig IV.20-22. Indeed, it is necessary to mention that at t = 0 s, the arms 1 and 2 have different radius ($r_1 = 1\ \mu m$ and $r_2 = 6\ \mu m$) as shown in Fig IV.20 and at this time the cylinders have the same temperature, where the initial undercooling is *uc* = 0.7 K. Both arms grow simultaneously inside the same covered volume that characterized by its fixed radius R_f (in this study $R_f = 20\ \mu m$). In order to evaluate how long the arms can grow and/or melt, we have analyzed the evolution of their radius over time as presented in Fig IV.20, where $r_1$and r_2 are the radius of the small and the big arms presented by blue and red, respectively. Both radius $r_1$and $r_2$vary in accordance with Eqs. IV. 33 and IV.34, respectively. whereas, the same cooling was applied in both arms (*CR*=1 K/s) as taken

in the studied experiment, [25]. One can notice that both arms grow at the first 10 s, this period characterized by a growth competition in growing between the arms during the solidification process, and this phenomenon is known as coarsening. Then, at t = 10 s, the small arm (its radius r_1) reaches its maximum value (about $r_1 = 4.654\ \mu m$) while the other arm (blue line continues to grow). Eventually, the small arm then melts (dies) due to the effect of the curvature ($\Delta T_r = \Gamma / m_l r_1$), disappears at t = 22.88 s while the other arm (red line) continues to growth until its radius reaches a value near the final enveloped volume R_f (closed the secondary arm dendrite spacing λ_2).

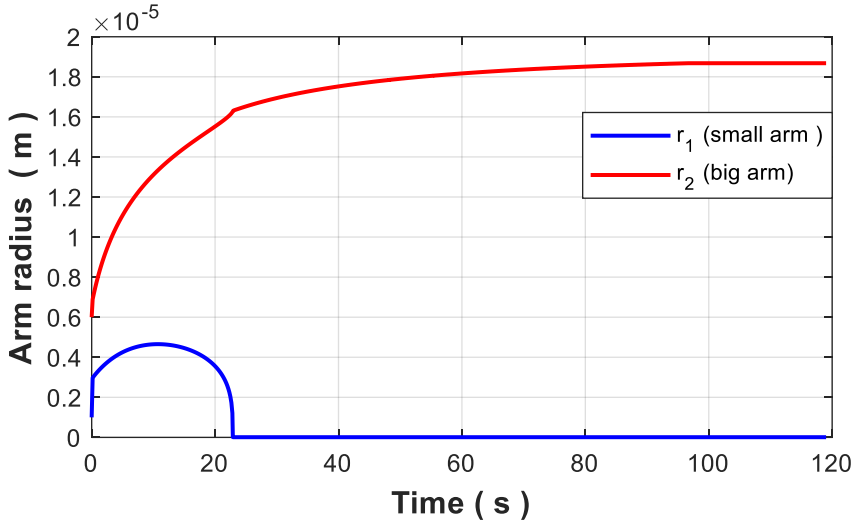

Fig. IV.20. The evolution of the arms radius during the coarsening phenomenon of Al-06wt%Cu alloy, the big arm radii presented by red and the small one presented by blue.

It is necessary to mention that when we solidify, we solidify by the solid concentration from the phase diagram. But when we melt, we melt by what is already solidify before, so the history must be recorded. Moreover, we have assumed an average concentration inside the solid, because we in fact do not recover all. In addition, there is a direct relation between the arm growth and its concentration. However, the solid concentration increases as the solid volume increase (solidification case), and vice versa. Fig IV.21 shows the evolution of the average solid concentration of the small and big arms presented by blue and red, respectively. In addition, the solid concentration that was taken from the phase diagram of Al-Cu alloy is also presented (black line). At t = 0 s both arms have the same initial solid concentration where $\widetilde{C_s} = 0.0055$ (initial condition). Indeed, the increase /or decrease of the solid concentration depend on the solidification /or melting of the arms. Both average solid concentrations increase as the arms grow, then at the same time when the small arm radius reaches ist maximum value, its solid

concentration also be the maximum ($\widetilde{C}_{s_1} = 6.6039\ 10^{-3}$ at about t = 10 s), this latter then decreases as the arm melt.

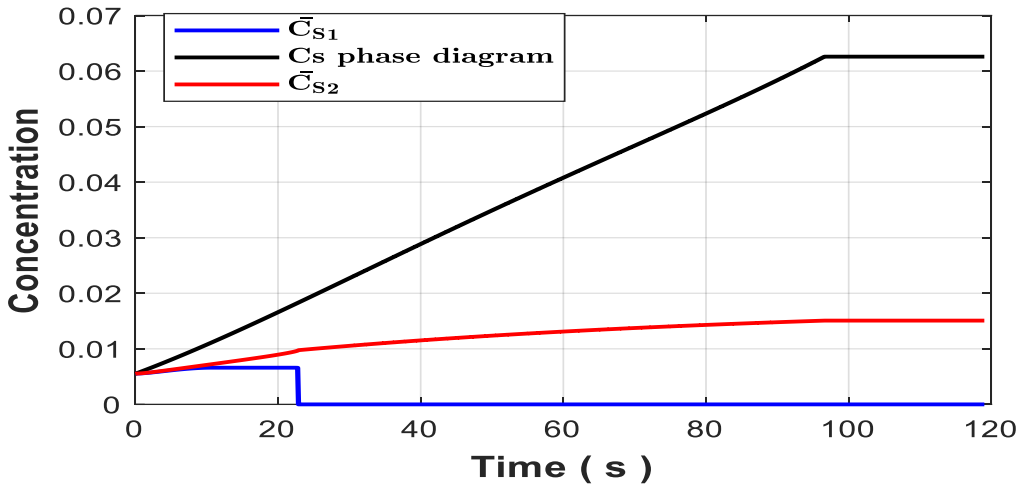

Fig. IV.21. The time evolution of the solid concentration of small and big arms presented by blue and red, respectively. Also, the solidus concentration of Al-06wt%Cu alloy which is taken from the phase diagram presented by black during the coarsening phenomenon.

Finally, the evolution of the mixture concentration (solid + liquid) during the coarsening phenomenon of Al-06wt%Cu alloy that varies in accordance with Eq. IV.39 is presented in Fig IV.22. This latter is constant during the coarsening process and its value corresponds to the initial concentration of the alloy'C_0' (in this case C_0 = 6%).

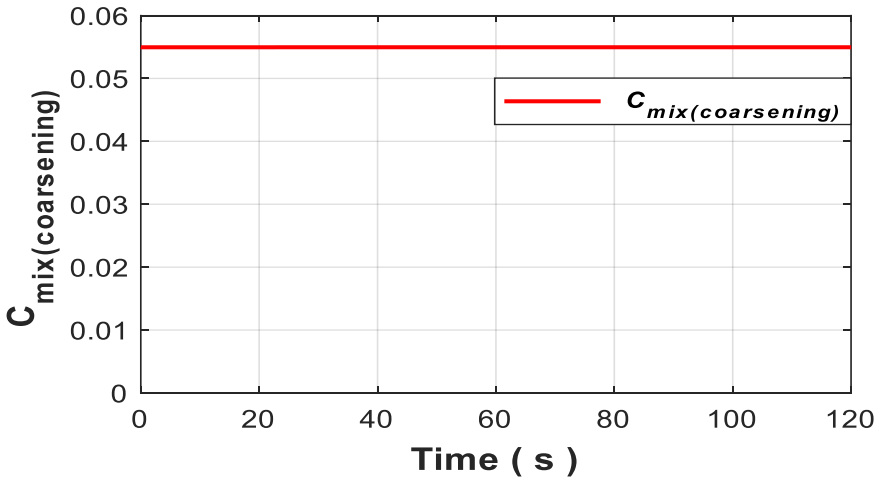

Fig. IV.22. The time evolution of the mixture concentration of Al-06wt%Cu alloy during the coarsening phenomenon.

IV.5. Coarsening phenomena of Sn-10wt%Pb alloy

This part is devoted to study the coarsening phenomenon that occurs during the solidification process of Sn-10wt%Pb alloy with keeping the same equations system as described in the

previous part (Eq. IV.33-39, see Table IV.4). The liquidus and solidus concentrations of the alloy and the physical properties used in this analyzes are presented in Appendix IV.

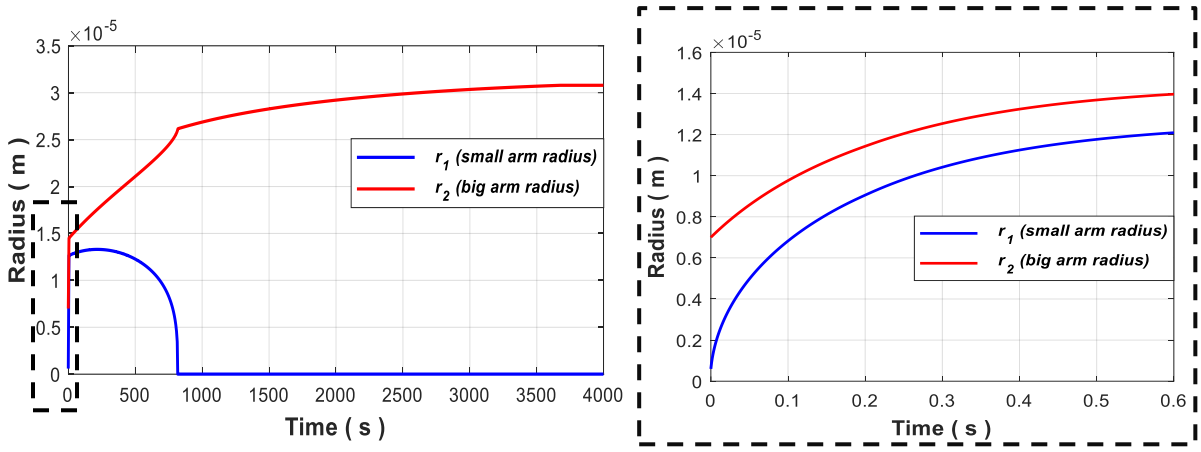

Fig. IV.23. (a) The evolution of the arms radius during the coarsening phenomenon of Sn-10wt%Pb alloy, the big arm radii presented by red and the small one presented by blue. (b) zoomed-in view of first nucleation during coarsening phenomenon.

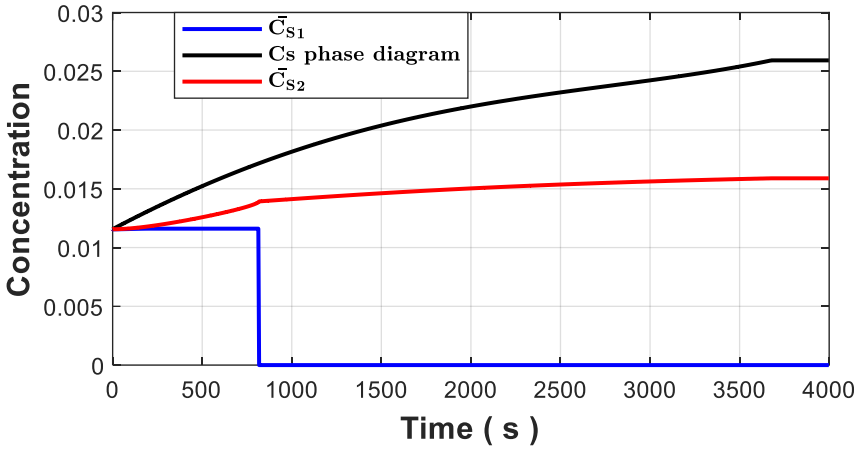

Fig. IV.24. The time evolution of the average solid concentration of small and big arms presented by blue and red respectively. Also, the solidus concentration of Sn-10wt%Pb alloy which is taken from the phase diagram presented by black during the coarsening phenomenon.

Fig IV.23 presents the time evolution of the arms radius during the coarsening phenomenon of Sn-10wt%Pb alloy. Both arms start growing with different initial radius ($r_1 = 0.6\,\mu m$ and $r_2 = 7\,\mu m$, see Appendix IV.1 (Table IV.1) and Fig IV.23 (b)), where the small and big arms are presented by blue and red, respectively. Both arms start growing at the same temperature (1.77°C of initial undercooling) consequently the same liquidus concentration (initial conditions) and also the same cooling rate (CR=0.01 K/s). At the first instants, a strong nucleation of both arms as shown in Fig IV.23 (b), where in in these first instants (from 0 s to 0.6 s), the growth of the small and big arms are $\Delta r_1 = 11.478\,\mu m$ and $\Delta r_2 = 6.952\,\mu m$,

respectively. Indeed, there is a strong growth competition in this period. The same behaviour occurs (coarsening of Sn-10wt%Pb alloy). However, the growth and melt take more time compared to the previous study (coarsening of Al-06wt%Cu alloy, see Fig IV.23 (a)), this behaviour is due to the small cooling rate used in this analyzes (*CR*=0.01 K/s), i.e., the small arm dies at t = 817.67 s where in the previous study it dies at t = 22.88 s.

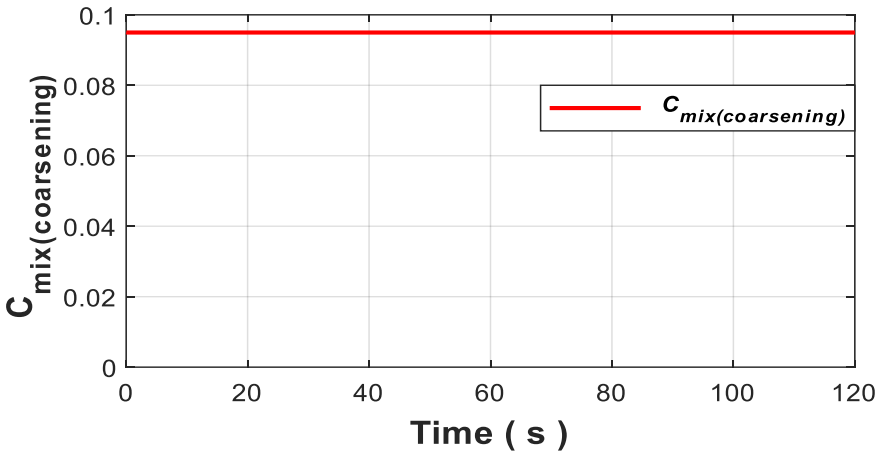

Fig. IV.25. The time evolution of the mixture concentration of Sn-10wt%Pb alloy during the coarsening phenomenon.

One can easily notice that the big arm grows quickly when there is a growth competition with the small one. Also, when the small arm dies (at t = 817.67 s) there is a jump in growth of the big arm (red line).

On other hand, the average solid concentrations which vary in accordance with Eq. IV.37 and 38 illustrate that the concentrations increase as the arm grows (solidification case) and vice versa in the melting case (see Fig IV.24). Moreover, the mixture concentration that presented in Fig IV.25 which varies in accordance with Eq. IV.39 shows that this latter always has a constant value corresponds mainly to the initial concentration of the alloy; in the current case $C_{mix(coarsening)} = 10$ wt%.

IV.6. Numerical results

Two-dimensional numerical simulation is implemented with a grid consisting of 23800 number of elements and 48240 number of nodes in order to simulate the more general case of the solidification of a binary alloy, where in addition to diffusive heat exchanges, convective exchanges exist within the liquid phase. For this, we focus on the case of the solidification of a tin-lead alloy with an initial lead concentration C_0 = 10-wt% (Sn-10wt%Pb) within the 'AFRODITE' experimental setup. The experimental process is similar to that described in

section III.4 (Chapter III). The alloy is initially in the liquid state. The natural convection is initiated by imposing a temperature gradient between the two vertical walls in contact with the two heat exchangers of the experimental set-up (see Fig. III.1 and Fig. III.4). This thermal gradient is maintained throughout the solidification process. It is calculated in the same way as presented in section III.4.3 (Chapter III) and is worth $\Delta T = 20$ K. The temperatures imposed on these walls are initially higher than the melting temperature of pure tin, then a cooling rate CR = -0.03 K/s is imposed on them. Such a study requires the consideration of different physical phenomena which appear during the solidification and whose consideration in the in the numerical formulation of the problem is important to ensure the quality of the results.

IV.6.1. Temperature evolution: experiment/numerical simulations

Numerical and experimental evolution of the temperature fields with time is shown in Fig IV.26, where the results are presented in the main zone in the cavity, this latter is covered by the array of 50 thermocouples (see the experimental results in right column). The numerical results are also presented in the same zone with the experimental, where this zone is covered by a white dashed line. The same behavior was observed as obtained previously in the case of solidification of pure tin under the effect of natural convection (described in the previous chapter), where natural convection plays an important role in the solidification process as shown in Fig IV.26 at t = 16000 s where there is a clockwise circulation eddy flow.

Indeed, the right wall is colder than the left one, for this reason we can notice in both numerical and experimental results that presented in Fig IV.26 at t = 16700 s, the first solid regions appear on this side of the cavity. The mushy zone appears and starts to be larger as the temperature becomes lower than the liquidus temperature T_L corresponding to the nominal concentration C_0 as illustrated in the second snapshot (at t = 16700 s). A second mushy zone appears on the side of the hottest wall (left wall) in later time, once its temperature has sufficiently decreased (thanks to the cooling rate applied) below the liquidus temperatures corresponding to the concentrations of the liquid (see Fig IV.26 at t = 17400 s). Both mushy zones then grow towards the interior of the cavity, enclosing the rest of the entirely liquid region that decreases gradually until its complete solidification.

Fig IV.26 also shows the evolution of the heat transfer regime within the cavity during the solidification process. Before the appearance of the first mushy zone on the right side of the cavity (at t_1 = 16000 s), the convective regime induced by the thermal gradient between the two cooled walls is dominant. After the appearance of this first mushy zone and before the appearance of the second one on the left (i.e., at t2 = 16700 s), the convective regime is still

present in the liquid region, but within the mushy zones that have already formed, it is the diffusive regime which dominates.

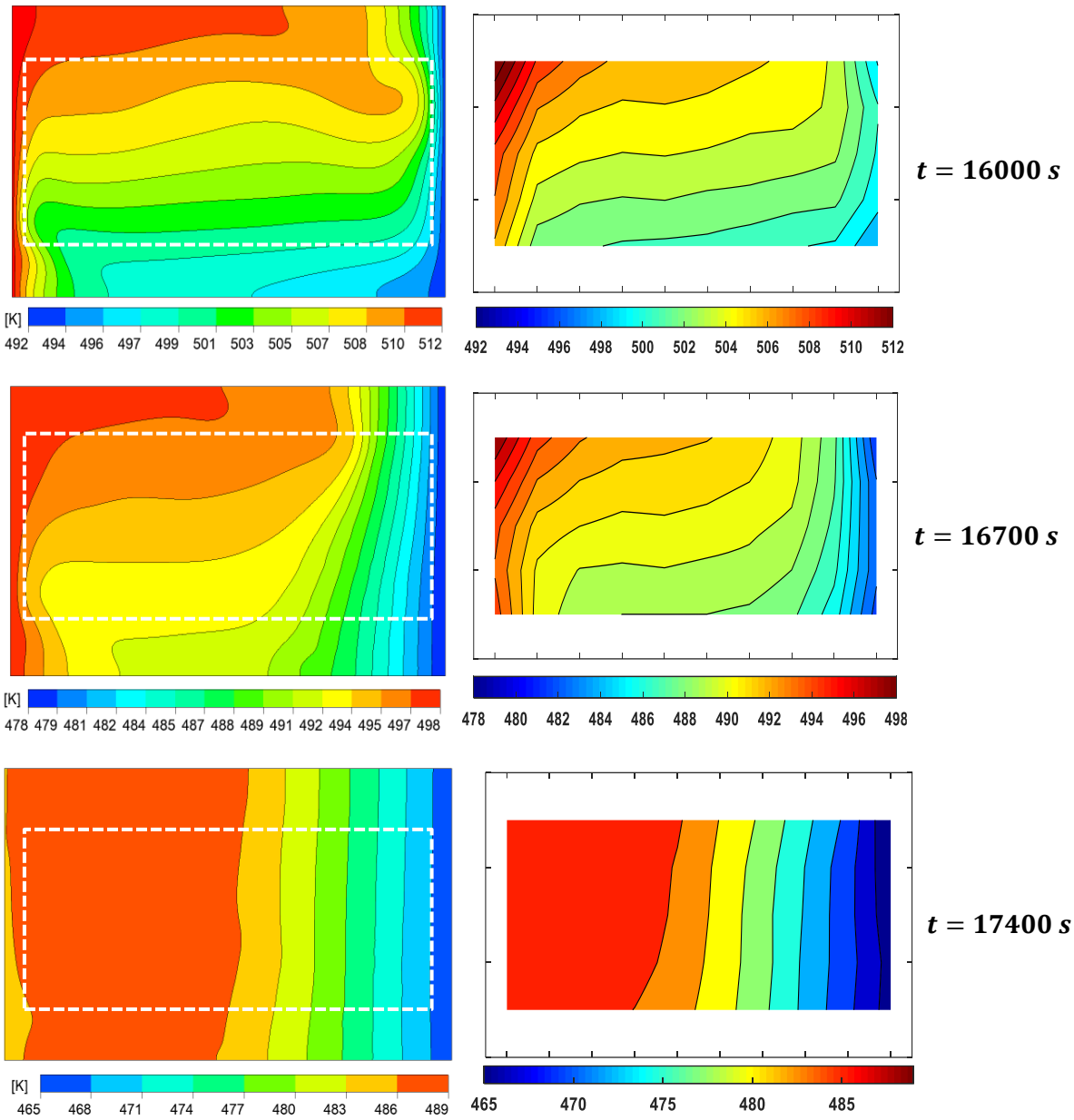

(a) Num **(b) Exp**

Fig. IV.26. Temperature maps at three selected times (t = 16000 s, t = 16700 s and t = 17400 s) during the solidification of Sn-10wt%Pb alloy. (a) Num (left column) and (b) Exp (right column) present the numerical and experimental results, respectively. The white dashed rectangle on the numerical snapshots represents the part of the domain in which thermocouples are present. Conversely, the white stripe all around the color map in the experimental snapshots corresponds to the part of the domain in which no thermocouple is present. The temperature color bar scales are in Kelvins.

The appearance of the mushy zone decreases the effective thermal gradient within the remaining liquid zone and the convective regime is gradually reduced. Once the second mushy

zone appears on the left and until the total solidification of the ingot, the diffusive regime is dominant. We conclude that the numerical and experimental results are in good agreement.

IV.6.2. Extra and inter dendritic liquid concentration

As described previously, solid, inter-dendritic liquid, and extra-dendritic liquid are the three phases that exist in our model (see Fig IV.1). Indeed, the two liquid phases are separated by the grain envelope (dashed line in Fig IV.1). In order to clarify the difference between them, we have presented the extra liquid and the inter dendritic concentrations as shown in Fig IV.27. The inter dendritic concentration is also in the mushy zone, and in this model there is a very strong coupling, we can see only a little difference between these two concentrations on the right side of the sample (at the level of solid region). However, in the extra liquid region (left part) they are exactly the same, but inside we have a very big difference as it appears in the right top part of the sample by yellow color and in the bottom right part by red color. In our model we have a very strong interaction coefficient; it means that as soon as the liquid goes inside (flow inter dendritic) should be less than the second to have equilibrium in terms of concentration. Moreover, if we increase the interaction coefficient between these two liquid concentrations in this case, we can have a big difference between those concentrations (at the level of mushy zone).

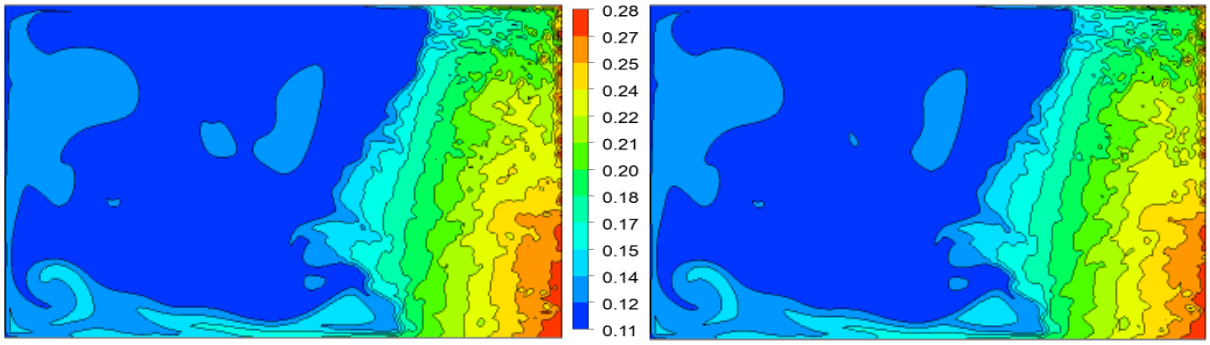

(a) **(b)**

Fig. IV.27. Numerical calculation of (a) Liquid concentration and (b) Interdendritic concentration snapshot at selected instant (t = 1667.56 s) during the solidification of Sn-10wt%Pb alloy.

IV.6.3. Solid fraction inside the envelope and solid concentration

Solidification occurs when microscopic dendrites grow as the liquid cooled below its solidification temperature. As soon as the first solid regions form from the right wall (see Fig IV.28 (a) at t = 1291.56 s), the velocities within the mushy zone decrease rapidly and tend toward zero. As explained earlier, the braking term (Eq. IV.5) assimilating the mushy zone to

a porous medium becomes dominant and forces the velocities to be zero as the solid forms. The solidification front then progresses from right to left (see Fig IV.28) reducing the liquid zone gradually. One can easily notice that there are many dendrites at the zone that separates the liquid and the mushy zone (i.e., the solidification front has a dendrite morphology). The extra liquid then flows between these dendrites envelopes, which causes the formation of the segregation channels as it appears in the bottom right part of the sample in Fig IV.28. Also, Fig IV.28 (b) and (c) reveal the appearance of the first segregation zones inside the mushy zone. The formation of the segregation channels is triggered by the irregular growth of the dendritic grain. Larger areas filled with Pb-rich inter dendritic liquid can be observed between dendrites with different growth angles. On other hand, a re-melting of dendrites observed in Fig IV.28 (a) and (b) and the formation of the freckles can be detected. In addition, the coarsening phenomenon plays an important role to the formation of these freckles due to the coalescence of the side branches which also creates inter dendritic liquid during the solidification process.

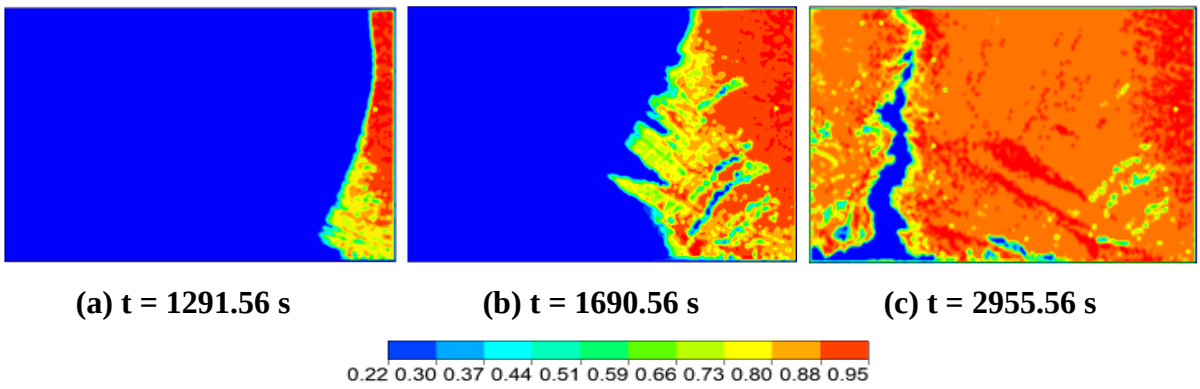

Fig. IV.28. Solid fraction inside envelope maps at selected instants during the solidification of Sn-10wt%Pb alloy under natural convection: (a) t = 1291,56 s, (b) t = 1690,56 s and (c) t = 2955,56 s.

The convective flow within the purely liquid region impacts the shape of the interface mushy-liquid zone due to the heat contribution of the hot wall. This influence is visible on Fig IV.28 at t = 1291.56 s and t = 1690.56 s where a curvature of the mushy-liquid zone interface is observed. Beyond these instants, this influence on the shape of the interface decreases gradually. This is due to the decrease of the convective intensity, in relation with the decrease of the thermal gradient driving the principal convective flow. Indeed, a large part of the temperature difference between the hot and cold walls is found in the mushy zone on the right part of the cavity, where the heat transfer regime is diffusive.

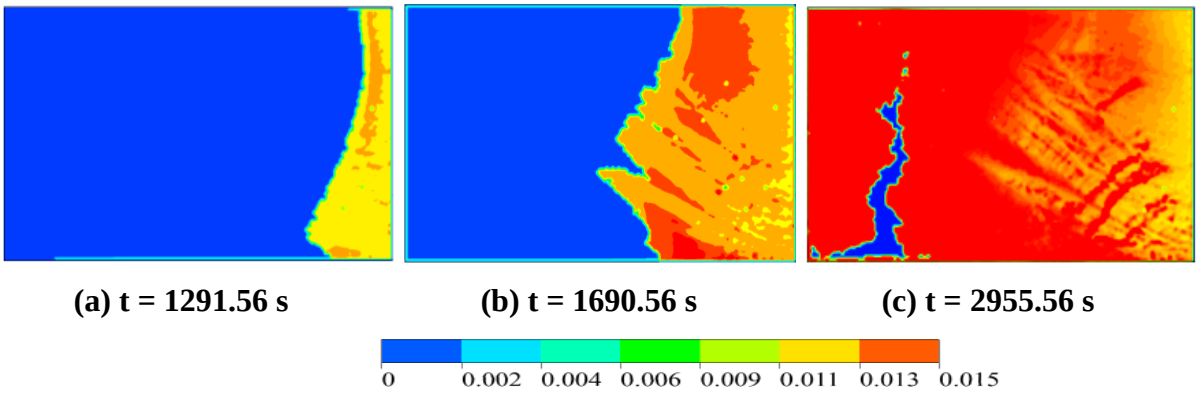

Fig. IV.29. Solid concentration inside the solid dendrite maps at selected instants during the solidification of Sn-10wt%Pb alloy under natural convection: (a) t = 1291,56 s, (b) t = 1690,56 s and (c) t = 2955,56 s.

The solid concentration inside the solid dendrite is also presented in Fig IV.29 at three different times during the solidification of Sn-10wt%Pb alloy under natural convection. The conditions are the same as mentioned previously (DT = 40 K and cooling rate: CR = 0.03K/s). The evolution of the solid fraction (Fig IV.28) allows distinguishing the liquid and solid regions, while the blue regions are completely liquid. At t = 1291.56 s, the sample is mainly liquid and solidification begins in the vicinity of the cold wall (the one on the right of the cavity at x_1 = 0,1 m) when the temperature imposed there drops below the liquidus temperature at the initial concentration C_0. As the mushy zone progress toward the left part of the sample (see Fig IV.29 (b) at t = 1690.56 s), the solid concentration regions will be larger with increasing in its value to about 1.5wt%. At final solidification stage, a second mushy zone appears on left and progresses toward right (see Fig IV.29 (c) at t = 2955.56 s), both mushy zones then progress as the sample solidify reducing the liquid zone. During this process, in addition to thermal exchanges, segregation in lead (Pb) is observed as solidification proceeds. The lead being more soluble in the liquid phase than in the solid phase, a part of this latter is rejected towards the liquid which will be enriched more and more. The last zone which will solidify is then the richest in lead. The blue zone that illustrated in Fig IV.29 (c) at t = 2955.56 s it is the segregation chimney appearing at the end of solidification.

IV.6.4. Mixture concentration

In the light of the previous presented concentrations (extra liquid, inter dendritic (inside the envelope) and solid (inside the dendrite) concentrations), it is necessary to define also the mixture of theses concentrations by the following equation:

$$C_{mix} = f_{env}\left(f_l\, C_l^{inter} + f_s\, C_s^{solid}\right) + (1 - f_{env})C_l \qquad \text{(IV.40)}$$

where f_{env} and C_l^{inter} are the liquid fraction inside the envelope and the inter dendritic concentration, respectively. (see Fig IV.1). where $f_{env} + f_l + f_s = 1$.

Although the main convective flow, which is due to the temperature gradient within the liquid zone, decreases, a solutal convection flow, due to the enrichment of the inter dendritic liquid and the liquid at the contact of the mushy zone thanks to the segregation of the solute, appears and contributes to maintain the total convective flow. Indeed, the difference in density between lead and tin drives the flow toward the bottom. This influence of the solute rejection on the flow, expressed in the buoyancy force term via the solutal expansion coefficient, maintains the descending flow along the first mushy-liquid zone interface appearing on the right side. At the time of the appearance of the second mushy zone on the left side, the total convective flow has decreased in intensity. It descends in the vicinity of the two enriched zones and ascends in the bulk liquid region. As the two mushy zones extend in size the convective flow gradually disappears. This is because, although solute rejection continues to occur (see Figure IV.31).

During this solidification process, the phenomenon of lead segregation can be observed. Fig IV.30 shows the evolution of the mixture concentration in the cavity during the process. The evolution of the solid fraction f_s, allows also distinguishing the liquid and mushy regions. In the initial state, a clockwise thermal convection occurred and the nominal concentration is equal to 10-wt%. As the superheat of the melt is extracted from the cold wall (right side) and the temperature there drops gradually below the liquidus temperature. With the appearance of the first mushy zone, the liquid can flow through the columnar dendrites, (see Fig IV.30 (a) and (b)), and segregation begins. The solute is rejected from solid to liquid where it is more soluble. As explained earlier, the rejection of lead favors the descend flow along the mushy-liquid interface zone. The zones at the bottom right of the cavity are therefore the first to be enriched in lead. The lead released during the early stages of the process (see Figure IV.30 at t = 1291.56 and t = 1690.56 s) is slightly evacuated by the convective flow which is still important.

After the decrease of the total convective flow and the main subsistence of the thermosolutal convection flow (descending flow along the mushy-liquid zone boundary on the right), lead segregation initially occurs primarily down the cavity (see Fig IV.30 (b) at t = 1690.56 s). As the process advances, a second downward solutal flow is caused by the enrichment of the liquid in the vicinity of the second mushy zone which appears on the left of the cavity (see Fig IV.30 (c) at t = 2955.56 s). The combination of these two downward flows generates an upward flow in the middle of the liquid region. This upward flow, combined with segregation increasingly

in the horizontal direction causes the formation of the segregation chimney (see Fig IV.30 (c) at t = 2955.56 s and Fig IV.31 (b)). This chimney is the trace of the last liquid regions to solidify. These regions are the richest in solute and thus have the highest lead concentrations (on the order of 13-wt%).

We can also see in Fig IV.30 in the blue zone that located in the right (coldest part) we have dendrites envelopes which are not completely solid. In between, purely liquid freckles develop (see Fig IV.30 (b) and (c)) red zone inside the mush). These freckles are generated by combined re-melting and coarsening phenomena. However, in the green and blue regions on the right side there are completely solid dendrites. In addition, it is necessary to mention that there are two main factors which are influenced the appearance of those freckles, the first is the permeability of the solid in the mushy zone (i.e., how much liquid can penetrate inside) and the second factor is the exchange of the solute between the concentration inter dendrite (inside the envelope) and the liquid concentration (C_l^{inter} and C_l).

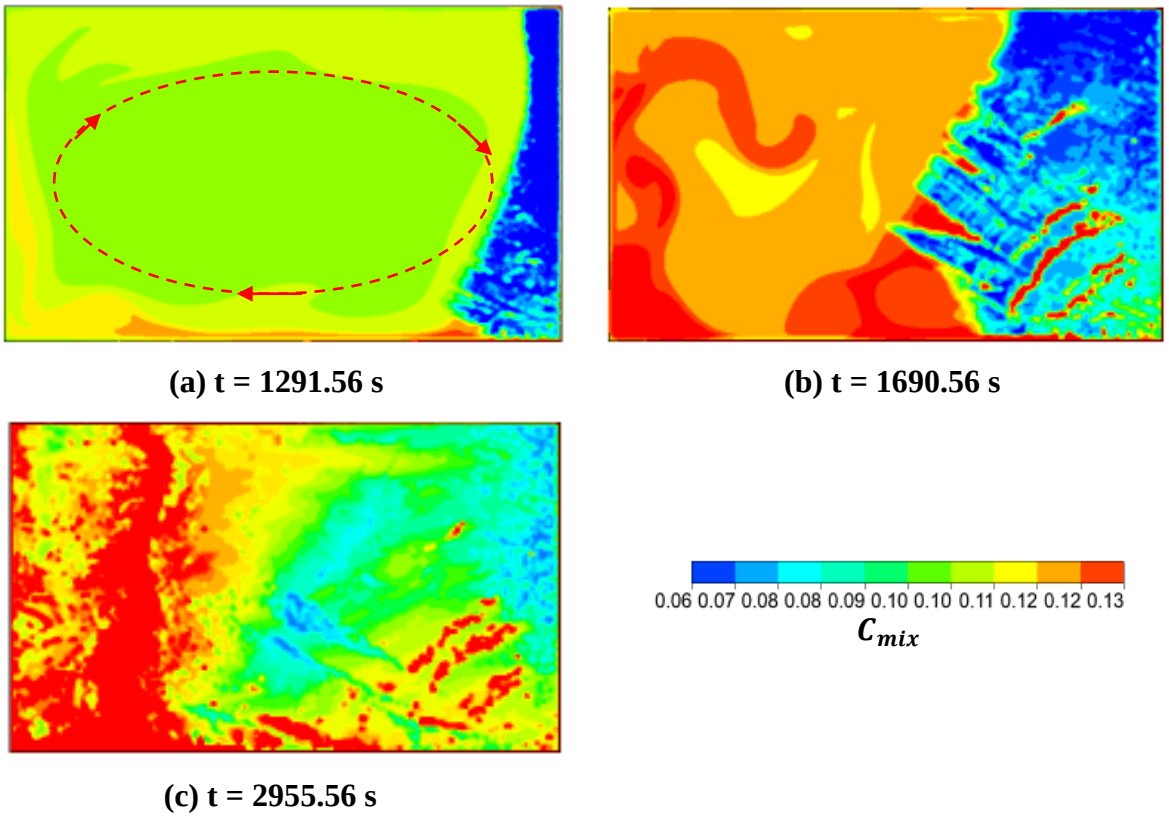

(a) t = 1291.56 s **(b) t = 1690.56 s**

(c) t = 2955.56 s

Fig. IV.30. Mixture concentration at (a) t = 1291.56 s, (b) t = 1690.56 s and (c) t = 2955.56 s during the solidification of Sn-10wt%Pb alloy under natural convection.

Now that the sequence of the solidification process has been detailed, we compare the results of our model with the experimental data obtained with the 'AFRODITE' setup. Fig IV.31 gives a qualitative view of the final segregation observed on the solid ingot with our model (right)

and that experimental (left) obtained by X-ray of the solidified ingot, [27]. The lead-rich areas appear in white while the poor regions are darker. The segregated channels forming at the bottom of the cold wall are clearly detected in our numerical model, and this latter gives enrichment in lead in this region. The chimney at the end of solidification, which corresponds to the last liquid parts that have solidified and which are also the most enriched in lead, is well found. This one seems to be highlighted in our numerical model where it occupies the whole height of the ingot. Note that on the experimental results, the black area at the top of the ingot at the level of the chimney (at the end of solidification) corresponds to a zone from which the alloy has withdrawn while solidifying, because in the solid state, the alloy is actually denser than in the liquid state, that will occupy less volume. Finally, the segregation obtained by the present model show a lower positive segregation band along the bottom wall, and segregation chunks at the lower right corner are also observed. From this comparison, we can notice that our simulation is not perfect at the chimney level, so we need equiaxed structures and this is might be the main reason.

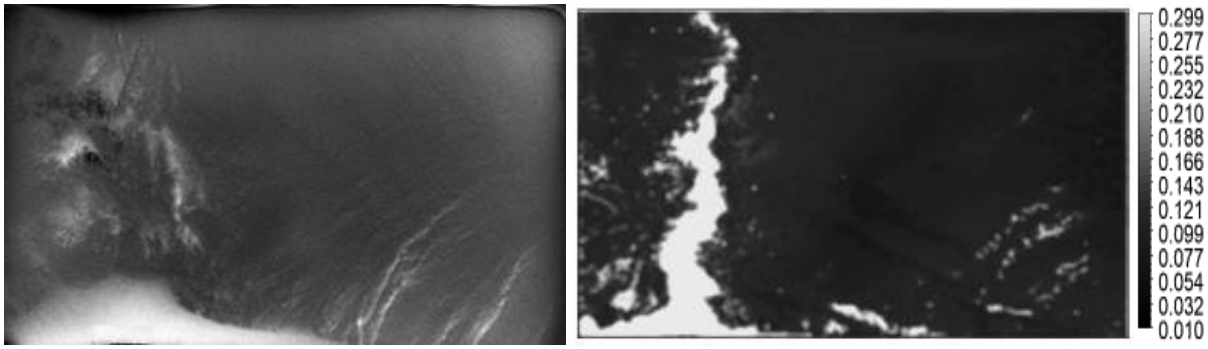

(a) Experimental **(b) Numerical**

Fig. IV.31. Qualitative comparison of the final segregation observed on the solid ingot. Right: numerical contour of the mixture concentration with a grey color scale ranging from 1 to 29 – wt.%; left: Experimental X-ray of the solid ingot (from [27]). The lead-rich areas appear light and the poor areas are darker.

IV.6.5. Grain structures

The solidification is generally a result of crystallization from the formation of solid phase nuclei within the liquid metal and then by the growth of these nuclei. This is called nucleation/growth. During solidification, there is a redistribution of the chemical elements which segregate and form differentiated phases (dendrites in our case). A two-dimensional numerical model is also developed to evaluate the grain structure evolution during the solidification process under the same mentioned conditions.

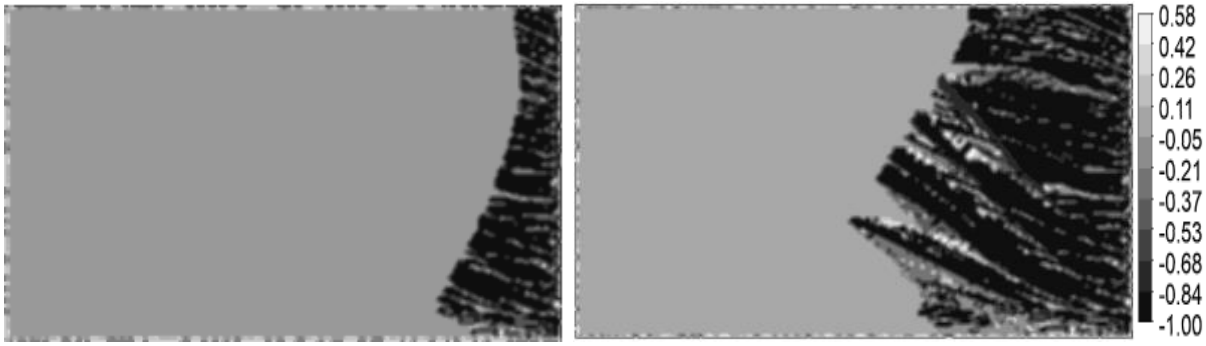

(a) t = 1291.56 s **(b) t = 1690.56 s**

Fig. IV.32. Evolution of the grain structure within the cavity during the solidification process of the Sn-10wt%Pb alloy at (a) t = 1291.56 s and (b) t = 1690.56 s. The temperature gradient is DT = 20 K and the cooling rate CR = -0.03 K/s.

Different colours represent different misorientation angles. The present model predicts an obvious upward inclined columnar structure from the right wall to the left (Fig IV.32 (a) and (b)). This is attributed to the downward inclined liquid flow ahead of the growth front; the columnar grains extend faster in the direction opposite to the fluid flow, resulting in the current grain selection.

In addition, In Fig IV.32 (a) and (b), there are a large number of grains which are nucleating at the wall on the right side. Initially each nucleated grains grow in a random direction. Due to competition many grains died quickly after their nucleation. Only survived grains which were growing on the preferential direction controlled by the mass transfer at the dendrite tips.

As detailed by L. Hachani [27], the post mortem analysis performed on the ingots is to reveal the macrostructure in order to know the shape and sizes of the grains and the location of the segregated channels in the ingot. It is very difficult to establish microstructure maps because tin is a very soft metal that tends to spread out during polishing and thus hide these microstructures. Macrostructure maps are not easier to make because of the size of the sample (*10×6 cm*) and the regularity of the polishing required for the chemical attacks to reveal the grains. The revelation of the macrostructure was achieved by several passes of a polishing paper (400 to 2400) and a chemical attack by a chemical solution composed of *75%* vol of HCL (37% mol/v) and *25%* vol HNO3 (*69.5%*). After leaving the mixture (HCl and HNO) for 10-15 minutes, the sample was wiped by cotton soaked in this mixture for one minute, then cleaned with water and then by alcohol and finally dried.

Experimentally, the conditions are: cooling rate CR = -0.03 K/s and experimental temperature difference ΔT = 40K. The corresponding macrostructure is shown in Fig IV.33 (a). The results show that:

- Solidification is globally columnar.
- The inclination of the columnar grains is compatible with the existence of an upstream-downstream flow along the advancing face.
- An equiaxed zone appears in the left part of the sample, indicating that a columnar-equiaxed transition occurred at the end of solidification.

The macrostructures are almost columnar with smaller grains in the left half-third (zone delimited by the red dashed line) which may correspond to equiaxed grains. The structures are initially columnar, but equiaxed grains are visible in the left part of the sample as the thermal gradient decreases consequently the CET mechanism occurs.

Numerically, Fig IV.33 (b) presents the grain structure of the solidification of Sn-10wt%Pb obtained by using a 20 K of difference temperature and 0.03 K/s of cooling rate. The results show that the microstructures are globally columnar and there is a good agreement between numerical and experimental measurement at the level of columnar structure (right part). In contrast, in our numerical model we did not detect the equiaxed regions. This is due to the fact that our model is purely columnar (i.e., equiaxed grains are not considered in our model). Also, if we see in the experimental grains they have different directions, because actually we have equiaxed grains all the time and then when they fall on the columnar front, they will make new grains (columnar grains). For this reason, we can notice that the experimental grains have different directions and we do not have this mechanism in our model. For that our simulation is not perfect in term of structures and more particularly our model is 2D not 3D.

(a) Experimental **(b) Numerical**

Fig. IV.33. Qualitative comparison of the final grain structure observed on the solid ingot. Right: (a) contour of the numerical grain structure with a grey color scale ranging from -1 to 1; left: (a) Experimental macrostructure (from [27]) of Sn-10wt%Pb alloy observed in the lateral plane. The conditions are; average experimental temperature difference $\Delta T = 40$ K and cooling rate: CR = 0.03K/s.

IV.7. Partial conclusion

A study on the segregation of alloy elements during the solidification of binary metallic alloys has been investigated. During such solidification, the kinetics of physical phenomena and transfers are different from those of phase changes of pure materials. The solidification treated is two-dimensional and the exchanges are convective-diffusive. Indeed, a numerical simulation of the solidification of Sn-10wt%Pb alloy within the 'AFRODITE' experimental setup was studied. In addition to the diffusive transfers, convective transfers induced by the thermosolutal convection flow within the liquid regions. A complete micro-segregation model contain of three phases was detailed. The numerical results show a reasonable agreement with the experimental results. Furthermore, qualitative comparison of numerical and experimental final segregation was achieved. However, it is important to underline those two segregation zones were observed: the zone of segregated channels located in the first layers of formed solids and the zone of so-called normal segregation corresponding to the last liquid at the end of solidification which presents in several numerical and experimental studies as a shape of chimney. On other hand, numerical and experimental qualitative comparison of the final grain structure is in good agreement at the level of columnar structure, but not equiaxed.

References chapter IV

[1] M. Wu and A. Ludwig, 'A three-phase model for mixed columnar-equiaxed solidification', *Metall. Mater. Trans. A*, vol. 37, no. 5, pp. 1613–1631, May 2006.

[2] L. Hachani, K. Zaidat, and Y. Fautrelle, 'Experimental study of the solidification of Sn–10wt.%Pb alloy under different forced convection in benchmark experiment', *Int. J. Heat Mass Transf.*, vol. 85, pp. 438–454, Jun. 2015.

[3] R. Boussaa, L. Hachani, O. Budenkova, V. Botton d, D. Henry, K. Zaidat, H. Ben Hadid, Y. Fautrelle., 'Macrosegregations in Sn-3 wt%Pb alloy solidification: Experimental and 3D numerical simulation investigations', *Int. J. Heat Mass Transf.*, vol. 100, pp. 680–690, Sep. 2016.

[4] Ch.-A. Gandin, T. Carozzani, H. Digonnet, S. Chen, and G. Guillemot, 'Direct Modeling of Structures and Segregations Up to Industrial Casting Scales', *JOM*, vol. 65, no. 9, pp. 1122–1130, Sep. 2013.

[5] T. Carozzani, C.-A. Gandin, H. Digonnet, M. Bellet, K. Zaidat, and Y. Fautrelle, 'Direct Simulation of a Solidification Benchmark Experiment', *Metall. Mater. Trans. A*, vol. 44, no. 2, pp. 873–887, Feb. 2013.

[6] A. I. Ciobanas and Y. Fautrelle, 'Ensemble averaged multiphase Eulerian model for columnar/equiaxed solidification of a binary alloy: I. The mathematical model', *J. Phys. Appl. Phys.*, vol. 40, no. 12, pp. 3733-3762, Jun. 2007.

[7] A. I. Ciobanas and Y. Fautrelle, 'Ensemble averaged multi-phase Eulerian model for columnar/equiaxed solidification of a binary alloy: II. Simulation of the columnar-to-equiaxed transition (CET)', *J. Phys. Appl. Phys.*, vol. 40, no. 14, pp. 4310-4336, Jul. 2007.

[8] M. Wu, A. Fjeld, and A. Ludwig, 'Modelling mixed columnar-equiaxed solidification with melt convection and grain sedimentation – Part I: Model description', *Comput. Mater. Sci.*, vol. 50, no. 1, pp. 32–42, Nov. 2010.

[9] M. Wu, A. Ludwig, and A. Fjeld, 'Modelling mixed columnar-equiaxed solidification with melt convection and grain sedimentation – Part II: Illustrative modelling results and parameter studies', *Comput. Mater. Sci.*, vol. 50, no. 1, pp. 43–58, Nov. 2010.

[10] C. Y. Wang and C. Beckermann, 'Equiaxed dendritic solidification with convection: Part I. Multiscale/multiphase modeling', *Metall. Mater. Trans. A*, vol. 27, no. 9, pp. 2754-2764, Sep. 1996.

[11] C. Y. Wang and C. Beckermann, 'A multiphase solute diffusion model for dendritic alloy solidification', *Metall. Trans. A*, vol 24, pages2787–2802 (1993).

[12] M. Rappaz and Ph. Thévoz, 'Solute diffusion model for equiaxed dendritic growth', *Acta Metall.*, vol. 35, no. 7, pp. 1487-1497, Jul. 1987.

[13] M. Rappaz and P. H. Thévoz, 'Solute diffusion model for equiaxed dendritic growth: Analytical solution', *Acta Metall.*, vol. 35, no. 12, pp. 2929–2933, Dec. 1987.

[14] M. Ahmadein, M. Wu, and A. Ludwig, 'Analysis of macrosegregation formation and columnar-to-equiaxed transition during solidification of Al-4wt.%Cu ingot using a 5-phase model', *J. Cryst. Growth*, vol. 417, pp. 65–74, May 2015.

[15] J. Ni and C. Beckermann, 'A volume-averaged two-phase model for transport phenomena during solidification', *Metall. Trans. B*, vol. 22, no. 3, p. 349, Jun. 1991.

[16] W. D. Bennon and F. P. Incropera, 'A continuum model for momentum, heat and species transport in binary solid-liquid phase change systems-I. Model formulation', *Int. J. Heat Mass Transf.*, vol. 30, no. 10, pp. 2161–2170, Oct. 1987.

[17] A. Kumar, M. Založnik, and H. Combeau, 'Study of the influence of mushy zone permeability laws on macro- and meso-segregations predictions', *Int. J. Therm. Sci.*, vol. 54, pp. 33–47, Apr. 2012.

[18] W Kurz, D. J. Fisher, *Fundamentals of Solidification*. 1989.

[19] S. McFadden and D. J. Browne, 'A generalised version of an Ivantsov-based dendrite growth model incorporating a facility for solute measurement ahead of the tip', *Comput. Mater. Sci.*, vol. 55, pp. 245-254, Apr. 2012.

[20] A. Kharicha, M. Stefan-Kharicha, A. Ludwig, and M. Wu, 'A scale adaptive dendritic envelope model of solidification at mesoscopic scales', *IOP Conf. Ser. Mater. Sci. Eng.*, vol. 84, Jun. 2015.

[21] M. Wu, J. Li, A. Ludwig, and A. Kharicha, 'Modeling diffusion-governed solidification of ternary alloys – Part 1: Coupling solidification kinetics with thermodynamics', *Comput. Mater. Sci.*, vol. 79, pp. 830–840, Nov. 2013.

[22] M. Založnik, "Transferts multi-échelles Modélisation multi-échelles". École thématique Solidification : fondamentaux et applications métallurgiques, juin 2021.

[23] J. Crank, *The mathematics of diffusion*, 2d ed. Oxford, Clarendon Press, 1975.

[24] E. Çadirli and M. Gündüz, 'The directional solidification of Pb-Sn alloys', *J. Mater. Sci.*, vol. 35, no. 15, pp. 3837-3848, Aug. 2000.

[25] H. Neumann-Heyme, K. Eckert, and C. Beckermann, 'Evolution of specific interface area in dendritic alloy solidification', *IOP Conf. Ser. Mater. Sci. Eng.*, vol. 84, Jun. 2015.

[26] M. Flemings, 'Coarsening in Solidification Processing', *Mater. Trans. - MATER TRANS*, vol. 46, pp. 895–900, May 2005.

[27] L. Hachani, 'Etude de l'influence de la convection naturelle et forcée sur le processus de la solidification : cas d'un alliage métallique binaire.', These de doctorat, Grenoble, 2013. Accessed: Mar. 29, 2021.

General Conclusions & Perspectives

GENERAL CONCLUSIONS AND PERSPECTIVES

The main objective of this work was to study the effect of natural and forced convection during the transition of liquid-solid phase change (solidification process) of pure tin and tin-lead binary metallic alloy. For this purpose, numerical models of solidification were realized with Comsol Multiphysics^{TM} which deals with the solidification of pure tin under the effect of natural convection, and forced convection generated by the application of a Traveling Magnetic Field (TMF), and Ansys software which simulates the solidification of tin-lead alloy (3-phase model) under only thermosolutal convection called also natural which is created by thermal and solutal gradients that was analyzed under several aspects: thermal, grain structure and concentration homogeneity (segregation). A particular interest in the configuration of solidification 'AFRODITE' setup, its crucible is assimilated to a differentially heated confined cavity. In this context, the purpose is to develop reliable numerical models to simulate the solidification processes, with a minimum computational time.

The first chapter of this work was therefore devoted to the bibliographical review on the solidification of pure metals and metal alloys in a general view, then, in a more detailed way, on the effect of natural/forced convection, the segregation phenomena and the crystal growth, which are the main object of this thesis. First, the modeling of liquid-solid phase change is considered for pure materials, and then for metallic alloys. The numerical approach used is the enthalpy method based on fixed-grid techniques which allows the resolution of a unique system of equations on the same studied domain (containing both the solid and liquid phases). It is well adapted to isothermal phase changes of pure materials. It has therefore been used to simulate the solid-liquid phase change of pure tin. In addition, the enthalpy approach is also suitable for the study of non-isothermal phase change with a mushy zone. It has therefore been used for the case of binary alloys solidification.

The numerical and experimental results were compared thanks to the 3D solidification model that was used to simulate the solidification of pure material (tin) under the effect of natural convection. The measured thermal fields and the solid-liquid front progress during the solidification period are in good agreement. This indicates that in the 3D simulation, the buoyancy convection is properly taken into account. In other side, the model used has also proven its ability to predict the process of tin solidification under forced convection generated by EMS in terms of velocity field, temperature behavior, and solidification front morphology. Also, the application of the EMS shown its effectiveness to homogenize and to master the temperature field during the stabilization stage (stage 04) on side, and on other it has an effect

on the solidification front morphology (stage 05) more particularly on the last liquid zone that was in the left bottom part in this model.

Of course, 3D numerical simulations are the most reliable to the real physics of the solidification phenomenon, but it remains expensive (in terms of computational time) for such processes of solidification, with so many coupled physical phenomena. For this reason, we have proposed a 2D model to simulate the solidification of a binary alloy by a three-phase numerical model, based on the resolution of momentum, energy and solute equations, considering the mushy zone as a porous medium taken into account by a Darcy term. This term contains a permeability factor *K* expressed from the liquid fraction and the secondary inter dendritic spacing λ_2. The multiphase volume or ensemble averaging technique was proposed in order to estimate the kinetic growth of the tip dendrite, based on *Ivantsov* dendrite growth model.

The 2D numerical simulation model of the Sn-10wt%Pb alloy solidification were compared to the experimental results, shows that the thermal fields are fairly reasonable results, this is because the model does not estimate particularly well the dissipative effects induced by the side walls (non-slip condition). Three other comparisons concern the ingot at the end of solidification. The first one, quantitative and also qualitative, consists in comparing the numerically mixture calculated concentration field with the X-Ray image of the solidified ingot by focusing on its largest face (100×60 mm^2). Indeed, on these images, the clear zones correspond to enrichment in lead. Thus, between the simulation and the experiment, we can see a similarity in the zones where the segregated channels appear. We also find the same arc shape of these channels. Finally, numerical and experimental qualitative comparisons of the final grain structure, the numerical results obtained present a partial agreement with the experimental results at the level of columnar structure, but not equiaxed. This model is interesting because it is reliable to the physics of the solidification of the binary alloy with a reduced calculation time.

The natural extension of this thesis would be, in terms of numerical modeling (more particular 3D models), to introduce an electromagnetic force in the three-phase solidification model or five-phase model (in the case where the equiaxed structure exist) in order to study the effects of convection in the presence of a variable magnetic field (in the direction of natural convection to promote it, in the opposite direction, an alternating field with a variable frequency) as it has shown its effectiveness to the homogenization of the temperature in the liquid bath during the solidification of pure tin. This offers the opportunity to avert defects due to segregation (concentration heterogeneity). Such defects are due to the effect of convection in the mushy

zone. These new calculations could allow a comparison with the solidification experiments under magnetic field that have already performed with AFRODITE. Another perspective would be to change the nominal concentration in order to see its influence on the formation of segregated channels and on the sedimentation of lead.

An application of this model on another geometrical configuration (for example a Bridgman experiment with a vertical temperature gradient) would also be interesting to validate it. There is a multitude of experiments done at the industrial or laboratory scale with variable geometries and different alloys that could be simulated.

Appendix

APPENDIX I

Appendix I.1. Phase diagram of Sn-Pb alloy

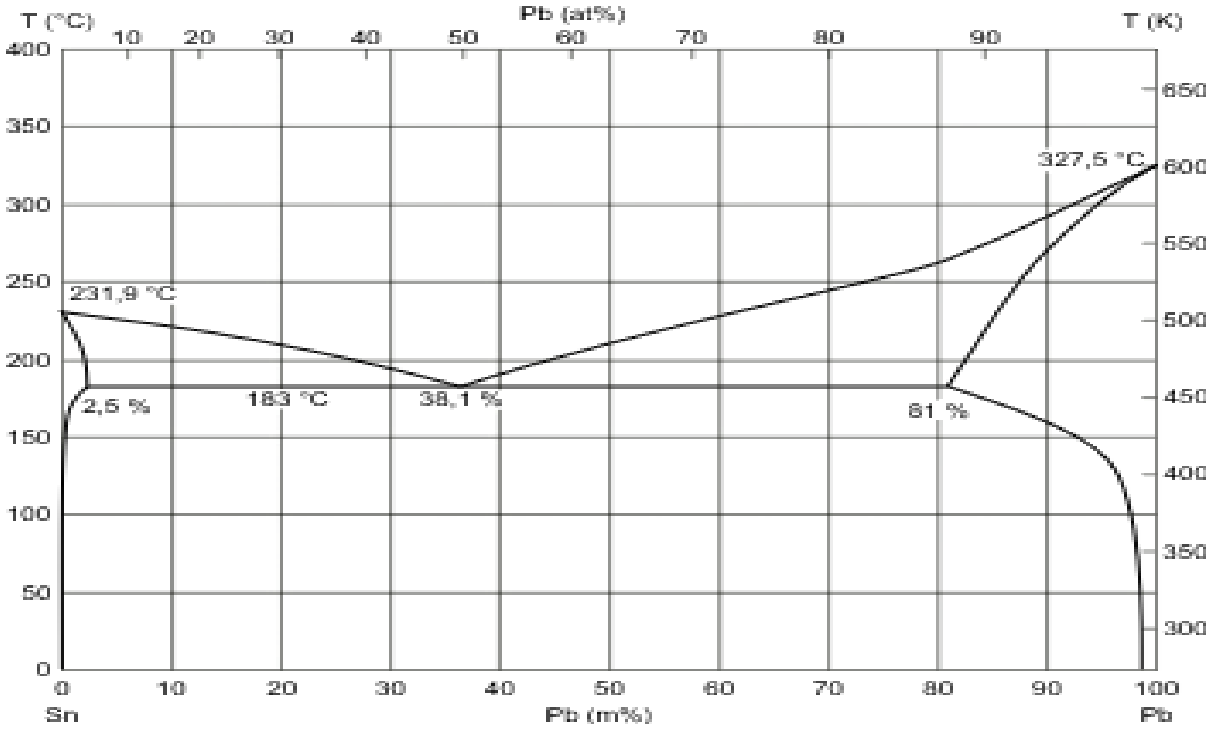

Appendix I.2. Thermo-physical properties of pure tin

Property	Unit	Value
Thermophysical data pure Sn		
Density, ρ	kg m^{-3}	7070
Coefficient of thermal expansion, β	K^{-1}	2.2e-5
Sn melting temperature, T_m	K	505
Enthalpy jump, *dH*	J kg^{-1}	59600
Solid metal heat capacity at constant pressure, *Cp1*	J/(kg.K)	200
Liquid metal heat capacity at constant pressure, *Cp2*	J/(kg.K)	318.81
Thermal conductivity, λ	W/ (m.K)	60
Dynamic viscosity, μ	Pa.s	0.00191
Kinematic viscosity, $\boldsymbol{\upsilon}$	m^2 s^{-1}	2.5e-7
Hot temperature, T_h	K	528
Cold temperature, T_c	K	508
Cooling rate, *CR*	K s^{-1}	0.03
Electromagnetic forces, Eq.		
Electrical conductivity, $\boldsymbol{\sigma}$	$\Omega^{-1}m^{-1}$	3.4 x 10^6
Frequency, *f*	Hz	50

Appendix I.3. The development of the electromagnetic force expressions

The expression of the electromagnetic force $\boldsymbol{F} = \boldsymbol{J} \times \boldsymbol{B}$ was developed for a confined configuration identical to that of our case, as follows:

$$\begin{cases} F_x = \frac{\sigma\omega k^*}{2} {A_0}^2\, exp(-2k^*z) + \frac{k^* A_0^2}{2} exp(-2k^*z)\left[\left(\frac{\pi}{2e}\right)^2 \frac{sin(2X^*)}{\mu} - \sigma\omega\, cos(2X^*)\right] \\ F_y = -\frac{\pi k^* \beta^* A_0^2}{2\mu e} exp(-2k^*z)\, cos(2X^*) + \frac{\pi A_0^2}{4\mu e}\beta^{*2}\, exp(-2k^*z)\, sin(2X^*) \\ F_z = \frac{A_0^2}{2}\left[\sigma\omega\beta^* - \left(\frac{\pi}{2e}\right)^2 \frac{k^*}{\mu}\right] exp(-2k^*z) - \frac{A_0^2}{2}\left[\sigma\omega\beta^* - \left(\frac{\pi}{2e}\right)^2 \frac{k^*}{\mu}\right] exp(-2k^*z)\, cos(2X^*) \\ \quad - \frac{A_0^2}{2}\left[\sigma\omega\beta^* - \left(\frac{\pi}{2e}\right)^2 \frac{k^*}{\mu}\right] exp(-2k^*z)\, sin(2X^*) \end{cases} \quad \text{(I.3.1)}$$

with $X^* = k^*x - \frac{\pi y}{2e} + \beta^* z - \omega t$

APPENDIX II

Appendix II.1. Thermal flux estimation method, based on complete quadratic element

This method uses a one-dimensional Lagrangian quadratic approximation in both directions ξ and η.

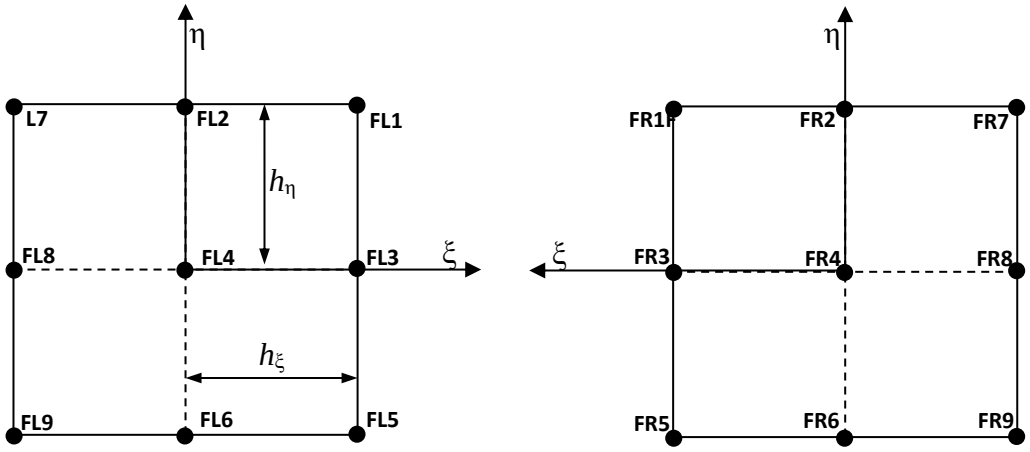

Fig. II.1. Diagram illustrating the distribution of the thermocouples of each exchanger on a complete quadratic element.

- **Interpolation functions**

{N}	$\{\partial N/\partial \xi\}$
FR1	$\frac{(1+2\xi)(1+\eta)\eta}{4}$
FR2	$-(1+\eta)\,\xi\,\eta$
FR3	$\frac{(1+2\xi)(1-\eta^2)}{2}$
FR4	$-2(1-\eta^2)\,\xi$
FR5	$\frac{-(1+2\xi)(1-\eta)\eta}{4}$
FR6	$(1-\eta)\,\xi\,\eta$
FR7	$\frac{-(1-2\xi)(1+\eta)\eta}{4}$
FR8	$\frac{-(1-2\xi)(1-\eta^2)}{2}$
FR9	$\frac{(1-2\xi)(1-\eta)\eta}{4}$

- **Application of the method**

It interpolates the temperature field using the functions Nn (x, y) defined previously:

$$T(x,y,t) = \sum_{n=1}^{9} N_n(x,y).T_n(t) \qquad \text{(II.1.1)}$$

Or:

$$\lambda.\left(\frac{\partial T}{\partial x}\right)_{\Gamma} = \lambda.\sum_{n=1}^{9} T_n(t)\left(\frac{\partial N_n(x,y)}{\partial x}\right) \qquad \text{(II.1.2)}$$

Γ : the exchange surface

- **Integration method on complete quadratic element**

In the exchange surface $\xi = 1$ and η [-1 ; +1]

$$\lambda.s.\left(\frac{\partial T}{\partial x}\right)_{\Gamma} = \frac{\lambda.s}{h_{\xi}}\int_{-1}^{+1}\left[\left(\frac{(1+2\xi)(1+\eta)\eta}{4}\right)FR1(t) + (-(1+\ \eta)\xi\ .\eta)FR2(t) + \left(\frac{(1+2\xi)(1-\eta^2)}{2}\right)FR3(t) + (-2(1-\ \eta^2)\ \xi)FR4(t) + \left(\frac{-(1+2\xi)(1-\eta)\eta}{4}\right)FR5(t) + ((1-\ \eta)\ \xi\ \eta)FR6(t) + \left(\frac{-(1-2\xi)(1+\eta)\eta}{4}\right)FR7(t) + \left(\frac{-(1-2\xi)(1-\eta^2)}{2}\right)FR8(t) + \left(\frac{(1-2\xi)(1-\eta)\eta}{4}\right)FR9(t)\right]_{\xi=1} d\eta \qquad \text{(II.1.3)}$$

$$\lambda.s.\left(\frac{\partial T}{\partial x}\right)_{\Gamma} = \frac{\lambda.s}{h_{\xi}}\int_{-1}^{+1}\left[\left(\frac{3(1+\eta)\eta}{4}\right)FR1(t) + (-(1+\ \eta)\ .\eta)FR2(t) + \left(\frac{3(1-\eta^2)}{2}\right)FR3(t) + (-2(1-\ \eta^2)\ )FR4(t) + \left(\frac{-3(1-\eta)\eta}{4}\right)FR5(t) + ((1-\ \eta)\ \eta)FR6(t) + \left(\frac{(1+\eta)\eta}{4}\right)FR7(t) + \left(\frac{(1-\eta^2)}{2}\right)FR8(t) + \left(\frac{-(1-\eta)\eta}{4}\right)FR9(t)\right]_{\xi=1} d\eta \qquad \text{(II.1.4)}$$

$$\lambda.s.\left(\frac{\partial T}{\partial x}\right)_{\Gamma} = \frac{\lambda.s}{h_{\xi}}\left[\left(\frac{3}{8}\eta^2 + \frac{3}{12}\eta^3\right)FR1(t) - \left(\frac{1}{2}\eta^2 + \frac{1}{3}\eta^3\ \right)FR2(t) + \left(\frac{3}{2}\eta - \frac{1}{2}\eta^3\right)FR3(t)\left(-2\eta + \frac{2}{3}\ \eta^3\right)\right)FR4(t) + \left(-\frac{3}{8}\eta^2 + \frac{3}{12}\eta^3\right)FR5(t) + \left(\frac{1}{2}\eta^2 - \frac{1}{3}\eta^3\ \right)FR6(t) + \left(\frac{1}{8}\eta^2 + \frac{1}{12}\eta^3\right)FR7(t) + \left(\frac{1}{2}\eta - \frac{1}{6}\eta^3\right)FR8(t) + \left(-\frac{1}{8}\eta^2 + \frac{1}{12}\eta^3\right)FR9(t)\right]_{-1}^{+1} \qquad \text{(II.1.5)}$$

$$\lambda.s.\left(\frac{\partial T}{\partial x}\right)_{\Gamma} = \frac{\lambda.s}{h_{\xi}}\left(\frac{FR1(t)}{2} - \frac{2}{3}FR2(t) + 2FR3(t) - \frac{8}{3}FR4(t) + \frac{1}{2}FR5(t) - \frac{2}{3}FR6(t) + \frac{1}{6}FR7(t) + \frac{2}{3}FR8(t) + \frac{1}{6}FR9(t)\right) \qquad \text{(II.1.6)}$$

- **Heat flow on the right side**

$$\phi_R(t) = \frac{\lambda.s}{h_\xi}\left(-\frac{FR1(t)}{2} + \frac{2}{3}FR2(t) - 2FR3(t) + \frac{8}{3}FR4(t) - \frac{1}{2}FR5(t) + \frac{2}{3}FR6(t) - \frac{1}{6}FR7(t) - \frac{2}{3}FR8(t) - \frac{1}{6}FR9(t)\right) \quad \text{(II.1.7)}$$

- **Heat flow on the left side**

$$\phi_L(t) = \frac{\lambda.s}{h_\xi}\left(\frac{FL1(t)}{2} - \frac{2}{3}FL2(t) + 2FL3(t) - \frac{8}{3}FL4(t) + \frac{1}{2}FL5(t) - \frac{2}{3}FL6(t) + \frac{1}{6}FL7(t) + \frac{2}{3}FL8(t) + \frac{1}{6}FL9(t)\right) \quad \text{(II.1.8)}$$

Where λ_{Cu} is the thermal conductivity of copper ($\lambda_{Cu} = 386W.m^{-1}.K^{-1}$), S the heat exchange surface ($S = 6.10^{-4}m^2$) and h_ξ is the step in the horizontal direction $\left(h_\xi = 15mm\right)$. (FL1, FL2, ...FL9) and (FR1, FR2, ..., FR9) are the thermocouples of the left and right exchanger respectively.

Appendix II.2. Instantaneous temperature matrices

Table II.1. The instantaneous temperature matrices recorded for the case of experimental natural convection

Time (s)	Temperature distribution (K)									
7609	519.80	515.16	513.88	513.54	513.71	513.22	512.42	511.83	511.15	507.91
	519.75	516.90	515.96	515.65	515.76	515.53	514.76	514.57	513.82	510.51
	521.30	518.65	517.88	517.56	517.94	517.51	516.85	516.51	515.84	513.00
	524.56	521.25	519.69	519.27	519.22	518.99	518.22	517.80	516.37	512.33
	527.67	523.29	520.81	520.01	519.62	519.47	518.65	517.81	515.43	510.35
7897	515.15	511.51	510.39	510.12	510.38	510.04	509.19	508.09	505.23	500.00
	515.11	512.75	512.01	511.64	511.84	511.68	510.81	510.06	506.89	501.56
	516.30	514.07	513.41	513.12	513.47	513.06	512.31	511.55	508.99	503.81
	518.73	516.14	514.80	514.44	514.40	514.19	513.36	512.64	510.06	504.30
	521.06	517.68	515.56	514.83	514.46	514.33	513.46	512.48	509.42	503.24
8735	504.49	505.13	505.19	505.60	504.14	500.49	496.07	491.31	486.59	479.31
	504.98	505.28	505.47	505.43	504.50	501.31	496.83	492.70	487.82	481.18
	505.11	505.19	505.42	505.45	504.98	501.98	497.74	493.49	488.86	482.70
	505.02	505.64	505.43	505.39	504.86	502.50	498.55	494.32	489.26	482.76
	504.42	505.47	505.18	504.88	504.13	502.41	499.01	494.85	490.31	485.21

APPENDIX III

Appendix III.1. Velocity field calculation

Table A.1. Time of passage of the solidification front recorded by each measurement point (10 thermocouples) (line located at mid-height of the sample). The table also gives the values of the velocity of the columnar front.

Nodes	Time of passage of the solidification front (s)	Estimation of the solidification front velocity $V_i = \Delta x / (Tag_{i+1} - Tag_i)$ in µm/s
L30	7900	$V_{30\text{-}29} = 45.45$
L29	8120	$V_{29\text{-}28} = 47.61$
L28	8330	$V_{28\text{-}27} = 57.14$
L27	8505	$V_{27\text{-}26} = 60.60$
L26	8670	$V_{26\text{-}25} = 83.33$
L25	8790	$V_{25\text{-}24} = 90.90$
L24	8900	$V_{24\text{-}23} = 95.23$
L23	9005	$V_{23\text{-}22} = 181.81$
L22	9060	$V_{22\text{-}21} = -250$
L21	9020	$V_{30\text{-}22} = 68.96$

Appendix III.2. Finite difference method

This appendix provides details concerning the discretization of the heat equation in the liquid zone (without latent heat).

The controlling heat equation:

$$\frac{\partial T}{\partial t} + \vec{U}.\vec{\nabla}T = \alpha \nabla^2 T \ ,$$

where α is the thermal diffusivity of the pure tin.

The heat equation is discretized by means of the finite difference method centred in space and a second order leap-frog scheme in time.

$$\left[\frac{\partial T}{\partial t}\right]_{(i,j)} = \left(\frac{T(i,j,k) - T(i,j,k-\delta t)}{\delta t}\right)$$

$$\left[\vec{\nabla}T\right]_{(i,j)}^{k-\delta t/2} = \left[\left(\frac{T(i,j+1,k-\delta t/2) - T(i,j-1,k-\delta t/2)}{2\delta x}\right)\left(\frac{T(i+1,j,k-\delta t/2) - T(i-1,j,k-\delta t/2)}{2\delta y}\right)\right]$$

$$[\nabla^2 T]_{(i,j)}^{k-\delta t/2} = \left[\left(\frac{T(i,j+1,k-\delta t/2) + T(i,j-1,k-\delta t/2) - 2T(i,j,k-\delta t/2)}{2\delta x^2}\right)\left(\frac{T(i+1,j,k-\delta t/2) + T(i-1,j,k-\delta t/2) - 2T(i,j,k-\delta t/2)}{2\delta y^2}\right)\right]$$

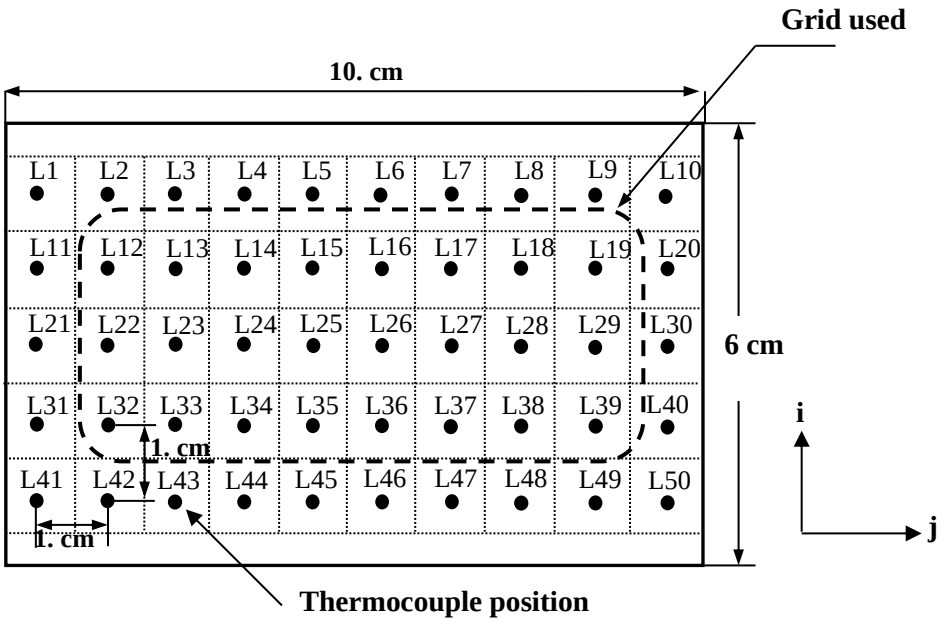

Fig. III. 1. Grid of points chosen for calculation of the field dynamic shown in the zone delimited by a discontinuous line.

APPENDIX IV

Appendix IV.1. Thermophysical properties and phase diagram of Sn-Pb alloy

Table IV.1. Thermophysical properties used in the coarsening of Sn-10wt%Pb alloy.

Properties	Description	Value
C_0	Initial concentration of alloy.	0.1
CR	Cooling rate, (K/s).	0.01
T_l	Liquidus temperature, ($°C$).	221.54
T_s	Solidus temperature, ($°C$).	183
uc	Undercooling, ($°C$).	1.77
Γ	Gibbs Thomson coefficient, ($m\ K$).	2.10^{-7}
D_l	Liquid Diffusion coefficient, ($m^2\ s^{-1}$).	10^{-9}
Initial conditions at t = 0 s.		
r_1	Initial radius of the small arm, (μm).	0.6
r_2	Initial radius of the big arm, (μm).	7
R_f	Final radius of the enveloped volume, (μm).	34.83
$\widetilde{C_0}$	Average liquid concentration.	0.1
$\widetilde{C}_{s_1}$	Solid concentration of the small arm.	0.0116
$\widetilde{C}_{s_2}$	Solid concentration of the big arm.	0.0116

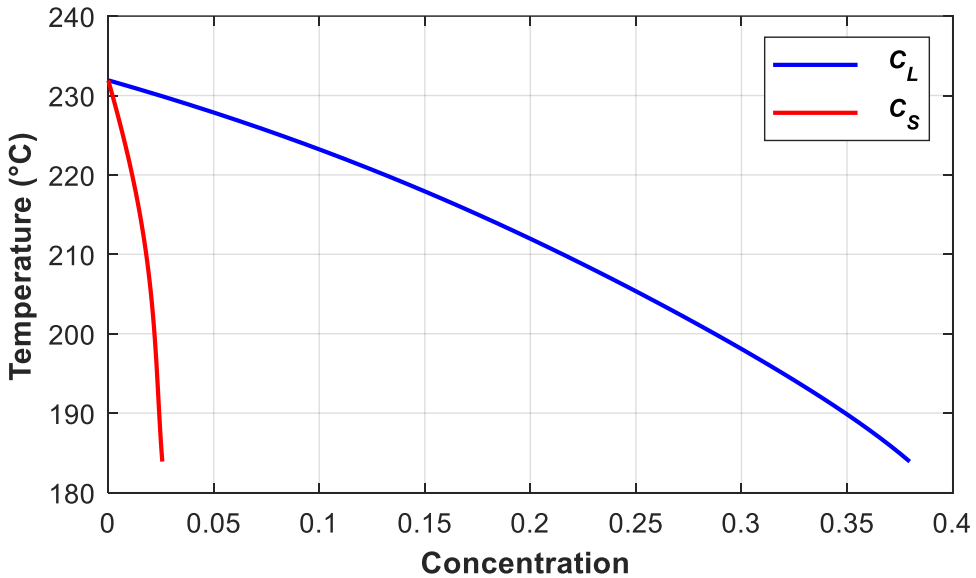

Fig. IV. 1. Phase diagram of Sn-Pb alloy.

$$C_L = p_1T^4 + p_2T^3 + p_3T^2 + p_4T + p_5 \quad \text{(IV.1)}$$

$$C_S = q_1T^4 + q_2T^3 + q_3T^2 + q_4T + q_5 \quad \text{(IV.2)}$$

Table IV.2. The corresponding constants of the liquidus and solidus concentration of Sn-Pb phase diagram.

$C_L(T)$				
p_1	p_2	p_3	p_4	p_5
$-3.4087.10^{-8}$	$2.7598.10^{-5}$	-0.008425	1.1423	-57.4175

$C_S(T)$				
q_1	q_2	q_3	q_4	q_5
$4.9099.10^{-9}$	$-4.2078.10^{-6}$	0.0013375	-0.18746	9.8205

Appendix IV.2. Phase diagram of Pb-Sn alloy (right side)

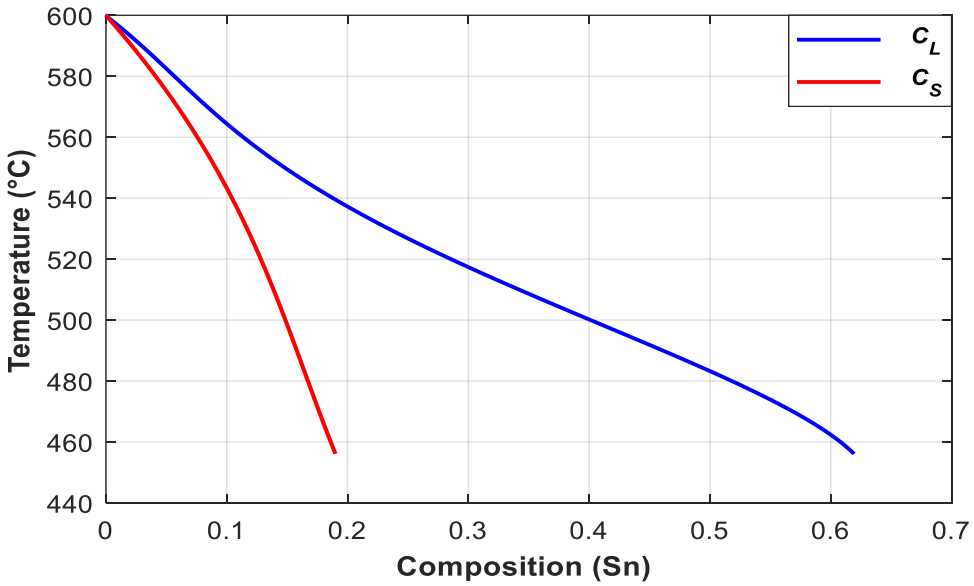

Fig. IV. 2. Phase diagram of Pb-Sn alloy.

$$C_L = p_1T^4 + p_2T^3 + p_3T^2 + p_4T + p_5 \quad \text{(IV.3)}$$

$$C_S = q_1T^4 + q_2T^3 + q_3T^2 + q_4T + q_5 \quad \text{(IV.4)}$$

Table IV.3. The corresponding constants of the liquidus and solidus concentration of Sn-Pb phase diagram.

$C_L(T)$				
p_1	p_2	p_3	p_4	p_5
$-2.9739.10^{-9}$	$6.4158.10^{-5}$	$-5.1601.10^{-3}$	1.8292	-240.28

$C_S(T)$				
q_1	q_2	q_3	q_4	q_5
$8.5229.10^{-11}$	$-2.0961.10^{-7}$	$1.8436.10^{-4}$	$7.0726.10^{-2}$	10.296

Appendix IV.3. Thermophysical properties and phase diagram of Al-Cu alloy

Table IV.4. Thermophysical properties used in the coarsening of Al-06wt%Cu alloy.

Properties	**Description**	**Value**
C_0	Initial concentration of alloy.	0.6
CR	Cooling rate, (K/s).	1
T_l	Liquidus temperature, (K).	645.5
T_s	Solidus temperature, (K).	548.2
uc	Undercooling, ($°C$).	0.7
Γ	Gibbs Thomson coefficient, ($m\ K$).	$2{,}4.10^{-7}$
D_l	Liquid Diffusion coefficient, ($m^2\ s^{-1}$).	3.10^{-9}
Initial conditions at t = 0 s.		
r_1	Initial radius of the small arm, (μm).	1
r_2	Initial radius of the big arm, (μm).	6
R_f	Final radius of the enveloped volume, (μm).	2
$\widetilde{C_0}$	Average liquid concentration.	0.6
$\widetilde{C}_{s_1}$	Solid concentration of the small arm.	0.0055
$\widetilde{C}_{s_2}$	Solid concentration of the big arm.	0.0055

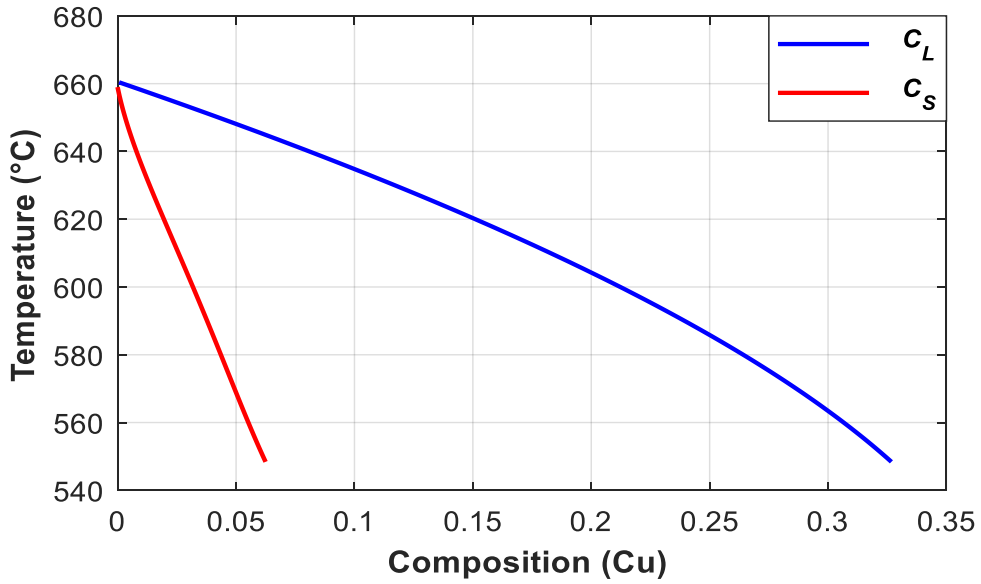

Fig. IV. 3. Phase diagram of Al-Cu alloy.

$$C_L = p_1 T^4 + p_2 T^3 + p_3 T^2 + p_4 T + p_5 \quad \text{(IV.5)}$$

$$C_S = q_1 T^4 + q_2 T^3 + q_3 T^2 + q_4 T + q_5 \quad \text{(IV.6)}$$

Table IV.5. The corresponding constants of the liquidus and solidus, concentration of Sn-Pb phase diagram.

$C_L(T)$				
p_1	p_2	p_3	p_4	p_5
$1.8778.10^{-11}$	$-3.8935.10^{-8}$	$1.7934.10^{-5}$	0.0014739	-1.152

$C_S(T)$				
q_1	q_2	q_3	q_4	q_5
$3.8154.10^{-10}$	$-9.065.10^{-7}$	0.00080682	−0.31942	47.585

Appendix IV.4

IV.4.1. Thermophysical properties of the Sn-Pb alloy

IV.4.1.1. The liquid density

In order to obtain the dependence of density on temperature and concentration, all the measurements results in the ranges of T – 600 K were approximated by S. V. Stanku *et al* [1] and presented in the following equation:

$$\rho_l = 7359.5 + 47.6554C - 0.10063C^2 - (0.74284 + 5.8927 \times 10^{-3}C)T \qquad \text{(IV.7)}$$

Where ρ_l is the density in $[kg/m^3]$, T is the temperature in Kelvin and C is the atomic concentration of Lead in the alloy.

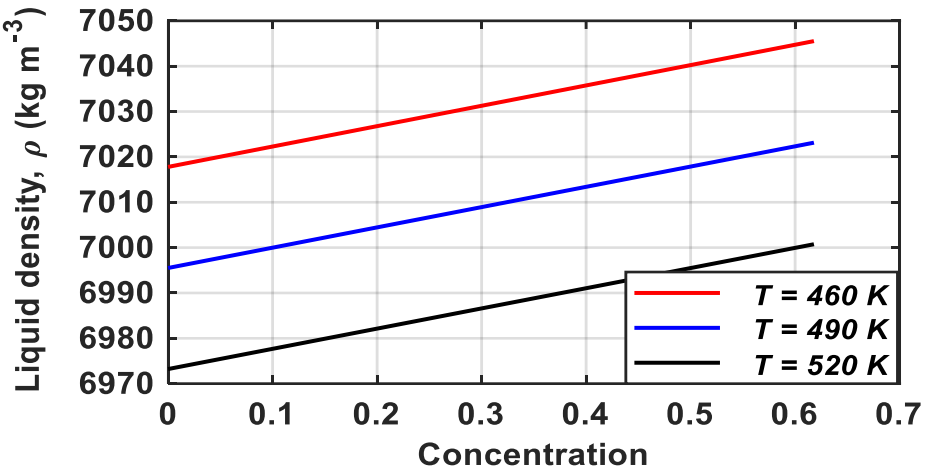

Fig IV.4. Measured value of the density vs the concentration composition for various temperatures.

Fig IV.4 shows the evolution of the density as a function of concentration with various temperatures: T = 460, 490 and 520 K are presented by red blue and black lines which varies in accordance with Eq. IV.7. One can notice that there is an inverse relation between the density and the temperature, while the density increases when the temperature decreases and vice versa. Also, continuous increase in density as the composition changes toward the eutectic composition.

The measurements of densities of several Pb-Sn liquid alloys are also presented by W. Gasior *et al* [2]. The experiments were carried out in the temperature range from 573 to 1200 K for the pure lead (Pb), pure tin (Sn), and 7 alloys with different initial compositions 0.1, 0.2, 0.261, 0.36, 0.5, 0.7, and 0.9 mole fraction of Pb (see Fig IV.5).

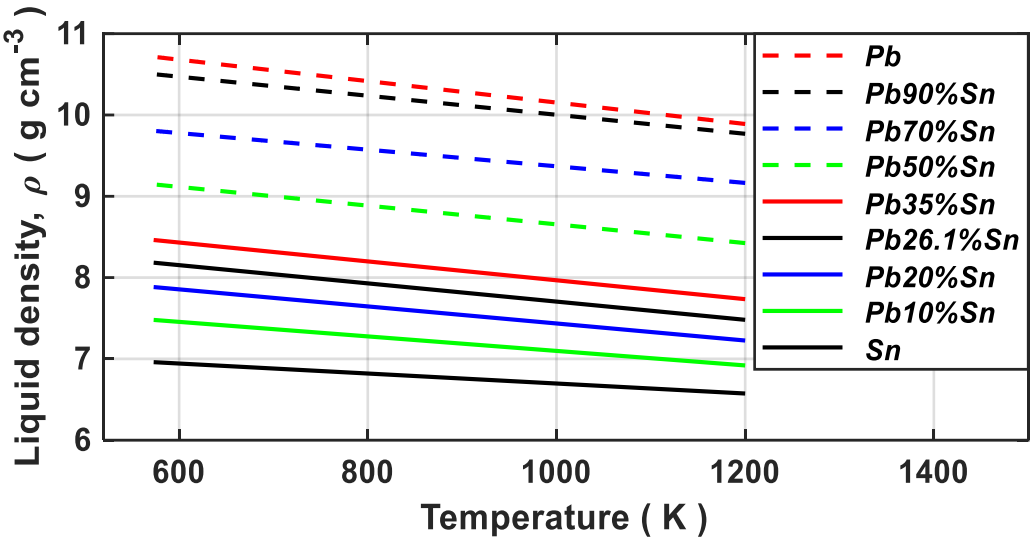

Fig IV.5. Temperature dependencies of the density of Pb-Sn liquid alloys, straight continuous lines present the densities obtained from Table IV.6.

Table IV.6. Temperature dependencies of the density of Pb-Sn liquid alloys with 'a' and 'b' are the parameter errors, [2].

X_{Pb}	$\rho = a + bT\ (g/cm^3)$
1.0000	11.4709 – 0.001318 T
0.9000	11.1727 – 0.001170 T
0.7000	10.3908 – 0.001022 T
0.5000	9.8066 – 0.001152 T
0.3500	9.1277 – 0.001161 T
0.2610	8.8256 – 0.001121 T
0.2000	8.4846 – 0.001049 T
0.1000	7.9910 – 0.000893 T
0.0000	7.3120 – 0.000615 T

In Fig. IV.5, the densities are calculated from the least-squares fits of Table IV.6 and their evolution presented as continuous lines (see Fig IV.5). The densities of tin and lead were also presented, it has been found that the temperature dependence of the density of the Pb-Sn liquid alloys are linear in the temperature range from 573 to 1200 K. Also, the densities decrease as the temperature increase. Moreover, the lead has a stronger density than the tin as shown in Fig IV.5.

T. Gancarz *et al* [3], have also studied the evolution of the density as a function of temperature as presented in Fig IV.6, indeed, we can notice that there is a good agreement between the current study and the previous one that have presented by W. Gasior *et al* [2] in terms of density of Sn-10wt%Pb alloy (the green continuous line in Fig IV.5).

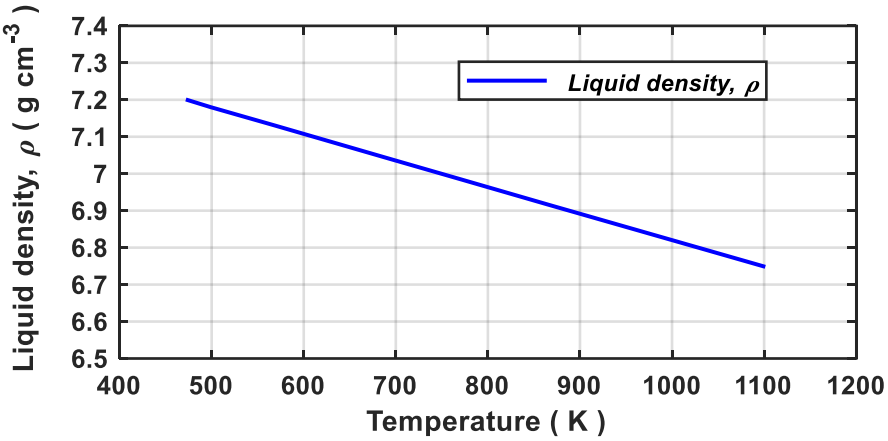

Fig IV.6. Temperature dependence of density of Sn-10wt%Pb alloy, [3].

IV.4.1.2. Liquid and solid thermal conductivity

The liquid and solid thermal conductivity of Sn-Pb alloy are defined as a function of the temperature have analysed by Osipenko [4] and were defined as follow:

$$\lambda_l(C_l[wt.\%]) = 25 + 0.02T - 0.35C_l + 0.002C_l^2[W/(m.K)] \quad \text{(IV.8)}$$

$$\lambda_s(C_l[wt.\%]) = 64.74 - 0.016T - 0.543C_s + 0.0023C_s^2[W/(m.K)] \quad \text{(IV.9)}$$

where λ_l and λ_s are the liquid and solid thermal conductivity respectively.

In the liquid state (Eq. IV.8), the thermal conductivity increases as the temperature increase (see Fig. IV.7 (b)). Also, we can see that there is a continuous decrease of the thermal conductivity as the initial composition changes (the composition near the pure tin has greater thermal conductivity). In another side, we can see in the solid case that the thermal conductivity decreases as the temperature increase (see Fig IV.7 (a)), this is due to the fact that the conductivity in the solid is higher than in liquid.

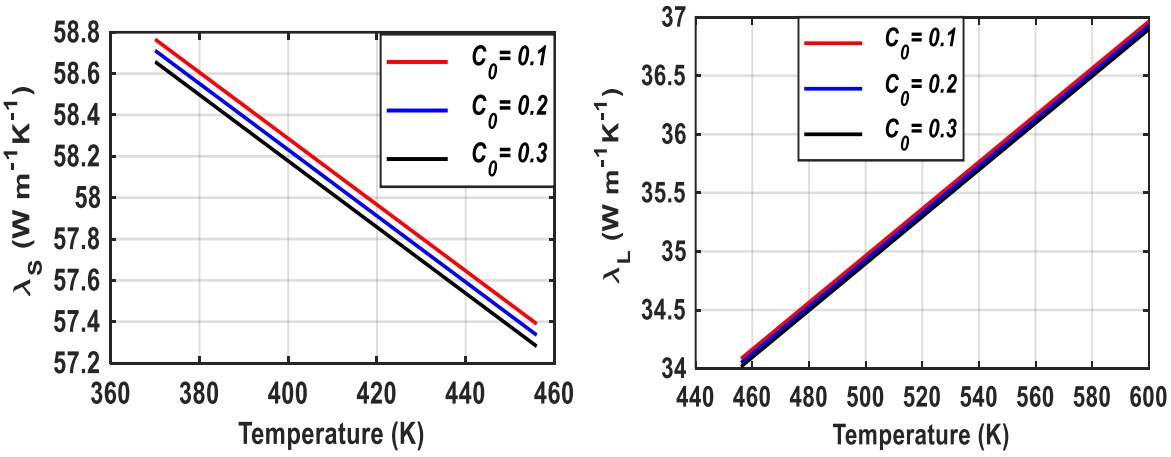

Fig IV.7. Measured value of: (a) the solid thermal conductivity and (b) the liquid thermal conductivity of the Sn-Pb alloy with different initial concentration.

S. Mhiaoui [5], has also analyzed the thermal conductivity of both liquid and solid of $Sn_{60}Pb_{40}$ alloy, by using the following expression:

$$\lambda_l = q_1 + q_2\sqrt{T} + q_3 T + q_4 T^2 \quad \text{(IV.10)}$$

$$\lambda_s = p_1 + p_2\sqrt{T} + p_3 T + p_4 T^2 + p_5 T^3 \quad \text{(IV.11)}$$

where the constants p and q are given in Table IV.7.

Table IV.7. Coefficients of polynomials adjusted on thermal conductivity of $\boldsymbol{Sn_{60}Pb_{40}}$ in the solid and liquid states.

Solid state	p_1	p_2	p_3	p_4	p_5
$Sn_{60}Pb_{40}$	48.40991	0.14599	0.018552	$-0.4602.10^{-3}$	$9.1703.10^{-7}$
Liquid state	q_1	q_2	q_3	q_4	
$Sn_{60}Pb_{40}$	9.56235	0.51364	0.016063	$-3.9743.10^{-6}$	

In Fig IV.8, the liquid thermal conductivity increases as the temperature increase, while it decreases in the solid state. However, the solid thermal conductivity is greater than the liquid thermal conductivity; this is due to the fact that the solid is a conductor (i.e., its conductivity should be greater than in liquid). The liquid and solid thermal conductivity vary in accordance with Eq. IV.10 and IV.11, respectively.

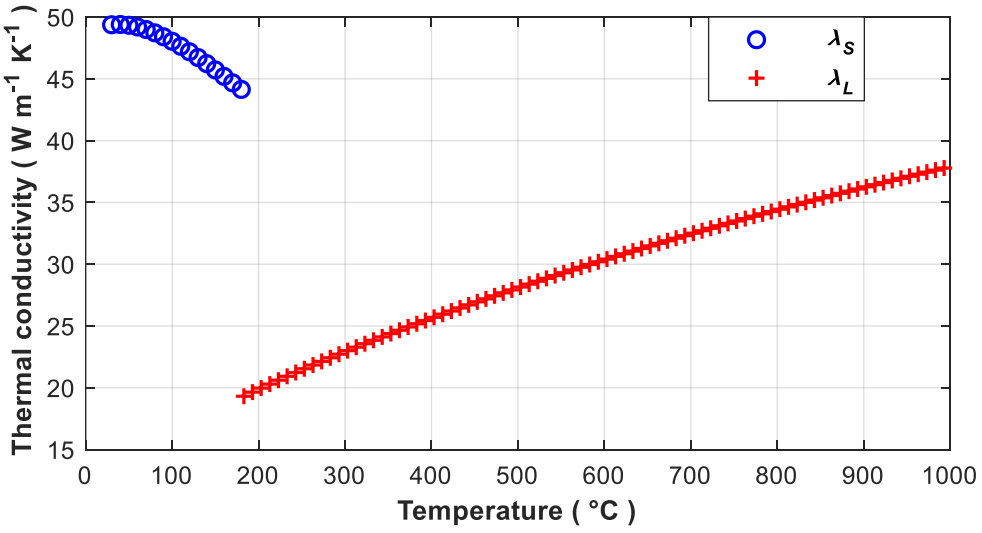

Fig IV.8. Thermal conductivity in the liquid (red circles) and solid (blue circles) state of $\boldsymbol{Sn_{60}Pb_{40}}$alloy, [5].

IV.4.1.3. The liquid diffusion

Diffusion is the net movement of particles from a region of higher concentration to a region of lower concentration. However, it is driven by a gradient in concentration. Also, chemical

diffusion is an irreversible transport phenomenon which tends to homogenize the composition of the medium. In the case of a binary mixture and in the absence of temperature and pressure gradients, the diffusion takes place from regions of higher concentration to regions of lower concentration. L. Hachani *et al* [6] have defined the diffusion coefficient for Pb in the liquid as follow:

$$D_l(T[K]) = 1.4 \times 10^{-7}\, exp\left(-\frac{2.29\times10^4}{RT}\right)[m^2/s] \qquad \text{(IV.12)}$$

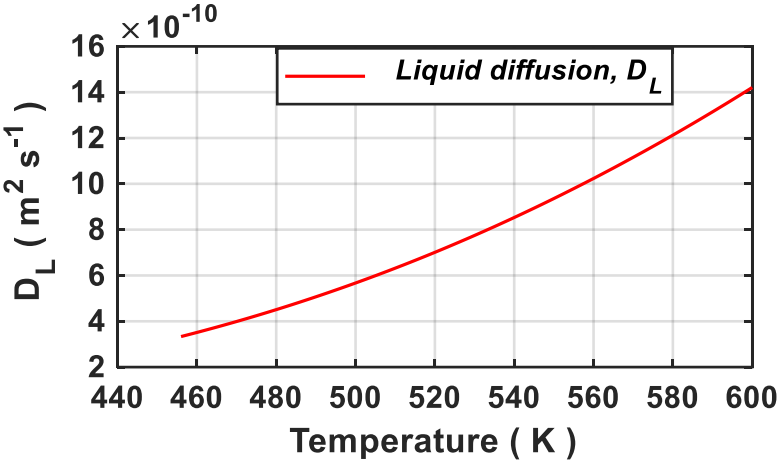

Fig IV.9. The liquid solute diffusivity of lead in pure tin.

Fig IV.9 presents the variation of the liquid diffusion coefficient which varies in accordance with Eq. IV.12. A smooth curve shows that the liquid diffusion increases as the temperature increase, (i.e., the liquid diffusion if greater in the purely liquid region than near the solid zone).

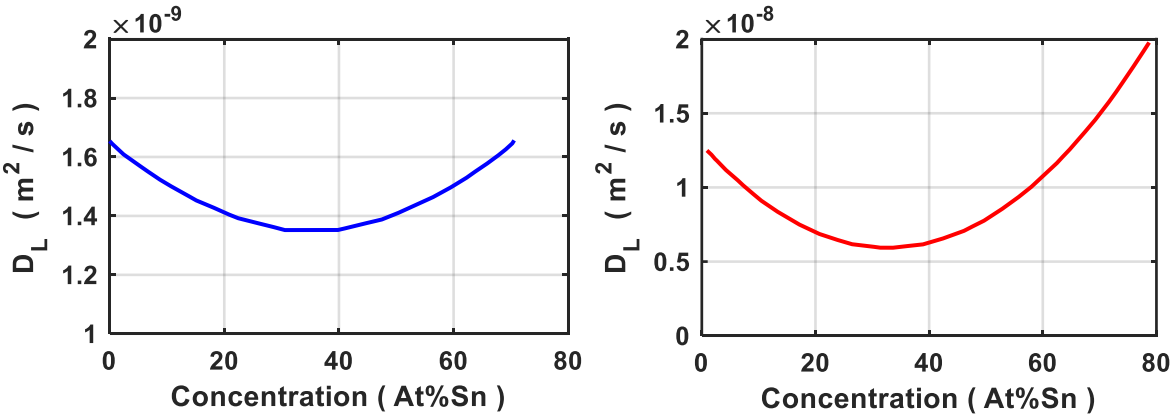

Fig IV.10. Variation of the liquid inter diffusion coefficient with concentration for the diffusion of Sn in Pb at 1031K and 668 K shown in (a) and (b) respectively, [7].

M. KLASSEN *et al* [7], have evaluated the liquid inter diffusion coefficient by using finite difference technique. They have supposed that the present values for the inter diffusion coefficients of Sn in Pb and for Pb in Sn are likely of the right order, but the temperature

dependence of the coefficients is likely incorrect, particularly at the higher temperatures. Also, it appears that all present and previous results for diffusion in Pb and Pb-rich alloys have been influenced by fluid flow.

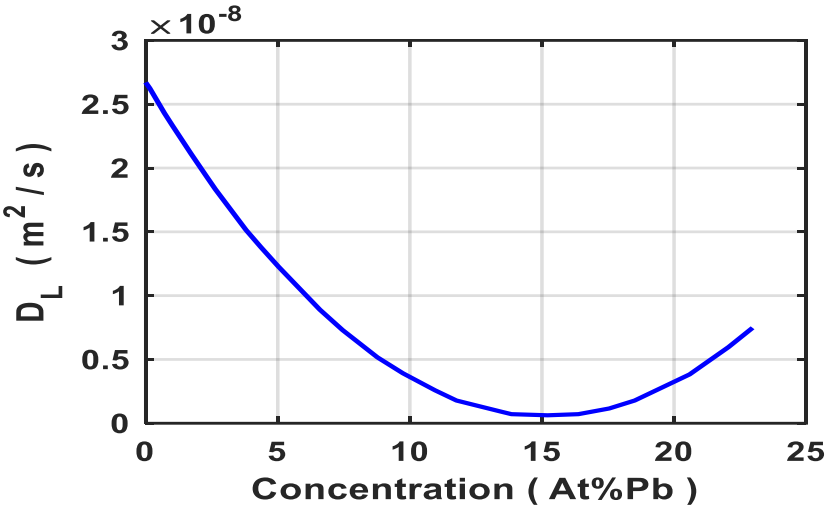

Fig IV.11. Variation of the inter diffusion coefficient with concentration for the diffusion of Pb in Sn at 1019K, [7].

IV.4.1.4. The liquid viscosity

The viscosity 'μ'of a fluid is a measure of its resistance to deformation at a given rate; it is well known that there is a direct relation between viscosity and temperature. Indeed, the viscosity increases during the solidification (as the temperature decrease) and it reaches its maximum value as the temperature decrease toward the solidus (T_{sol} = 456 K). The maximum value of the viscosity presents the solid phase (see Fig IV.12-13 and Fig IV.15-16), this latter causes a zero-velocity consequently stops the liquid movement. Yu. Plevachuk *et al* [8] have measured the liquid viscosity and they have approved that the direct results for each concentration showing good viscosity reproducibility as presented in Fig IV.12 and IV.13.

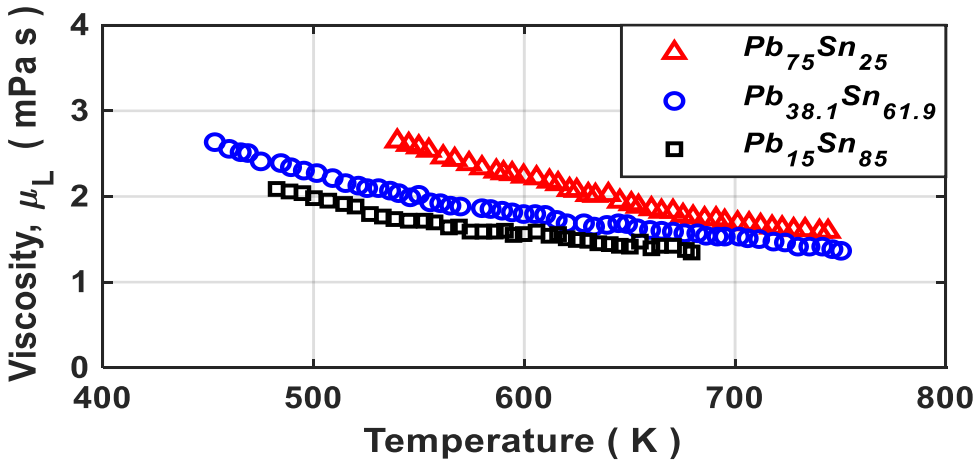

Fig IV.12. The liquid viscosity vs. temperature for $Pb_{15}Sn_{85}$, $Pb_{38.1}Sn_{61.9}$ and $Pb_{75}Sn_{25}$ liquid alloys, [8].

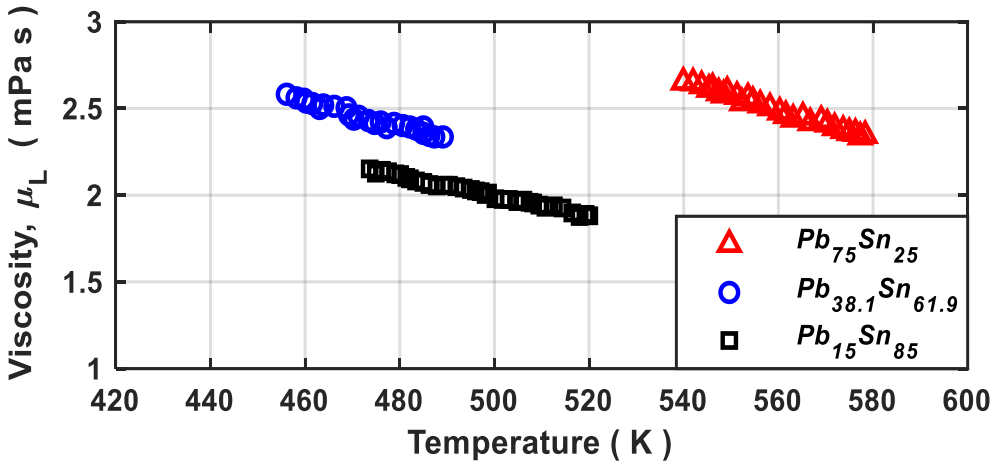

Fig IV.13. Viscosity vs. temperature for $Pb_{15}Sn_{85}$, $Pb_{38.1}Sn_{61.9}$ and $Pb_{75}Sn_{25}$ liquid alloys near T_{liq}, [8].

It should be noted that the viscosity as the most structural sensitive property does not reveal any peculiarity and exhibit a smooth exponential variation in the entire temperature range. On other hand, the viscosity increases also as the concentration composition increases as shown in Fig IV.14 which shows a rapid increase of the velocity as the concentration composition of Lead (Pb) increases until it reaches the eutectic composition then it will increase slowly.

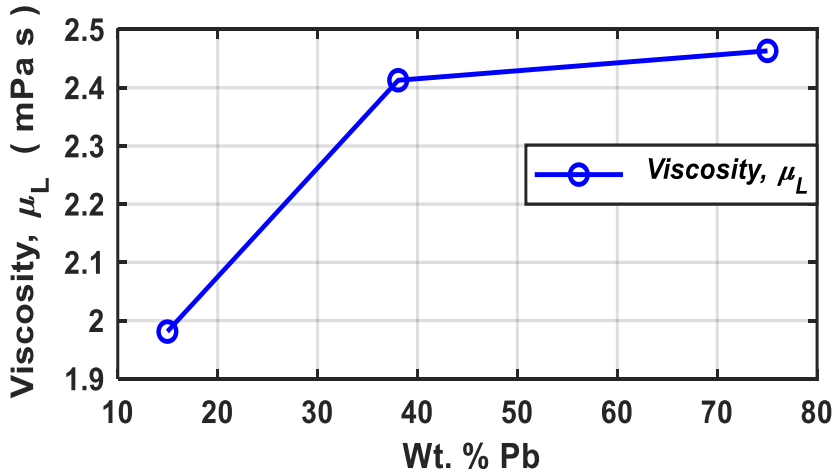

Fig IV.14. Viscosity vs. concentration of lead for the equally overheated melts at T_{liq} + 20 K, [8].

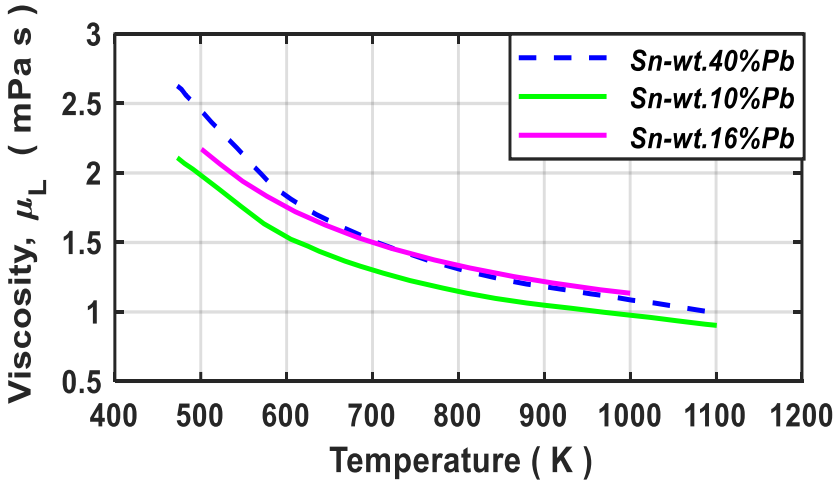

Fig IV.15. The evolutions of the liquid viscosity as a function of temperature for Sn-40wt%Pb, Sn-10wt%Pb and Sn-16wt%Pb alloys presented by blue, green and violate respectively, [3].

In addition, S. Mhiaoui [5] has evaluated the viscosity as presented in Fig IV.16, which shows the evolution of the viscosity as a function of temperature of $Sn_{90}Pb_{10}$ alloy. We can show clearly that when the temperature increases the viscosity decreases (liquid region), this is due to the fact that the viscosity is stronger in the solid than in liquid region. Also, the viscosity of liquid varies approximately exponentially with temperature (see Fig IV.12, IV.13, Fig IV.15 and Fig IV.16). This variation is described by Arrhenius law which is presented as follow, [5]:

$$\mu(T) = \mu_0 e^{\left(\frac{E_a}{RT}\right)} \qquad \text{(IV.13)}$$

where μ_0 is constant in [mPa.s], R is the gas constant ($J\ mol^{-1}\ K^{-1}$) and E_a is the activation energy ($J.mol^{-1}$).

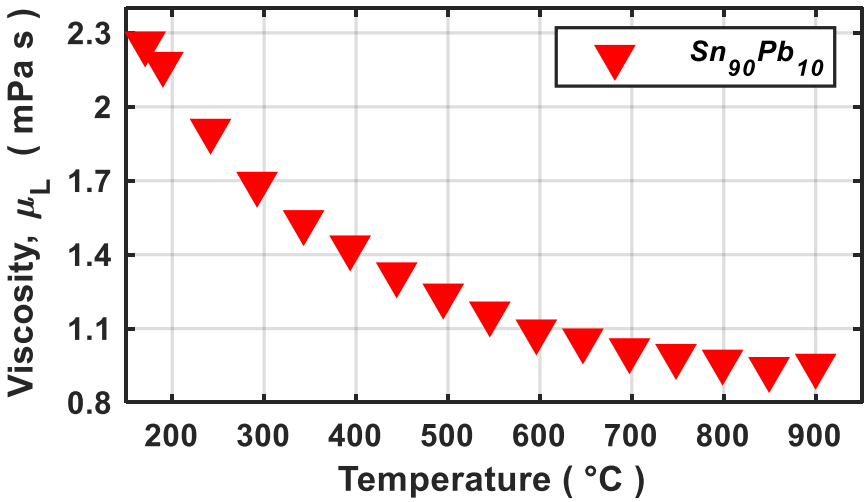

Fig IV.16. The liquid viscosity of $Sn_{90}Pb_{10}$ alloy as a function of temperature, [5].

The activation energy E_a and the constant μ_0 that presented in Eq. IV.13 are defined in Table IV.8.

Table IV.8. Determination of parameters $\boldsymbol{\mu_0}$ and $\boldsymbol{E_a}$ of $Sn_{60}Pb_{40}$ and $Sn_{90}Pb_{10}$ alloys, [5].

	$\mu(T) = \mu_0 e^{\left(\frac{E_a}{RT}\right)}$	
Alloys	μ_0 [*mPa.s*]	E_a [*KJ.mol*$^{-1}$]
$Sn_{60}Pb_{40}$	0.4791±0.0084	6.688±0.120
$Sn_{90}Pb_{10}$	0.4772±0.0066	5.893±0.067

IV.4.1.5. Thermal and solutal expansion coefficients

The density of the liquid changes as a function of the temperature or of the composition as discussed previously [1] and the liquid decreases during cooling stage. Enrichment in solute also makes it possible to increase or decrease the density of the liquid (Eq. IV.7). R Boussaa [9], has explained that these variations in density are characterized by the thermal expansion coefficients β_t and solutal β_c are defined by the following equations:

$$\beta_t = -\frac{1}{\rho_{ref}}\frac{d\rho_l}{dT} \quad \text{(IV.14)}$$

by derivation the liquid density ρ_l (Eq. IV.7) we will get:

$$\beta_t = \frac{1}{\rho_{ref}}(0.742841 + 5.8927 \times 10^{-3}C) \quad \text{(IV.15)}$$

However, the solutal expansion coefficient is the evolution concentration of the liquid density as follow:

$$\beta_c = -\frac{1}{\rho_{ref}}\frac{d\rho_l}{dC} \quad \text{(IV.16)}$$

Then, by derivation the liquid density ρ_l (Eq. IV.7) we will obtain:

$$\beta_c = -\frac{1}{\rho_{ref}}(47.6554 - 2 \times 0.10063 \times C - 5.8927 \times 10^{-3}T) \quad \text{(IV.17)}$$

where $\rho_{ref} = 7258{,}937\ [\mathrm{kg/m^3}]$

Density gradients create convective motions due to the differences in buoyancy force. However, we can see in Fig IV.17 (a) the solutal expansion coefficient that varies in accordance with Eq. IV.17 is frequently more 10 times greater than the coefficient of thermal expansion which is presented in Fig IV.17 (b) and it varies accordance with Eq. IV.15. In addition, β_c increases gradually as we increase in the initial concentration and it also increases as the temperature increases (see Fig IV.17 (a)). The same behavior was shown in Fig IV.17 (b) while, the thermal expansion coefficient increases with the concentration increase.

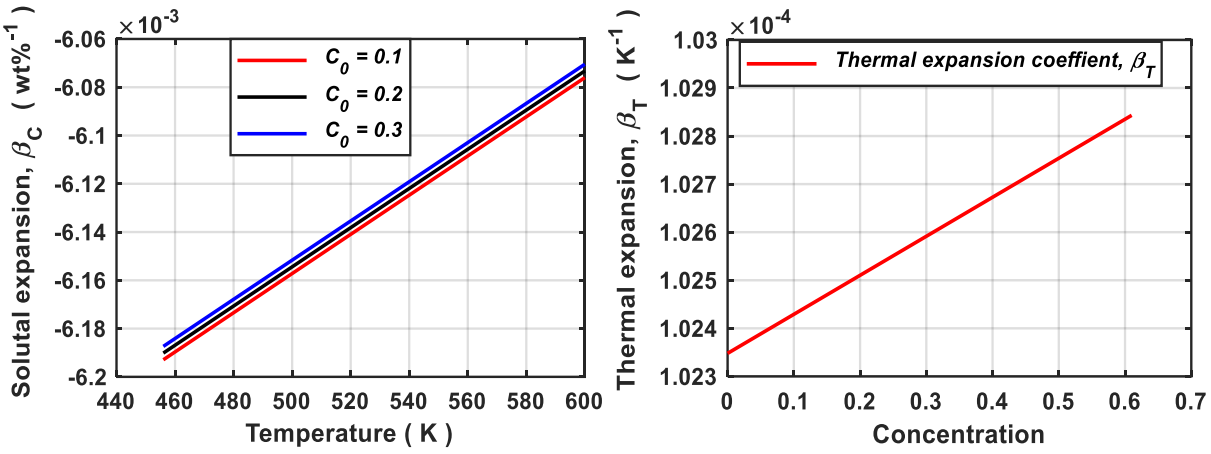

(a) (b)

Fig IV.17. (a) The evolution of solutal expansion coefficient vs Temperature for different initial concentration C_0 = 0.1, 0.2 and 0.3 presented by red, black and blue, respectively. (b) the evolution the thermal expansion coefficient vs concentration.

References appendix IV

[1] S. V. Stankus and R. A. Khairulin, « The density of alloys of tin—lead system in the solid and liquid states », *High Temp.*, vol. 44, n° 3, p. 389-395, mai 2006.

[2] W. Gąsior, Z. Moser, and J. Pstruś, « Density and surface tension of the Pb-Sn liquid alloys », *J. Phase Equilibria*, vol. 22, n° 1, p. 20-25, janv. 2001.

[3] T. Gancarz, J. Pstruś, W. Gąsior, et H. Henein, « Physicochemical Properties of Sn-Zn and SAC + Bi Alloys », *J. Electron. Mater.*, vol. 42, n° 2, p. 288-293, févr. 2013.

[4] V. P. Osipenko, « Thermal conductivity of alloys of the systems Sn-Pb and Sn-In in the solid and liquid states », *Sov. Phys. J.*, vol. 13, n° 12, p. 1570-1573, déc. 1970.

[5] S. Mhiaoui, « Propriétés physiques de soudures sans plomb à l'état liquide et solide », PhD dissertation in Physics, Paul Verlaine - Metz, 2007.

[6] L. Hachani, K. Zaidat, B. Saadi, X. D. Wang, et Y. Fautrelle, « Solidification of Sn–Pb alloys: Experiments on the influence of the initial concentration », *Int. J. Therm. Sci.*, vol. 91, p. 34-48, mai 2015.

[7] M. Klassen et J. R. Cahoon, « Interdiffusion of Sn and Pb in liquid Pb-Sn alloys », *Metall. Mater. Trans. A*, vol. 31, n° 5, p. 1343-1352, mai 2000.

[8] Yu. Plevachuk, V. Sklyarchuk, A. Yakymovych, B. Willers, et S. Eckert, « Electronic properties and viscosity of liquid Pb–Sn alloys », *J. Alloys Compd.*, vol. 394, n° 1, p. 63-68, mai 2005.

[9] R. Boussaa, « Étude de l'influence de la convection naturelle lors de la solidification de métaux purs et d'alliages métalliques binaires : expériences et simulations », These de doctorat, Lyon 1, 2014.

Abstract– As part of the PNE project (Program National Exceptional), this work aims to contribute to the development of a numerical tool predicting the influence of natural and forced convection on the phase change of pure metals and metallic alloys. The geometrical configuration considered throughout this study was chosen to correspond to the crucible of an experimental benchmark called 'AFRODITE', developed at the SIMAP-EPM laboratory in Grenoble/France. Different numerical models (2D and 3D) have been proposed to study different cases of solidification of pure metals and metallic alloys involving segregation phenomena. The 3D model, based on the enthalpy-porosity approach, has been applied to the case of pure tin solidification in order to study the effect of two types of dynamic configuration: purely thermal/natural convection and forced convection driven by an electromagnetic stirring generated by an external traveling magnetic field. Regarding the 2D model (based on three-phase crystal growth kinetics) under thermosolutal convection, it has been developed in order to better understand, master and control the solidification process of metallic alloys, in terms of final crystal structure and the defects that occur during solidification, including segregation at the meso and macroscopic scales. The numerical models developed are validated by in-situ and real time measurements of temperatures at any point of the solidification system, which allows a quantitative and qualitative validation.

Résumé– Dans le cadre du projet PNE (Programme National Exceptionnel), ce travail vise à contribuer au développement d'un outil numérique prédisant l'influence de la convection naturelle et forcée sur le changement de phase des métaux purs et d'alliages métalliques. La configuration géométrique considérée tout au long de cette étude a été choisie de manière à correspondre au creuset d'un benchmark expérimental appelé 'AFRODITE', développé au laboratoire SIMAP-EPM de Grenoble/France. Différents modèles numériques (2D et 3D) ont été proposés pour traiter des cas de solidification de corps pur et d'alliages métalliques avec ségrégation. Le modèle 3D basé sur l'approche d'enthalpie-porosité, a été appliquée au cas de la solidification de l'étain pur afin d'étudier l'effet de deux types de configuration dynamique : convection purement thermique/naturelle et convection forcée issue d'un brassage électromagnétique généré par un champ magnétique externe glissant. Quant au modèle 2D (basé sur la cinétique de croissance cristalline triphasique) sous convection thermosolutale, a été réalisé afin de mieux comprendre, maîtriser et contrôler le processus de solidification des alliages métalliques, en termes de structure cristalline finale et les défauts qui surviennent lors de la solidification, notamment la ségrégation à l'échelle meso et macroscopique. Les modèles numériques développés sont validés par des mesures in-situ et en temps réel des températures en tout point du système de solidification, ce qui permet une validation quantitative et qualitative.

ملخص– كجزء من مشروع البرنامج الوطني الاستثنائي، يهدف هذا العمل إلى المساهمة في تطوير أداة رقمية تتنبأ بتأثير الحمل الحراري الطبيعي والقسري على تغيير الطور للمعادن النقية وكذا السبائك المعدنية. تم اختيار الشكل الهندسي الذي تم تبنيه خلال هذه الدراسة بحيث يتوافق مع بوتقة معيار تجريبي يسمى "افروديت" الذي تم تطويره في مختبر العلوم وهندسة المواد والعمليات/المعالجة الكهرومغناطيسية للمواد في غرونوبل / فرنسا. تم اقتراح نماذج عددية مختلفة (ثنائية وثلاثية الأبعاد) لمعالجة حالات تصلب الأجسام النقية والسبائك المعدنية مع ظاهرة الانعزال الجسيمي. تم تطبيق النموذج ثلاثي الأبعاد القائم على مقاربة الاونثالبي-المسامي في حالة تصلب القصدير النقي لدراسة تأثير نوعين من الهيئة الديناميكية: الحمل الحراري الطبيعي البحت والحمل القسري الناجم عن التحريك الكهرومغناطيسي والذي بدوره ناتج عن المجال المغناطيسي المتنقل الخارجي. أما بالنسبة للنموذج ثنائي الأبعاد (المعتمد على حركية النمو البلوري ثلاثي الأطوار) تحت الحمل الحراري الطبيعي ، فقد تم تنفيذه من أجل فهم أفضل وإتقان والتحكم في عملية تصلب السبائك المعدنية ، من حيث التركيب البلوري النهائي والعيوب التي تحدث أثناء التصلب ، ولا سيما الانعزال الجسيمي على النطاق المتوسط والعياني. تم التحقق من صحة النماذج الرقمية المطورة من خلال قياسات مباشرة في الموقع وفي الوقت الحقيقي لدرجات الحرارة في أي نقطة من نظام التصلب ، مما يسمح بالتحقق الكمي والنوعي.